

Strategies for faster impregnation in melt thermoplastic resin transfer molding process

THÈSE N° 8763 (2018)

PRÉSENTÉE LE 24 AOÛT 2018

À LA FACULTÉ DES SCIENCES ET TECHNIQUES DE L'INGÉNIEUR
LABORATOIRE DE TECHNOLOGIE DES COMPOSITES ET POLYMÈRES
PROGRAMME DOCTORAL EN SCIENCE ET GÉNIE DES MATÉRIAUX

ÉCOLE POLYTECHNIQUE FÉDÉRALE DE LAUSANNE

POUR L'OBTENTION DU GRADE DE DOCTEUR ÈS SCIENCES

PAR

Damiano SALVATORI

acceptée sur proposition du jury:

Prof. C. Hébert, présidente du jury
Prof. V. Michaud, directrice de thèse
Dr G. Orange, rapporteur
Prof. J. Bréard, rapporteur
Prof. F. Sorin, rapporteur



ÉCOLE POLYTECHNIQUE
FÉDÉRALE DE LAUSANNE

Suisse
2018

*The duty of the men of culture is
today more than ever
to sow doubts
rather than harvest certitudes.*

Norberto Bobbio

Abstract

Continuous fiber thermoplastic composites are potential substitutes of steel in structural automotive components, since they combine fiber strength and rigidity with ductility, potential recyclability and low density of the thermoplastic (TP) matrix. Resin transfer molding (RTM) is a process for composite production, involving direct impregnation of a reinforcing fabric in a closed rigid mold with a liquid resin. The duration of the impregnation step is directly proportional to the resin viscosity and inversely proportional to the fabric in-plane permeability. As a result, the high viscosity of melt thermoplastic resins (mTP) generally precludes their use in RTM, in particular to reach production volumes in line with the automotive sector. However, recent development of high-fluidity (HF) TPs, with medium range viscosity (10-50 Pa s) opens new possibilities for mTP-RTM.

The goal of this thesis is to explore strategies to enhance the impregnation kinetics in mTP-RTM with HFTP by further increasing the fabric in-plane permeability. The effect of modified fabric architectures was investigated through experiments allowing visualization of flow propagation and permeability measurement using model fluids on a modified non-crimp fabric. A saturated permeability of ca 10^{-9} m² for 46 vol% fibers was measured. The mesoscopic pore-space of the compacted fabrics was imaged with X-ray Tomography, and analyzed to propose permeability predictions based on the large channels geometry, which agreed well with the experimental results. Capillary effects were assessed over a broad range of capillary numbers (from $4 \cdot 10^{-5}$ to 0.4) by direct comparison of unsaturated and saturated permeability. Permeability in these dual-scale fabrics is governed by viscous flow in the meso-channels. As a result, provided that the capillary number exceeds a threshold value, their permeability can be rather accurately measured by carrying out unsaturated measurements, neglecting micro-flow and capillary effects.

Further improvement up to 10^{-8} m² for 46 vol% fibers was achieved by introducing a flow-enhancing structure, made by polymer 3D-printing in the core of a woven fabric stack. The resulting flow was markedly dual-scale, going first very quickly in the core and later through the fabric. Optimized impregnation time was obtained by pulling vacuum prior to injection, letting the fluid flow within the core to the outlet, which is then closed, and finally continue the injection through thickness to complete saturation.

A proof of concept with epoxy resin showed that a poly(lactic acid) spacer led to an increased bending stiffness of 20%, but strong reinforcement gradients. Using a sacrificial spacer made of polycaprolactone, which melted during resin cure (80°C) allowed full fabric relaxation and a more homogeneous fibers distribution.

Finally, these findings were applied to the development of a mTP-RTM mold to produce plates with HF polyamide 6 matrix. An 11 cm-long plate with 46 vol% glass fibers was impregnated in 7 min (1 min in the core, 6 min through the fabric) using high temperature spacers compared to more than 45 min without, also with improved bending stiffness by 26%. This concept is conceivably scalable to larger parts, since the bottleneck of the whole process is transferred to the saturation step. A preliminary cost analysis was carried out to evaluate the scalability of this technique as compared to alternative compression TP-RTM or a baseline epoxy RTM process.

Keywords: thermoplastic composites; resin transfer molding; liquid composite molding; melt thermoplastic processing; fabric permeability; dual-scale flow; unsaturated permeability; capillary effects; 3D-printing.

Résumé

Les composites thermoplastiques à fibres longues pourraient remplacer l'acier pour des pièces de structure dans l'industrie automobile, car ils allient résistance et rigidité des fibres avec la ductilité, recyclabilité potentielle et faible densité d'une matrice thermoplastique (TP). Le moulage par transfert de résine (RTM-TP) est un procédé de fabrication par imprégnation directe d'une résine fluide dans un tissu de renfort placé dans un moule rigide fermé. La durée de l'imprégnation est directement proportionnelle à la viscosité du fluide et inversement proportionnelle à la perméabilité dans le plan du renfort. La haute viscosité des TP fondus restreint leur utilisation en RTM, en particulier pour des grands volumes de production. Néanmoins, le récent développement de TP haute fluidité (TPHF) (viscosité 10-50 Pa s) ouvre de nouvelles possibilités pour le RTM-TP.

Cette thèse se propose d'explorer des stratégies pour augmenter la cinétique d'imprégnation dans le RTM-TP en augmentant la perméabilité des renforts. L'effet de la modification de l'architecture du renfort est analysé par des expériences permettant de visualiser l'écoulement et mesurer la perméabilité avec des fluides modèles. Une perméabilité saturée d'environ 10^{-9} m^2 pour 46 vol% de fibres a été mesurée pour un nouveau renfort non-crêpé, 10 fois plus que celle d'un renfort tissé de référence. L'espace poral des renforts compactés a été révélé par Tomodensitométrie RX, et analysé pour prédire la perméabilité basée sur la géométrie des canaux, en bon accord avec les valeurs expérimentales. Les effets capillaires sont évalués dans une large gamme (nombre capillaire Ca entre $4 \cdot 10^{-5}$ et 0.4) par comparaison directe des perméabilités saturée et insaturée. La perméabilité de ces renforts à deux échelles est dictée par les écoulements visqueux dans les méso-canaux. En conséquence, si Ca est au delà d'une certaine valeur critique, la perméabilité peut être correctement mesurée par des tests non-saturés, négligeant les effets capillaires et le fluide dans les mèches.

Une amélioration de la perméabilité jusqu'à 10^{-8} m^2 pour 46 vol% de fibres a été atteinte en introduisant une structure creuse (*spacer*) au milieu d'un empilement de renforts. Un écoulement à forte séparation d'échelle en résulte, très rapide dans les canaux puis à travers le tissu. Le temps d'imprégnation est optimisé en évacuant le moule avant l'injection, laissant le fluide s'écouler le long des canaux puis en maintenant la pression d'injection pour forcer la saturation transverse. Un test avec une résine époxyde et un *spacer* en PLA a augmenté la rigidité en flexion du composite de 20%, mais avec des forts gradients de taux de fibre. Avec un *spacer* sacrificiel en PCL, qui fond pendant

la réticulation de la résine, une distribution plus homogène des fibres est obtenue par relaxation du tissu.

Finalement, ces résultats ont été appliqués pour la production de plaques par RTM-TP avec du polyamide 6 à haute fluidité. Une plaque de 11 cm de longueur et 46 vol% de fibres est imprégnée en 7 min (1 min dans les canaux et 6 min dans le tissu), en utilisant des *spacers*, comparée à 45 min sans. En principe, ce concept peut s'appliquer facilement à de plus grandes pièces, puisque la limite est transférée à l'étape de saturation, qui dépend de l'épaisseur. Une étude de coût préliminaire conclut ce travail, pour évaluer la mise à l'échelle du procédé, en comparaison avec le compression-RTM-TP ou un procédé RTM époxy traditionnel.

Mots-clés: composites thermoplastiques; moulage par transfert de résine; moulage de composites par voie liquide; mise en œuvre de thermoplastiques à l'état fondu; perméabilité de tissus; écoulement double échelle; perméabilité insaturée; effets capillaires; impression 3D.

Acknowledgements

This thesis is the result of four years of work at the Laboratory for Processing of Advanced Composites (LPAC), previously Laboratory of Technology of Composites and Polymers (LTC), at the Ecole Polytechnique Fédérale de Lausanne (EPFL). The project has been funded by the Swiss Competence Center for Energy Research (SCCER-Mobility) and Solvay (Research Center of Lyon, France), which are thankfully acknowledged.

I want to express my deep gratitude to my advisor, Prof. Véronique Michaud, who has trustfully supported me during these four years. She gave me the chance to carry out this project dosing a large degree of freedom with numerous helpful inputs. I am very thankful for her continuously positive and enthusiastic attitude. Many thanks to Prof. Jan-Anders Månson, for accepting me in the lab four years ago, and to Dr. Pierre-Etienne Bourban, Dr. Christopher Plummer and Dr. Sara Dalle Vacche, who have followed the advancement of this project since the beginning during our internal meetings and informal discussions. I want to thank all the members of the jury, Prof. Joël Bréard, Dr. Gilles Orange, Prof. Fabien Sorin, and Prof. Cécile Hebert, who expressed great appreciation and gave precious comments to improve the quality of this thesis. Thanks to all the members of the SCCER-Mobility Capacity Area 3, in particular to Prof. Clemens Dransfeld and Julia Studer from the Institute of Polymer Engineering at Fachhochschule Nordwestschweiz (FHNW), for the many fruitful discussions we had, and Martin Eichenhofer from the Laboratory of Composite Materials and Adaptive Structures (ETH Zurich) who kindly provided some useful materials. Thanks to Jérôme Maupetit from ChomarTM (Le Cheylard, France) for providing large amounts of glass fabrics. The mechanical workshop at the Institute of Materials (ATMX) is kindly acknowledged for helping with the design and manufacturing of tools and setups.

Thanks to all the people I met at LPAC, and previously at LTC. Some of them contributed actively to this project, others were often open to suggestions, and with most of them we shared many amusing moments. The border between colleagues and friends is often quite vague. Thanks to Dr. Yves Leterrier, for the curious scientist he is; Cécile, for always helping with a smile; Helena, who has significantly contributed to part of the experiments; Maxime, who helped with the design of an important setup; Amaël, for organizing leisure activities and lab cleaning; Mathieu, my messy office mate, who was always available for a quick help; Feyza, always so kind and helpful; Pierre, my very first French teacher; Joris, for his ability of doing self-mockery; Luis, my first office mate, who friendly welcomed me in the first place; Yong-Hoon, because there is always time for a beer; Yann, for his good mood; and all the others who contributed to make the lab

such an enjoyable environment. Thanks also to all the students with whom I have had the pleasure to work for their valuable contribution: Lucien, Sheerin, Thibault, Francesco, Robin and Johnathan. Last of this list, but not least, I am infinitely grateful to Dr. Barış Çağlar, the person without whom this work would have been less successful. He is one of the smartest researchers I have ever met; he turned out to be one of my best friends.

Many other people have been part of my life during these four years of personal and professional growth. I am afraid I fail in the attempt of expressing how lucky I feel I am. Thanks to Daniele, the very person who has been present since day zero till the end of this adventure. We have shared similar doubts and issues, but also the same passions. Even though in the future our paths might diverge, I know that I have found a true friend. Thanks to Fede and Marta, for their non-invasive, respectful, constant presence that always makes me feel home. They have been there during the toughest moments, and I am honored to be one of their best friends. Thanks to Matteo, a colleague, a friend and a flat mate at once, for being such a generous and optimistic person. Thanks to the other “pasta eaters”, Tommaso, Claudia, Alessandra and Fabio, who welcomed me and made me feel home since my first day in Lausanne. Thanks to all the other friends in Lausanne, Büşra, Edoardo, Chiara, Federico, Mathieu and Natalia, for the good time spent together. Thanks to Alice, for having been such an important part of my life. Thanks to my friends in Rome, particularly to Matteo, Paolo, Stefano and Lorenzo, who came all the way to visit me with lots of food supplies; we had so much fun! Thanks to Alessandro, Federica and Antonio, my high-school friends; even though we are far, we always manage to reconvene, and it is like we are still the same, despite so many changes. Thanks to my parents and siblings, for the love and affection they show me whenever I am back. Finally, thanks to Lara, who inspires me to always give my best. She is total acceptance and sweet encouragement. She is the one who always believes in me and gives me hope for the future. She is my greatest achievement.

Contents

Abstract	v
Acknowledgements	ix
Contents	xi
List of Figures	xv
List of Tables	xxi
Abbreviations	xxiii
Symbols	xxv
1 Introduction	1
1.1 Lightweight materials in transportation	3
1.2 Motivations and objectives	7
1.3 Research framework	11
1.4 Thesis plan	12
2 State of the art	15
2.1 Thermoplastic polymers and composites in the automotive industry	15
2.1.1 Polymer matrix composites	16
2.1.2 Thermoplastic matrices	19
2.1.3 Specific requirements	23
2.2 Physical properties of thermoplastic polymers	25
2.2.1 Rheology of thermoplastic polymers	25
2.2.2 Polymer crystallization	26
2.3 Manufacturing of polymer matrix composites	29
2.3.1 Compression molding	30
2.3.2 Liquid composite molding	32
2.4 Modeling of Liquid Composite Molding	36

2.4.1	Permeability measurements	38
2.4.2	Capillary effects	40
2.4.3	Differences between unsaturated and saturated permeability	43
2.5	Permeability enhancement	45
2.5.1	Effect of textile architecture on permeability	45
2.5.2	Effect of a second solid phase on permeability	48
2.6	Conclusions	49
3	Materials and methods	51
3.1	Materials	51
3.1.1	Test-fluids for flow studies	51
3.1.2	Glass-fabrics	52
3.1.3	High-fluidity thermoplastic matrices	53
3.2	Methods	54
3.2.1	Flow studies	54
3.2.2	Characterization of thermoplastic matrices	60
3.2.3	Production and analysis of composite plates	64
4	Flow studies on selected fabrics	67
4.1	Characterization of two highly-permeable fabrics	67
4.1.1	Fabric compaction	68
4.1.2	Permeability measurements	70
4.2	Permeability and capillary effects in a channel-wise non-crimp fabric	71
4.2.1	Saturated permeability	72
4.2.2	Microstructural analysis	73
4.2.3	Unsaturated permeability	82
4.3	Conclusions and outlook	87
5	Enhancing permeability with spacers	89
5.1	Concept	89
5.2	Design and fabrication	91
5.2.1	3D model design	91
5.2.2	Preform structure	92
5.2.3	Fabrication by 3D-Printing	93
5.3	Experiments	94
5.3.1	Compression tests on spacers	95
5.3.2	Compaction tests on sandwich preforms	96
5.3.3	Flow studies on sandwich preforms	97
5.3.4	Impregnation with epoxy resin	99
5.4	Results and discussion	100
5.4.1	Compression and compaction	100
5.4.2	Flow experiments	101
5.4.3	Plates analysis	105
5.5	Conclusions and outlook	108

6	Process improvement	111
6.1	Characterization of High-Fluidity Thermoplastics	111
6.1.1	Differential Scanning Calorimetry (DSC)	111
6.1.2	Thermogravimetric Analysis (TGA)	112
6.1.3	Rheology	113
6.1.4	Tensile tests	116
6.1.5	Dynamic Mechanical Analysis (DMA)	117
6.1.6	Conclusion	118
6.2	Preliminary tests	118
6.2.1	Design of mTP-RTM mold	118
6.2.2	Impregnation with iPP on G-PLY in two stacking configurations	120
6.2.3	Impregnation strategies of G-PLY with iPP	123
6.2.4	Impregnation of G-PLY with HFPA6	126
6.3	Strategies for faster impregnation with HFPA6	128
6.3.1	Mold modification	128
6.3.2	Preforms	129
6.3.3	Experiment: plates production and analysis	130
6.3.4	Results and discussion	134
6.3.5	Conclusion	141
6.4	Conclusions and outlook	142
7	Scale-up scenarios	145
7.1	Compression RTM	146
7.2	Cost model	146
7.2.1	Materials	147
7.2.2	Production line	147
7.2.3	Data input	148
7.2.4	Results	151
7.3	Conclusion	155
8	Conclusions and perspectives	157
A	Compression molding with HFPA66	163
B	Viscosity reduction with nanoparticles	167
	Bibliography	175
	Curriculum Vitae	189

List of Figures

1.1	Average material consumption for new light-duty vehicles in the U.S., model years 1995, 2000, and 2012 (Ward’s Communication 2013). . . .	5
1.2	Example of analysis of (a) life-cycle and (b) operational costs for different materials and processes: steel, sheet molding compound (SMC), glass mat thermoplastic (GMT), structural resin injection molding (SRIM) with glass fibers (GF) and carbon fibers (CF), and a magnesium alloy. . .	6
1.3	Processing temperature and viscosity of TS and TP resins used in composite manufacturing.	8
1.4	Schematic representation of (a) compression molding and (b) liquid composite molding processes.	10
1.5	Expected temperature cycle for mTP-RTM process.	11
1.6	SCCER Mobility organization.	12
1.7	Plan of the thesis.	14
2.1	Some applications of fiber reinforced PP in car components.	20
2.2	Chemical structure of the most relevant aliphatic polyamides.	22
2.3	Chemical structure of (a) a PPA and (b) an aramid (here Kevlar®). . . .	23
2.4	Typical values of SEA for some materials.	24
2.5	Dependence of viscosity on (a) molecular weight and (b) molecular weight distribution.	27
2.6	Viscosity as a function of molecular weight for a linear (blank squares) and an hyperbranched (solid squares) polyester.	27
2.7	Intermediate forms for thermoplastic composites: (a) pre-impregnated tow; (b) film-stacking; (c) powder-impregnated fiber bundle; (d) sheath-coated powder-impregnated fiber bundle; (e) non-commingled yarn; and (d) commingled yarn.	31
2.8	Schematic representation of the flow through a fibrous preform showing the pressure profile for (a) a fully saturated case, and unsaturated flow (b) without and (c) with the presence of capillary pressure drop at the flow front.	39
2.9	Criterion for dual or single scale flow estimation, the line showing the regions where Da is higher or lower than 10^{-3}	47
3.1	Pictures of (a) a leno-weave, (b) a stitched non-crimp and (c) a 2×2 twill weave fabrics; the red arrow indicates the direction of high-flow (0°). . .	53
3.2	Setup used for flow experiments and production of plates via TS-RTM; six heating cartridges, not shown, are embedded in the bottom steel part. . .	57

3.3	Example of squared flow front, pressure and capillary number evolution with time for an experiment, showing the range of analysis.	59
3.4	Geometric parameters for a dog-bone polymer sample for tensile test.	62
3.5	Operating range for single-cantilever setup in DMA.	63
3.6	Schematic representation of lateral cross-section view of the TP-RTM tool.	64
4.1	Schematics of the cross section transverse to the flow direction for the five stacking architectures.	68
4.2	Compaction pressure for the different fabric stacks. The compaction was carried out at a constant speed of 0.017 mm s^{-1} until a thickness of 3 mm, which was then kept constant to let the fabric relax and measure the force decay.	69
4.3	Scheme of the change in the stack architecture under compaction if slipping occurs.	70
4.4	Saturated and unsaturated permeabilities of different stack architectures	71
4.5	Saturated permeability for G-PLY, G-WEAVE and G-FLOW fabrics; the numerical permeability calculated from G-PLY meso-channel geometry (Eqs. 4.3 and 4.4) is also reported (see Section 4.2.2).	73
4.6	3D images reconstructed from Computer X-Ray Tomography of G-PLY with (a) 4, (b) 5 and (c) 6 layers and G-WEAVE with (d) 5, (e) 6 and (f) 8 layers.	75
4.7	Cross section views from Computed X-Ray Tomography showing unit cells (left-hand side) and binary-converted images showing varying meso-channel shapes (right-hand side) for (a-b) 4, (c-d) 5 and (e-f) 6 layers of G-PLY; respectively 11, 12 and 18 unit-cells were used for image analysis of the three samples, each containing either one rectangular or two parallel triangular meso-channels.	75
4.8	Aspect ratio and area of the channels cross-section for (a) 4, (b) 5 and (c) 6 layers samples.	76
4.9	Scheme of (a) rectangular channel, (b) rectangular and triangular channels in series, and (c) triangular channels in parallel.	78
4.10	Example of unit cell of G-PLY, showing (a) geometrical parameters and (b) the three flow zones.	80
4.11	Flow front at capillary number (a) 0.000068 and (b) 0.0028 for G-WEAVE, and (c) 0.00013 and (d) 0.38 for G-PLY.	84
4.12	(a) Unsaturated-to-saturated permeability ratio and (b) capillary pressure vs. average capillary number for the whole series of tests.	86
5.1	Side-view of sandwich preform, where the core region represents the spacer.	90
5.2	Three-dimensional design of (a) unit cell and (b) full spacer; $t = 1.5 \text{ mm}$, $b=1 \text{ mm}$, $h = 1 \text{ mm}$, w variable.	91
5.3	Scheme of cross-section perpendicular to flow of a sandwich-like preform with core spacer, showing local and global fiber volume fraction.	93
5.4	Top-view of 3D-printed spacers with varying mesh-size.	94

5.5	Spacers for flow studies (in PLA) and plate production (in PCL) of mesh size 6×6 (mm).	94
5.6	Subdivision of preform top-view in unit cells for flow front detection and image analysis.	98
5.7	Scheme of cross-sectional view perpendicular to flow of preform structures for three plates produced with epoxy resin via TS-RTM; the red boxes show the cross-sections of beams cut for flexural tests, each containing two beams of the spacers.	100
5.8	Schematic view of a plate with spacer, showing the four samples cut for flexural tests (in red) and for cross-section visualization (in blue); (a) cross-section in the middle of a 3D unit cell; (b) cross-section close to a transverse beam.	100
5.9	(a) Compressive stress-strain curves and (b) compressive strength for the five PLA spacers of varying mesh-size and the PCL- 6×6 spacer.	102
5.10	(a) Absolute and (b) normalized pressure evolution during compaction-relaxation tests.	103
5.11	Measured and calculated saturated permeability for preforms with spacers with different mesh size and without spacer; G-PLY fabric is also reported for comparison.	104
5.12	Flow at different stages for experiments without any spacer (a) and with spacer and brake mechanism based on (b) dam-zone and (c) closed outlet (dark red = fully saturated, dark blue = dry).	105
5.13	Optical magnification of the cross-section of samples G-WEAVE/PLA- 6×6 in the middle of a 3D unit cell (a) and close to a transverse beam (b), G-WEAVE/PCL- 6×6 (c) and G-WEAVE/no-spacer; (a) and (b) are also referred to in Fig. 5.8.	107
5.14	Typical stress-strain curves for flexural tests on samples with and without spacers.	108
6.1	Crystallization time $t_{1/2}$ against isothermal crystallization temperatures. Inset: isothermal crystallization peak at 240°C with baseline subtraction.	112
6.2	TGA measurements on HFPA.	113
6.3	Rheology measurements on HFPA66.	114
6.4	Constant flow measurements on HFPA6 at 1 s^{-1} and iPP Borflow at 0.1 s^{-1} in air.	115
6.5	Arrhenius plot for HFPA66 and HFPA6.	115
6.6	Stress-strain curve of the tensile test on different polyamide samples.	116
6.7	Storage modulus evolution vs. temperature for HFPA66 and HFPA6.	117
6.8	(a) Mold assembly and (b) top-view of the fabric cavity.	119
6.9	Void distribution on two plates of G-PLY, with stacking architecture 5P and 5P-alt, impregnated with iPP (Borflow™ HL512B).	121
6.10	Optical microscopy images of transverse cross section for the two plates 5P and 5P-alt at three different position (close to inlet, middle of the plate, close to outlet).	122
6.11	Middle plate of the mTP-RTM modified with a screw, which allows to control opening/closing of the inlet/outlet.	123

6.12	Temperature cycle for an injection with application of vacuum and saturation step.	124
6.13	Scheme of cut-off samples for burn-off analysis (B) and optical microscopy (M), for (a) single and (b) double inlet injections (dimensions in cm).	125
6.14	Void distribution along the plate; each point is averaged on three locations equally distant from the inlet. (Refer to Table 6.4 for the # number)	126
6.15	Fluorescence micrographs for samples #1 (a-b) and #3 (c-d).	127
6.16	Void distribution along the plate for samples referred in Table 6.5.	128
6.17	(a) Picture of the mold after modification with heating cartridges and inlet screw, and side-view of the mold in a hot press in a schematic representation (b) and with IR camera during heating (c) and cooling (d) (the temperature scale on the right is in °C, while the temperature on the top-left refers to the center of the image).	129
6.18	Typical temperature evolution measured at the mold cavity.	130
6.19	Schematic structure of the preforms (a) G-WEAVE only, (b) G-PLY and (c) G-WEAVE+spacers, and (d) top-view of CFR-PEEK rod spacers placed on top of the fifth layer of G-WEAVE.	131
6.20	Schematic side-views of impregnation morphology for (a) "standard" in-plane flow and (b) "vacuum + saturation" dual-scale flow; in the latter, 1 and 2 correspond to the "flow step" and "saturation step", respectively.	132
6.21	Schematics of samples cut from plates for flexural test (F, green), burn-off (B, red) and optical microscopy (M, blue) analysis, and (a) for sample 2-3 and (b) for samples 2-5, 2-6, 2-7, 2-8, 2-9 (burn-off was performed only on G-PLY samples).	133
6.22	Top-side view of the plates produced from the tests listed in Table 6.6; flow direction from left to right (both sides for sample 2-8); plates dimensions of 11 × 7.5 cm.	135
6.23	Optical micrographs of the cross-sections transverse to flow direction and close to the outlet for plates 2-3, 2-5 and 2-6.	137
6.24	Optical micrographs of the cross-sections transverse to flow direction and close to the outlet for plates 2-7, 2-8 and 2-9.	139
6.25	Void content along the plate measured by burn-off method for samples 2-7, 2-8 and 2-9.	140
7.1	Schematics of the impregnation in C-RTM process at Solvay's.	147
7.2	Production line for RTM process with epoxy and G-WEAVE.	149
7.3	Production line for mTP-RTM process with HFPA6 and G-PLY.	149
7.4	Production line for mTP-RTM process with HFPA6 and G-WEAVE + spacer.	150
7.5	Production line for C-RTM process with HFPA6 and G-WEAVE.	150
7.6	Manufacturing cost per part as a function of the volume of production per year for the four scenarios.	153
7.7	Manufacturing cost vs. production volume for the four scenarios, broken down into cost categories, starting from 5k parts per year of production volume.	154

A.1	Scheme of a typical sample processing route. Case 1: constant pressure applied during the whole cycle. Case 2: a minimum pressure applied until the beginning of the cooling, then high pressure applied during the cooling phase.	164
A.2	Interaction-plot for the flexural strength, within a set of four conditions of impregnation time and applied pressure.	165
A.3	Cross-section of sample 11 at two different magnifications.	166
B.1	Particle-size distributions of colloidal silica Ludox® SM.	171
B.2	Relative viscosity as a function of silica nanoparticles volume fraction for the three different fluids.	172
B.3	Time-evolution of pressure-normalized squared flow-front position for PEG solutions with and without silica nanoparticles.	173

List of Tables

1.1	Automotive materials with corresponding mass reduction and relative cost, which include both materials and manufacturing.	4
1.2	Properties of conventional aluminum and steel and some advanced composites.	4
2.1	Physical and mechanical properties of typical thermoplastic resins for polymer matrix composites.	19
2.2	Physical and mechanical properties of selected polyamides.	22
3.1	Properties of glass fabrics (Chomarat™).	52
3.2	Properties of test fluids used for permeability measurements; the viscosity was measured at constant shear rate of either 100 s^{-1} (water/colorant), 10 s^{-1} (PEG 2%) or 1 s^{-1} (all other fluids).	55
4.1	Stacking architectures compressed to a thickness of 3 mm thickness. (F = G-FLOW; P = G-PLY; minus sign indicates opposite orientation in the normal axis).	68
4.2	Fabric samples configurations, compacted to a thickness of 3 mm.	72
4.3	Geometrical parameter and permeability of the meso-channels for the 4, 5 and 6-layers samples. Experimental saturated permeability is also reported.	79
4.4	Equivalent permeability calculations.	83
5.1	Flow experiments with different impregnation strategies.	98
5.2	Elastic modulus and strength of samples produced via RTM measured by 3-point bending tests.	107
6.1	Melting point, glass transition and crystallization temperatures of the HFPA6.	112
6.2	Arrhenius activation energy and pre-exponential factor of HFPA6.	114
6.3	Ultimate tensile stress and elastic modulus of different polyamide samples.	116
6.4	Impregnation strategies of G-PLY with iPP.	124
6.5	Impregnation with HFPA6 and 5P-alt.	128
6.6	List of mTP-RTM tests performed with HFPA6 on three different pre-forms and with different impregnation strategies.	132
6.7	Impregnation time and flexural modulus of six samples produced via mTP-RTM.	141

7.1	Duration of the RTM cell for each scenario.	148
7.2	Common input data for all the scenarios.	151
7.3	Input data for the RTM cell of the four scenarios.	152
A.1	List of samples prepared by compression molding.	164
B.1	List of samples PEG-silica for rheological study.	170

Abbreviations

CM	Compression Molding
C-RTM	Compression Resin Transfer Molding
CF	Carbon Fiber
CFR	Carbon Fiber-Reinforced
DMA	Dynamic Mechanical Analysis
DSA	Drop Shape Analyzer
GF	Glass Fiber
GFR	Glass Fiber-Reinforced
GMT	Glass Mat Thermoplastic
FRP	Fiber-Reinforced Polymer
FDM	Fused Deposition Modeling
HFPA	High-Fluidity Polyamide
HFTP	High-Fluidity Thermoplastic
LCM	Liquid Composite Molding
LPAC	Laboratory for Processing of Advanced Composites
LVDT	Linear Variable Differential Transformer
mTP-RTM	melt Thermoplastic Resin Transfer Molding
NCF	Non-Crimp Fabric
OEM	Original Equipment Manufacturer
PA	Polyamide
PBT	Polybutylene Terephthalate
PCL	Polycaprolactone
PEEK	Polyether Ether Ketone
PEG	Polyethylene Glycol

PLA	Poly(Lactic Acid)
PP	Polypropilene
PPA	Polyphthalamide
PPS	Polyphenylene Sulfide
RTM	Resin Transfer Molding
SCCER	Swiss Competence Center for Energy Research
SEA	Specific Energy Absorption
SMC	Sheet Molding Compound
SRIM	Structural Resin Injection Molding
TGA	Thermogravimetric Analysis
TP	Thermoplastic
TPC	Thermoplastic Composite
TP-RTM	Thermoplastic Resin Transfer Molding
TS	Thermoset
TSC	Thermoset Composite
TS-RTM	Thermoset Resin Transfer Molding
UD	Unidirectional
UTM	Ultimate Testing Machine
VARIM	Vacuum Assisted Resin Infusion Molding

Symbols

A_c	cross-sectional area of a channel	μm^2
A_w	areal weight	g/m^2
Ca	capillary number	
Da	Darcy number	
E	elastic modulus	GPa
E_a	activation energy	kJ mol^{-1}
K	permeability	m^2
$K_{channel}$	channel permeability	m^2
K_{eq}	equivalent permeability of a unit cell	m^2
$K_{meso-channel}$	longitudinal permeability of a meso-channel	m^2
K_{meso}^{\parallel}	longitudinal permeability of meso-pores	m^2
K_{meso}^{\perp}	transverse permeability of meso-pores	m^2
K_{micro}^{\parallel}	longitudinal permeability of fiber bundles	m^2
K_{micro}^{\perp}	transverse permeability of fiber bundles	m^2
K_{sat}	saturated permeability	m^2
K_{SFF}	squared flow-front unsaturated permeability	m^2
K_{unsat}	unsaturated permeability	m^2
$L(t)$	flow-front position as a function of time	m
P	pressure	bar (Pa)
P_c	cross-sectional perimeter of a channel	μm
ΔP_{γ}	capillary pressure	bar (Pa)
ΔP_{app}	applied pressure difference	bar (Pa)
Q	volumetric flow rate	m^3/s
Q_{out}	volumetric flow rate at the outlet	m^3/s

R_f	fiber radius	μm
R_{hyd}	hydraulic resistance	$\text{Pa s}/\text{m}^3$
R_s	permeability ratio	
T_c	crystallization temperature	$^{\circ}\text{C}$
T_g	glass-transition temperature	$^{\circ}\text{C}$
T_m	melting point	$^{\circ}\text{C}$
u_l	flow front velocity	m s^{-1}
V_f	fiber volume fraction	
$V_{f,max}$	maximum theoretical fiber volume fraction	
ϵ	strain/deformation	
η	viscosity	Pa s
ρ	density	g/cm^3
γ	surface tension	N m^{-1}
σ	stress/strength	MPa
σ_c	compressive strength	MPa
σ_t	tensile strength	MPa
ψ^2	square flow front vs. time slope	m^2/s

*Dedicated to the person without whom
this thesis would not have been written:
myself.*

n.b. The most relevant people have already been mentioned in the acknowledgments.

Chapter 1

Introduction

Nowadays, the increasing energy demand and the international requirements for environmental sustainability constitute one of the major driving factors for the scientific community and industries to synergically develop the knowledge and technologies necessary to progress to a low-carbon economy. With the Paris Agreement (2015), the signatory countries committed to individually set new, stricter targets for the reduction of greenhouse gases. In 2011, the European Commission had already established the objective for a reduction of 80-95% emissions by 2050 (as compared to 1990) and analyzed the potential of reduction in various sectors [1]. In particular, a potential reduction of around 60% has been later identified for mobility, which has been decided as the 2050-objective for this sector [2, 3]. Similarly, in Switzerland, following the nuclear disaster in Fukushima, Japan (May 2011), the Federal Council and Parliament decided to discontinue any plan to build new nuclear power plants and definitively close the five existing ones, which contribute to about 40% of Swiss' electricity production, at the end of their operating life. As a consequence, the need of a complete reorganization of the Swiss energy network has emerged, leading to the definition of the Energy Strategy 2050. The stated objective is the optimization of energy production and consumption, which involves, among other objectives, development of renewable energies, enhancement of buildings and mobility efficiency, and improvement of electric power transmission.

With regard to mobility, reduction of vehicles' mass (technically known as light-weighting) has been identified as one of the most effective routes to pursue reduction of greenhouse gases emissions and fuel consumption [4–9], along with more efficient

propulsion methods and thermal management. For instance, it has been estimated that lightweighting can contribute to 40% of CO₂ reduction by 2050 compared to 1990 levels in Europe [9]. However, the trend since the 1970s reflects an overall increase of the average weight of light-duty vehicles [6, 8, 9], partly due to customers' preference for more powerful cars, which have bigger engines and larger dimensions, but also to the increased technical complexity and vehicle comfort (e.g. components for safety, climate control, entertainment, electronics). In order to ideally reach the 1970s levels, an inversion of this tendency is necessary. It seems unlikely that this will happen spontaneously, but rather under the influence of an authority (e.g. local governments) or of customers' choices. Consumers should be informed about the beneficial long-term effects of buying lighter vehicles (i.e. lower fuel consumption leading to lower impact on the environment and lower operational costs). On the other hand, manufacturers should perceive as economically advantageous the shift to novel car concepts, which include, for instance, minimization of the number of components or use of lighter materials. In addition, the development of novel materials or manufacturing processes that allow low-cost production of light automotive components, which at the same time possess reliable mechanical properties for the given application, such as stiffness or impact resistance, is not straightforward. Research efforts from different fields, including materials science, process engineering, thermal management, cost analysis and life cycle assessment are required. The present thesis is intended to be an academic contribution to the development of a novel manufacturing process for the production of a specific class of materials (continuous glass fiber reinforced thermoplastics) from a materials science perspective. However, as it typically happens, some of the findings can be possibly generalized and applied to other materials and processes.

The overall research goal is presented in this introductory chapter. First, a brief summary on the past decades' evolution in the automotive sector in terms of vehicles' weight and materials will be presented. Secondly, the motivations and the objectives of the research, as well as the funding framework, will be discussed. Finally, the plan of the thesis will be outlined.

1.1 Lightweight materials in transportation

Many feasibility and benchmark studies about the opportunity of weight-saving in transportation have been carried out in recent years by car manufacturers and research institutions, as several reports, journal's articles and books show [4–15]. Although the necessity and the possibilities of lightweighting have been widely recognized, the average mass of newly produced vehicles in the US and in the EU has steadily increased between years 1980s and 2000 [6, 8, 9]. However, this was counterbalanced by the development of more efficient technologies used in vehicles, resulted in rather steady fuel economy (measured as distance traveled per liter of fuel), as well as reduced acceleration time [6, 8, 9]. In other words, consumers' preferences for larger and faster vehicles have played as major driving factors for the evolution of vehicles design and engineering. Attempts to limit fuel consumption were mainly due to economical and geopolitical reasons (the effects of 1970s oil crisis spread for decades). Finally, the environmental aspect has been seriously taken into account only in recent years, and since 2005 an inversion, or at least a slowdown, of the vehicle mass trend could be observed [6, 8, 9].

Lightweighting can be achieved by replacing existing components with lighter ones. Steel remains the most used material, besides being the densest, meaning that there is scope for mass reduction by replacing it with lighter materials. Table 1.1 shows the potential mass reduction for a range of materials, among which fiber-reinforced polymers (FRP), along with their relative cost. Indeed, raw material and manufacturing cost represent the major limitations for lightweighting.

Nevertheless, a trend in the use of lighter materials has been observed in the past years, as shown for instance in Fig. 1.1. Steel and cast iron with components made of high strength steel, aluminum, plastics and polymer composites (Fig. 1.1). In particular, when it comes to structural applications, FRP composites are recognized as the ideal candidates for replacing steel. FRP materials are composed of fibers (typically glass or carbon), which are surrounded by a polymeric matrix. The fibers provide strength and stiffness, while the matrix has the role of keeping them together, protecting from the environment and reducing the overall density. In addition, a broad range of both fiber and matrix materials are available, and the organization of the fibers (e.g. unidirectionally or

randomly distributed) also has a major effect on the mechanical properties. Therefore, FRP can feature an interesting combination of properties, such as low density, resistance to corrosion, ductility and impact resistance, as well as being very versatile in terms of manufacturing design [11, 12, 16]. A comparison of properties of common steel and aluminum with three typical types of composites is shown in Table 1.2.

Table 1.1: Automotive materials with corresponding mass reduction and relative cost, which include both materials and manufacturing, reproduced from [16].

Lightweight material	Relative cost (per part)*	Material replaced	Mass reduction (%)
High Strength Steel (HSS)	1	Mild steel	10-25
Aluminum	1.3-2	Steel, cast iron	40-60
Magnesium	1.5-2.5	Steel, cast iron	60-75
Magnesium	1-1.5	Aluminum	25-35
Glass FRP composites	1-1.5	Steel	25-35
Carbon FRP composites	2-10+	Steel	50-60
Al matrix composites	1.5-3+	Steel, cast iron	50-65
Titanium	1.5-10+	Alloy steel	40-55
Stainless steel	1.2-1.7	Carbon steel	20-45

*assuming HSS=1

Table 1.2: Properties of conventional aluminum and steel and some advanced composites, reproduced from [16].

Material	Specific Modulus (10^6 N m kg^{-1})	Specific Tensile Strength (10^6 N m kg^{-1})	Density (g/cm^3)
SAE 101 Steel (cold-worked)	26.3	46.4	7.87
Aluminum 6061-T6	25.7	115	2.70
Unidirectional high-strength CF/epoxy	88.9	1000	1.55
Unidirectional E-glass fiber/epoxy	21.2	522	1.85
Random GF/epoxy	5.48	71	1.55

In addition to material cost, other factors limit the use of FRP composites in high-volume industries. Firstly, original equipment manufacturers (OEMs), which supply components for the automotive industry, are rather reluctant to shift from well-established manufacturing processes (such as sheet metal forming) to novel ones. Secondly, the wide range of choice of processing routes for composites' production may be a deterrent. Moreover, in many cases composite manufacturing processes cannot sustain the production rates required by the automotive industry. Composite compression molding techniques have gained some popularity, thanks to similarities with sheet metal

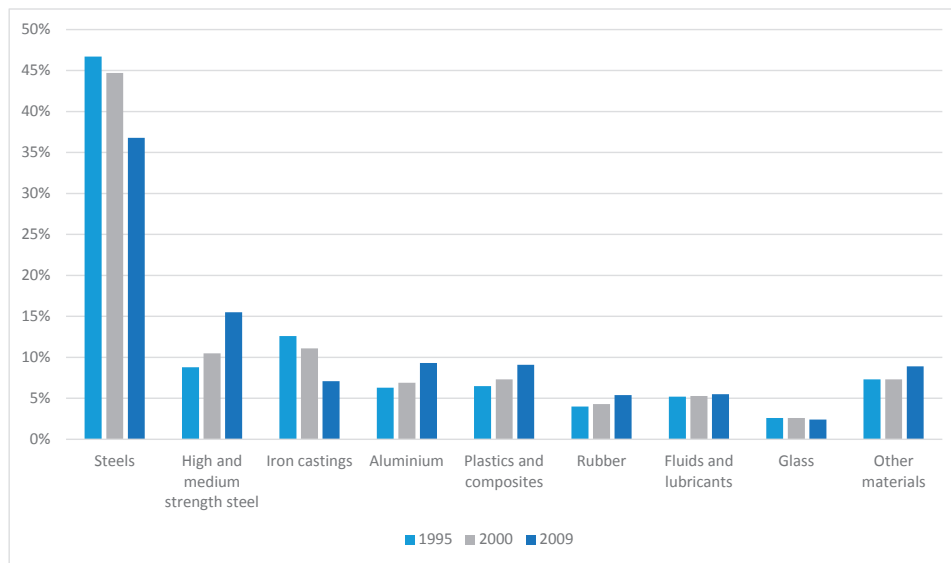


Fig. 1.1: Average material consumption for new light-duty vehicles in the U.S., model years 1995, 2000, and 2012 (Ward's Communication 2013).

forming, allowing quite short cycle times (1-3 min). However, they are limited in terms of shape complexity. Another large class of techniques is called liquid composite molding (LCM), which allows production of complex parts without need of further assembly, welding and shaping, thus reducing cost and time of post-processing. The production time represents a major limiting factor for LCM techniques, since it is difficult to reach high production volumes, and this has a dramatic effect on the final cost*.

Production cycle time is not the only factor affecting costs. Many factors have to be taken in consideration to analyze cost and environmental impact in replacing materials. Cost analysis should include both life cycle and operational costs. Life cycle costs cover manufacturing (equipment, power consumption, cycle times, etc.), raw materials (mining, synthesis, production), use (fuel consumption) and End-Of-Life (disposal, recycling, etc.). Operational costs are important from a consumers' point of view. An

*In compression molding, an intermediate material in form of a sheet containing both the reinforcing fibers and the polymeric matrix is heated and pressed in a mold in order to give it the final shape. In LCM, the fibers are placed in the cavity of a mold, which is then filled with the liquid matrix; subsequently, the matrix is solidified. The differences between compression molding and LCM processes will be further discussed in Section 2.3.

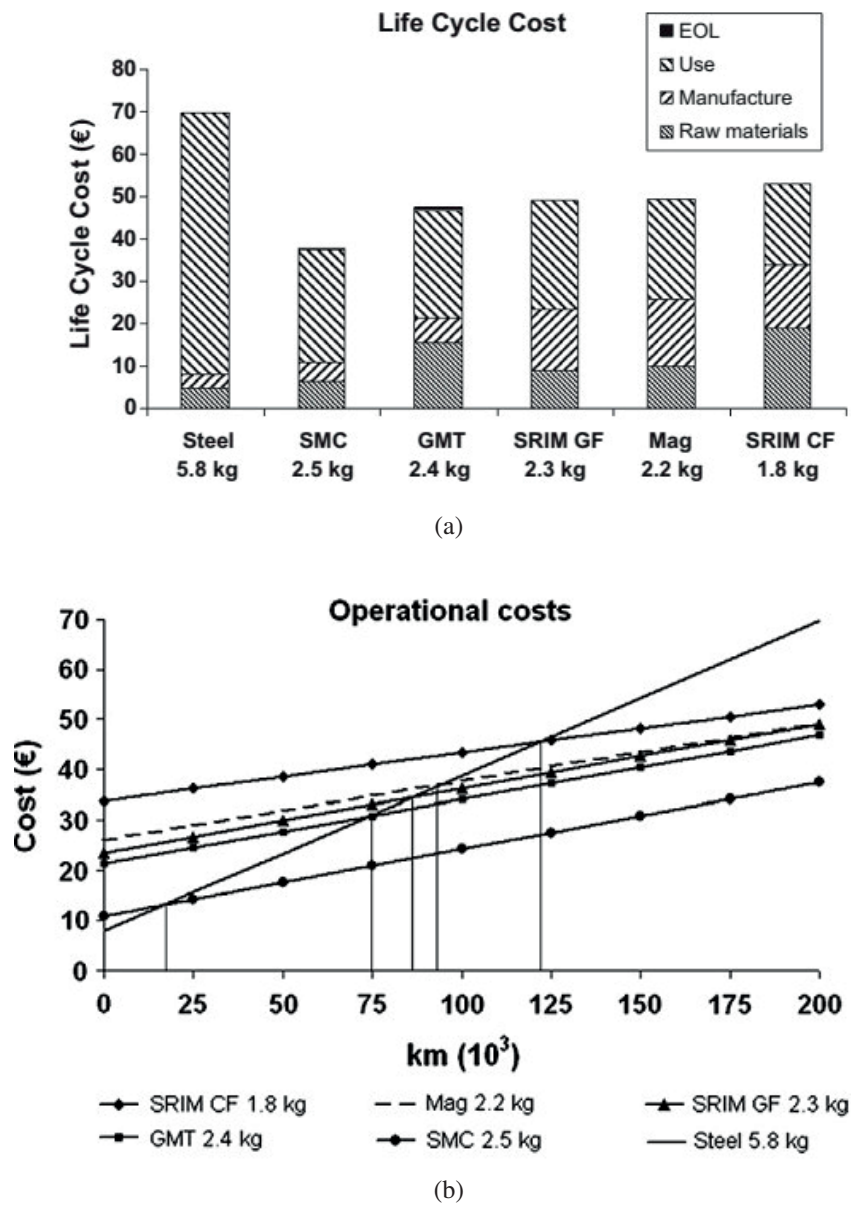


Fig. 1.2: Example of analysis of life-cycle (a) and operational (b) costs for different materials and processes: steel, sheet molding compound (SMC), glass mat thermoplastic (GMT), structural resin injection molding (SRIM) with glass fibers (GF) and carbon fibers (CF), and a magnesium alloy [15].

example of cost analysis for a car component is reported in Fig. 1.2, which shows the life-cycle and operational costs for some materials and processes, in particular steel and several types of composites [15]. Steel was found to be the cheapest for manufacturing and raw materials cost, but it appeared to become much less convenient when the cost related to the use phase was considered (Fig. 1.2a). Indeed, it can be observed in cost vs. ride distance graph (Fig. 1.2b) that the operational cost of steel increases much faster than lightweight competitors. However, it is the initial cost that determines whether the use of composite pays off in short or long ride distance, and it is strongly dependent on both raw materials (fibers and matrix) and manufacturing technique. For example, sheet molding compound (SMC), which is a rather inexpensive class of composites, becomes cheaper than steel after less than 25 000 km, while other materials and techniques require longer ride distances to become more advantageous. Therefore, it is of major importance for composite manufacturers to reduce the initial cost, which is the sum of raw materials and manufacturing cost. Both are affected by the processing technique. Raw materials cost can decrease as a result of increased volume of production/extraction and use of recycled materials, which is the case for carbon fibers [17]. However, the quantity of raw material needed for the production of a given part also depends on the amount of waste produced, which in turn depends on the composite processing technique. Equipment and power consumption are the main entries of manufacturing cost, which is amortized if high volume of production is achieved, i.e. short cycle-time; these are all affected by the manufacturing technique. Hence, reducing manufacturing cost of composites is a major motivation for the present study.

1.2 Motivations and objectives

The long-term goal of this research is to develop a novel process for high-volume production of continuous fiber-reinforced thermoplastic composites (TPC) for automotive components, in order to cost-effectively replace heavy structural parts typically made of steel. TPCs are already well established in the industry for low-cost non-structural parts (e.g. glass mat thermoplastics), or, at the opposite, for expensive, high-performance, niche applications. Many efforts are being made by the industries in order to bring TPCs

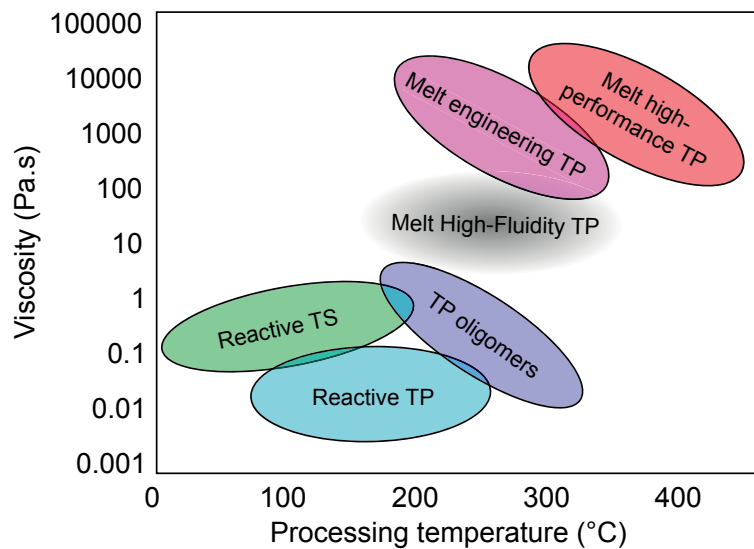


Fig. 1.3: Processing temperature and viscosity of TS and TP resins used in composite manufacturing, adapted from [18].

to high-volume production of structural components. The present dissertation represents a contribution to this industrial challenge.

Polymer matrix composites are classified according to the type of matrix. A major distinction is made between thermoset (TS) and thermoplastic (TP) matrices, which have very different physico-chemical properties, and, as a consequence, require different processing conditions and equipment. As an example, Fig. 1.3 shows ranges of viscosity and processing temperature for some typical classes of resins used in composite manufacturing.

Typically, TPCs are produced by compression molding (Fig. 1.4a), which is suitable for high-volume production, but needs intermediate products (e.g. pre-impregnated sheets) that have to undergo a thermoforming or consolidation step, requiring costly equipment (e.g. a hydraulic press). High temperature and pressure are necessary to soften the TP matrix and give shape to the component.

TSs are typically used in LCM processes, in which the reinforcing fibers in form of textile are placed inside a mold with the shape of the final component, and then a liquid precursor of the matrix (i.e. a reactive thermoset or thermoplastic resin) is injected in the mold so as to impregnate the fabric and finally solidify (Fig. 1.4b). LCM has the advantage of being a single-stage process, requiring in principle less expensive equipment. Moreover, complex shapes can be produced, thus avoiding further welding or assembling

steps and reducing waste of scrap material for parts finishing. The major drawback is the small rate of production due to long processing time. Indeed, the duration of the impregnation step is proportional to the square of the distance the resin has to flow inside the mold, as well as to the viscosity of the filtrating fluid[†]. This is typically very low for reactive systems (<1 Pa s, see Fig. 1.3), but at least one thousand times higher for melt TPs, which would imply impregnation times incompatible with high-volume production. Therefore, LCM has always been applied to reactive systems, typically thermosets or reactive thermoplastics systems, which are yet on the development stage (at least for polyamides or higher temperature polymers). Apparently, there is a gap between reactive and melt processing in FRP composites manufacturing (Fig. 1.3). TPs with low melt viscosity are available on the market, but have typically poorer mechanical properties than engineering TPs, and therefore are not suitable as matrix material for structural applications. Recently, however, high-fluidity TPs (HFTP), in particular polyamides or even higher service temperature polymers, with properties comparable to engineering TPs, have been developed, in particular by Solvay, which allows to envisage alternative processing concepts to compression molding or high-pressure short-fiber injection processes.

The long-term objective of the present research is the development of a novel LCM process for the production of TPCs with melt thermoplastic polymers (notably polyamides) as impregnating resins, which will be subsequently called melt thermoplastic resin transfer molding (mTP-RTM, melt TP-RTM, or melt-RTM)[‡]. The expected temperature cycle for the production of one single component in mTP-RTM process is shown in Fig. 1.5. First, both the polymeric matrix and the mold containing the fabric have to be heated up above the melting temperature of the polymer. Secondly, the melt is injected at low pressure inside the mold, where fabric impregnation takes place. Finally, the mold is cooled down, so as to solidify the matrix, and the part is removed from the mold. The duration of the injection-impregnation step is the major limiting factor to the

[†]The model predicting resin flow velocity during fabric impregnation and its relation with resin viscosity, fabric permeability, flow distance and fluid pressure will be detailed in Section 2.4 in Chapter 2.

[‡]RTM is a subcategory of the LCM process family, in which both top and bottom parts of the mold are rigid, typically being made of steel; hence, the fabric is compacted during mold closing, and later the polymer is injected. In other LCM processes, like vacuum-infusion, the bottom only is rigid, while the top is a flexible airtight film; in this case, vacuum is pulled out from the mold, and the fabric is compacted under the effect of atmospheric pressure.

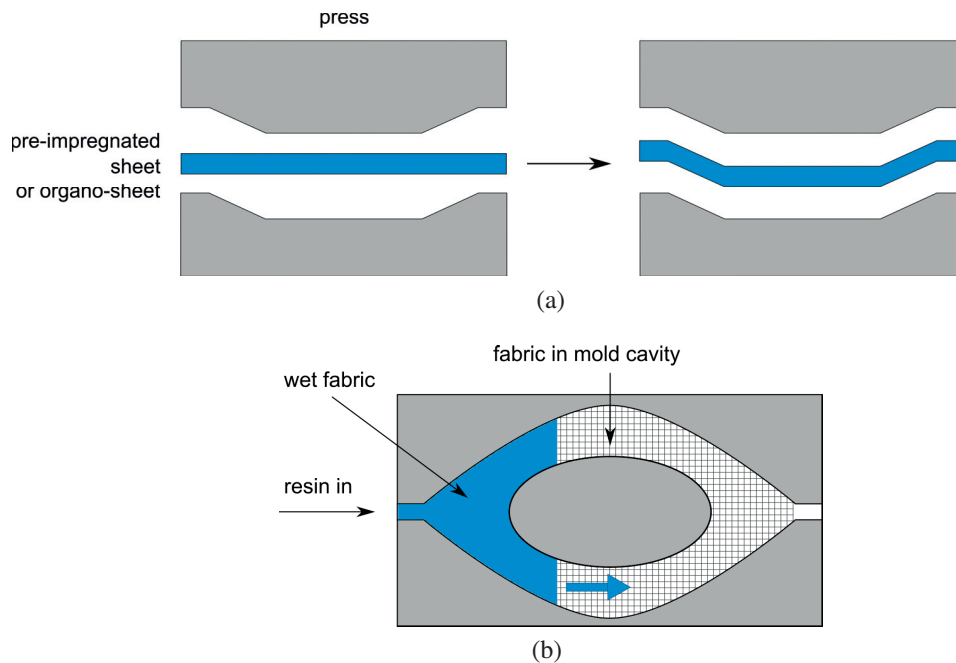


Fig. 1.4: Schematic representation of (a) compression molding and (b) liquid composite molding processes.

development of mTP-RTM, due to high viscosity of melt TP. In this work, high-fluidity TPs (HFTPs), with viscosity in the range of 10-50 Pa s, are used as resins, allowing significant reduction of the impregnation time. Yet, HFTPs are between 10 and 1000 times more viscous than reactive systems, which makes impregnation of large parts still quite slow. Besides, textile properties also affect the impregnation time, and particularly the *permeability*, a measure of the resistance that a porous medium (i.e. the dry fabric) opposes to fluid flow. In order to produce parts that are capable of high performances, a high content of fibers is desirable, which dramatically reduces the permeability of the preform, making it more difficult to impregnate. In principle, the process could also be enhanced by injecting the polymer in the mold at a higher rate or pressure, but with risk of displacing or destroying the reinforcing fabric. In addition, it might not fill the mold uniformly, resulting in regions with high void content, which detrimentally affect the quality of the final part.

In conclusion, the ultimate goal of this thesis is to reduce the duration of the impregnation step to a cycle-time compatible with high-volume production (<10 min for a medium-sized part). This is achieved by tackling both the processing and materials

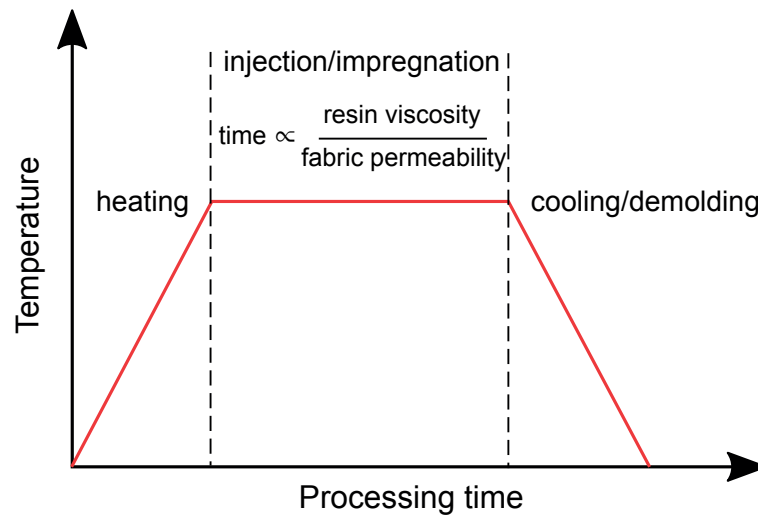


Fig. 1.5: Expected temperature cycle for mTP-RTM process.

level. Specifically, it will be shown that the presence of preferential flow channels inside the fabric can greatly enhance its permeability, resulting in fast flow. These channels can be either innate to the type of fabric or artificially introduced by means of a second solid phase; both options will be explored. Basic studies will be performed so as to gain an understanding of the physical phenomena involved in the impregnation process in presence of large channels. Strategies will be investigated in order to reach an optimum between impregnation time and quality, and assessed from an economic point of view.

1.3 Research framework

The present research is part of a broader program funded by Innosuisse (previously CTI) through the Swiss Competence Center for Energy Research (SCCER) in the framework of the Energy Strategy 2050 decided by the Swiss government. Within this framework, a broad research program, which involves several institutions inside the Confederation, has been proposed on the topic "Efficient Technologies and Systems for Mobility". The aim of this "SCCER Mobility" project is to find new technologies, processes and systems with a substantial impact on energy efficiency and CO₂ reduction. For this purpose, the plan is organized in two innovation fields (A and B) and five Capacity Areas (CA), as shown in Fig. 1.6.

The Laboratory for Processing of Advanced Composites (LPAC) at the EPFL cooperates in the Capacity Area A3 for the "Minimization of vehicular energy demand"

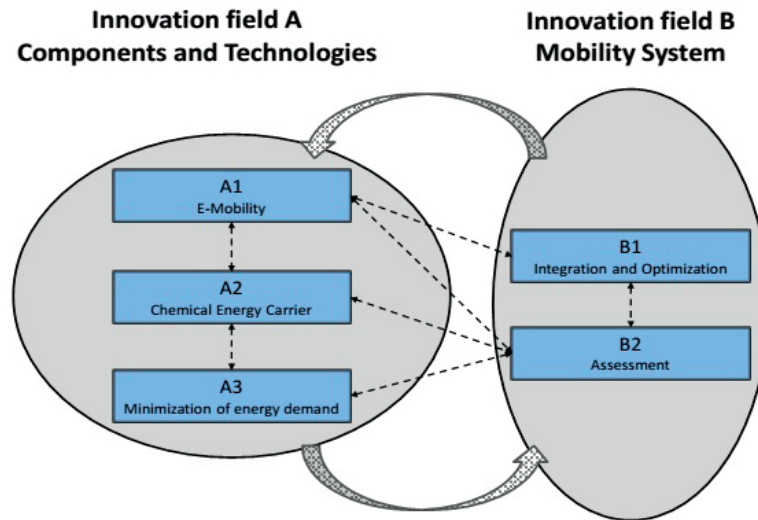


Fig. 1.6: SCCER Mobility organization.

with the objective of optimizing a thermoplastic liquid composite molding process for the low-cost, high-volume production of automotive components. The research is conducted in parallel with other research groups in Switzerland. Three laboratories at ETHZ are involved in the SCCER-CA3. The group of Composite Materials & Adaptive Structures focuses on the development of new yarn technologies, in particular of novel fiber coatings with high-performance thermoplastic polymers. The Laboratory for Complex Materials explores novel micro-/nano-structured materials inspired by nature. The Aerothermochemistry & Combustion Systems Laboratory studies the optimization of vehicles' energy consumption through the evaluation of systems to provide auxiliary power (e.g. thermal energy) in conventional powertrains. At the Institute of Polymer Technology at *Fachhochschule Nordwestschweiz* (FHNW) the investigation focuses on compression RTM with high-fluidity thermoplastics (HFTP). This research is also funded by the industrial partner Solvay (Research Center of Lyon, France), which develops and supplies the HFTP polymers used in this project.

1.4 Thesis plan

Fig. 1.7 summarizes the plan of this thesis. Chapter 2 offers a review of the state of the art in thermoplastic composite manufacturing for the automotive industry, with a

special focus on LCM processes. Materials and methods used or developed in this work are described in Chapter 3.

Chapter 4 concerns studies on fluid flow through fabric preforms. Specifically, an existing fabric with a particular structure and high permeability is studied and a relation to its peculiar meso-structure and flow properties determined both experimentally and through a numerical model. The purpose is to gain a solid base on flow propagation in high-permeability porous media (flow morphology, capillary effects, etc.) performing injection in a closed mold using model fluids. The advantage of these studies is that they can be carried out at room temperature with stable model fluids (constant viscosity, no thermal degradation).

In Chapter 5, a novel strategy for enhancement of permeability by insertion of solid spacers in the fabric preform is explored. The idea behind is to exploit one of the advantages of LCM processes, in which functional features can easily be included in the part. In this case, additional components are used to enhance the molding process and at the same time increase the stiffness of the final material.

In Chapter 6, mTP-RTM process is developed and optimized using HFTP matrices. Solvay has formulated novel high-fluidity polyamides (HFPA), with intermediate viscosity (1-100 Pa s), which represents a breakthrough for the development of mTP-RTM process. These polymers have been chemically modified to reduce the viscosity without significantly affecting the mechanical properties. A polyamide-6,6 (HFPA66) and a polyamide-6 (HFPA6) were supplied by Solvay, and are used for process development and optimization using a custom-made, lab-scale tool.

Finally, in Chapter 7 scenarios for scaling-up to industrial production are explored. The results shown in this chapter are partly taken from a Master project carried out at Laboratory for Processing of Advanced Composites and in collaboration with the Technology Assessment Group at Paul Scherrer Institute (Villigen, Switzerland) and the Institute of Polymers at FHNW (Windisch, Switzerland).

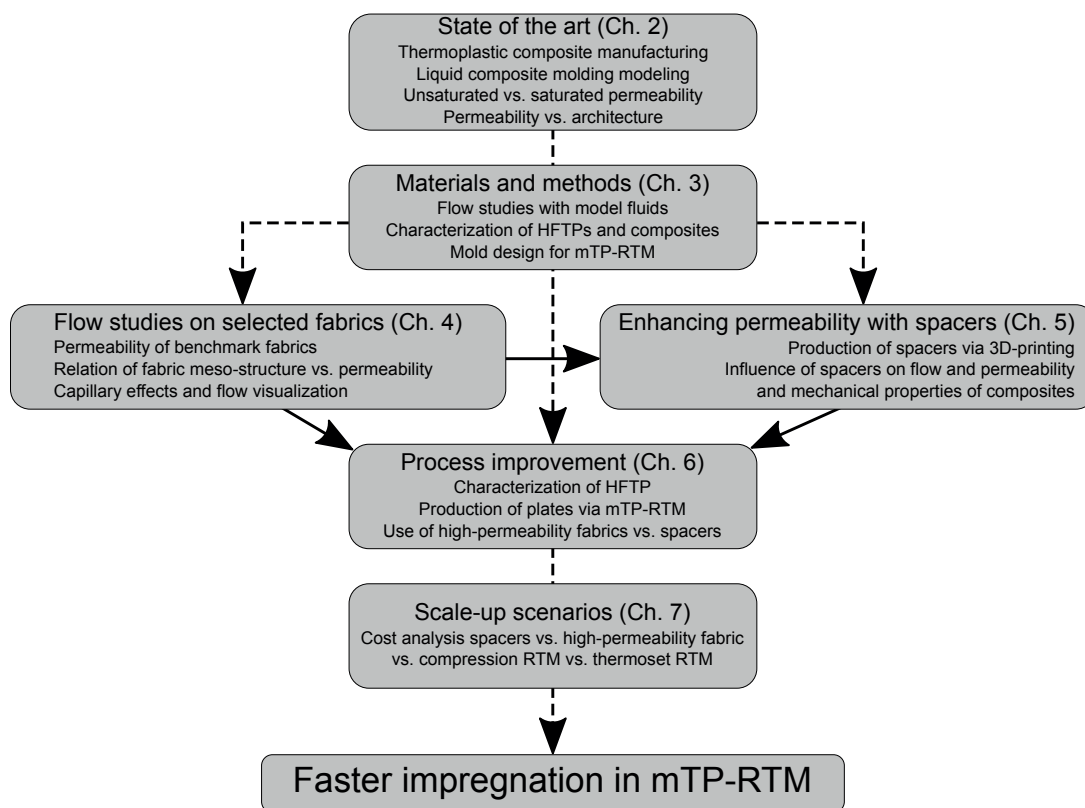


Fig. 1.7: Plan of the thesis.

Chapter 2

State of the art

The state of the art is conceptually divided in two parts. The first part (Sections 2.1, 2.2 and 2.3) deals with benchmark thermoplastic and thermoplastic composite materials and manufacturing processes. In particular, in Section 2.3 the early steps in the development of mTP-RTM are illustrated. The second part (Sections 2.4 and 2.5) reviews scientific research in the domain of liquid composite molding, focusing in particular on the definition of permeability and all the related aspects, i.e. modeling, measurements, capillary effects, and influence of preform architecture.

2.1 Thermoplastic polymers and composites in the automotive industry

Polymer matrix composites (PMC) are good candidates to replace steel for lightweighting in vehicles. In particular, thermoplastic composites (TPCs) are gaining ground as lightweight structural components. The reasons lie in their mechanical properties (ductility, toughness), high recyclability, weldability, freedom of design, and energy absorption (i.e. crashworthiness). In this section, the state of the art of thermoplastic composites currently employed in the automotive industry will be briefly outlined.

2.1.1 Polymer matrix composites

Polymer matrix composites have been widely used in many industrial sectors (aeronautics, automotive, nautical, sports, chemicals, etc.) for decades. Their properties result from the combination of a reinforcement with high strength and modulus (typically fibers) with a low-density polymer matrix, and range from low density, corrosion resistance, electrical resistance, low thermal conductivity, formability, to variable optical properties.

In fiber-reinforced polymer (FRP) composites, the fiber reinforcement is the primary load-bearing constituent and determines the main mechanical response of the composite. The matrix holds the fibers together and transfers the load to the fibers through the interfaces; it also acts to protect the fibers from UV, solvents or other external aggression. Common reinforcements are carbon and glass fibers. Carbon fibers are possibly the best choice for high-performance composites, owing to their outstanding stiffness and mechanical strength. They are widely used in sectors such as sport, automotive, and aerospace, but mainly for high-end use. Indeed, their cost is quite high, due to the highly power-consuming production process, representing the main limit for their use in high-volume applications. E-glass is the main reinforcement used in composite applications. Its properties are generally worse than carbon fibers (higher density, lower modulus, lower fatigue resistance), but the cost is lower and it is a good electrical insulator. As a consequence, it is the first choice in high-volume applications. Polymeric fibers represent a further alternative. Aramid fibers (such as Kevlar®) are synthetic polymeric fibers of the polyamide family (Section 2.1.2). They have the lowest density and highest strength-to-density ratio among the reinforcing fibers, but their high cost limits their employment to niche applications. Another drawback of aramid fibers is moisture absorption. Natural fibers (e.g. jute, flax, and hemp) are also becoming increasingly popular due to their recyclability.

The forms in which the fibers are used in composites determine the behavior of the material under mechanical load. A general classification is made depending on the aspect ratio (length/diameter). Fibers with high aspect ratio (typically higher than 2000) are said *continuous*, while those with low aspect ratio are said *discontinuous*. Continuous FRP have better mechanical properties than their discontinuous counterpart, but

they are highly anisotropic. They are classified depending on the reinforcement architecture: aligned fibers (uni-, bi- or tri-directional), randomly oriented (mat), and textiles (woven, braided or knitted fabrics). Unidirectional (UD) composites have the best properties (close to those of the fibers) along the fiber direction, but poor (close to those of the polymer) in transverse direction. Multi-directional (bi- or tri-axial) and textiles are also called *laminates*. They have good in-plane mechanical properties (although not as high as UD due to crimp), but also poor in the out-of-plane direction. Moreover, they are subject to delamination and shear between different planes (inter-ply shear stress). New 3D fabrics are now gaining interest, such as interlock fabrics or 3D textiles with yarns going through the thickness [19–21]. However, these are still rather expensive and find use in critical applications, such as engine fan blades.

The matrix properties determine the ductility, toughness, chemical and thermal resistance, electrical insulation, humidity absorption, as well as other properties of the composite. Furthermore, the manufacturing process is highly dependent on the type of matrix in use. The main classification is made on the nature of the polymer. It is possible to distinguish between thermo-hardening (thermosets), which cannot be remelted once they are polymerized, and thermo-softening (thermoplastics) polymers, which can be softened or melted above the glass transition temperature (T_g) and melting temperature ($T_m > T_g$), if semi-crystalline, respectively.

In their initial monomer state, TSs are highly fluid resins which polymerize directly during or immediately after the impregnation of the fibers. Catalysts (*curing agents*) are added to the monomer to promote the polymerization. During the reaction (*cure*), inter-chain covalent bonds (*cross-links*) form, leading to an increase in the molecular weight of the material and creation of macromolecules (and to an infinite molecular weight when gelation point is reached). This results in reduced mobility of molecules, which form an intricate, cross-linked network. It is not possible to increase much chain's mobility with temperature and thus thermoset polymers do not melt or soften once they are cross-linked, but will only undergo thermal decomposition. This implies that thermoset composites cannot be shaped by thermoforming (apart from a new class of TS called vitrimers that was recently developed at ESPCI* and makes use of dynamic covalent

**École supérieure de physique et de chimie industrielles de la ville de Paris*, Paris, France.

bonds [22, 23]). In general for TS matrices, there are two possible processing routes. The resin can be made to polymerize after the impregnation of the fibers placed in a mold in the desired final shape, or it can be first partially cured to reach a given viscosity and impregnated into thin fiber layers (*prepregs*). Following the second approach, it is possible to produce high volumes of prepregs (tapes or sheets) that will be assembled at the desired angles and then shaped by completing the curing reaction. This is achieved by applying heat and pressure in a mold with a desired shape. As the cure is thermally-activated, it is necessary to store prepregs at low temperature (unless latent reactants are used, such as DICY [24]). This implies higher storage costs and limited shelf life. TSs present several environmental issues: some of the reactants, catalysts and solvents may be harmful to the environment (styrene, amines, etc.) and they cannot be easily recycled as they cannot remelt. Another consequence of the molecular structure of TSs is their generally low toughness and ductility, which confers poor impact resistance.

TPs do not exhibit these drawbacks, and offer a broad range of other opportunities. They are usually purchased in their polymerized state, in form of powders, pellets, fibers, or tapes. The main advantages of TPs upon TSs are their improved weldability, formability, recyclability and impact resistance, which are all consequences of their higher molecular mobility. Different TPC parts can be easily welded and joined applying heat. This allows a high degree of design freedom. Above the T_g , TPCs are very ductile, which allows them to be stamped (thermoforming). Unlike TSs, the TP matrix can then be melted and recycled at the end of the component's life. Another important characteristics of TPCs is toughness, which confers high impact resistance and energy absorption. This is a very important aspect for automotive applications, and will be discussed in Section 2.1.3. For all these reasons, TPCs appear to be ideal candidates for lightweight automotive components. However, they also suffer from drawbacks which have limited their entry into these markets: temperature and creep resistance are limited for the widely available low cost TPs such as polypropylene, so higher-end TPs must be used for structural parts, polyamide being the first possible compromise. As a result, their processing temperature is high, viscosity is also high to ensure high molecular weight, and the resulting cycle times and costs are generally too high to be competitive.

In addition to reinforcement and matrix, interface can be considered as the third

basic element in a composite. It is through the interface that the load is transferred from the matrix to the reinforcement. A weak interface bonding can be caused for instance by poor impregnation of the fibers, void presence, and sub-optimal fiber surface compatibility with the matrix. As a result, specific surface treatments (sizings) must be applied to fibers when combination with TP is sought.

2.1.2 Thermoplastic matrices

Table 2.1: Physical and mechanical properties of typical thermoplastic resins for polymer matrix composites [16].

Thermoplastic Polymer	Tensile Modulus (GPa)	Tensile Strength (MPa)	Melting Point (°C)	Density (g/cm ³)
Polypropylene (PP)	1.50-1.75	28-39	134-165	0.89-0.91
Polyamide (PA)	0.7-3.3	40-86	211-265	1.03-1.16
Polyphenylene Sulfide (PPS)	3.4-4.3	28-93	280-282	1.35-1.43
Polybutylene Terephthalate (PBT)	1.75-2.5	40-55	230	1.24-1.31
Polyetherketoneketone (PEKK)	4.4	110	360	1.31
Polyetheretherketone (PEEK)	3.1-8.3	90-110	340-344	1.3-1.44
Polyetherimide (PEI)	2.7-6.4	100-105	220	1.26-1.7
Polyethersulfone (PES)	2.4-8.62	83-126	220	1.36-1.58

Table 2.1 lists the mechanical properties of some of the most relevant TPs. Polypropylene (PP) is by far one of the cheapest polymers on the market. It is reinforced with glass fibers (Twintex®) in various car components, some of which are shown in Fig. 2.1. PP has a relatively low melting point (Table 2.1) and low melt-viscosity, which allows it to be easily processed by injection molding and extrusion. Low density, low cost and good mechanical properties make PP the most employed TP matrix in automotive applications, except for fully structural parts such as the body in white (BIW), which has to pass through high temperatures during the painting/coating process.

Polyamides

Engineering polymers such as polyamide (PA) and polybutyleneterephthalate (PBT) are promising candidates for high-performance automotive applications, and their potential

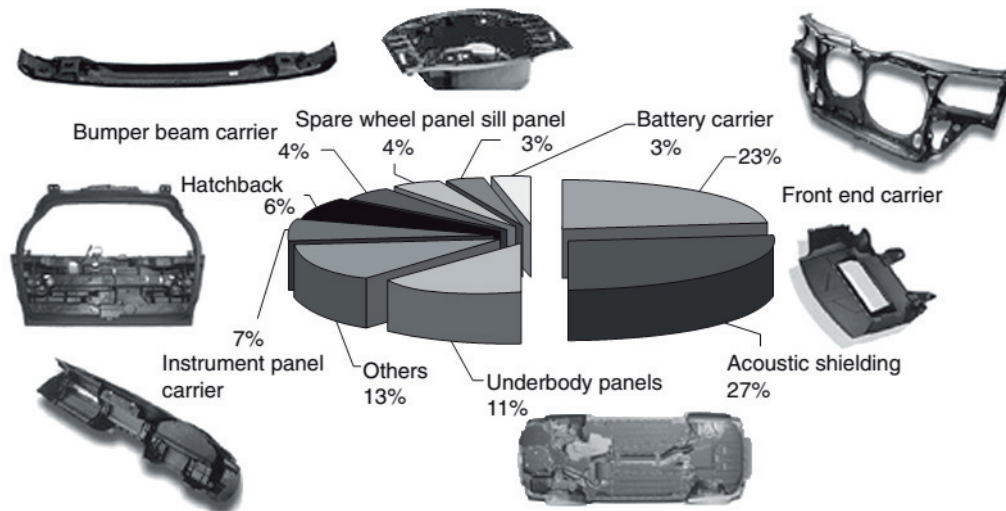


Fig. 2.1: Some applications of fiber reinforced PP in car components [25].

has not been fully developed yet. PA in particular is emerging as the matrix of choice for high-volume automotive applications, thanks to an excellent combination of price, mechanical properties and recyclability. PAs have a range of properties, as reported in Table 2.1. This is due to the existence of several grades of PA with different chemical structures, which are labeled depending on the number of carbon atoms carried by the monomers involved in the condensation reaction (a diacid and a diamine, or a lactam). The most common are PA-6 (nylon), PA-6,6 (nylon 6,6), PA-12 (nylon 12). PAs also have excellent properties from the point of view of crashworthiness. A case-study presented in [11] showed that a thermo-formed GFR-PA6 beam demonstrator had more than double the specific energy absorption (SEA) compared to steel and aluminum, higher specific failure energy in a 3-point bending test and comparable stiffness. The research concluded with cost analysis showing that the composite and metal price-volume curves cross at 50000 parts per year, with the first becoming more convenient (comparable with aluminum). The environmental impact appeared to be much more favorable too, due to the high recyclability of the PA matrix.

Polyamides are characterized by the presence in the repeating unit of an amide group CONH, which forms from the condensation of a diamine ($\text{H}_2\text{N}-\text{R}-\text{NH}_2$) and a dicarboxylic acid ($\text{HOOC}-\text{R}'-\text{COOH}$), from self-condensation of an amino acid, or from the ring-opening of a lactam (cyclic amide). The highly polar amide groups of

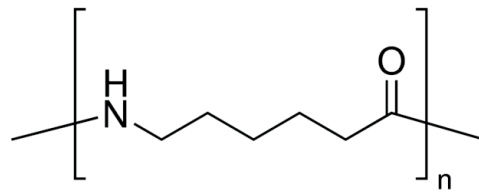
parallel chains form strong interactions (hydrogen bonds), which leads to the high crystallinity of PAs. Such substantial intermolecular interactions are also responsible for the high melting point and mechanical properties of PAs, as well for the insolubility to most of the solvents. On the other hand, the amide groups make PAs highly hygroscopic, i.e. they absorb moisture from the atmosphere. PAs' hygroscopicity is a problem to deal with especially in melt processing. In the melt state, the equilibrium reaction between condensation and degradation takes place:



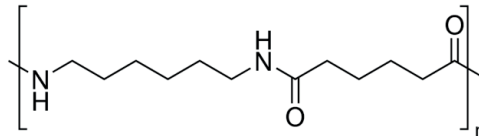
Excess of water shifts the equilibrium towards the monomers, thus induces breakage of the amide bond (degradation), whereas water removal induces further condensation between free carboxylic and amine ends. Moreover, water is a plasticizer, i.e. it lowers T_g .

The nature of the R and R' in the monomers is the main factor affecting the polymer's properties. If they are aliphatic sequences, they provide flexibility to the amorphous phase, resulting in high toughness of the final polymer. Moreover, the length of the aliphatic sequence determines the density of the amide groups. Thus, the longer it is, the lower the forces necessary to separate interacting chains, and thus the lower the melting point, tensile strength, rigidity and hardness, but also the hygroscopicity. For example, PA12 has intermediate properties between PA6 and polyethylene. PA6 and PA66 are the ones with the best combination of properties among the aliphatic PAs. The chemical structures of PA6, PA66 and PA12 are shown in Fig. 2.2.

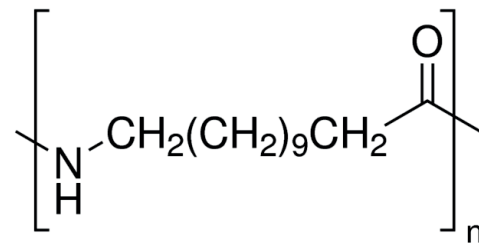
When R or R' are aromatic radicals, the polymer is called aromatic polyamide, or aramid, which show even higher performance [26]. Impressive impact and thermal resistance are achieved. The aromatic rings in the polymer chain raise the melting point and glass transition and improve chemical resistance. Hence they are used to replace metals in high temperature automotive and aeronautic applications. Two popular trademarks under which aromatic PAs are commercialized are Nomex® and Kevlar®, which is famous for being employed in body armours and helmets. Aramids can be also produced in form of high-strength fibers. Due to their high melting point ($> 300\text{ }^\circ\text{C}$), they are suitable as reinforcement in melt liquid composite molding processing. If only R' is aromatic (i.e. the acid monomer is a terephthalic acid) they are said semi-aromatic



(a) PA6 is obtained by ring-opening of caprolactam (6-Carbon lactam).



(b) PA66 is obtained from polycondensation of hexamethylenediamine and adipic acid.



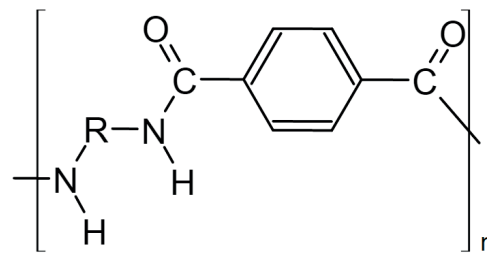
(c) PA12 is obtained by ring-opening of lauryllactam (12-Carbon lactam).

Fig. 2.2: Chemical structure of the most relevant aliphatic polyamides.

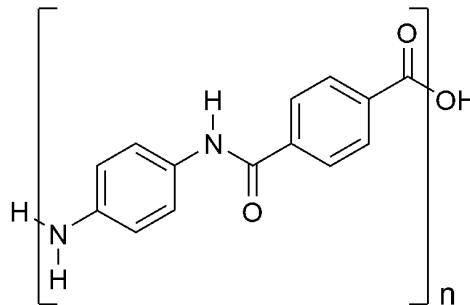
polyamides, or polyphthalamides (PPA), which combine performances of aromatic PAs with processability of aliphatic PAs [27]. However, these tend to be limited by their high brittleness at room temperature, and further research is still ongoing to reach a better compromise [28]. The repeating unit of a semiaromatic and an aromatic PA are shown in Fig. 2.3. Physical and mechanical properties of selected polyamides are reported in Table 2.2. For comparison, the high-fluidity PA developed by Solvay [29] is also displayed.

Table 2.2: Physical and mechanical properties of selected polyamides.

Polyamide	Tensile Modulus (GPa)	Melting Point (°C)	Specific Gravity
PA-6	2.8	215	1.13
PA-6,6	3	264	1.14
PPA	3.8	302-329	1.20
HFPA66	3-4.2 [29]	256-262	1.14



(a)



(b)

Fig. 2.3: Chemical structure of (a) a PPA and (b) an aramid (here Kevlar®).

2.1.3 Specific requirements

In automotive applications, specific mechanical properties are required depending on the component under consideration. For structural applications (e.g. for the BIW) main properties are stiffness and fatigue resistance, either in bending or torsion. The stiffness is determined by both part geometry and material intrinsic properties, namely elastic modulus and density. In particular, the ratio between these two characteristics is used as an index for material selection in lightweighting.

Another major aspect is *crashworthiness*, which is the ability of a component to dissipate energy during an impact, thus preserving passengers' safety. Composite materials offer a number of possibilities in the design of energy-absorbing structures. The two main parameters to be considered in crashworthiness studies are the specific energy absorption (SEA, kJ/kg) and the rate of work decay (kJ/s) [30]. These are affected by the intrinsic properties of the matrix and fiber materials, as well as by the architecture of the fibers. Indeed, it has been found that the specific energy absorption depends on textile orientation and arrangement [31, 32]. For instance, several studies reported that

woven and braided fabrics have higher SEA than unidirectional (UD) reinforced composites [33, 34]. Regarding the matrix materials, thermoplastic polymers have higher fracture toughness when compared to thermosets, and this is correlated with the specific energy absorption of TPC [35]. From this point of view, TPCs are excellent candidates for structural vehicle components. It has been reported that fiber volume fraction also has an influence on the SEA, but it is also correlated to the fiber/matrix materials and textile architecture [11]. Generally speaking, it seems that the SEA increases with the fiber content, but in the case of chopped short fibers the SEA drops above a certain value of the fiber volume fraction [36]. Fig. 2.4 shows the comparison of SEA values for different materials. Carbon fiber reinforced thermoplastics have the highest SEA compared to the others.

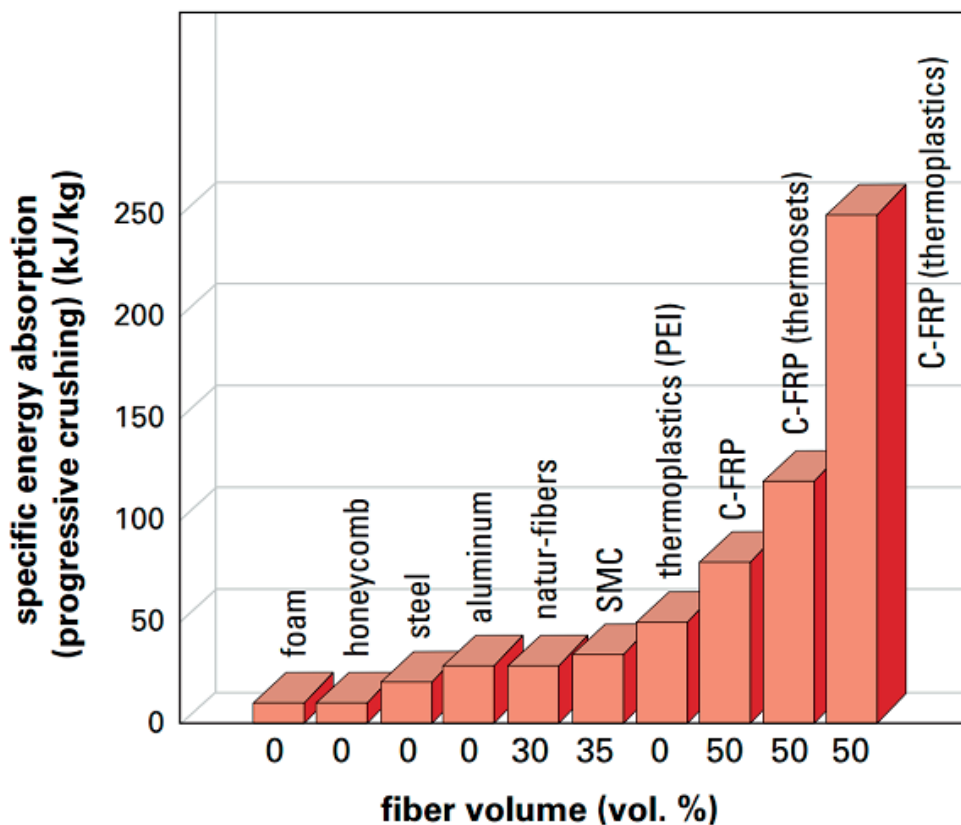


Fig. 2.4: Typical values of SEA for some materials [37].

Another issue to consider, in the case of dynamic loaded parts, is fatigue resistance, which is usually very good for polymer matrix composites. Driveshaft and springs are quite important examples of parts subject to fatigue. It has been shown that in the case

of continuous random glass-fiber, the matrix has a minor influence on the fatigue behavior [38]. In the example, polypropylene and an epoxy resin were compared. On the other hand, several studies show the influence of fiber type and orientation on the fatigue resistance, as well as on torsional stiffness. For instance, Badie et al. [39] have shown that carbon/epoxy driveshafts have higher torsional stiffness and fatigue life when compared with glass/epoxy, and that a stacking sequence $90^\circ/0^\circ$ of laminates undergoes a more gradual failure than the sequence $\pm 45^\circ$.

2.2 Physical properties of thermoplastic polymers

2.2.1 Rheology of thermoplastic polymers

Melted polymers are usually non-newtonian fluids, i.e. their viscosity depends on shear rate, thus can vary depending on the processing conditions. For instance, if high pressure is applied to force the impregnation of the reinforcement (as in the injection molding), the fluid will experience high shear rates. Thus, a deep knowledge of the rheology of thermoplastic polymers is fundamental for the study of composites processing, in particular in LCM techniques, where the fluid viscosity greatly affects the impregnation kinetics[†].

Polymer viscosity is increased by all the factors that reduce macromolecules mobility. For instance, at high temperature, enough energy is available for the molecules to overcome the roto-vibrational energetic barrier. Shear rate also affects the viscosity. Typically, for a linear polymer in the melt state, viscosity is constant at low shear rates, from zero to a certain critical value, after which it begins to decrease. This rheological behavior is known as "pseudoplasticity", or shear thinning, and has been explained as a consequence of disentanglement due to high shear forces [40]. A high degree of entanglement between polymer chains is a major cause of reduced mobility. The longer the chain, the higher the probability of entanglement and number of "knots". Indeed, a correlation between viscosity and average molecular weight has been demonstrated [41].

[†]The effect of resin viscosity on flow rate is modeled by Darcy's law, which will be introduced in Section 2.4.

Viscosity at zero shear-rate (η_0), also known as Newtonian viscosity, is linearly dependent on molecular weight M , but above a certain critical value M_c the relation is [42]

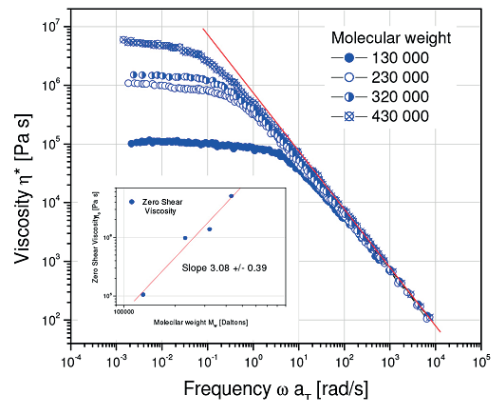
$$\eta_0 \propto M^{3.4}, \quad (2.2)$$

and is valid for linear chain polymers. Fig. 2.5a shows an example of the increase of viscosity at low shear rates with molecular weight. Low molecular weight polymers are easier to process, because of their low viscosity, but exhibit reduced performance. On the other side, viscosity at high shear rate is qualitatively correlated with molecular weight distribution. The shear-thinning onset (the frequency at which viscosity begins to decrease) moves towards lower rate values for narrower distributions. An example of the rheological behavior of melt polymer dependence on molecular weight distribution is shown in Fig. 2.5b, where the red and the blue points correspond to a narrow and a broad distribution, respectively.

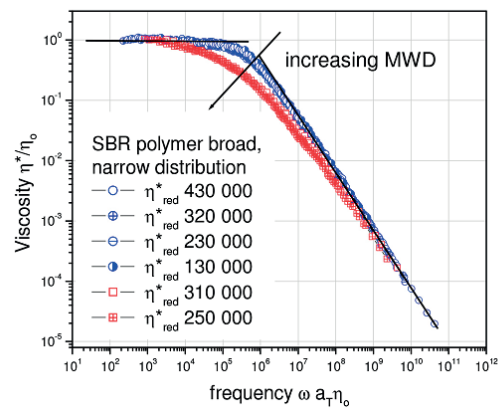
Non-linear polymers rheology is quite different. The viscosity depends on the number, length and distribution of branches. For instance, few long branches entangle more than a single linear chain of same molecular weight, and this results in higher viscosity. On the contrary, hyperbranched and dendritic polymers have very low viscosity. The chains are closed in a packed, perfect spherical structure and there is no entanglement. Thus, a hyperbranched polymer has much lower viscosity than a linear polymer with the same molecular weight (Fig. 2.6). This is particularly true at high molecular weight [44]. Reviews of synthesis and applications of hyperbranched and dendritic polyamides have been proposed by Klok et al. [45] and by Gao and Yan [46].

2.2.2 Polymer crystallization

The final properties of a solid polymer depend on the degree of crystallization. Most of thermoplastics are amorphous or semi-crystalline. In the crystalline regions of a bulk polymer, macromolecular chains are organized in thin flat *lamellae*, which in turn are concentrically arranged to form spherical structures, the *spherulites*, which can be observed by a polarized optical microscope.



(a)



(b)

Fig. 2.5: Dependence of viscosity on (a) molecular weight and (b) molecular weight distribution [43].

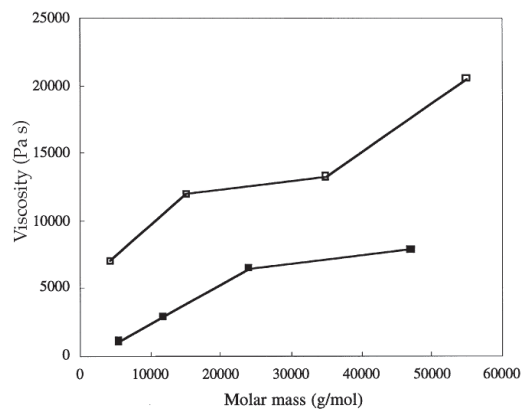


Fig. 2.6: Viscosity as a function of molecular weight for a linear (blank squares) and an hyper-branched (solid squares) polyester [47].

The kinetics of crystallization from the melted polymer at a given temperature can be described by the Johnson-Mehl-Avrami-Kolmogorov (JMAK) theory (usually referred to simply as the Avrami model) [48–50], according to which the degree of conversion into crystalline phase can be expressed by an exponential law of the type

$$\alpha(t) = 1 - e^{-kt^n} \quad (2.3)$$

where t is the crystallization time, k is a temperature-dependent coefficient and n is called the Avrami exponent. These two parameters are specific for the system under consideration. k is a temperature dependent kinetics rate constant. n is usually an integer number related to the geometry of crystallites and nucleation type. In case of spontaneous nucleation (all nuclei start growth at the same time), n can assume values 1, for uni-dimensional configurations (fiber or rod-like), 2, for two-dimensional (disk or platelet-like), and 3, for three-dimensional shapes (spherulites). In case of so-called sporadic nucleation (nuclei start growth at a certain rate), n can be 2 (1D), 3 (2D) or 4 (3D) [51]. For example, for a homogeneous continuous (sporadic) nucleation with constant nucleation rate N (number of nuclei formed per unit time per unit volume) and linear three-dimensional growth rate G , we have $n = 4$ and $k = \frac{\pi N G^3 \rho_S}{3 \rho_L}$, given ρ_S and ρ_L the density of the liquid and of the spherulite [52]. Eq. 2.3 gives the typical sigmoidal curve kinetics observable in many conversion processes, and at the very early stage (i.e. for $t \rightarrow 0$) the crystallization proceeds with time as a power of n ,

$$\alpha(t) \approx kt^n. \quad (2.4)$$

More generally, for non-constant nucleation and radial growth rate, the Avrami model predicts for the degree of conversion at time t the following expression [50]

$$\alpha(t) = 1 - \exp \left[-\frac{4\pi}{3} \int_0^t d\zeta N(\zeta) \left(\int_\zeta^t d\xi G(\xi) \right)^3 \right]. \quad (2.5)$$

From this equation one can derive Eq. 2.3. Furthermore, in the case of instantaneous heterogeneous nucleation at $t = 0$ (again considering G and N as constants), Eq. 2.5

can be simplified removing the integrals to give [53]

$$\alpha(t) = 1 - \exp \left[-\frac{4\pi}{3} N G^3 t^3 \right]. \quad (2.6)$$

If one considers the "delay" of the crystallization due to the energetic barrier (i.e. the crystallization time τ), it can be considered $\alpha(t) = 0$ for $t < \tau$ and

$$\alpha(t) = 1 - \exp \left[-\frac{4\pi}{3} N G^3 (t - \tau)^3 \right] \quad (2.7)$$

for $t > \tau$. Similarly, for a non-isothermal crystallization process, assuming a constant nucleation rate N (but still depending on the crystallization time τ), and a growth rate G which varies with time, it will be for $t > \tau$

$$\alpha(t) = 1 - \exp \left[-\frac{4\pi}{3} N(\tau) \left(\int_{\tau}^t d\xi G(\xi) \right)^3 \right]. \quad (2.8)$$

A study of the isothermal crystallization kinetics of the HFPA66 developed by *Solvay*, in which classical DSC and flash-DSC were combined in order to cover a broad range of crystallization temperatures, reported an Avrami exponent of about 3, leading to the conclusion that three-dimensional crystallites nucleate instantaneously [54, 55].

2.3 Manufacturing of polymer matrix composites

Material properties are directly related to processing routes and conditions. This is particularly true in composite manufacturing, where the final properties of parts depend dramatically on the interaction between matrix and fillers that takes place precisely during the process. For example, in the case of long-fiber reinforcements, the matrix has to flow through the empty space between fibers, and mechanical properties are affected by the degree of impregnation. In the case of short fibers or particles, these are easily displaced or tilted under the effect of matrix flow. Hence, it is very important to gain a deep knowledge of the process, since this affects the microstructure and the final properties of the material.

Composites processing techniques are broadly reviewed in literature [56, 57]. A common distinction, based on the nature of the polymer, is often made between thermoset and thermoplastic composites fabrication methods. In this section, a brief summary of processing routes of polymer matrix composites in closed molds will be presented. The distinction will be made here between compression molding (CM) and liquid composite molding (LCM), where both TSs and TPs can be employed, and which are both potentially suitable methods to produce TP reinforced parts for the transport industry.

2.3.1 Compression molding

In compression molding, the raw material is a pre-impregnated stack of fabric layers placed between the upper and lower parts of a mold, where it is pressed and heated to give the final shape. Heat and pressure are maintained for the time necessary for the TS to cure or for the TP to impregnate the fibers and consolidate. In some cases, the TP prepreg is first preheated, for example by infrared heaters, then transferred to the cold press for stamping and cooling. The process is one of the shortest for composites manufacturing, with cycle times in the order of few minutes, which is very appealing for high-volume industries. One of the disadvantages is the necessity of heavy and expensive press equipment. In addition, only simple flat/detachable shapes can be produced, requiring further assembly and finishing steps and a certain amount of waste. The raw material can be a pre-impregnated sheet of either TS (sheet molding compound, SMC, or long fiber prepregs) or TP (glass mat thermoplastics, GMT, or organo-sheets).

SMCs contain a stack of cut fiber layers pre-impregnated with partially cured and thickened TS resins. It makes SMC still flexible, and allows them to be deformed and to flow to obtain the final shape. The fibers, in general 25mm in length, are randomly oriented. Compression moulding of long fiber thermoset prepregs is also commonly used; in that case, the prepreg also has a given limited shelf-life, and is placed in the heated press, then formed (with only limited flow this time) and cured before demolding. A main limiting factor will be the reaction time for curing the resin. The resin and the reinforcement can also be mixed to form a kind of paste that is placed in the mold and

flattened by the press. This is called bulk molding compound (BMC) and in this case the fibers can only be discontinuous (e.g. chopped glass fibers).

GMTs are tapes of randomly oriented short glass fibers embedded in a TP matrix. Typically, they are pre-heated and then stamp-formed in a cold mold. Organo-sheets feature continuous reinforcement, and they are available as either fully impregnated sheets (Fig. 2.7a) or as unconsolidated dry mixtures of the polymer and the fibers. For example, in film stacking, TP films are inserted between two or more reinforcing fabric layers

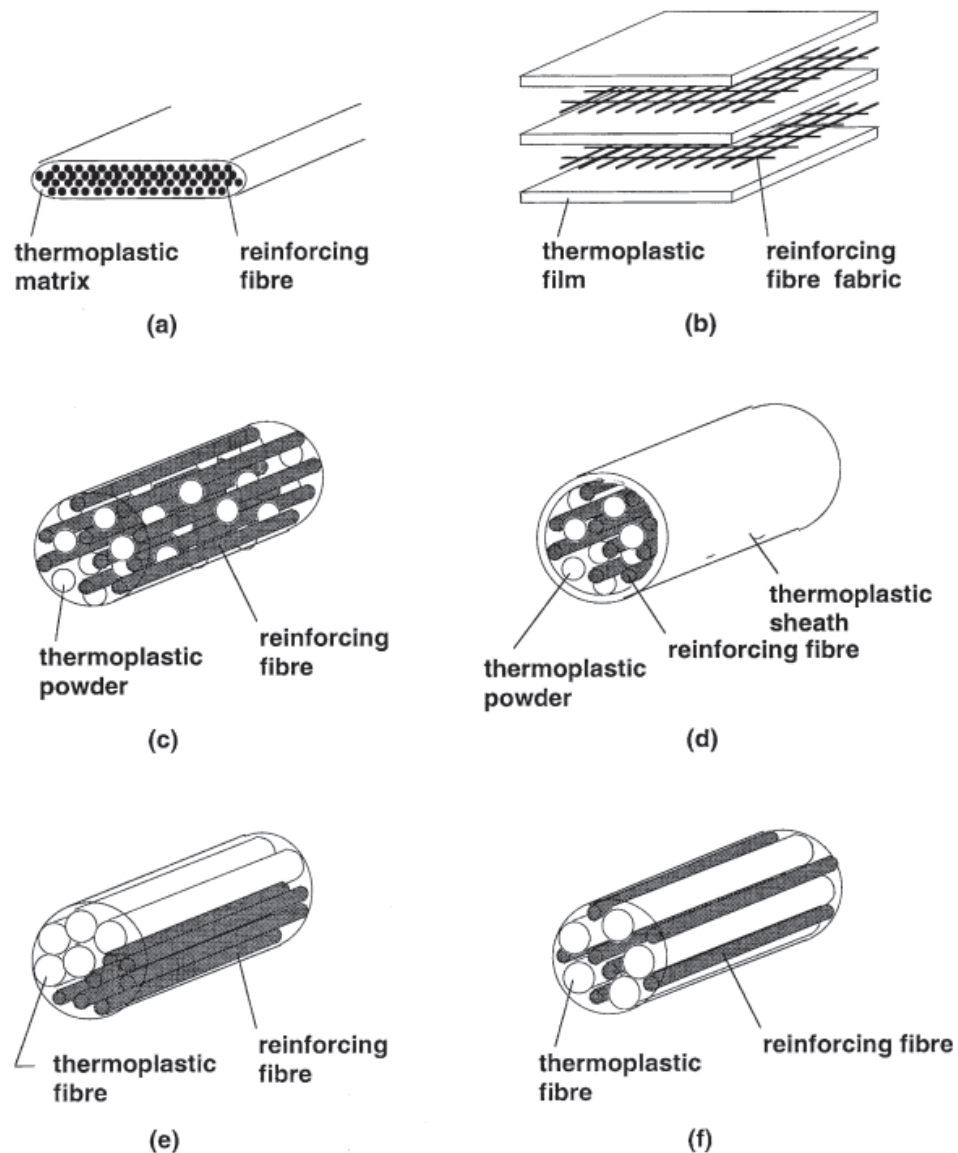


Fig. 2.7: Intermediate forms for thermoplastic composites: (a) pre-impregnated tow; (b) film-stacking; (c) powder-impregnated fiber bundle; (d) sheath-coated powder-impregnated fiber bundle; (e) non-commingled yarn; and (f) commingled yarn [58].

(Fig. 2.7b). TP can be introduced inside the fiber bundles in form of powder (Fig. 2.7c), and possibly coated by a TP sheath (Fig. 2.7d), or in form of fibers (Fig. 2.7e-f). Inside the hot press, the polymer is melted and the pressure forces it to flow between the fibers. Clearly, the fluid matrix has to flow a larger distance in the film-stacking than in the other systems, which are therefore more desirable in order to reach a good degree of impregnation in a shorter processing time. Compared to TS pre-pregs, GMTs and organo-sheets do not need to be stored at low temperature and have a longer shelf-life. Limiting factors are the time to reach full impregnation and, if a pre-heating step is not used, for cooling.

2.3.2 Liquid composite molding

Liquid composite molding (LCM) is a family of molding processes where the liquid matrix or its precursor is forced to flow through the dry reinforcement and subsequently consolidate the interface bond matrix/fiber in order to provide optimal mechanical properties to the finished part. The liquid is forced to flow through the reinforcement driven by a pressure gradient through the mold, created by applying either a positive pressure at the inlet or a negative pressure at the outlet, i.e. by connecting a vacuum pump. LCM comprises a number of different techniques. In vacuum assisted resin infusion molding (VARIM), the mold has a rigid bottom and a flexible top consisting in a vacuum-proof bag; vacuum pulled at the outlet drives resin flow and fabric compaction. Resin transfer molding (RTM) is a typical LCM process where the impregnation takes place in a closed, rigid mold, allowing a more precise control of the part thickness; in this case, pressurized resin is injected (e.g. by means of a pressure pot or a pump). Due to their lower viscosity ($< 1 \text{ Pa s}$), thermoset resins are the most suitable matrices for this kind of processes, requiring low applied pressure and curing temperature (typically below $200 \text{ }^\circ\text{C}$). LCM techniques, notable RTM, for production of TPCs are not very common, and are rather on research phase. They can be distinguished between reactive and melt processing.

Reactive TP-RTM

Similarly to thermosets, thermoplastics can be produced by impregnation of a reactive solution containing the monomers that polymerizes *in situ* during fabric impregnation. Reactive impregnation has been widely investigated in the past. Reactive RTM of PA12 has been investigated at LPAC (previously LTC) [59–64]. For an overview of TP reactive impregnation see the review of van Rijswijk and Bersee [18], whose group has also worked intensively on polyamides [65–70]. For other literature references see also [71, 72]. Research in the field of reactive TP-RTM with polyamides is still ongoing. For instance, Maazouz et al. recently investigated the time-temperature-transformation for polymerization-crystallization of PA6 from caprolactam, in order to determine a processing window for TP-RTM [73].

The use of low-viscosity, solvent-free oligomer precursors can be considered a middle ground between reactive and melt impregnation. Oligomers are short-chain molecules whose polymerization has somehow been blocked, for example by an end-capping agent. Cyclic butylene terephthalate (CBT®) is a successful example of low-viscosity (below 0.1 Pa s) oligomeric precursor which is used to produce thermoplastic composites through conventional thermoset techniques [74–77]. In CBT, the polymerization is blocked by the formation of cyclic oligomers, that are subsequently opened to complete the reaction and form poly(butylene terephthalate) (PBT) at about 200 °C. PBT is mainly used as an electric and thermal insulator, and for its resistance to chemical agents, rather than for load-bearing components.

A further step in this direction has been made in 2007 by NASA laboratories [78]. They developed a novel polyimide oligomeric resin with viscosity of 1–3 Pa s to demonstrate the feasibility of RTM with engineering-grade thermoplastics at very high temperatures. In this process, fabric impregnation and matrix polymerization occurred at 288 °C and 371 °C, respectively. Such high temperatures are acceptable for expensive high-performance aerospace components, but they are unlikely to be sustainable for high-volume productions as in the automotive industry.

A more recent and commercially successful example of reactive TP-RTM is the acrylic-based Elium® resin system developed by Arkema. It has properties very similar to TS resins (viscosity below 1 Pa s and comparable mechanical properties), and it

can be processed even at room temperature 100 °C [79–81]. Similarly to TSs, acrylic resins undergo radical reaction, unlike polyamides which polymerize by polycondensation, and therefore there is no formation of byproducts. However, the resulting polymer is a TP, as there is no cross-linking between macromolecules. In addition, it is an amorphous polymer, and there are no issues of simultaneous occurrence of polymerization and crystallization, which is the case for reactive PA systems [67, 82].

Melt TP-RTM

Thermoplastic melts from polymerized resins are usually more viscous than TSs and reactive TP resins[‡], thus require high pressure equipment, and also need higher temperatures to remain in the melt state until impregnation is completed. A major advantage of melt-processing is to avoid the use of solvents and other volatile compounds that may form during the reaction. If not evacuated from the mold, they could eventually remain trapped in the matrix and form voids that would affect the fiber bonding. Furthermore, the *in situ* polymerization may not be well reproducible fully reproducible and present problems due to the inhibition of the reaction depending on the (moisture, atmosphere, etc.). Development of thermoplastic polymers with viscosity down to 1 Pa s is paving the way to melt TP-RTM. However, very few studies on the process have been carried out so far.

A few years ago, Solvay has developed and patented high-fluidity polyamides that are suitable for direct melt-impregnation of dry fabrics [83, 84]. Orange et al. showed the feasibility of fabric impregnation with these resins (notably high-fluidity PA66 grades of viscosity <20 Pa s) at low injection pressure (<15 bar) resulting in low void content [29], but the application to manufacturing of TPC parts at high-volume production is still not straightforward. An R&D Consortium (*TAPAS-LCM*) involving academic and industrial researchers in France (among which Solvay) had been set up with the purpose to investigate novel LCM processes with HFTPs. Researchers from different institutions have been working on different fronts: characterization and optimization of high-fluidity TPs, enhancement of fabric permeability[§], and process optimization. In particular, the

[‡]See Fig. 1.3 in Chapter 1.

[§]Permeability, a crucial property of a reinforcing fabric, is a measure of how easily a porous medium can be impregnated by a fluid. It will be further discussed in Section 2.4.

issues related to the development of this process have been broadly addressed in the doctoral thesis of Cazaux [85] and Faraj [86]; results were also presented in conferences and journals [54, 55, 87–91]. Cazaux investigated mTP-RTM process through in-plane glass-fabric impregnation with several grades of HFPA66 injected at constant flow-rate [85]. Composite plates of size 40 cm × 30 cm could be produced with an impregnation time of 30 min. However, achievement of full impregnation at the micro-scale was a major issue. Indeed, it was shown that it was rather difficult for the melt polymer to infiltrate within the micro-pores of the fiber bundles, and this was ascribed to poor wettability of the resin-fabric system, especially at high injection flow-rate. In addition, at high flow-rate (or pressure) the local permeability of the fiber bundles is reduced due to the compression exerted by the fluid. It was therefore suggested that flow-rate, which was also observed to cause fabric deformation, should be lowered in order to minimize void content. As a result, only small parts (<40 cm) could be produced in a reasonably short processing time (<10 min). Alternatively, the possibility to perform the injection through the thickness of the preform driven by compression (C-RTM) came as a potentially good solution, which is currently investigated by J. Studer at FHNW, and N. Hautefeuille at *Ecole Centrale Nantes*, as well as directly by Solvay. In parallel, permeability improvement was also addressed, in order to increase the velocity of resin flow through the reinforcing fabric. In [87, 88], Cazaux et al. reported improvement of permeability for a UD reinforcement without affecting the fiber content. Similarly, Syerko et al. developed a model for permeability enhancement by optimization of the fabric geometrical parameter[¶] [90].

Process development is still at an early stage, and further studies are required in order to bring it to an industrial scale. Production rate must be increased, and at the same time part quality and performance have to be preserved. One of the scientific contributions of the present thesis is the investigation of strategies to further accelerate the impregnation step using improved preform architectures. In the next section, material and process parameters (namely resin physico-chemical properties, fabric volume fraction and permeability, and pressure of injection) and their drastic influence on the time of the impregnation step in LCM will be reviewed.

[¶]The topic of permeability enhancement will be addressed in Section 2.5.

2.4 Modeling of Liquid Composite Molding

LCM processes are modeled with a continuum mechanics approach [92, 93]. The reinforcing fabric is treated as a compressible porous medium with wholly interconnected porosity, which is infiltrated by an incompressible fluid. The mass conservation equations for the solid (the fibers) and liquid (the resin) phases are written as:

$$\frac{\partial V_f}{\partial t} + \nabla(V_f u_s) = 0 \quad (2.9)$$

and

$$\frac{\partial[(1 - V_f)S]}{\partial t} + \nabla((1 - V_f)S u_l) = 0 \quad (2.10)$$

where V_f is the fiber volume fraction, u_s the local velocity of the solid, u_l the local velocity of the liquid inside the pores, S is the saturation defined as $S = \frac{V_l}{1 - V_f}$, being V_l the volume fraction of the infiltrating liquid. For the momentum equation, the Darcy's law is generally applied [92, 94]

$$(1 - V_f)S(u_l - u_s) = -\frac{K}{\eta} \nabla P \quad (2.11)$$

where K is the permeability of the porous medium (m^2), η is the resin viscosity, and ∇P is the pressure gradient that drives the fluid flow.

A major application of Darcy's law is prediction of flow propagation and mold filling time. This requires accurate definition of pressure distribution in the mold, characterization of resin viscosity evolution and determination of fabric permeability, which can be either measured or predicted numerically. Permeability can be regarded as a sort of hydraulic conductivity and it is found to be dependent on fiber radius (R_f), fiber volume fraction (V_f), and fabric architecture (e.g. random mat, woven, non-crimp). Since all of these fabric parameters also affect the performance of the final composite, an optimum has to be found between production rate and part properties. For instance, permeability can be increased by reducing fiber volume fraction, but this has a detrimental effect on composite strength and elastic modulus.

Permeability modeling and measurement is not straightforward, due to the statistical nature of porous media. According to the Carman-Kozeny model applied to an

isotropic porous medium (originally a granular bed^{||}), the permeability K in Eq. 2.11 could be expressed as [95, 96]

$$K = c \frac{(1 - V_f)^3}{V_f^2} \quad (2.12)$$

$1 - V_f$ being the porosity and c a constant.

This model is not applicable to fiber reinforcements which have a maximal packing density, hence $V_{f,max} < 1$, above which the permeability drops to zero. In the most general case, permeability is a three-dimensional tensor, thus it requires nine values to be fully defined, but for textile fabrics, which have clear principal orientation, it can be diagonalized and it becomes possible to define only three values for the permeability, two for the in-plane directions ($x-y$) and one transverse to the layer, or through-thickness (z). For an aligned array of fibers, longitudinal (parallel to the fiber direction) and transverse permeability models proposed by Gebart's [97] are often used:

$$K_{\parallel}^s = \frac{8R_f^2}{C} \frac{(1 - V_f)^3}{V_f^2} \quad (2.13)$$

$$K_{\perp}^s = C' R_f^2 \left(\sqrt{\frac{V_{f,max}}{V_f}} - 1 \right)^{5/2} \quad (2.14)$$

where $V_{f,max}$ is the maximum theoretical fiber volume fraction, R_f is the fiber radius, C and C' are constants which depend on the textile architecture. From this model it is not possible to optimize the reinforcement architecture in order to enhance resin flow and impregnation without affecting the fiber volume fraction, diameter or arrangement^{**}. These models neglect to consider the heterogeneous, multi-scale nature of porosity in textiles. Single fibers are organized in bundles, which are knitted, stitched or woven, forming a fabric layer. A number of plies are then laid up and compacted in the mold to form a fibrous preform. The pores within the fiber bundles (intra-tow space), of the order of few μm , constitute the micro-porosity. At this scale, capillary forces may affect the flow by either sucking or repelling the fluid. The pores between the bundles (inter-tow space) constitute a meso-scale porosity where flow is purely viscous. At the macro-scale, the whole fabric reinforcement is considered as a homogeneous porous medium,

^{||}Early studies of fluid flow through porous media were made in soil mechanics.

^{**}The influence of fiber arrangement on permeability will be discussed in Section 2.5.

regardless of its micro- and meso-structure.

2.4.1 Permeability measurements

Permeability measurements are object of debate as they lack reproducibility [98, 99]. Poor reproducibility is mainly due to the statistic nature of porous media and to the numerous variables involved in the experiments (temperature, applied fluid pressure, surface tensions, fluid chemistry and rheology, fabric type and compaction, setup design, methodology of data analysis, human errors). In most LCM processes (as in RTM), the impregnation proceeds along the fabric-plane. Thus, assuming that no flow takes place in the vertical direction, only the in-plane permeability is considered to be relevant, and the through-thickness permeability can be neglected.

Permeability measurements rely on Darcy's law Eq. 2.11 under the hypothesis of full saturation ($S = 1$) and static solid phase ($u_s = 0$). In a typical experiment, a test fluid of known viscosity is forced to impregnate the fabric under consideration inside a rigid mold. The impregnation can be performed either by injecting the fluid under constant pressure at the inlet, or by imposing a constant flow-rate^{††}. If pressure distribution is defined, a measurement of fluid velocity allows to indirectly measure fabric permeability, and vice versa. In constant-pressure experiments, two types of measurements are possible, depending whether fluid flow-rate is measured after the mold has been completely filled (saturated or steady-state) or during fabric impregnation by visualization of the flow-front advancement through a transparent mold (unsaturated or transient-state) [98, 99].

In saturated unidirectional measurements conducted at constant fluid pressure at the inlet, the flow rate Q_{out} of the outcoming fluid can be expressed as

$$\frac{Q_{out}}{A} = (1 - V_f)u_l \quad (2.15)$$

A being the cross section of the fabric stack. Assuming a linear gradient throughout the mold (Fig. 2.8a), the saturated permeability can be expressed from Darcy's law

^{††}If not specified, constant-pressure experiments are assumed in the rest of the thesis.

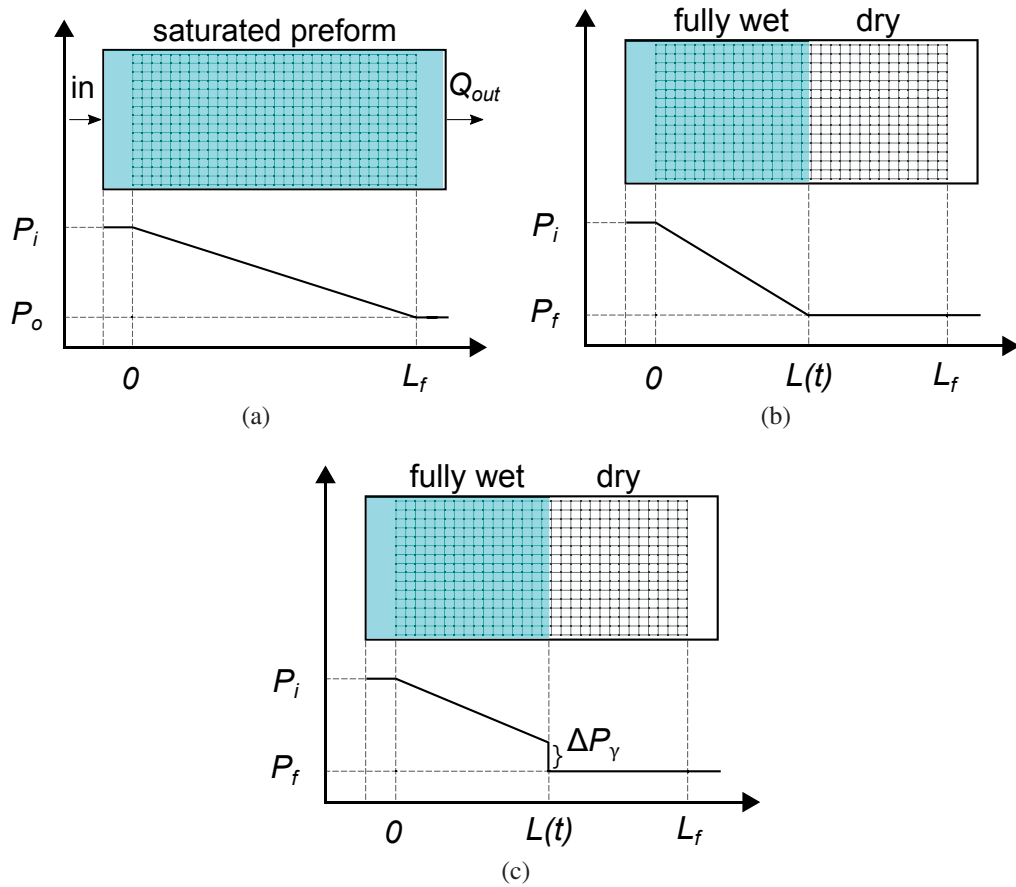


Fig. 2.8: Schematic representation of the flow through a fibrous preform showing the pressure profile for (a) a fully saturated case, and unsaturated flow (b) without and (c) with the presence of capillary pressure drop at the flow front.

(Eq. 2.11) as

$$K_{sat} = -\frac{Q_{out}\eta L_f}{A\Delta P} \quad (2.16)$$

where L_f is the length of the fabric in the flow direction and $\Delta P = P_f - P_i$ the negative pressure difference between the outlet (P_o) and the inlet (P_i) of the mold (Fig. 2.8a), and $\nabla P = \Delta P/L_f$ [93, 98].

In unsaturated measurements and under the same hypothesis (unidirectional, in-plane flow under constant pressure difference and linear pressure gradient^{‡‡}), plus the additional "slug-flow" assumption (Fig. 2.8b)^{§§}, integration of Darcy's law leads to a

^{‡‡}During unsaturated flow at constant inlet pressure, the pressure profile is not strictly linear, as shown for instance in [100], but rather parabolic, though progressively approaching linearity when the flow-front gets closer to the outlet. This is explained by the presence of an unsaturated region behind the flow-front, which in turn is related to the dual scale of porosity in fabrics.

^{§§}In "slug-flow", the fabric is either fully wet or dry, and the two regions are sharply separated by a narrow flow-front.

linear relation between the square of the flow front position and time

$$L^2(t) = \frac{2K_{unsat}\Delta P}{(1 - V_f)\eta} t = \psi^2 t. \quad (2.17)$$

The constant ψ^2 can be measured in an impregnation experiment, where the evolution of the flow-front position $L(t)$ of a fluid of known viscosity through a fabric preform in a transparent mold is recorded. This allows to indirectly measure the unsaturated permeability, which is defined as

$$K_{unsat} = -\frac{(1 - V_f)\eta\psi^2}{2\Delta P} \quad (2.18)$$

where ΔP is now the constant negative pressure difference maintained between the inlet and the dry fabric^{¶¶} (Fig. 2.8b) [92, 93, 98]. This is also known as the Squared Flow Front (SFF) method. An alternative approach consists in measuring as many K_{unsat} as the number of positions examined (e.g. each 1 cm), i.e.

$$K_{unsat}^i = -\frac{(1 - V_f)\eta}{2\Delta P} \frac{L^2(t_i)}{t_i}, \quad (2.19)$$

rather than a constant value from the slope.

2.4.2 Capillary effects

In LCM processes, the interaction between the flowing resin and the fibrous network takes place at different scales. Indeed, fibers are arranged in bundles, forming a complex network of micro-pores inside the bundles (intra-tow space) and meso-pores between the bundles (inter-tow space)^{***}. This results in a competition between different types of forces driving the flow. Typically, purely viscous flow dominates in the inter-tow space, while capillary forces can have an effect in the narrow intra-tow space. It is therefore important to quantify these forces, which can influence

During the impregnation in an LCM process, three different phases are in contact at the front of the infiltrating fluid: the liquid matrix, the solid fibers and the gaseous

^{¶¶}The pressure right ahead the flow-front is the same as the one at the outlet, typically atmospheric pressure (~ 1 bar) or vacuum (~ 0 bar).

^{***}In the order of $10\ \mu\text{m}$ for micro-pores and from $100\ \mu\text{m}$ to few millimeters for meso-pores

atmosphere. For a static drop of liquid on a solid surface in a given gaseous atmosphere at thermodynamic equilibrium, Young's equation predicts the contact-angle θ_0

$$\gamma_{sv} = \gamma_{sl} + \gamma_{lv} \cos \theta_0 \quad (2.20)$$

where γ are the surface tensions between solid, liquid and vapor phases. The fluid is said to be wetting for $\theta < 90^\circ$ and non-wetting for $\theta > 90^\circ$. Static wettability is an important property of a resin-fabric system, as it affects the quality of the fiber-matrix interface in the final composite, which justifies the need of choosing the appropriate sizing for an optimal adhesion between fibers and matrix.

However, it has been proven that wettability is actually a dynamic property of the resin-fabric system, and as such it can influence whether the resin will preferentially flow in the intra- or inter-tow spaces [62]. Similarly to the case of a drop in equilibrium on a surface (static wetting), the angle formed between the three phases at the fluid-fiber-air interface during the impregnation is determined from out of equilibrium thermodynamic considerations. During the infiltration, the fluid moves under the influence of an external pressure, thus the equilibrium hypothesis falls. For viscous polymeric fluids, the dynamic contact angle of a fluid of viscosity η moving at a velocity u_l is given by the Hoffman-Voinov-Tanner law [101, 102]

$$\theta_D \approx \sqrt[3]{\theta_0 + c_T Ca} \quad (2.21)$$

where c_T is the empirical Tanner coefficient, and Ca is the ratio between viscous forces and surface tension, called capillary number, defined by

$$Ca = \frac{u_l \eta}{\gamma_{lv}}. \quad (2.22)$$

As the fluid infiltration into the dry fibrous preform proceeds, a pressure difference due to surface tensions is created at the flow-front (Fig. 2.8c). From a thermodynamic approach, this capillary pressure drop can be expressed as [103, 104]

$$\Delta P_\gamma = -S_f \gamma_{ma} \cos(\theta) \quad (2.23)$$

where S_f is the total area of matrix-fiber interface per unit of volume, γ_{ma} the matrix-air surface tension, and θ the (dynamic) contact angle.

In slug-flow assumption, the capillary pressure drop is localized at the moving flow-front, which separates the dry fabric from the fully saturated region (Fig. 2.8c). This gives an additional pressure term, which modifies the pressure gradient. The total pressure difference between inlet and outlet becomes

$$\Delta P = P_f - P_i + \Delta P_\gamma = \Delta P_{app} + \Delta P_\gamma \quad (2.24)$$

with ΔP_{app} the negative pressure difference applied between the dry fabric P_f and the fluid at the inlet P_i . From Eqs. 2.23 and 2.24, if $\theta < 90^\circ$, then ΔP_γ is negative, the pressure gradient becomes steeper and flow is enhanced by capillary suction. Conversely, if $\theta > 90^\circ$, then ΔP_γ is positive and opposite to the applied pressure gradient, which becomes less steep^{†††}, and the flow is slowed down. Typical values of capillary pressure in LCM range from few to tens of kPa [62, 105, 106], hence capillary effects may not be neglected, especially for infiltration conducted under very low applied pressure.

Several studies have investigated the role of capillary forces in composite manufacturing [60, 62, 104, 105, 107–111]. The dual peak porosity distribution in the fabric (micro- and meso-porosity) is responsible for dual-scale flow^{‡‡‡}, which can be responsible for void entrapment during fabric impregnation [60, 62, 110, 112–118]. If capillary forces are high compared to viscous forces, micro-flow will dominate and macro-voids can be trapped in the inter-tow spaces. Conversely, if capillary forces are negligible, flow in the inter-tow space is dominant and micro-voids can be trapped within the intra-tow spaces. Depending on the fluid pressure or flow-rate, both micro- and macro-voids can be observed at different positions along a produced part [119]. Previous studies indicated that voids can be minimal when the flow velocity corresponds to an equilibrium point between capillary and viscous forces [60, 112–115, 117]. For this reason, the capillary number (Eq. 2.22) is typically considered in void minimization studies. The optimal Ca value should be that for which capillary and viscous forces compensate, resulting in comparable flow velocities in the inter- and intra-tow regions, which leads to

^{†††}This is the case shown in Fig. 2.8c.

^{‡‡‡}The fluid flows at different velocity in the intra- and inter-tow spaces.

a minimum void content in the final part [60, 113–115, 117].

A method for measuring the capillary forces, inspired from soil science literature, was initially developed in metal-matrix composite processing [104], and later applied also in LCM [62, 105, 111]. Considering slug-flow assumption and capillary pressure drop localized at the flow-front, inserting Eq. 2.24 in Eq. 2.18 leads to

$$K = -\frac{(1 - V_f)\eta\psi^2}{2(\Delta P + \Delta P_\gamma)}. \quad (2.25)$$

Isolating the term ψ^2 , we find

$$\psi^2 = -\frac{2K(\Delta P + \Delta P_\gamma)}{(1 - V_f)\eta}. \quad (2.26)$$

Based on Eq. 2.26, the capillary pressure drop for a given fluid-fabric system can be extrapolated from a series of unsaturated permeability measurements performed at different constant applied pressures. The x-intercept of the plot ψ^2 against ΔP_{app} is then taken as the value for the capillary pressure drop. This approach requires slug-flow assumption to hold, which might not be the case if strong dual-scale flow occurs. Moreover, a value obtained with this procedure is to be considered as largely approximate, as ΔP_γ is velocity-dependent, and therefore it is expected to vary with the applied pressure, in virtue of Eqs. 2.21 and 2.23.

2.4.3 Differences between unsaturated and saturated permeability

Ideally, unsaturated and saturated permeability should be equal, as it is supposed to depend only on the fabric architecture and not on the fluid or pressure used during the experiment. However, differences between the two values are often observed and object of study [100, 120–125], and they are typically attributed to deviations from the slug-flow hypothesis or, more rarely, to capillary effects. Intuitively, from Eqs. 2.25 and 2.26, the existence of a capillary pressure between the flow-front and the dry fabric may alter the velocity of the fluid and lead to erroneous unsaturated permeability measurement. On the contrary, saturated permeability is not supposed to be affected by capillarity. In

some cases, the permeability ratio, defined as

$$R_s = \frac{K_{unsat}}{K_{sat}}, \quad (2.27)$$

is explicitly calculated. Some authors claim that R_s should be always lower than 1 because the dry tows would oppose resistance to the macro-flow, which is therefore slowed down. However, values above 1 have been also observed.

Steenkamer et al. [120] reported a large dependence of unsaturated permeability on the type of test-fluid used (vinyl ester resin, motor oil and corn syrup were used), and related it to capillary effects. Conversely, Hammond and Loos [126] did not report any significant differences in permeability for both a glass fabric (plain weave) and a carbon fabric (8-harness satin) measured with corn oil, water or epoxy resin. Moreover, they obtained similar results for saturated and unsaturated permeability ($R_s \sim 1$), although only a limited range of capillary numbers was investigated (roughly between 0.001 and 0.02). Lundström et al. [121] observed that unsaturated permeability was always slightly higher than the saturated one ($R_s > 1$) for different fluids (paraffin oil, polyester and vinylester resin) and fabrics (a non-crimp and a woven). Capillary number was not reported, but the pressure range was between 0.4 and 1.6 bar.

Bréard et al. [100] addressed the problem of the difference between unsaturated and saturated permeability as related to the existence of an unsaturated region behind the advancing flow-front. By measuring the unsaturated permeability at different flow-front positions during injection experiments (Eq. 2.19), they found that R_s tended to a constant value lower than 1. However, when the flow-front was approaching the outlet, it increased until $R_s \sim 1$. This final increase was attributed to the achievement of a fully saturated state, whereas the constant value lower than 1 in the central part of the mold was observed to vary with the fabric architecture^{§§§}. The authors suggested that R_s is strongly related to the dual-scale porosity of a fabric. The assumption was that inter-tow flow was always dominant and micro-flow in the intra-tow pores delayed, and that the latter slowed down the former, thus leading to underestimation of permeability. A possible influence of capillary effects was suggested but not investigated, and there was no mention of the capillary number range at which the experiments were carried out.

^{§§§}A random mat, a bidirectional and a unidirectional fabrics were compared.

In the present work, the permeability ratio will be directly related to capillary effects. It will be shown in Section 3.2.1 that, if slug-flow assumption holds, the permeability ratio R_s can be related to the capillary pressure drop from the relation

$$R_s = 1 + \frac{\Delta P_\gamma}{\Delta P_{app}}. \quad (2.28)$$

ΔP_γ is dependent on capillary number, and thus R_s is expected to be as well. The investigation is done on a wide range of values of Ca (between $4 \cdot 10^{-5}$ and $4 \cdot 10^{-1}$).

2.5 Permeability enhancement

In this section, strategies for permeability improvement will be grouped in two classes, namely those relating permeability to fabric architecture and those investigating the effect of an external phase, such as flow meshes or channels and solid inclusions.

2.5.1 Effect of textile architecture on permeability

Evidences show that fibers' arrangement at the meso-scale greatly influences the overall permeability, and in many cases the simple Carman-Kozeny model (Eq. 2.12) and Gebart's equations (Eqs. 2.13 and 2.14) fail in predicting permeability, as they do not take into account the dual distribution of porosity in the fabric. The problem was addressed by Summerscales and coworkers in a series of published works. In [127] a model based on the concept of hydraulic radius was presented to demonstrate the effect of fiber clustering on permeability of unidirectional fiber arrays; for a constant number of fibers (i.e. constant fiber volume fraction), clustering resulted in larger inter-tow space, with subsequent enhancement of fluid flow rate. This was proven experimentally on a 2×2 twill carbon fabric, where a varying number of flow-enhancing tows along the flow direction was bound with a filament, resulting in denser tows and larger inter-tow pores [128–130]. However, along with permeability enhancement, a non-uniform distribution of fibers in these fabrics caused deterioration of mechanical properties, both in compression and in interlaminar shear tests [131]. In another study, they observed an increase of permeability proportional to the amount of large pores ($> 0.25\text{mm}^2$) for three different carbon fabric architectures (a 2×2 twill, a 5-harness satin and a

5-harness satin with bound flow-enhancing tows), and a corresponding deterioration of interlaminar shear strength [132]. More recently, the problem of geometry-permeability relation in dual porosity textiles was addressed by means of a numerical approach by Syerko et al. [90]. The study aimed at designing a fabric with optimal combination of permeability and mechanical properties. They considered as meaningful parameters the meso-channel size h , where mesoscopic flow takes place (inter-tow space), and local transverse permeability of fiber bundles k_{\perp} , which governs micro-flow (intra-tow space). More specifically, the Darcy number, defined as $Da = k_{\perp}/h^2$, was used as a criterion to determine the dual or single-scale nature of flow. In particular, for $Da > 10^{-3}$ micro-flow is considered to be negligible, and single-scale flow takes place, as illustrated in Fig. 2.9. In case of fiber clustering at constant V_f , it is clear that h and k_{\perp} cannot vary independently. Increasing the distance h between tows causes a reduction of the size of intra-tow pores, i.e. of tow permeability k_{\perp} . Nevertheless, it was shown that h affects the in-plane macro-permeability more than k_{\perp} . In other terms, the overall in-plane macro-permeability is determined mainly by the meso-pores size itself rather than by permeability of micro-pores.

Several studies proved that non-crimp fabrics (NCFs) typically have higher permeability compared to woven textiles, due to the pronounced bimodal distribution of porosity, which is responsible for a dual-scale type of flow [133–139]. Shih and Lee [133] carried out an experimental work in which they compared permeability of six different glass fabric architectures (a stitched unidirectional, a stitched bidirectional, a continuous strand random mat, a 4-harness woven, and two plain weaves with different tow size) at varying fiber volume fractions. They suggested a simple model where different scales of porosity (i.e. inter-tow and intra-tow spaces) are considered as media with different permeability connected either in series or in parallel, demonstrating a better data fit compared to the simple Carman-Kozeny model. It was found that the most permeable architecture was the bidirectional fabric, where permeability was dominated by flow in the large inter-tow gaps, and only to a small extent by micro-flow within the intra-tow pores. This architecture was therefore modeled as a high-permeability medium connected in parallel to a low-permeability medium, and the corresponding permeability was found

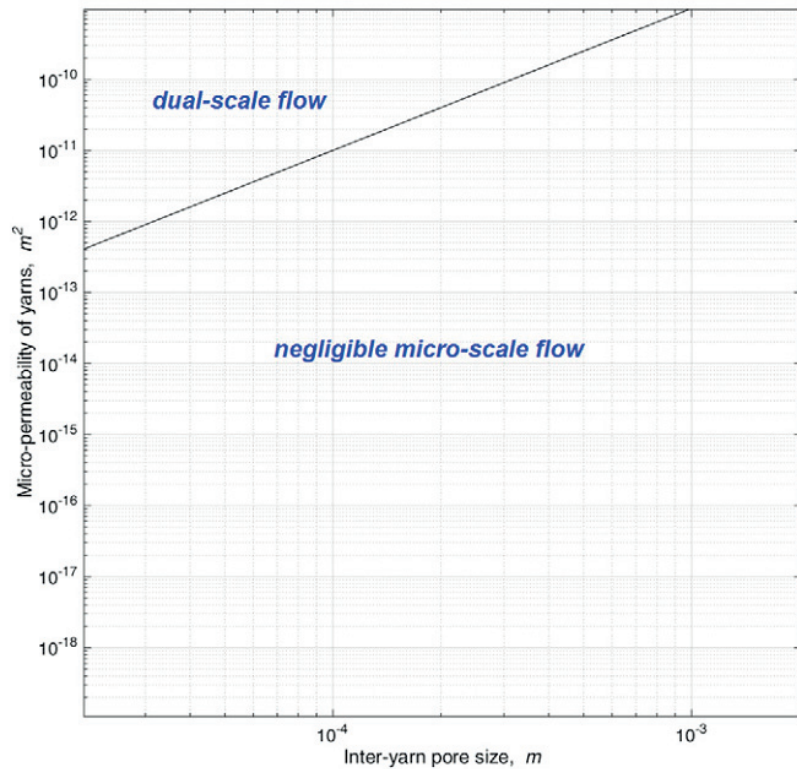


Fig. 2.9: Criterion for dual or single scale flow estimation, the line showing the regions where Da is higher or lower than 10^{-3} [90].

to be in good agreement with the experimental results. Lundström [134] proposed a simple geometrical model where the inter-tow meso-channels cross-sections perpendicular to flow direction were assumed to be rectangular under compaction rather than cusped squares. Under this assumption, the macro-permeability was taken as a combination of permeability of longitudinal and perpendicular tows and channels/gaps. Comparison with experiments on stitched bidirectional NCFs proved that only meso-flow in the inter-tow channels was important to determine the overall macro-permeability, and micro-flow in the intra-tow gaps could be neglected. The slight overestimation of permeability was attributed to the assumption of squared meso-channels, whereas they were observed to be cusped squares in reality. Martin et al. measured permeability of quasi-UD NCFs for different architectures of the low-tex backing layer for a large range of fiber volume fractions [139]. In particular, it was found that a higher stitch density was responsible for more heterogeneous fiber distribution (i.e. denser tows and larger meso-channels) and lower deformability, which resulted in lesser nesting. As a result, in-plane permeability along the UD tows was enhanced.

For woven fabrics, meaningful parameters are the weave pattern, yarn density, linear density (TEX number), areal weight, crimp ratio (the linear shrinkage of a yarn caused by weaving). Rieber et al. [140] measured the influence of these parameters on the in-plane permeability for a series of 19 different types of woven fabrics, and they found that permeability decreased less with fiber volume fraction for open (less dense) fabrics, i.e. with gaps between yarns. Moreover, a higher degree of anisotropy between the two principal directions was observed for low crimp ratio and for twill weave compared to plain weave.

2.5.2 Effect of a second solid phase on permeability

The presence of a third phase other than the reinforcement and the resin, i.e. a second solid phase, has been a matter of investigation in the past years. In particular, the effect of flow enhancing medium such as flow meshes has been largely investigated [141–145]. In Vacuum Assisted Resin Infusion molding (VARIM), also known as Seeman Composite Resin Infusion molding (SCRIMP) or Vacuum Assisted Resin Transfer molding (VARTM), a highly permeable layer (flow mesh) is laid on top of the fabric stack in order for the resin to rapidly flow from inlet to outlet, and later impregnate the fabric stack in the through-thickness direction. The flow mesh is a two-dimensional grid, which is meant to be removed from the final part. The mold top is actually a flexible vacuum bag, which allows fabric compaction to be achieved upon application of vacuum from the outlet. The pressure difference, which drives the flow, is also determined by the application of vacuum at the outlet, whereas the resin reservoir is kept at atmospheric pressure. Therefore, the maximum attainable pressure difference is limited to 1 bar. A large part of literature investigates the effect of distribution media on flow propagation and pressure distribution (i.e. porosity and thickness evolution) during and after mold filling. For instance, Lee and coworkers showed that flow propagation and filling time during VARIM was improved when a channel-wise flow medium was used instead of a flow mesh [141, 142]. Kracke et al. [146] investigated the influence of two different flow channel systems (one with short channels and one with channels almost as long as the fabric preform) on filling time. In both cases, a great reduction of filling time was observed, with minor differences between the two. However, when a macroscopic

imperfection (a folded strip of fabric) was manually introduced in the preform, longer channels led to a more uniform fluid distribution and shorter filling time.

In parallel, the use of second solid phase is also a matter of study in preforming technology. Polymeric binders in form of particles are commonly used to increase the preform stability, and these have an effect on preform permeability and on mechanical properties of the final composite. For instance, Caglar et al. [147] used model glass beads to investigate the effect of spherical inclusions on permeability, and demonstrated the relationship between their size and volume fraction, as well as the intrinsic pore size distribution of the fabric, on permeability. The recent rapid spreading of 3D-printing technologies raised an interest in researchers for its use in preforming. Szebenyi et al. studied the influence of a 3D-printed PCL interphase, directly printed on top of a carbon fabric layer, on the mechanical properties of composite plates produced with epoxy resin via vacuum-infusion [148]. The presence of the interphase was responsible for lower compaction, i.e. higher thickness of the plate, comparable bending modulus, reduced bending strength, but increased ductility; effects of this interphase on preform permeability were not studied. Tonejc et al. also recently investigated the effect of PLA strands directly printed on fabric layers as binders to stabilize the stack preform, observing a modification of flow front advancement in radial permeability experiments; however, the mean permeability was more or less unchanged [149].

2.6 Conclusions

Melt TP-RTM is a novel process for production of TPC components that combines advantages of both LCM and TP manufacturing. Small volume of production related to long cycle time represents the main obstacle to scaling-up. Impregnation of a densely-packed fibrous reinforcement with a highly-viscous molten polymer is the bottleneck of the process line. According to physical laws which govern infiltration of a liquid through a porous medium, process rate can be enhanced by either increasing fabric permeability or reducing resin viscosity.

This research aims at permeability improvement by exploitation of pronounced dual-scale of porosity in the fibrous preform. The main experimental investigation is performed through flow studies, which allow direct visualization of flow propagation

through the reinforcement and measurement of fabric permeability. This kind of experiments are quite convenient, since they are performed with stable model fluids of known viscosity and typically at room temperature, allowing to predict flow phenomena in processing conditions (i.e. with real resin and high temperature). The experimental work is carried out in order to investigate basic phenomena and to explore strategies for permeability enhancement. The main novelty is represented by the pronounced duality of pores' size distribution, with wide channels that lead the flow throughout the reinforcement. This is both observed in a commercial NCF (Chapter 4) and intentionally induced by insertion of a second solid phase produced by 3D-printing within the preform (Chapter 5). The findings from flow studies will be therefore exploited to investigate strategies for reduction of impregnation time in real, lab-scale processing conditions (Chapter 6).

Chapter 3

Materials and methods

The present chapter describes the materials that were used throughout the whole project, as well as the methods followed for experiments (equipment and procedures) and data treatment.

3.1 Materials

The materials used in the present study can be divided in three groups: test-fluids for flow and permeability studies; glass fabrics for flow studies and composite plates production; and high-fluidity thermoplastic matrices.

3.1.1 Test-fluids for flow studies

Several fluids with varying viscosity and surface tension were used to study the flow behavior and the permeability of glass-fabrics. The first class of fluids were water solutions of poly(ethylene glycol) (PEG 35 kg mol⁻¹, Sigma Aldrich) at various concentrations. These fluids are characterized by a high surface tension (close to water), ease of use and cleaning, and allow obtaining different viscosities by changing the polymer concentration. The second type of fluids used were silicon oils Bluesil™ 47V1000 and 47V12500 (Bluestar Silicones), with a dynamic viscosity of 1000 mm²/s and 12 500 mm²/s, respectively, and density 0.973 g/cm³*

*Values from manufacturer.

3.1.2 Glass-fabrics

The reinforcement of choice for high-volume applications is glass fibers, which represents a good compromise between cost and performance. Carbon fibers offer the best properties, but their cost is still very high at the present day. Natural fibers have been gaining ground in the past few years, but they have to be excluded for high-temperature processes because of thermal degradation.

The glass fabrics used in this study were supplied by Chomarat (France). For all the fabrics, the provided value of glass density was 2.62 g/cm^3 and the fiber radius was $7.55 \mu\text{m}^\dagger$. G-FLOWTM (520 g/m^2) is a glass-only fabric conceived for thermoset infusion processes with leno-weave architecture, where two warp yarns are twisted around the weft yarns (Fig. 3.1a). G-PLYTM (720 g/m^2) is a non-crimp fabric, consisting of dense tows (240 g/m^2) bound and stitched with a polyester yarn on an almost continuous layer of transverse fibers (480 g/m^2), which create large channels of width of 3-4 mm (Fig. 3.1b). A modification of G-PLY with glass stitches was also supplied, which in addition has a higher areal weight of 900 (480 in both warp and weft directions) and smaller channels. This fabric, which will be referred to as G-PLY (GS), was used only for the process improvement part (Section 6.3), where thermal stability at high temperature was required. G-WEAVETM (600 g/m^2) is a woven 2×2 twill with large tows of 4 mm width (Fig. 3.1c). Both G-PLY and G-WEAVE have a polyamide-compatible sizing. Properties of these three glass fabrics are reported in Table 3.1.

Table 3.1: Properties of glass fabrics (ChomaratTM).

Fabric	Type	Areal weight [0°] (g/m ²)	Areal weight [90°] (g/m ²)	Stitches density (g/m ²)
G-FLOW TM	leno weave	280	280	-
G-PLY TM	non-crimp	240	480	5
G-PLY TM (GS)	non-crimp	480	480	-
G-WEAVE TM	2×2 twill	300	300	-

[†] Average value obtained from optical microscopy of the cross section of embedded fibers.

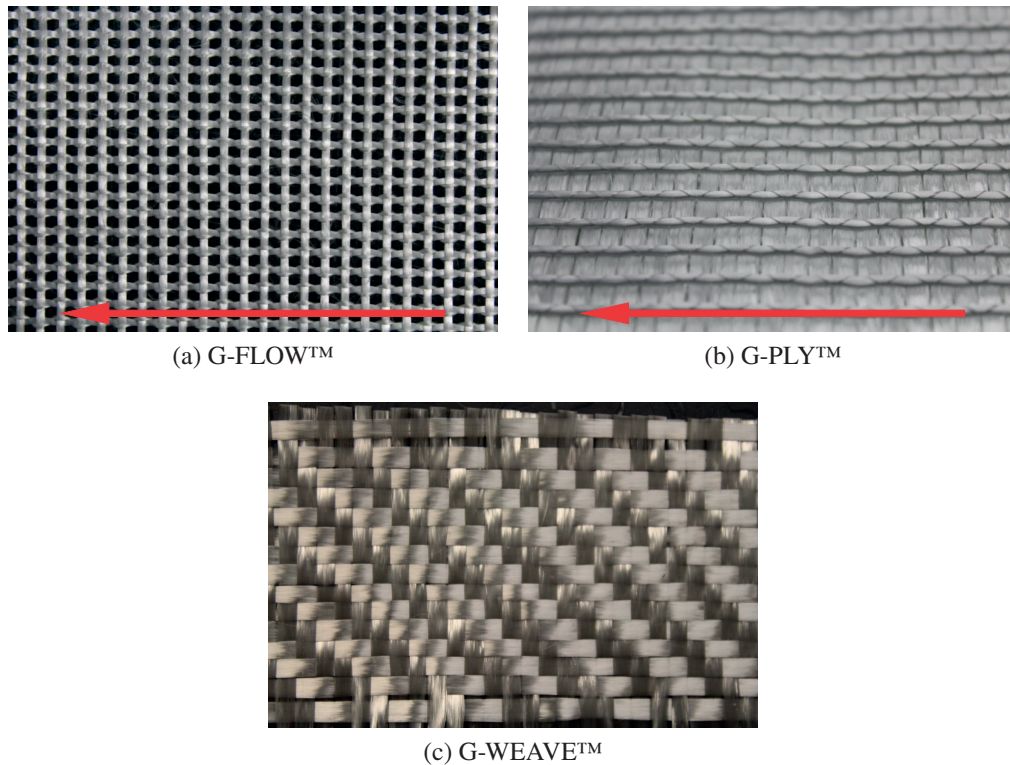


Fig. 3.1: Pictures of (a) a leno-weave, (b) a stitched non-crimp and (c) a 2×2 twill weave fabrics; the red arrow indicates the direction of high-flow (0°).

3.1.3 High-fluidity thermoplastic matrices

Two high-fluidity polyamide (HFPA) grades in form of pellets have been provided by Solvay, a polyamide-6,6 (HFPA66) and a polyamide-6 (HFPA6). The former is a research grade still in development phase, whereas the latter is a commercial grade (Evolite™ HF XS1480).

The HFPA66 is more suited for structural applications, owing to its higher elastic modulus. However, it has a high melting point (265-270 °C), and a narrow processing temperature window, as it degrades fast above 290 °C. The HFPA6 has a lower melting point (around 220 °C) and a better stability up to 300 °C. The mechanical properties are not as good as the HFPA66, and it is unlikely to be employed in highly loaded structural parts. Nevertheless, it is a good test-polymer to be used as matrix for the process improvement study. As polyamides are highly hygroscopic, and their rheological behavior is dramatically affected by moisture content, a drying treatment at 110 °C under vacuum overnight is usually performed on the pellets. The density of both these polymers is

1.14 g/cm³

A third thermoplastic polymer was used for the process study, which allowed an investigation at lower temperatures. It is an isotactic polypropylene (i-PP) from Borealis (Boreflow™ HL512FB). It is claimed to have a melt flow index of 1200 at 230 °C, but it has very poor mechanical properties. The density value provided by the producer is 0.902 g/cm³.

3.2 Methods

The experimental methods are grouped in three domains: flow studies; characterization of HFTP matrices; and production and analysis of composite plates.

3.2.1 Flow studies

Flow experiments consist in direct visualization of fabric impregnation with model fluids of known viscosity and measurement of fluid flow rate, which allow to indirectly determine permeability of fibrous preforms by virtue of Darcy's law (Eq. 2.11). In this study, flow experiments were employed to measure permeability of glass fabrics introduced in Section 3.1.2 and analyze the role of capillary phenomena during impregnation (Chapter 4). In addition, permeability of glass fabrics with flow-enhancement spacers is also investigated (Chapter 5).

Fluids characterization

Test fluids used in flow experiments need to be fully characterized. Determination of permeability with Darcy's law requires accurate knowledge of viscosity-temperature dependence. Fluid density is also needed to convert mass flow rate into volumetric flow rate for saturated permeability measurement (Eq. 2.16). Both viscosity and surface tension are then used to determine capillary number (Eq. 2.22). Therefore these properties of the test fluids introduced in Section 3.1.1 were characterized. Viscosity was measured in continuous shear mode in a concentric cylinder rheometer (AR2000ex, TA Instruments), by means of a Peltier Couette setup. A constant shear-rate was imposed while

Table 3.2: Properties of test fluids used for permeability measurements; the viscosity was measured at constant shear rate of either 100 s^{-1} (water/colorant), 10 s^{-1} (PEG 2%) or 1 s^{-1} (all other fluids).

Fluid	Viscosity (20 °C) Pa s	E_a $\text{kJ K}^{-1} \text{ mol}^{-1}$	A Pa s	Density g/ml	Surface tension mN/m
Water/Colorant	0.00125	-12.41	$7.679 \cdot 10^{-6}$	0.997*	68.9
PEG 2%	0.00280	-18.73	$1.292 \cdot 10^{-6}$	1.001*	59.9
PEG 16.7%	0.111	-20.67	$2.312 \cdot 10^{-5}$	1.026*	57.3
PEG 30%	0.841	-21.41	$1.290 \cdot 10^{-4}$	1.050*	56.6
BlueSil 47V1000	1.13	-13.29	$4.835 \cdot 10^{-3}$	0.970*	21.1*
BlueSil 47V12500	13.6	-13.26	$5.876 \cdot 10^{-2}$	0.973*	21.1*

*values at 25 °C

the temperature was varied from 15 to 25 °C at a heating rate of 0.1 °C/min and constant shear rate. The resulting viscosity vs. temperature curve was then fitted with an Arrhenius-type law:

$$\eta = A \exp \frac{E_a}{RT}. \quad (3.1)$$

and constants E_a and A were determined for each fluid. Density of PEG solutions was taken from literature [150], whereas for silicon oils values from manufacturer were used. Surface tension in air of all fluids was measured at ambient temperature (around 20 °C) through the pendant drop method on a Drop Shape Analyzer (DSA30, Krüss). Table 3.2 summarizes the properties of test fluids used for flow experiments.

Fabric compaction

The response of a fabric stack under compression (i.e. compaction) depends on fabric material and architecture, fiber volume fraction, number of plies, stacking sequence and orientation [151]. Typically, the pressure necessary to compact a given fabric preform at a prefixed thickness is measured. Not only it is useful to know how much pressure is necessary to apply to close the mold, but also to gain an insight into the deformation mechanisms which the fabric undergoes. Compaction tests were performed on a universal testing machine Walter+Bai AG Series LFL-125kN by placing the fabric stack between two platens. In a typical test, the cross-head was moved at constant speed of 1 mm/min down to a given thickness. The force was measured with a load cell (either 10 or 125 kN) both during compression and at constant thickness, and it was observed to first reach a maximum and then decrease, as a consequence of fabric relaxation, i.e. local

rearrangement of fibers. An LVDT (linear variable differential transformer) device was sometimes used to measure the upper platen displacement, but only in those experiments when forces higher than 10 kN were generated. Otherwise, the cross-head displacement was directly used to measure the compacted thickness. Compaction pressure was calculated dividing the measured force by the area of contact between the platens and the fabric[‡].

Fabrication of spacers by 3D-printing

Three-dimensional structures were fabricated by Filament Deposition Modeling (FDM) in both poly(lactic acid) (TreeD Filaments) and poly(capro-lactone) (3D4Makers[§]), in order to investigate their effect on flow propagation when inserted in the middle of a fabric stack[¶]. An Ultimaker2+ 3D-printer was used for the fabrication. The thermoplastic polymer in form of a filament feeds a hot extruder with a nozzle of 0.25 mm diameter. The extruder had two degrees of freedom, being able of horizontal movement (xy -plane), while the bed moved vertically (z -axis), following a 3D model. The three-dimensional design was performed on a 3D-modeling software, such as SketchUp, and it was exported into an .stl file. This was consequently opened with "slicing" software Ultimaker Cura, which cuts the model into a series of horizontal slices of a given thickness and determines the path (a series of x,y coordinates) the extruder has to follow to deposit it. Other parameters that could be controlled are nozzle speed, layers thickness, nozzle and bed temperature, cooling fan speed. In the present work, layers of polymer of thickness 0.1 mm were deposited at varying speeds and temperature, according to the observed quality of the printed structures. Printing speed was varied in a range between 6.25 and 37.5 mm s⁻¹. Nozzle and bed temperature were respectively 210 °C and 60 °C for PLA, and 180 °C and 35 °C for PCL.

[‡]Platens' and fabrics' size are detailed in Chapter 4 and Chapter 5, where compaction experiments are illustrated.

[§]PCL 99 filament 2.85 mm, purity >99%, $M_n = 47.5 \pm 2.0$ kDa, $M_w = 84.5 \pm 1.0$ kDa, $T_m = 60$ °C.

[¶]The detailed procedure will be described in Chapter 5.

Permeability measurements

Flow experiments for permeability measurement of all fibrous preforms were carried out using the setup shown in Fig. 3.2, which mainly comprises a rigid mold with a transparent glass top and an injecting unit. A single experiment allows simultaneous measurement of both unsaturated and saturated permeability values, which are measured from the velocity of the fluid during fabric impregnation (transient state) and after the fabric is fully impregnated (steady state), respectively.

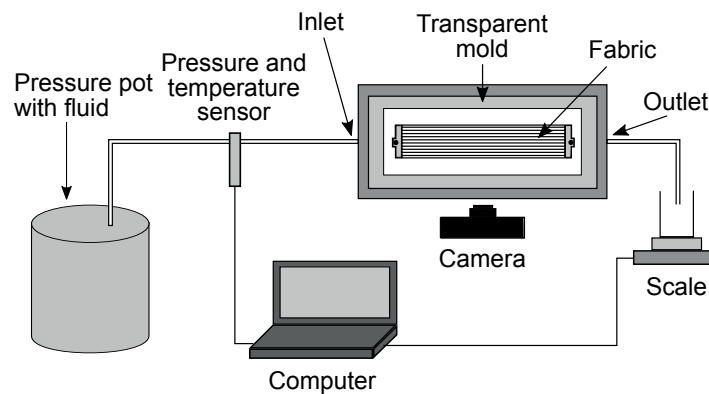


Fig. 3.2: Setup used for flow experiments and production of plates via TS-RTM; six heating cartridges, not shown, are embedded in the bottom steel part.

The fabric stack height was kept constant for all the experiments, by compacting it within a metallic frame, the thickness of which was accurately measured with a digital caliper and used as preform thickness. A silicone joint between the frame and the fabric prevented fluid leakage and minimized race-tracking. The fluid was injected into the mold cavity from a pressure pot constantly supplied with compressed air, which guaranteed a constant pressure to be applied on the fluid reservoir. The actual relative fluid pressure and temperature were measured right before the inlet with a sensor Keller Series 35XHTT. The advancement of the flow front was recorded through the glass top with digital camera Canon EOS700D. Lines were drawn equally spaced by 1 cm on the glass transversely to the flow direction. The video was subsequently analyzed so as to construct a plot of flow front position versus time by reporting the time at which the flow front reached each line. Outcoming fluid was collected in a beaker and continuously weighed with a scale. Mass flow rate was then converted into volumetric flow rate by dividing it by the fluid density for saturated permeability determination.

Unsaturated permeability was calculated from experimental data according to the squared flow front (SFF) method [99], which is recommended for unidirectional, in-plane flow under constant applied pressure, as

$$K_{SFF} = -\frac{\psi^2(1 - V_f)\eta}{2\Delta P} \quad (3.2)$$

where ψ^2 is the slope of the linear plot of the square of flow front position as a function of time, ΔP the applied pressure difference, η fluid viscosity, and V_f fiber volume fraction, calculated from actual fabric mass for each experiment as

$$V_f = \frac{A_w n}{t \rho_{glass}} \quad (3.3)$$

where A_w is the areal weight of the fabric, n the number of plies in the stack, t the thickness of the mold cavity, and ρ_{glass} the bulk density of the glass, which was always taken as 2.62 g/cm^3 (value provided by manufacturer). The data for the analysis was taken from the last part of the unsaturated flow, when the pressure was stabilized, typically starting from an impregnated length of 13 cm. The pressure, as well as the velocity used to calculate the capillary number from Eq. 2.22, were taken as average values in the same range. As an example, Fig. 3.3 shows the evolution with time during an impregnation of square flow front position, capillary number and pressure, and the range of data used for the analysis. The saturated permeability was calculated from the flow rate of the fluid at the outlet, Q_{out} , using the following relation

$$K_{sat} = -\frac{Q_{out}\eta L_f}{A\Delta P} \quad (3.4)$$

where A is the cross-section area of the fabric stack, L_f is its length and ΔP is the average pressure during saturated flow. For each test, the fluid viscosity was calculated from the Arrhenius law (Eq. 3.1) using the average experimental temperature. Finally, for each experiment the ratio between unsaturated and saturated permeability was simply calculated as

$$R_s = \frac{K_{SFF}}{K_{sat}}. \quad (3.5)$$

The ratio R_s defined in Eq. 3.5 was used to investigate the role of capillary pressure

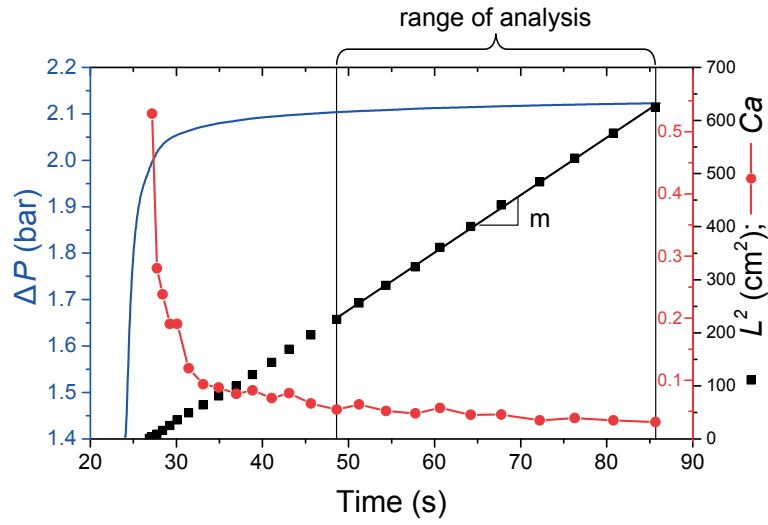


Fig. 3.3: Example of squared flow front, pressure and capillary number evolution with time for an experiment, showing the range of analysis.

during unsaturated flow. If the slug-flow assumption holds (Section 2.4.2), it can be shown that

$$R_s = 1 + \frac{\Delta P_\gamma}{\Delta P_{app}}. \quad (3.6)$$

Therefore, when $\Delta P_\gamma > 0$, the ratio is smaller than 1. The capillary pressure-drop has opposite sign with respect to the applied pressure, and the flow is non-wetting. As a consequence the measured unsaturated permeability should be smaller than the saturated. Conversely, if $\Delta P_\gamma < 0$ the ratio is higher than 1, and the flow is (partially) wetting.

It should be noticed that capillary number, defined in Section 2.4.2 as

$$Ca = \frac{u_l \eta}{\gamma_{lv}}$$

is not constant for infiltrations performed under constant applied pressure, unlike those at constant flow-rate. In fact, in such experiments the flow-front velocity u_l is not constant, but a decreasing function of time:

$$u_l = \frac{\psi}{2\sqrt{t}}. \quad (3.7)$$

It follows that capillary number is higher at the early stages of the impregnation, when the flow-front is close to the inlet, and it decreases progressively as the flow proceeds through the reinforcement towards the outlet, as shown in Fig. 3.3. A range of Ca is therefore

associated to each experiment at constant pressure. An average Ca is determined for each experiment in the same range of unsaturated permeability measurement (the last 10-12 cm).

3.2.2 Characterization of thermoplastic matrices

The thermoplastic polymers introduced in Section 3.1.3 were characterized in terms of rheology, thermal stability and crystallization. Effects of drying treatment and environmental conditions during tests (namely air or nitrogen atmosphere) was also investigated.

Differential Scanning Calorimetry (DSC)

DSC experiments were conducted on a DSC Q100 (TA Instruments). Single pellets were sealed in aluminum crucibles and measurements were carried out under constant N_2 flow of 50 mL min^{-1} . Heating scans were performed to measure the glass transition temperature (T_g) and melting point (T_m) of the two HFPA. Crystallization is typically studied by cooling from the melt state, and it is distinguished between isothermal and non-isothermal crystallization. In non-isothermal, crystallization temperature depends on the cooling rate, whereas in isothermal, the phenomenon occurs at different time-scales. Non-isothermal crystallization temperature was determined for HFPA66 for two different cooling rates ($100 \text{ }^\circ\text{C min}^{-1}$ and $30 \text{ }^\circ\text{C min}^{-1}$). Isothermal crystallization of HFPA66 was studied by rapidly cooling from the melt state ($300 \text{ }^\circ\text{C}$) to different temperatures in the range 236 to $250 \text{ }^\circ\text{C}$ to measure the evolution of the crystallization peak at constant temperature. The isothermal-crystallization peaks were analyzed subtracting a baseline obtained by cooling of an empty crucible. The running integrals of the peaks were analyzed and fitted with the Avrami equation for isothermal crystallization (Eq. 2.5), and the Avrami exponent was extrapolated. The time $t_{1/2}$ at which the running peak integral reached half of the final value (half-conversion time) was then plotted against the crystallization temperature T_c .

Thermogravimetric Analysis (TGA)

TGA measurements were conducted on a TGA4000 (Perkin Elmer) under air or nitrogen atmosphere, placing $\sim 10 \text{ mg}$ of polymer in alumina crucibles. Heating scans were

performed to measure the degradation temperature. Isothermal measurements above the melting point were performed to assess the melt stability.

Rheology

The rheological properties were measured on a rheometer AR 2000ex (TA Instruments) on a plate-plate configuration, with aluminum plates of 25 mm of diameter, in a closed oven, and using liquid nitrogen for temperature regulation.

Flow-mode measurements on the melt polymers (HFPA66, HFPA6 and iPP-Bor-flow) were performed at different temperatures to study the viscosity stability in time. The shear-rate was selected in the Newtonian plateau. The effect of atmosphere, either air or nitrogen, was studied. Oscillatory frequency sweep measurements under nitrogen were also performed on the HFPA66. This method allows to perform measures on a large range of frequencies up to around 600 rad s^{-1} , overcoming the issue of fluid flowing out of the plate, hence to perform successive measurements on the same sample.

Viscosity values from constant shear-rate measurements on HFPA66 and HFPA6 were used to construct an Arrhenius plot to determine the flow activation energy (E_a) and pre-exponential factor (A), according to Arrhenius law (Eq. 3.1).

Tensile Tests

Tensile tests were conducted on dog-bone shaped samples made of HFPA66, HFPA6 and reference PA66, obtained by micro-injection molding. In order to evaluate the effect of moisture content during melt processing, two types of HFPA66 samples were produced, using pellets which were either previously dried (at $110 \text{ }^\circ\text{C}$ in vacuum overnight) or not. An increase of molecular weight, thus of mechanical properties, is expected from the condensation equilibrium reaction (Eq. 2.1). A further drying treatment ($110 \text{ }^\circ\text{C}$ in vacuum overnight) was performed on all the dog-bone samples prior the mechanical test. This is necessary since polyamides are highly hygroscopic and moisture content dramatically affects their mechanical properties.

Dog-bone samples were produced from the polymer pellets through extrusion-injection. The pellets were melted in a twin-screw micro-extruder (at $280 \text{ }^\circ\text{C}$ for the two

PA66s and 250 °C for the HFPA6), from which the melt was transferred into a piston-equipped cylinder heated at the same temperature, and finally injected to a cold mold (120 °C) with a dog-bone-shape cavity. The injecting pressure was set to 6 bar. In order to prevent polymer degradation during the melting, nitrogen was kept flowing in the melting chamber. The sample geometric parameters, with reference to Fig. 3.4, are as follows: overall length (LO) 74 mm, width of the narrow section (W) 4 mm, thickness (T) 2 mm, overall width (WO) 12 mm, length of the narrow section (L) 25 mm. Prior to the test, all the samples have been conditioned at 110°C under vacuum overnight (around 14h).

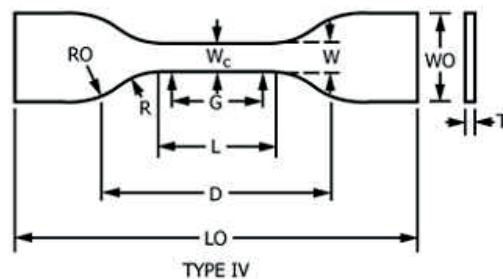


Fig. 3.4: Geometric parameters for a dog-bone polymer sample for tensile test [152].

The tensile tests were performed with a mechanical testing equipment Walter+Bai AG Series LFL-125kN. The force was measured with a 10 kN load-cell and the deformation with an extensometer. The standard ASTM D638-10 was used as a guide for the geometrical factors of the test. Initial distances of 45 mm between the grips (D) and of 20 mm between the extensometer arms (gauge length, G) have been chosen. Stress-strain curves have been obtained from the force-deformation data using the aforementioned geometric factors.

Dynamic Mechanical Analysis (DMA)

DMA measurements were conducted on a DMA Q800 (TA Instruments) with a single-cantilever setup. The sample beam was screwed on the two ends on a fixed and on an oscillating clamp. In DMA it is important that sample stiffness falls in the operating range of the machine. The graph in Fig. 3.5, which shows the operating range in terms of Young's modulus of the material and Geometry Factor (GF) for single-cantilever

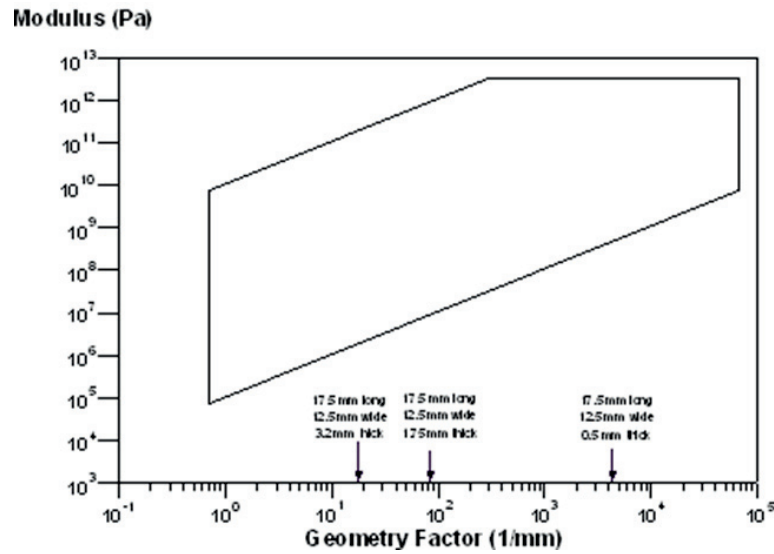


Fig. 3.5: Operating range for single-cantilever setup in DMA.

setup, can help to make sure that sample dimensions are adequate. The GF for single-cantilever is calculated as:

$$GF = \frac{1}{F} \left[\frac{L^3}{12I} + 2S(1 + \nu) \frac{L}{A} \right] \quad (3.8)$$

where L is span-length between the clamps; A the sample cross-sectional area; $I = t^3w/12$ is the geometric moment (for rectangular samples of thickness t and width w); ν the Poisson's ratio of the material; and F and S are the clamping and shearing factor, which were taken as 0.9 and 1.5, respectively (DMA Q800 user's guide). Sample dimensions have to be chosen so that the GF falls in the window of Fig. 3.5 during the whole test. For temperature ramps, change of Young's modulus should be taken into account. For this study, samples of cross-section $\sim 8 \times 3$ mm were prepared, which, considering a span-length of 17.5 mm and Poisson's ratio of 0.4, led to a GF of $\sim 30 \text{ mm}^{-1}$. Considering an approximate modulus of 3 GPa at the lower test temperature (0 °C) and 0.3 GPa at the highest (200 °C for PA6 and 250 °C for PA66), the GF should fall in the operating range during the whole test.

3.2.3 Production and analysis of composite plates

mTP-RTM

A novel lab-scale tool designed and manufactured for the production of small plates via mTP-RTM is schematically represented in Fig. 3.6. A compact design was conceived so as to minimize the equipment cost and complexity. The tool, entirely machined in steel and treated with nitrogen for surface-hardening, embodies the fabric cavity and two melting pots and injection pistons, and it requires an external source for heating and for applying pressure on the pistons. The two pots and pistons allow for impregnation to be performed from both sides. Two screws are used to open or close the inlet/outlet gates, two holes of 3 mm of diameter. It is also possible to connect a vacuum pump to the outlet. The cavity has dimensions of 3 mm thickness, 98 mm width and 158 mm length. Thermocouples can be inserted in specific holes close to the melting pots and to the cavity.

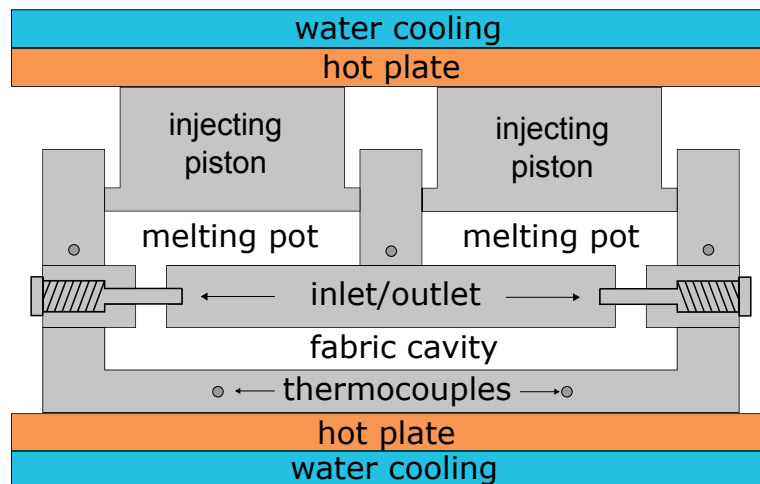


Fig. 3.6: Schematic representation of lateral cross-section view of the TP-RTM tool.

The heating step above the polymer melting point is carried out by convection in an oven. Heating rate depends on the mass and thermal capacity of the mold. Typically, an average heating rate of $5\text{ }^{\circ}\text{C min}^{-1}$ was achieved. The injections are conceived to be performed by means of a hydraulic hot press (Fontijne Presses). The upper plate of the press exerts a constant force on the pistons, hence on the melt polymer. The actual fluid pressure is not measured, but it is to be calculated dividing the applied force by the area of the pistons in contact with the melt (3090 mm^2 each). Once the inlets

are opened, the melt would be forced to flow in the underlying cavity. Cooling step is realized utilizing the cooling system of the press, with water circulating above/below the top/bottom plates, as depicted in Fig. 3.6. Evidently, a temperature gradient could be created throughout the mold in the vertical direction during cooling. In any case, the bottom-plate contributes to cooling of the composite in the cavity much more than the top-plate, because it is closer and the surface area of contact is much larger.

Flexural tests

Flexural properties of composite samples were evaluated with a mechanical testing machine Walter+Bai AG Series LFL-125kN in a three-point bending configuration. The ASTM standard D7264 was used as a reference for samples preparation and elastic modulus and flexural strength calculations [153]. Rectangular beams were cut off from a composite plate, and their thickness and width were accurately measured with a micrometer and a caliper, respectively. The span-length, i.e. the length between the two support points, should be kept constant during a series of tests. The ratio between span-length and sample thickness is also important, the standard value being 32:1. It is recommended that the same ratio should be used when comparing different samples. The length of the sample beam has a minor importance, though it is suggested that it is around 20% longer than the span-length.

From force-displacement data, maximum flexural stress σ and strain ϵ at the outer surface were calculated as

$$\sigma = \frac{3PL}{2bh^2} \quad (3.9)$$

$$\epsilon = \frac{6\delta h}{L^2} \quad (3.10)$$

where P is applied force, L the span-length, δ the mid-span deflection, and b and h the width and the thickness of the sample. The flexural strength was then taken as the stress at failure (maximum value of P). The flexural modulus was then obtained from stress-strain plot as the slope in the elastic range.

Impregnation analysis

To analyze the degree of impregnation, small samples (typically $\approx 1.5 \text{ cm} \times 1.5 \text{ cm}$ or $1.3 \text{ cm} \times 1.3 \text{ cm}$) were cut off from composite plates with a diamond-blade saw. Qualitative analysis was carried out by optical imaging. The samples were embedded in epoxy resin (Epofix™ resin and hardener) and polished with SiC foils on an automated polishing machine (Struers) for observation in reflected light microscope (Olympus BH2). Polishing was performed following a step-wise procedure, reducing the roughness (from grit 500 to 4000) and increasing the applied force (typically from 10 to 50 N).

For quantitative analysis, the burn-off method, consisting in size and mass measurement of the samples before and after the matrix is burned off [154, 155], is typically employed. The void volume fraction is calculated as

$$V_v = 1 - V_m - V_f \quad (3.11)$$

where V_m and V_f are the volume fractions of matrix and fibers, to be determined from

$$V_m = \frac{m_i - m_f}{\rho_m v_s} \quad (3.12a)$$

$$V_f = \frac{m_f}{\rho_f v_s} \quad (3.12b)$$

where m_i and m_f are initial and final mass of the sample (before and after burn-off), ρ_m and ρ_f are the density of matrix material and of glass fibers, and v_s is the volume of the sample, the product of measured width, length and thickness.

Chapter 4

Flow studies on selected fabrics

In this chapter, the results of flow studies performed on selected glass fabrics introduced in Section 3.1.2 are reported and discussed. In the first section, G-PLY and G-FLOW, two fabrics with flow-enhancing properties, are evaluated in terms of permeability and compaction, both as plain fabrics and combined in different stacking architectures. In the second section, the relation between meso-structure and permeability of G-PLY is more thoroughly investigated. A novel method to evaluate the influence of capillary effect is also assessed.

4.1 Characterization of two highly-permeable fabrics

Five different fabric architectures obtained from G-PLY and G-FLOW have been designed and investigated in terms of compaction and permeability. The permeability was measured through uni-directional, in-plane, constant-pressure flow experiments as described in Section 3.2.1. The test fluid was a solution of PEG (35 000 g mol⁻¹) 16.7%wt in water (Table 3.2). Fluid pressure was always set below 1 bar.

The five different fabric stacks investigated are summarized in Table 4.1 and schematically represented in Fig. 4.1. Wherever it is not explicitly specified, the flow and impregnation experiments on the G-FLOW and G-PLY fabrics were always performed along the [0°] direction (red arrows in Fig. 3.1), for which the permeability is supposedly higher. The first two consisted in simple stacks of five plies of G-FLOW and G-PLY stacked with the same orientation. In the third architecture, five layers of G-PLY were

laid alternately with opposite orientation in the normal axis (hence the minus sign). The last two stacks consisted of a combination of four G-PLY and one or two G-FLOW, stacked in the sequence as indicated in Table 4.1.

Table 4.1: Stacking architectures compressed to a thickness of 3 mm thickness. (F = G-FLOW; P = G-PLY; minus sign indicates opposite orientation in the normal axis).

Designation	Stacking sequence	V_f (%)
5F	{F,F,F,F,F}	36
5P	{P,P,P,P,P}	46
5P-alt	{P,-P,P,-P,P}	46
4P-1F	{P,-P,F,P,-P}	43
4P-2F	{P,F,P,-P,F,-P}	50

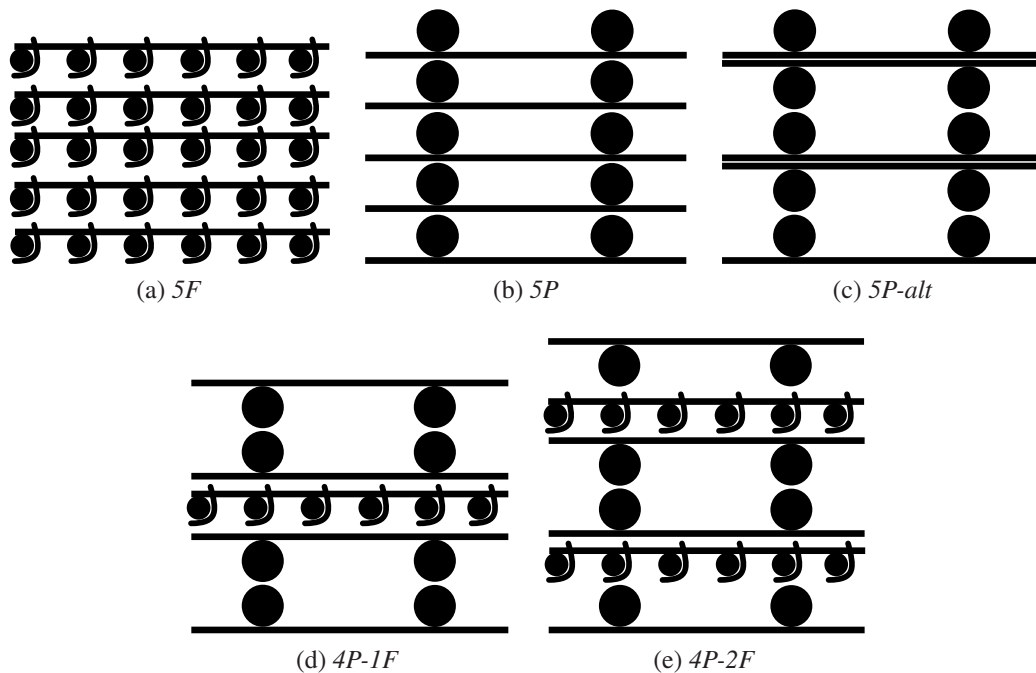


Fig. 4.1: Schematics of the cross section transverse to the flow direction for the five stacking architectures.

4.1.1 Fabric compaction

The compaction of fabric stacks was measured using a mechanical testing machine Walter+Bai AG Series LFL-125kN. The fabric stack was cut and placed on a square plate of 10 cm side, so as to completely cover the surface. The top plate, of same size, was connected to a 10 kN load-cell. The fabric was compressed at a constant speed of

0.017 mm s^{-1} down to the same thickness as the mold cavity, that is 3 mm, and held for few minutes in order to let the fabric relax. The force was divided by the compressed area (100 cm^2), and reported as a compressive stress. Normally, the compliance of the cross-head should be considered to correct the real position (compliance correction), but it can be considered as a minor effect in this range of force ($< 5 \text{ kN}$). The displacement of the cross-head was used to determine the distance between the two plates.

The change in time of compaction pressure for the different fabric stacks is displayed in Fig. 4.2. 5F required the lowest pressure, consistently with the fact that it has the lowest content of fibers (36%). The difference between the 5P and the 5P-alt, for which fiber volume fractions are similar, is attributed to the layers' slipping during compaction. If this is the case, the transverse layer in the 5P might bend, with the longitudinal tows acting as bending-points (Fig. 4.3a). On the other hand, in the 5P-alt slipping results in nesting of the longitudinal tows (Fig. 4.3b), which explains the lower pressure necessary for compaction. Regarding the two hybrid stacks, unsurprisingly 4P-1F required intermediate pressure between 5F and 5P-alt, whereas a higher pressure was expected for the 4P-2F, since it had the highest fiber volume fraction.

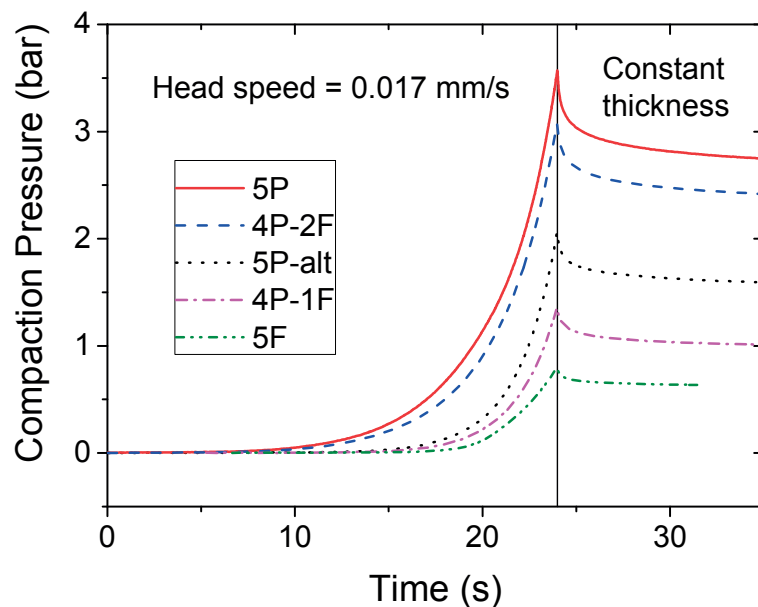


Fig. 4.2: Compaaction pressure for the different fabric stacks. The compaction was carried out at a constant speed of 0.017 mm s^{-1} until a thickness of 3 mm, which was then kept constant to let the fabric relax and measure the force decay.

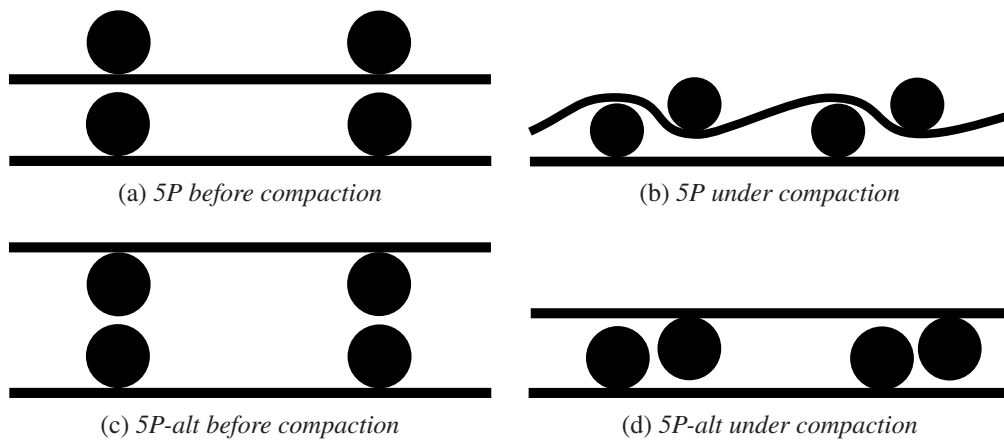


Fig. 4.3: Scheme of the change in the stack architecture under compaction if slipping occurs.

4.1.2 Permeability measurements

The results of saturated and unsaturated permeability measurements on the different stacks are shown in Fig. 4.4. Firstly, it should be noticed that all the fabrics have a high permeability compared to standard fabrics, as typical values at this fiber volume fraction should rather lie in the range $1 \cdot 10^{-10} < K < 1 \cdot 10^{-11} \text{ m}^2$ [99], and that the unsaturated and saturated permeability values differ slightly, the reason of which will be discussed in the next session.

Secondly, although the G-FLOW seems to have a more open structure (Fig. 3.1), this is not reflected in the longitudinal permeability of the 5F stack, which is comparable to the G-PLY stacks (5P and 5P-alt), in spite of having a lower fiber content (36% against 46%). This can be explained by considering the cross section of the two fabrics. The G-PLY is a non-crimp fabric, which creates wide channels along the flow direction, whereas the G-FLOW is a leno-weave, which is characterized by an open grid-like structure in the through-thickness direction, which seems to be less efficient for the in-plane flow. This fabric would be better suited for compression RTM, for example, than in-plane RTM, as evaluated in the present work.

A third remarkable feature is the difference between 5P and 5P-alt, which differ only in the stacking orientation, resulting in wider channels. Moreover, as previously discussed, under compaction, the 5P might deform in such a way that the transverse layer bends, consequently obstructing the channels.

Finally, the introduction of one or two layers of G-FLOW did not bring any advantage. The permeability of the two hybrid stacks (4P-1F and 4P-2F) is comparable to or lower than that of the stacks with G-PLY only.

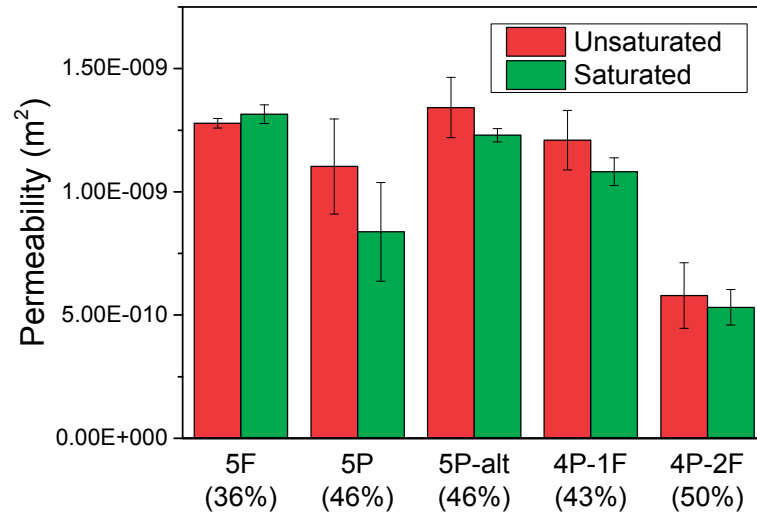


Fig. 4.4: Saturated and unsaturated permeabilities of different stack architectures

4.2 Permeability and capillary effects in a channel-wise non-crimp fabric

In the previous section it was demonstrated that G-PLY has a higher permeability than G-FLOW. This is likely to be related to its peculiar architecture, and specifically on the organization of the fibers along the flow direction. In this second part, the relation between the fabric meso-structure and in-plane permeability of G-PLY was investigated using a 2×2 twill weave with a more "standard" architecture (G-WEAVE, see Section 3.1.2) as a reference fabric.

For each fabric type, six configurations with different fiber volume fractions have been studied. Different fiber contents were obtained upon variation of the number of layers compacted in a constant thickness of 3 mm, as reported in Table 4.2. Permeability measurements were conducted over a wide range of capillary numbers (between $4 \cdot 10^{-5}$ and $4 \cdot 10^{-1}$) using the fluids reported in Table 3.2, in order to evaluate the role of capillary phenomena and their influence on flow front morphology. The methodology

described in Section 3.2.1 was employed for saturated and unsaturated permeability measurements, and for the determination of permeability ratio and capillary number. The meso-structure of the fabric preforms was analyzed from Computed X-Ray Tomography* images, from which a simple numerical permeability model was proposed. Finally, the generally observed discrepancy between unsaturated and saturated permeability was quantified and explained in light of the capillary number and fabric architecture.

Table 4.2: Fabric samples configurations, compacted to a thickness of 3 mm.

Fabric	Layers	$V_f(\%)$
G-PLY	4	36.47 ± 0.14
G-PLY	5	45.78 ± 0.40
G-PLY	6	55.24 ± 0.27
G-WEAVE	5	38.00 ± 0.08
G-WEAVE	6	45.07 ± 0.12
G-WEAVE	8	60.72 ± 0.19

4.2.1 Saturated permeability

Fig. 4.5 displays the measured values of saturated permeability for the six fabric configurations. The value for G-FLOW[†] is also shown for comparison. The permeability of G-PLY is almost one order of magnitude higher than that of G-WEAVE for comparable fiber content, and is also higher than that of typical glass fabrics, which makes it suitable for fast impregnation with highly viscous resins. This is attributed to the different meso-structures of the two fabrics, as the characteristics at micro-scale (e.g. sizing and fiber radius) are the same. It is worth comparing with the saturated in-plane permeability measurements in [85, 87] for a unidirectional glass-fabric featuring meso-channels. In that case, values around $6 \cdot 10^{-9} \text{ m}^2$ at 45 vol% of fibers, thus slightly lower than G-PLY, were measured. A major difference between the two cases is the size of the meso-channels (larger in G-PLY). The relation between microstructure and permeability is discussed in the next section.

*RX Solutions, PIXE Platform, EPFL, Switzerland.

[†]From Fig. 4.4.

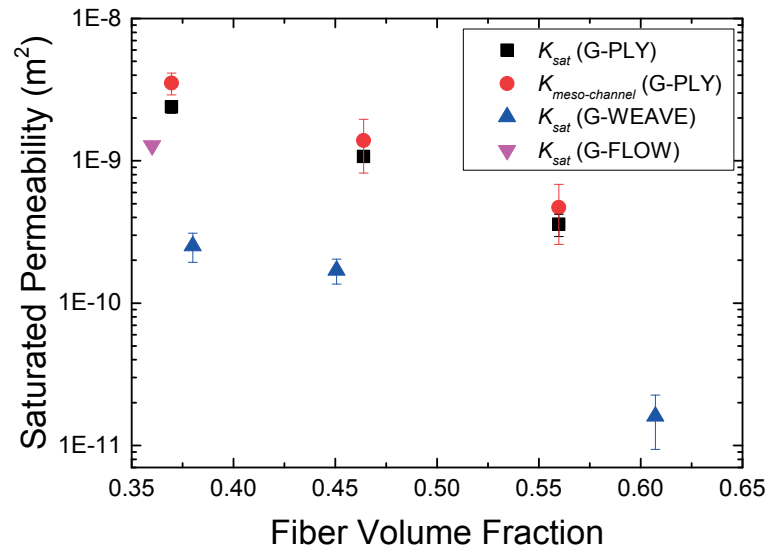


Fig. 4.5: Saturated permeability for G-PLY, G-WEAVE and G-FLOW fabrics; the numerical permeability calculated from G-PLY meso-channel geometry (Eqs. 4.3 and 4.4) is also reported (see Section 4.2.2).

4.2.2 Microstructural analysis

Fabrics microstructural characterization

Microstructures of the two fabric types were characterized using a laboratory X-ray microtomograph[‡]. Samples were inserted into cylindrical PMMA containers and compacted to the thickness of 3 mm as detailed in [147]. Six fabric samples were analyzed, reproducing the same configurations as in the permeability experiments (Table 4.2). During the measurements, the generator voltage and the current intensity were set to 160 kV and 200 μ A and 2000 radiographs were acquired with the size of 2176×1792 pixels from the incremental rotation of the samples with respect to the X-ray source. In a following reconstruction operation, 3D grayscale images of absorption coefficients were obtained with a voxel size of $9.87 \times 9.87 \times 9.87 \mu\text{m}^3$.

The tomographic reconstructions for the six samples, with a size of $1475 \times 1475 \times 304$ voxels, are shown in Fig. 4.6. In order to investigate the channel structure of scanned G-PLY samples, 3D images were converted to 2D slices along the x-direction (i.e., each slice was on the yz-plane) and each 2D slice was segmented to consist of fiber bundles and meso-channels. Segmentation was achieved using Fiji [156], and a standard thresholding procedure was followed by additional morphological operations.

[‡]RX Solutions, PIXE Platform, EPFL, Switzerland.

Fig. 4.7 illustrates 2D slices and their corresponding binary images; meso-channels of the samples showed distinct characteristics in terms of their cross-sectional geometries. Channels in 4-layer and 6-layer samples exhibited rectangular and triangular shapes, respectively; whereas the 5-layer sample contained both rectangular and triangular meso-channels. Even though the nesting and layer shifting mechanisms are beyond the scope of this study, it is obvious that increasing the number of layers caused shrinkage of the rectangular channels combined with bending of the bundles in the transverse direction, which in turn resulted in the formation of smaller triangular channels. For the 5-layer sample, intermediate compaction results in hybrid channels' shape, with both triangular and rectangular channels forming at different locations along the longitudinal direction. To quantify the channel geometry, Analyze Particles plugin of Fiji was used in all 2D slices except those corresponding to the interbundle gaps between the adjacent transverse bundles. In addition to the area and perimeter of the pores, the aspect ratio of each pore's bounding box was also measured and used as a shape descriptor to distinguish between rectangular and triangular pore geometries as will be detailed in Section 4.2.2.

Meso-channel geometry

In order to analyze the channel cross-section throughout the whole sample, 3D binary subvolumes were cropped to contain individual meso-channels. This operation resulted in 11, 12 and 18 3D subvolumes for 4-, 5-, and 6-layer samples, respectively (see Fig. 4.7). Each 3D subvolume consists of 2086 slices, from which we analyzed on average 14591 ± 199 rectangular cross-sections for 4-layer sample, 6871 ± 124 rectangular and 1332 ± 214 triangular cross-sections for 5-layer sample, and 2651 ± 385 triangular cross-sections for 6-layer sample. Fig. 4.8 shows the aspect ratio and the area of the detected cross-sections in each slice of the samples as well as typical channel geometries and their bounding boxes. A comparison between the channel characteristics of different samples indicates that rectangular channels typically cover a larger area than the triangular channels and their bounding boxes have larger aspect ratios. Both channel types are present in 5-layer sample and results in two clusters in terms of aspect ratio and area as observed in Fig. 4.8. This confirms that, in the 5-layer sample, the channels are locally constricted due to local compaction and bending of bundles, thus a rectangular channel

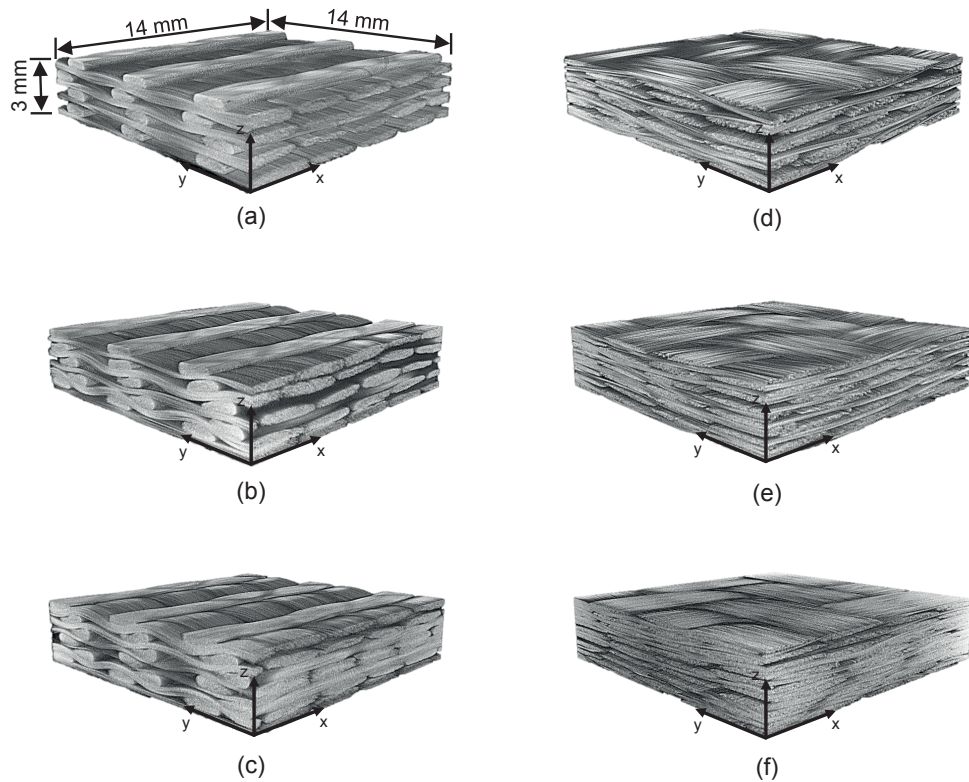


Fig. 4.6: 3D images reconstructed from Computer X-Ray Tomography of G-PLY with (a) 4, (b) 5 and (c) 6 layers and G-WEAVE with (d) 5, (e) 6 and (f) 8 layers.

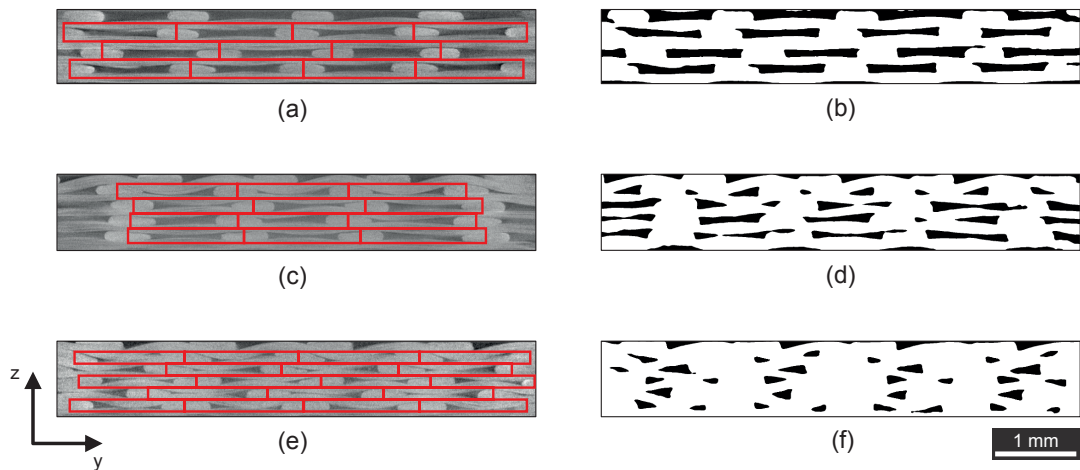


Fig. 4.7: Cross section views from Computed X-Ray Tomography showing unit cells (left-hand side) and binary-converted images showing varying meso-channel shapes (right-hand side) for (a-b) 4, (c-d) 5 and (e-f) 6 layers of G-PLY; respectively 11, 12 and 18 unit-cells were used for image analysis of the three samples, each containing either one rectangular or two parallel triangular meso-channels.

splits into two smaller triangular channels, which later on converge back to form a single rectangular channel.

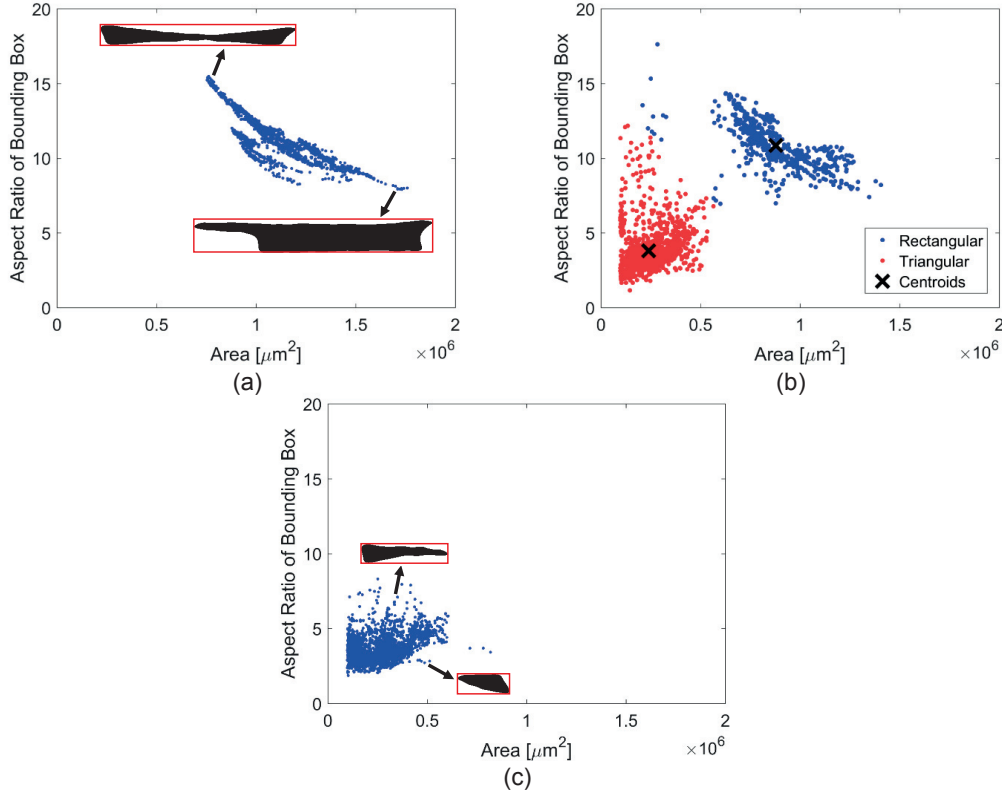


Fig. 4.8: Aspect ratio and area of the channels cross-section for (a) 4, (b) 5 and (c) 6 layers samples.

Estimation of permeability from meso-channels geometry

Using a circuit analogy, the pressure drop in a channel is related to the flow rate as

$$-\Delta P = R_{hyd} Q_{out} \quad (4.1)$$

where R_{hyd} is the hydraulic resistance. Even though expressions for hydraulic resistance of ideal cross-sections (i.e., circle, ellipse, rectangle, etc.) can be found, channels encountered herein are far from ideal. Thus, R_{hyd} of each channel was calculated using the general expression as proposed by Bruus [157]:

$$R_{hyd} = \frac{2\eta L_c P_c^2}{A_c^3} \quad (4.2)$$

where P_c and A_c are respectively the perimeter and area of the channel cross-section, and L_c is the channel length. The characteristic R_{hyd} of each channel in Fig. 4.7 was estimated using the median perimeter and median area measurements obtained using the Analyze Particles plugin. Combining Eqs. 3.4, 4.1 and 4.2, permeability of the 4-layer and 6-layer samples are then calculated as

$$K_{meso-channel} = \frac{A_c^3}{2P_c^2 A} \quad (4.3)$$

where A is the cross-sectional area of the unit cell (red boxes in Fig. 4.7) along the flow direction with width of 5 mm corresponding to the center-to-center distance between two adjacent tows in a layer and the height of 0.75 and 0.5 mm calculated as $3/n$ (mm), n being the number of layers. In the 5-layer sample, two triangular channels are considered as two resistances in parallel, in series with another resistance corresponding to the rectangular channel (see Fig. 4.9). To calculate the R_{hyd} of each channel type, channels are clustered into two groups using the area and aspect ratio of the bounding box in k -medoids function of Matlab (see Fig. 4.8 for clusters) using the median perimeter and median area values of each cluster. Once the permeabilities of triangular and rectangular channels ($K_{meso,t}$, $K_{meso,r}$) are calculated using Eq. 4.3, permeability of a full meso-channel is then calculated as

$$K_{meso-channel} = \frac{l_r + l_t}{\frac{l_r}{K_{meso,r}} + \frac{l_t}{K_{meso,t}}} \quad (4.4)$$

where l_r and l_t are the relative lengths of rectangular and triangular channels, calculated by using the number of elements in each respective cluster. It should be noted that A in Eq. 4.3 is the cross-sectional area of the unit cell with the width of 5 mm and the height of 0.6 mm. Permeability results are presented in Table 4.3 along with the characteristics of the channel cross-sections, and are also reported in Fig. 4.5 for comparison with the experimental results. The comparison between experimental and meso-channel based permeability values shows that this model, despite its simplicity, results in a reasonably close estimation of permeability, within the same order of magnitude as experimental results. Eq. 4.2 overestimates the permeability of rectangular channels if the aspect ratio

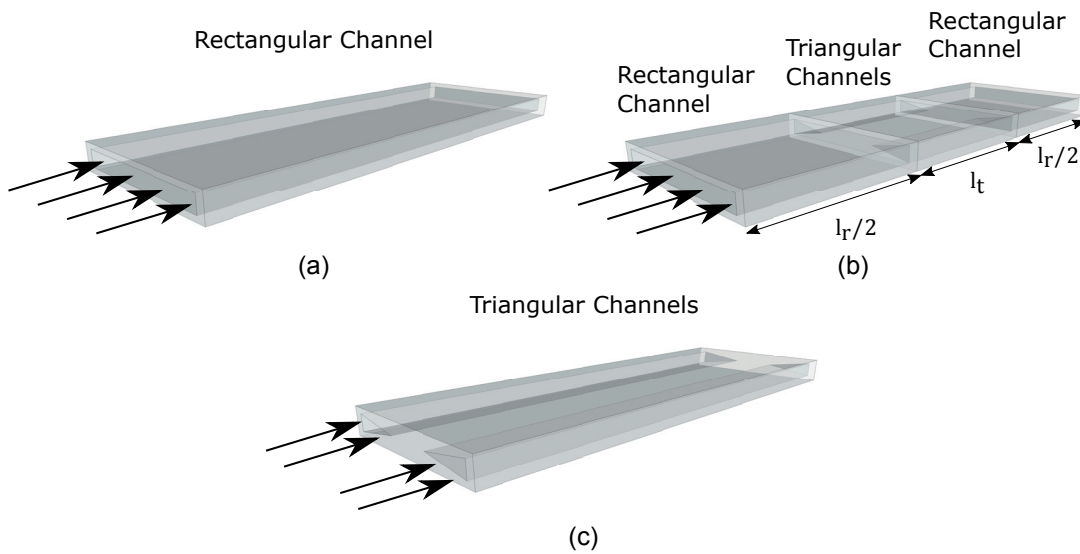


Fig. 4.9: Scheme of (a) rectangular channel, (b) rectangular and triangular channels in series, and (c) triangular channels in parallel.

is higher than 2.27, obtained by solving Eq. 4.2 and the expression for R_{hyd} of rectangular cross-section ($R_{hyd} = \frac{12\eta L_c}{1-0.63\frac{h}{w}} \frac{1}{h^2 w}$); aspect ratios of rectangular cross-sections are significantly higher than this critical value in both 4- and 5-layer samples (see Fig. 4.8). The overestimation due to this formulation is 32.3% for an aspect ratio of 1:10, a typical value of aspect ratio as seen in Fig. 4.8a. In addition, triangular channels are assumed to be all identical in the model and this can contribute to an overestimation of permeability. However, identification of individual channels is not straightforward and requires a pore network analysis, which is beyond the scope of this work.

Equivalent permeability of the unit cell

Circuit analogy for estimation of equivalent resistance in channels is valid for low Reynolds numbers and, in case of non-crimp biaxial fabrics, can be extended to calculate the equivalent permeability of the unit cell by taking into account the three distinct flow zones as shown in Fig. 4.10:

- flow through the meso-channel, with permeability K_{meso}^{\parallel} ,
- flow through fiber bundles along the flow, with permeability K_{micro}^{\parallel} ,
- flow through the transverse bundles with permeability K^{\perp} , which is broken down to two components:

Table 4.3: Geometrical parameter and permeability of the meso-channels for the 4, 5 and 6-layers samples. Experimental saturated permeability is also reported.

	$A_{c,r}(10^5 \mu\text{m}^2)$	$P_{c,r}(10^3 \mu\text{m})$	$A_{c,t}(10^5 \mu\text{m}^2)$	$P_{c,t}(10^3 \mu\text{m})$	$l_r(\mu\text{m})$	$l_t(\mu\text{m})$	$K_{\text{meso-channel}}(\text{m}^2)$	$K_{\text{sat}}(\text{m}^2)$
4 layers	10.25 ± 0.76	8.18 ± 0.33	0	0	1	0	$(3.52 \pm 0.61) \cdot 10^{-9}$	$(2.39 \pm 0.23) \cdot 10^{-9}$
5 layers	9.041 ± 0.931	7.77 ± 0.49	3.045 ± 0.624	3.08 ± 0.34	0.516 ± 0.119	0.484 ± 0.119	$(1.39 \pm 0.57) \cdot 10^{-9}$	$(1.074 \pm 0.096) \cdot 10^{-9}$
6 layers	0	0	2.490 ± 0.616	2.59 ± 0.39	0	1	$(4.71 \pm 2.12) \cdot 10^{-10}$	$(3.58 \pm 0.64) \cdot 10^{-10}$

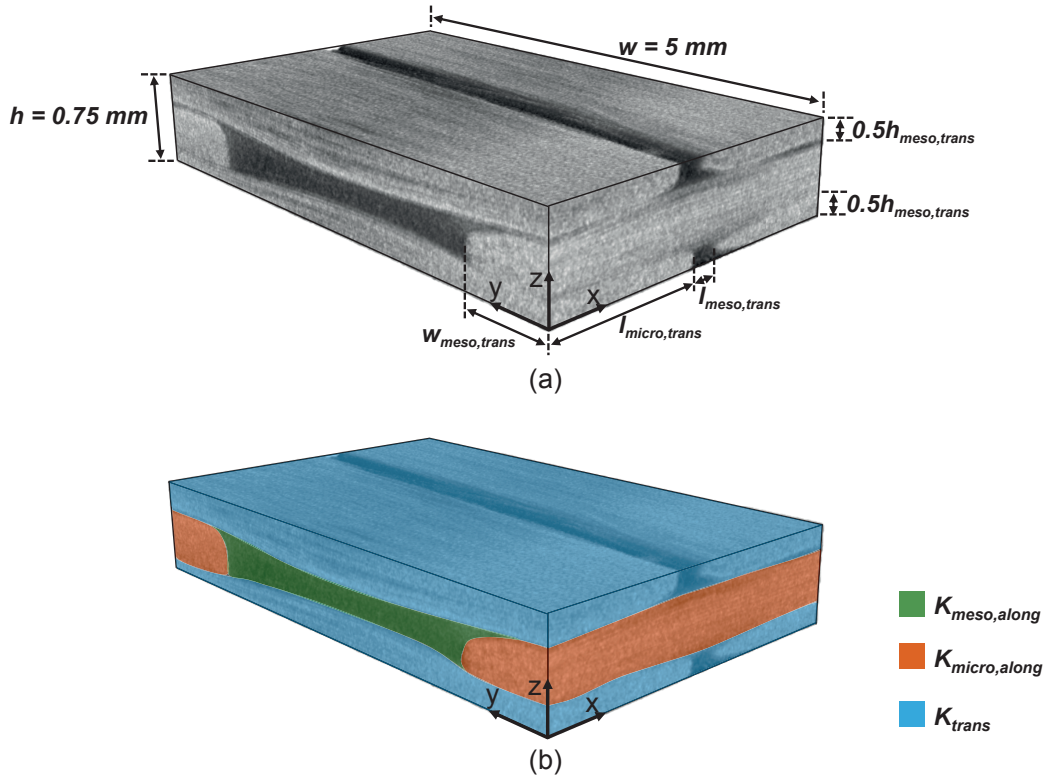


Fig. 4.10: Example of unit cell of G-PLY, showing (a) geometrical parameters and (b) the three flow zones.

- flow through fiber bundles perpendicular to flow (K_{micro}^{\perp}),
- flow through the meso-channel between two adjacent fiber bundles perpendicular to the flow (K_{meso}^{\perp}) [134, 136, 137].

$K_{\text{meso}}^{\parallel}$ was calculated using the methodology detailed in the previous section except that this time, it was based on the cross-sectional area (A_c) of the channel itself, instead of that of the unit cell (red boxes in Fig. 4.7), reducing Eq. 4.3 to the following:

$$K_{\text{meso}}^{\parallel} = \frac{A_c^2}{2P_c^2} \quad (4.5)$$

In order to calculate the permeability within the bundles parallel and perpendicular to the flow, the volume fraction of bundles ($V_{f,\text{micro}}^{\parallel}$ and $V_{f,\text{micro}}^{\perp}$) were calculated by manually fitting splines to at least 40 individual bundle cross-sections in each direction. Using the TEX value (1200 for both warp and weft bundles) and fiber radius, the values of volume fractions reported in Table 4.4 were calculated. Permeability of the bundles along and

transverse to flow direction were calculated using Gebart's equations, i.e. respectively

$$K_{micro}^{\parallel} = \frac{8}{C_1} \frac{(1 - V_{f,micro}^{\parallel})^3}{(V_{f,micro}^{\parallel})^2} R^2 \quad (4.6)$$

and

$$K_{micro}^{\perp} = C_2 \left(\sqrt{\frac{V_{f,max}}{V_{f,micro}^{\perp}}} - 1 \right)^{5/2} R^2 \quad (4.7)$$

where $C_1 = 53$, $C_2 = \frac{16}{9\pi\sqrt{6}}$ and $V_{f,max} = \frac{\pi}{2\sqrt{3}}$ for hexagonal fiber arrangement [97], and $R = 7.55 \pm 0.89 \mu\text{m}$ is the average fiber radius. The meso-channel between the two transverse bundles, whose permeability is denoted by K_{meso}^{\perp} , is assumed to have a rectangular cross-sectional area with a width of 5 mm (spacing between the centers of two bundles along the flow) and with height equal to the height of transverse bundles (h_{meso}^{\perp}). Permeability of this rectangular channel is calculated as

$$K_{meso}^{\perp} = \frac{(1 - 0.63 \frac{h}{w})h^2}{12}, \quad (4.8)$$

where h and w are height and width of the unit cell, respectively. The equivalent transverse permeability (K^{\perp}) is calculated by considering the meso- and micro-flow and is calculated as

$$K^{\perp} = \frac{l_{meso}^{\perp} + l_{micro}^{\perp}}{\frac{l_{meso}^{\perp}}{K_{meso}^{\perp}} + \frac{l_{micro}^{\perp}}{K_{micro}^{\perp}}} \quad (4.9)$$

since the two channels are treated as two resistances connected in series (see Fig. 4.10). As shown in Fig. 4.10, the three flow zones in the unit cell, namely flow in the parallel bundles (orange), flow in the meso-channel (green) and the transverse flow (blue) take place in parallel. Using the relative cross-sectional area of each of the three zones in the unit cell (c_1 , c_2 , and c_3 , see Table 4.4), the overall equivalent permeability is thus:

$$K_{eq} = c_1 K_{meso}^{\parallel} + c_2 K_{micro}^{\parallel} + c_3 K^{\perp} \quad (4.10)$$

Values are reported in Table 4.4. A comparison between K_{eq} and $K_{meso-channel}$ calculated in the previous section show that the results are very close (less than 8% deviation) for all of the three samples, validating the approach presented in the previous section which

considers only flow in the meso-channels. K_{micro}^{\perp} from Table 4.4 can be used to evaluate the Darcy number for the scale-separation criterion proposed by Syerko et al. [90][§]. A value lower than 10^{-3} is found, confirming that single-scale flow in the meso-channels is dominant.

4.2.3 Unsaturated permeability

The differences in architecture of the two fabric types influence the unsaturated flow morphology for different capillary numbers, as illustrated in Fig. 4.11. The G-WEAVE shows a "classic" behavior, with a narrow unsaturated zone confined at the flow front for both low (Fig. 4.11a) and high (Fig. 4.11b) Ca values. At low Ca , flow is slightly faster in the intra-tow region, because driven by capillarity, resulting in no visible dry regions in the saturated zone behind the flow front (Fig. 4.11a), whereas at higher Ca flow is dominant in the inter-tow spaces, causing entrapment of dry spots in the fiber bundles (Fig. 4.11b). Conversely, in the G-PLY, flow is never dominant in the fiber bundles. At low Ca the flow front morphology remains rather close to "slug-flow", showing no leading flow in the bundles (Fig. 4.11c), whereas at higher Ca , the fluid clearly flows faster in the meso-channels than in the bundles, leaving behind a large unsaturated area (Fig. 4.11d).

Varying the applied pressure, fluid type and fiber volume fraction, it was possible to perform experiments in a range of average capillary numbers spanning over four orders of magnitude. Due to its particular structure with large channels, which confers to G-PLY such a high permeability, this fabric was able to allow flow of high viscosity fluids (> 10 Pa s) at relatively low pressure (< 5 bar) and without destruction or visible deformation of the preform architecture, allowing to reach capillary numbers as high as 0.4. In G-WEAVE, Ca could not exceed ~ 0.04 ; beyond this value fabric deformation was observed. For each experiment, the ratio between unsaturated and saturated permeability defined in Eq. 3.5 was reported as a function of capillary number; overall results are given in Fig. 4.12a, where each point corresponds to a single experiment. The error bars on the x-axis correspond to the standard deviation for the capillary number in the range of analysis of each test[¶]. The large scatter of data points is attributed

[§]See also Section 2.5.1 in Chapter 2.

[¶]Cf. Fig. 3.3.

Table 4.4: Equivalent permeability calculations.

	K_{meso}^{\parallel} (m ²)	$V_{f,micro}^{\parallel}$	K_{micro}^{\parallel} (m ²)	$V_{f,micro}^{\perp}$	K_{micro}^{\perp} (m ²)	H_{meso}^{\perp} (m)	K_{meso}^{\perp} (m ²)	H_{micro}^{\perp}	K^{\perp} (m ²)	c_1	c_2	c_3	K_{eq} (m ²)
4 layers	$(1.08 \pm 0.13) \cdot 10^{-8}$	0.644	$9.33 \cdot 10^{-13}$	0.375	$4.92 \cdot 10^{-11}$	$(4.65 \pm 0.73) \cdot 10^{-4}$	$1.70 \cdot 10^{-8}$	0.896 ± 0.0436	$5.48 \cdot 10^{-11}$	0.321	0.190	0.489	$3.53 \cdot 10^{-9}$
5 layers	$(5.23 \pm 1.31) \cdot 10^{-9}$	0.675	$6.44 \cdot 10^{-13}$	0.425	$3.81 \cdot 10^{-11}$	$(4.25 \pm 0.69) \cdot 10^{-4}$	$1.42 \cdot 10^{-8}$	0.9158 ± 0.0539	$4.16 \cdot 10^{-11}$	0.242	0.226	0.532	$1.29 \cdot 10^{-9}$
6 layers	$(2.28 \pm 0.43) \cdot 10^{-9}$	0.689	$5.47 \cdot 10^{-13}$	0.458	$3.26 \cdot 10^{-11}$	$(3.63 \pm 0.86) \cdot 10^{-4}$	$1.05 \cdot 10^{-8}$	0.9405 ± 0.0481	$3.47 \cdot 10^{-11}$	0.204	0.266	0.530	$4.83 \cdot 10^{-10}$

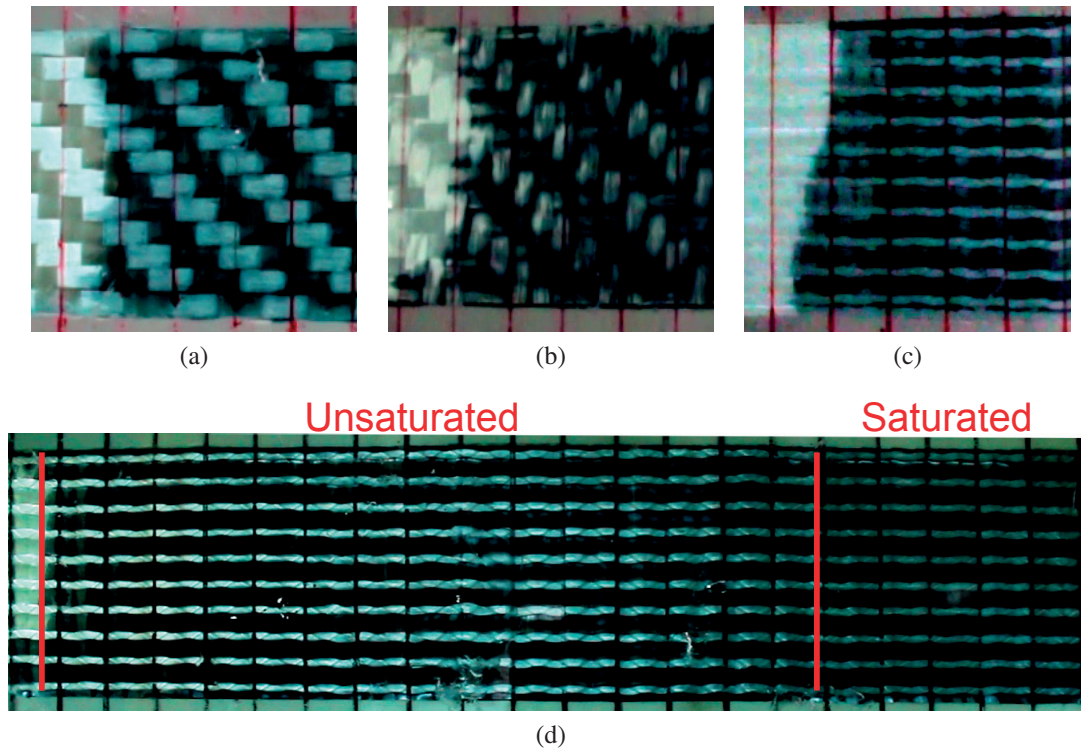


Fig. 4.11: Flow front at capillary number (a) 0.000068 and (b) 0.0028 for G-WEAVE, and (c) 0.00013 and (d) 0.38 for G-PLY.

to variations of capillary number and to experimental variability in permeability measurements, which is largely documented for this kind of tests [98]. Nonetheless, trends are observed: at small capillary numbers, R_s is higher than 1 for all experiments, and decreases rapidly as Ca increases. For $0.0005 \lesssim Ca \lesssim 0.01$, values smaller than 1 are mainly observed for G-WEAVE. Finally, for higher Ca , R_s increases again to around 1 or above. This behavior results from the competition between capillary phenomena within the fiber bundles (intra-tow) and viscous flow in the gaps between the bundles (inter-tow). When Ca is low, fluid is driven in the narrow intra-tow spaces by capillary forces, leading (in accordance with Eq. 3.5) to an overestimation of the unsaturated permeability compared to the saturated value. This is particularly true for the G-WEAVE, for which the highest R_s values were observed at $Ca < 0.0005$. Above a critical Ca , viscous flow starts to dominate, and R_s is expected to drop below 1, as the fluid flows preferentially in between the tows. This transition from wetting to non-wetting flow as Ca increases was observed in non-crimp carbon fabrics in [62], and is confirmed in this

study for the G-WEAVE, for capillary number values between $5 \cdot 10^{-4}$ and $1 \cdot 10^{-2}$. However, for G-PLY, R_s remained close to 1 in most of the experiments at higher capillary numbers. However, this cannot be attributed to capillary effects, as flow mostly takes place in the inter-tow spaces (meso-channels), delaying impregnation of the fiber bundles. When the inter-tow spacing is large, saturated permeability was shown above to be well predicted, even when flow taking place in the tows is totally neglected. As a result, the flow kinetics measured for G-PLY are dominated by flow in the meso-channels, and do not differ much from those observed close to the critical capillary number, for which flow takes place equally in both tows and channels.

Following Eq. 3.6, capillary pressure can be estimated as

$$\Delta P_\gamma = \Delta P(R_s - 1). \quad (4.11)$$

The results are plotted in Fig. 4.12b. For the G-WEAVE, $\Delta P_\gamma < 0$ at low Ca and mainly $\Delta P_\gamma > 0$ at high Ca , confirming the transition from wetting to non-wetting at $Ca^* \sim 0.0005$. For G-PLY, $\Delta P_\gamma \sim 0$ at mid-low Ca , i.e. capillary effects are negligible. For higher Ca , the negative capillary pressure values are to be considered as an apparent pressure (apparent wetting). This rises from the fact that for this fabric and at high Ca the flow is definitely far from the slug-flow assumption, and Eq. 4.11 is no longer valid.

The critical capillary number corresponding to a transition from wetting to non-wetting (Ca^*) has been discussed by previous authors [60, 62, 112, 114, 115, 117] in view of process optimization, as it corresponds to a minimum void content. As a result, it is often referred to as optimum capillary number. At this value, capillary and hydrodynamic forces compensate and fluid flows at the same velocity in the inter- and intra-tow regions, leading to a minimum amount of entrapped voids in the final composite. Values between 10^{-3} and 10^{-2} have been reported by these authors. In the present study, a lower value (approximately 0.0005) is observed. This is not surprising, as the optimal capillary number is expected to vary with fabric architecture and type [112, 117]. For instance, carbon fibers have smaller diameter and higher specific surface area, which is responsible for stronger capillary effects. Consequently, the value Ca^* , at which viscous forces overcome capillary forces, is expected to be higher (see for example [60, 62]). It is also worthy to note that the standard deviation on capillary number in this study lies

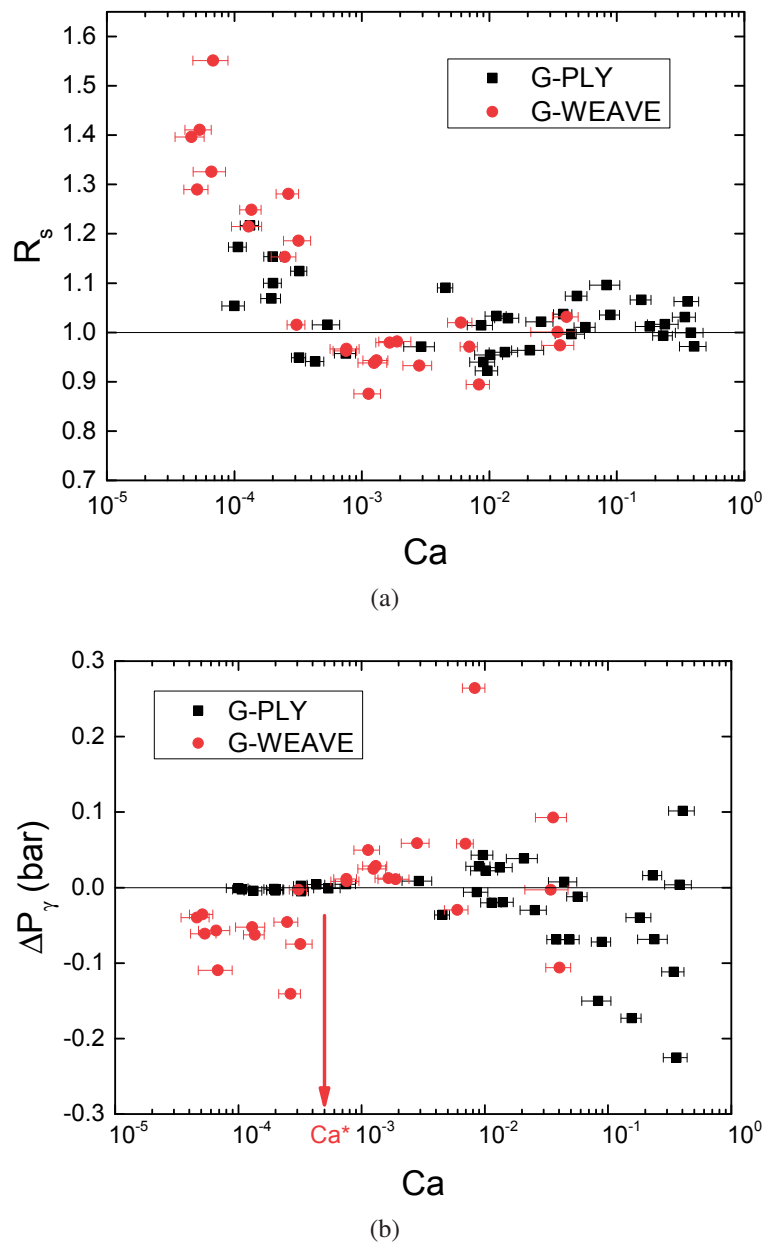


Fig. 4.12: (a) Unsaturated-to-saturated permeability ratio and (b) capillary pressure vs. average capillary number for the whole series of tests.

between 15 and 25%, as it was estimated in established flow regions under constant applied pressure. In order to find a more precise optimum capillary number, constant flow rate experiments should be performed [60, 62]. However, these are more difficult to perform, both in terms of experimental practicality (constant-flow-rate injecting system is needed, like a pump or syringe) and of data analysis (optimal capillary number is determined from capillary pressure drop taken as the y-intercept of the inlet-pressure build-up graph, which is dramatically affected by the chosen range of analysis). On the

contrary, the experimental methodology hereby proposed would allow to determine the optimal capillary number for a given fabric by a small series of constant-pressure tests performed at different capillary numbers by simply comparing unsaturated and saturated permeabilities.

4.3 Conclusions and outlook

Two high-flow glass-fabrics have been characterized in terms of compaction and permeability. The G-PLY, a stitched non-crimp fabric, appears to have higher permeability compared to the G-FLOW, a leno-weave fabric. Five different stack architectures were evaluated, among which the configuration of five G-PLY layers with alternated orientation had the higher permeability, since wider channels are created in this stack. Even though these channels are partially blocked upon compaction, as a consequence of plies slipping, the alternated configuration retains its higher permeability. This was explained considering the nesting mechanism compared to the bending, which takes place in the normal G-PLY (5P).

The influence of channels in determining the permeability of G-PLY was further investigated through flow studies, microstructure characterization and a numerical model, using a regular woven fabric (G-WEAVE) as a reference. Saturated permeability was found to be one order of magnitude greater for the G-PLY. It is however important to note that the flow front is, in many cases with this fabric, not uniform; care must be taken to ensure full impregnation of the tows in processing composites with these materials. We demonstrated that permeability for these fabrics is dominated by viscous flow along the meso-channels for a broad range of capillary numbers. As a result, a numerical model based on the hydraulic circuit analysis, which requires a rather basic knowledge of the flow channels' geometry provides good agreement with experimental results. Implementation of a model taking into account the micro-flow in the intra-tow pores confirms this trend, with only minor improvement on the permeability estimation.

The ratio of unsaturated over saturated permeability was also measured through constant-pressure experiments performed over a wide range of capillary numbers. This ratio can be theoretically estimated from the solution of Darcy's law taking into account or not the capillary pressure at the flow front; it is directly related to the ratio of capillary

pressure over applied pressure. Experimental results confirmed that for a rather classic woven fabric (G-WEAVE), R_s is much greater than 1 at low capillary numbers, and decreases as flow velocity increases, to drop below 1 above a critical Ca value, which may represent the optimal Ca value as identified to ensure low porosity in LCM. For G-PLY, a similar behavior is initially observed, however R_s remains close to 1 for all capillary numbers above the critical value. This is attributed to the dominant effect of inter-tow flow in the overall flow kinetics. This work contributes to the long debate in the LCM community between unsaturated versus saturated flow measurement, to indicate that, in particular for fabrics which have a strong dual-scale nature, unsaturated permeability measurements can indeed provide an accurate measurement of permeability, as long as care is taken to perform the experiment at high enough Ca to favor inter-tow flow. Ca should however remain low enough to prevent fabric distortion during the experimental measurement.

A direct consequence of this type of flow is that a large unsaturated region is always left behind the flow-front, even when this has reached the outlet. This might represent a problem in terms of void content of the final composite and can be regarded as the other side of the coin of permeability enhancement. In a melt-TP-RTM process, the fluid is a polymer of viscosity up to 50 Pa s, injected at a pressure up to 10 bar. This means that we can expect capillary numbers in the range 0.1 to 1. In order to avoid a large void content, a possible solution would be to adopt the following steps during the process: first, prior to polymer injection, vacuum should be applied at the outlet of the mold, in order to remove all the air from the dry fabric. Then, the melt polymer can be injected in the mold. Once the fluid flowing in the inter-tow channels has reached the outlet, a large content of voids in the intra-tow spaces has been left behind. At this point, the outlet should be closed, and injection should continue, in order to fill all the micro-voids and fully impregnate the fabric. Another strategy is to place lower permeability fabrics or "dams" at the end of the flow path, so as to reduce the flow of the resin in these areas, hence allowing progressive saturation of the tows. These strategies are object of study in the next chapters.

Chapter 5

Enhancing permeability with spacers

In Chapter 4 it was demonstrated that the presence of meso-channels is the key to permeability enhancement, in accordance with previous findings (Section 2.5). An increase of permeability of one order of magnitude was observed between a standard woven fabric (2×2 twill) and a NCF with a specific stitching pattern, which is responsible for formation of large inter-tow channels in the preform. However, such a peculiar fabric requires dedicated production, in particular temperature resistant stitches, when mTP-RTM is concerned, which might result in higher manufacturing cost. Also, as observed in the previous chapter, these may lead to large non-saturated zones, which may be difficult to control, and to a strong local inhomogeneity in the final material, with large resin-rich areas. In this chapter, we present an alternative strategy for creating channels in a fibrous preform of any architecture by introducing a second solid-phase in the preform, which will be called *spacer*.

5.1 Concept

The basic idea behind flow enhancement with spacers, as investigated in this study, is illustrated in Fig. 5.1, which schematically shows the side view of a preform compacted in an RTM mold. A highly permeable region is created in the fabric preform, in order to allow for fast long-range infiltration in the in-plane direction (red arrow). Later, fabric impregnation is achieved by through-thickness flow (blue arrows). Though through-thickness permeability is typically two or three orders of magnitude lower than that

in-plane, the flow distance is also very short (few millimeters). Since flow time t is quadratically dependent on the flow length L , and inversely proportional to permeability K ($t \propto \frac{L^2}{K}$), shorter impregnation times are thus predicted.

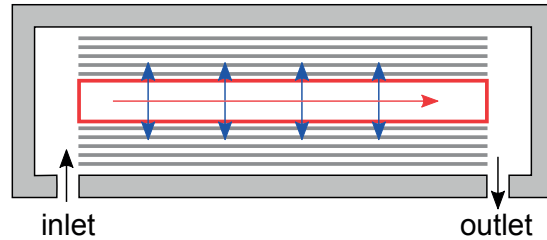


Fig. 5.1: Side-view of sandwich preform, where the core region represents the spacer.

This strategy resembles what is typically carried out in VARIM, where a flow mesh is inserted between the top fabric layer and the vacuum bag, and impregnation is obtained by through-thickness flow. However, this is the only similarity the two concepts share. Firstly, the strategy proposed in this study is conceived for RTM; this implies that the preform, composed of a fabric stack and flow-medium, is compacted to a constant thickness in a rigid mold, unlike VARIM, where the mold top is flexible and compaction is limited to atmospheric pressure (i.e. the final thickness is dependent on the preform response under compaction).

Secondly, a positive injecting pressure can be imposed on the fluid, which can be higher than 1 bar, and fluid can be injected even during a post-filling stage, unlike VARIM, where it is necessary to close the inlet in order to have effective compaction. With our strategy, fluid can be over-injected so as to achieve optimal impregnation, but care should be taken so as to slow it down once it reaches the outlet.

Thirdly, the spacer has a three-dimensional structure, so that it is stiff enough in order to withstand fabric compaction and open gaps. 3D-Printing by Fused Deposition Modeling (FDM) was chosen as technique for production of the spacers.

Finally, the spacer is inserted in the middle of the fabric stack, as the core of a sandwich structure, and it is meant to remain as part of the final composite, or to eventually melt and dissolve in the matrix. In the first case, a composite sandwich structure with predictably improved bending and torsional stiffness will be obtained. In the latter case, the fabric will relax and a more homogeneous distribution of fibers in the matrix could be achieved; this implies that the material of choice has to be solid and stiff during

in-plane flow, and melt or dissolve during the subsequent through-thickness impregnation.

5.2 Design and fabrication

5.2.1 3D model design

The spacer design was performed on 3D modeling software SketchUP. It was conceived as a three-dimensional square lattice, where the repeating unit is a three-dimensional frame with solid walls along the flow direction (Fig. 5.2a). The final structure is an array of solid beams and channels along the flow direction, kept together by thinner transverse beams (Fig. 5.2b). The longitudinal beams are the structural components of the spacer, and they are accountable for bearing the compaction of the fabric. Beams' thickness t and width b were kept constant for all the structures to 1.5 and 1 mm, respectively. The spacers feature rectangular channels along the flow direction of constant height $h = 1$ mm and width w . Square gaps of size $w \times w$ allow through-thickness flow. Channel's width w was varied between 2 mm and 6 mm. Therefore, increase of spacer permeability, both in-plane and out-of-plane, and concurrent decrease of compressive stiffness, is expected for larger w . A too small mesh size could result in an excessively stiff structure, which would require too high pressure for compaction. On the other hand, a too large mesh size could cause the fabric to nest in the transverse gaps and eventually block the channels. Another meaningful parameter is b , which is expected to affect the stiffness of the longitudinal beams, but which was kept constant in this study.

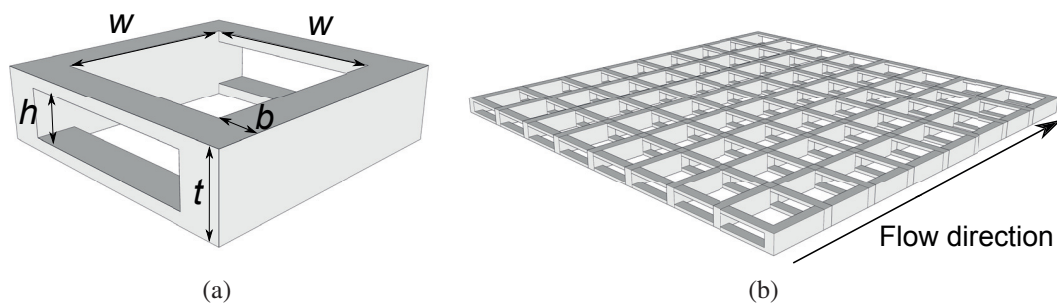


Fig. 5.2: Three-dimensional design of (a) unit cell and (b) full spacer; $t = 1.5$ mm, $b = 1$ mm, $h = 1$ mm, w variable.

5.2.2 Preform structure

Ideally, during the transverse flow phase, the spacer would melt so that the fabric can relax and optimal impregnation and fiber distribution can be achieved in the final composite. However, it is conceivable that it would remain solid and stay rigidly embedded in the matrix, resulting in a sandwich-like composite. Unlike VARIM, in RTM process final part thickness is given by the mold-cavity depth, therefore global fiber volume fraction is determined a priori, and it is not affected by the presence of the spacer. However, a substantial difference will be locally created. Local volume fraction can easily be determined using the well-known formula (Eq. 3.3)

$$V_f = \frac{A_w n}{t \rho_{glass}}$$

In this study, we used a cavity of 5 mm thickness, and 10 layers of 2×2 twill glass fabric G-WEAVE^{TM*}, which leads to a global fiber content of 45.8%. In presence of a spacer of thickness 1.5 mm, the 10 fabric layers would be confined in a thickness of 3.5 mm, which corresponds to a local fiber volume fraction in the regions above and below the spacer (i.e. the skins) of 65.4%, if the spacer does not deform. A schematic of the fabric preform with spacer is depicted in Fig. 5.3. Fabric layers were always placed with fiber bundles parallel to spacer's beams, and always with the same lay-up[†].

According to the findings of Chapter 4, the longitudinal in-plane permeability of the preform in Fig. 5.3 can be easily predicted from the channel's shape and size. Combining the equation for saturated permeability (Eq. 3.4) to the equation for the pressure drop in a channel (Eq. 4.1) and the hydraulic resistance of a rectangular channel [157], i.e.

$$R_{hyd} = \frac{12\eta L}{(1 - 0.63 \frac{h}{w}) h^3 w}, \quad (5.1)$$

where η is fluid viscosity, and L , h and w channel's length, height and width, the following expression for the saturated permeability of a sandwich preform channel is obtained:

$$K_{channel} = \frac{(1 - 0.63 \frac{h}{w}) h^3 w}{12A}, \quad (5.2)$$

*Refer to Section 3.1.2 in Chapter 3.

[†]Notice that G-WEAVE has the same areal weight of fibers in the two principal in-plane directions.

where A is the area of a cross-sectional unit-cell of the preform containing one channel (Fig. 5.3).

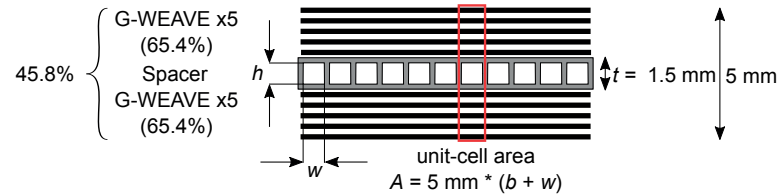


Fig. 5.3: Scheme of cross-section perpendicular to flow of a sandwich-like preform with core spacer, showing local and global fiber volume fraction.

5.2.3 Fabrication by 3D-Printing

Spacers were fabricated in poly(lactic acid) (PLA) and polycaprolactone (PCL) using a Fused Deposition Modeling (FDM) technique, on a 3D-Printer Ultimaker 2+. PLA and PCL were extruded through a nozzle of 0.25 mm diameter at a temperature of $210 \text{ }^\circ\text{C}$ and $180 \text{ }^\circ\text{C}$ respectively. Bed temperature and nozzle speed were set to $60 \text{ }^\circ\text{C}$ and around 25 mm s^{-1} for PLA. For PCL, bed temperature was set to $35 \text{ }^\circ\text{C}$, while the printing speed varied between 6.25 mm s^{-1} for the bottom layer to 37.5 mm s^{-1} for the longitudinal beams. Printed 3D-spacers were let to cool down before being detached from the substrate.

Five different mesh sizes $w \times w$ were investigated, with w varying from 2 to 6 mm. Spacers of size $\approx 3 \text{ cm} \times 3 \text{ cm}$, similar to the ones shown in Fig. 5.4, were produced in PLA for the compression and compaction tests described in the next section. An additional spacer of mesh 6 was printed in PCL. More spacers were printed in size $5 \text{ cm} \times 20 \text{ cm}$, as shown in Fig. 5.5. These spacers were used either for flow studies (PLA) or to produce real plates with epoxy resin (both PCL and PLA). In the case of PCL spacers, the top transverse layer was not printed, because the viscosity was so high that bridging (printing of suspended features) was not optimal. The absence of the top transverse layer can be observed in Fig. 5.5. It is worth noticing that this geometry with only one transverse array of beams allows for more efficient and rapid production, along with slightly higher channels. However, it could cause partial nesting of the glass fabric.

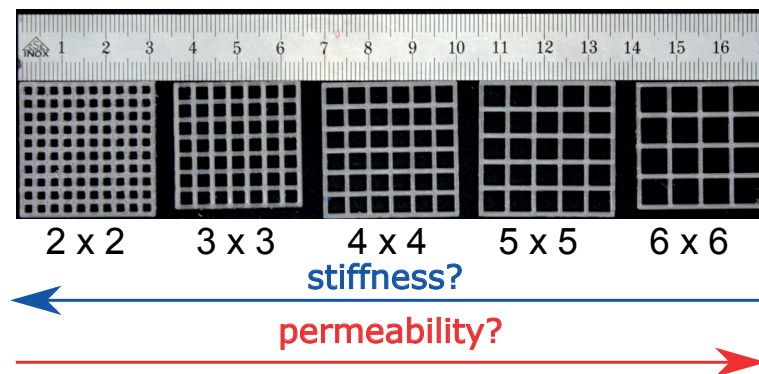


Fig. 5.4: Top-view of 3D-printed spacers with varying mesh-size.

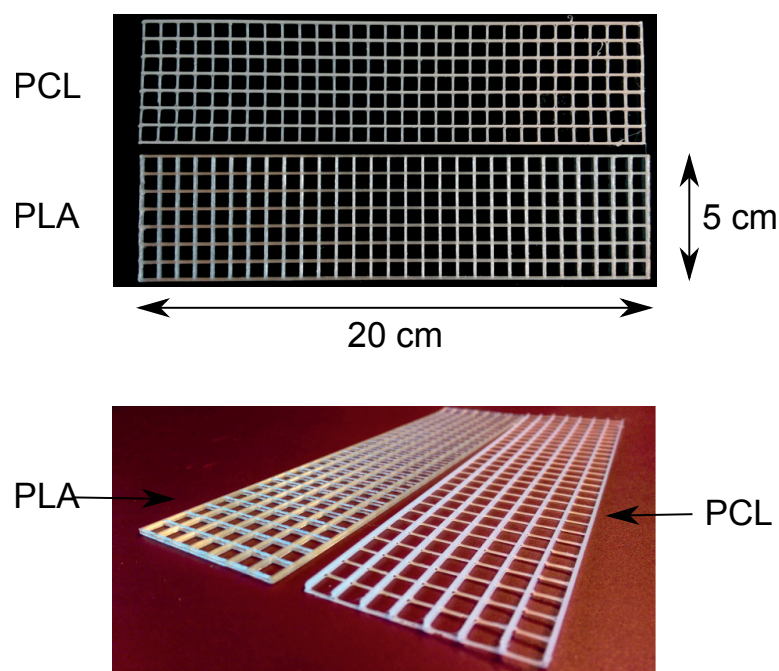


Fig. 5.5: Spacers for flow studies (in PLA) and plate production (in PCL) of mesh size 6×6 (mm).

5.3 Experiments

Three-dimensional spacers printed in PLA and PCL were characterized alone in compression tests, and combined with glass fabric in sandwich-like preforms (Fig. 5.3) in terms of compaction and permeability. The presence of a second solid phase in the preform inevitably has an effect on its response under compaction. For instance, a higher pressure for closing the mold will be required, and at the same time the spacer has to withstand such a pressure without breaking. It is therefore useful to characterize the compressive strength of the spacer itself, as well as the force necessary to compact the

preform in a given thickness. Fabrics behave as viscoelastic materials, with a time-dependent response. Under constant deformation they can experience stress relaxation, caused by a reorganization of the fiber bundles. During nesting, fiber bundles of a layer can slide into the gaps of neighbor layers. In the case of the spacers, fiber bundles might nest into the transverse gaps of the spacer. Flow experiments were carried out with the experimental setup described in Section 3.2.1. The goal of these studies was to quantify the enhancement of permeability for different channel size and possibly find a relation between spacer stiffness, fabric nesting and preform permeability. Intuitively, the presence of the spacer will also affect the morphology of flow front, which will also be matter of investigation.

Finally, as proof of concept, composite plates were prepared via TS-RTM. The objective was to prove the two concepts mentioned in the introduction of this chapter. After full impregnation is achieved, the spacer could remain intact after the impregnation and function as a stiffener, or, alternatively, soften or melt and flatten under the compaction of the fabric, which would consequently relax and achieve a more homogeneous distribution of the yarns throughout the plate's thickness. In the former case, the spacer should have a melting point higher than the curing temperature of the resin, whereas in the latter it should have a lower melting point, so as to guarantee that the fabric has the time to relax before the gel point[‡].

5.3.1 Compression tests on spacers

Compression tests on spacers were carried out taking the cue from ASTM standard for compressive properties on rigid cellular plastics [158], in order to determine their compressive strength and stiffness. Three different spacers of size around 3 cm (Fig. 5.4) were printed for each mesh-size in PLA and for mesh-size 6×6 in PCL, and tested between two metal plates larger than the samples. The top plate was smaller than the bottom and was circular, of diameter 45 mm. The force F was recorded by the 125 kN load cell and displacement d was measured with an LVDT device, while the upper plate was displaced at a constant speed of 1 mm/min. Force and displacement data were

[‡]All the mechanical tests in this chapter were performed on an UTM *Walter+Bai AG Series LFL-125kN* as described in Chapter 3.

transformed into stress σ and strain ϵ according to

$$\sigma = \frac{F}{S} \quad (5.3)$$

$$\epsilon = \frac{d}{t} \quad (5.4)$$

where t and S are spacer's thickness (≈ 1.5 mm) and horizontal area (≈ 3 cm \times 3 cm), respectively. The dimensions were accurately measured with a caliper. Compressive strength σ_c was arbitrarily defined as the stress at 15% deformation, where 0% was taken as the x -intercept of the linear regression in the elastic region.

5.3.2 Compaction tests on sandwich preforms

Sandwich preforms were tested in compaction down to a given thickness using a 10 kN load-cell, using the same setup used for the compression tests. During these tests, rather low forces were measured, therefore no LVDT was used, and cross-head displacement was directly taken as a measure of compaction thickness. For each type of spacer (five in PLA of varying mesh-size and one in PCL of mesh-size 6×6), three samples were produced and tested with glass fabric layers in a preform as depicted in Fig. 5.3. The spacers used for compaction were printed with same design as those tested in single compression (Fig. 5.4). For each test, ten freshly-cut layers of G-WEAVE of size 5 cm \times 5 cm, hence larger than the spacers and larger than the top plate, were cut and laid with the same orientation on a larger bottom plate. Three tests on plain fabric (without spacer) were also performed. For the sandwich preforms, the compaction pressure was calculated by dividing the measured force by the horizontal area of the spacer, which carries the load. For the fabric only, the area of the circular upper plate of diameter 45 mm was used. The upper plate was displaced at a constant speed of 1 mm/min until the preform was compacted to 5 mm thickness. Force was continuously measured at this constant thickness for 4 min, so as to evaluate the fabric relaxation.

5.3.3 Flow studies on sandwich preforms

An aqueous solution of PEG 16.7%wt with a small amount of food colorant for contrast enhancement was used as test fluid (viscosity of 0.11 Pa s at 20 °C[§]). The preforms with 10 layers of G-WEAVE and core spacer were placed in a mold cavity of 5 mm thickness[¶]. Care was taken in order to apply a minimum compacting pressure according to compaction experiments. For these tests, spacers of size 5 cm × 20 cm were printed, and glass fabric was cut to the same size. One single spacer was produced for each type of architecture. Two series of tests were performed. In a first series, the five architectures were tested and compared against that of the plain fabric. In the second series, one type of architecture was selected in order to investigate different impregnation strategies.

Permeability of spacers with different mesh size

For each spacer, a test was performed injecting the fluid at constant pressure. Saturated permeability was measured from the flow rate of fluid at the outlet Q_{out} , according to Eq. 3.4:

$$K_{sat} = -\frac{Q_{out}\eta L}{A\Delta P},$$

where ΔP is the applied pressure difference between inlet and outlet, η the fluid viscosity, $L = 20$ cm the preform length, and $A = 2.5$ cm² the cross-sectional area of the preform.

Impregnation strategies with spacers

As pointed out in Chapter 4, the presence of channels enhances in-plane permeability, but at the same time it exacerbates the duality of flow, which proceeds quickly in the channels and later within the fiber tows. This might be an issue for the quality of impregnation. Therefore, it is necessary to find a route to exploit channels to quickly transfer the fluid from inlet to outlet, and subsequently slow it down and force it to flow transversely so as to infiltrate within the fiber bundles.

Three experiments were performed using a spacer design based on the unit cell shown in Fig. 5.2a with mesh size 6 × 6 ($w = 6$ mm). In all the experiments, listed in Table 5.1, the fluid was injected with the same applied pressure, and vacuum was

[§]Refer to Table 3.2 in Chapter 3.

[¶]Flow studies were performed using the setup described in Section 3.2.1, Chapter 3.

pulled in the mold cavity from the outlet for 1 min prior the injection and during the injection. In the first two experiments the fluid was slowed down so as to prevent it to flow out of the mold and force transverse fabric impregnation. The "brake" mechanism was different: in the first experiment, a dam-zone was created at the end of the fabric, making use of a microporous membrane which allows air but not a liquid to pass through it (Goretex membrane); in the second one, once the fluid had reached the outlet, this latter was closed (i.e. no more vacuum was being pulled) while the inlet was kept open and more pressurized fluid was being injected. A third experiment without any spacer (i.e. 10 layers of G-WEAVE) was also conducted. All the experiment continued for at least 10 min in order to reach a full saturation state.

Fluid infiltration was recorded with a digital camera Canon EOS 700D with a frame acquisition rate of 29 fps. The goal of these experiments was to compare filling times by image analysis. The video frames were subdivided in unit cells as shown in Fig. 5.6. A MatLab code was used to generate horizontal and vertical lines, which would follow the fiber bundles' borders. The images were binarised and saturation was defined for each cell at any frame using the fully saturated state (the final frame of the video) as a reference.

Table 5.1: Flow experiments with different impregnation strategies.

Experiment	Configuration	Inlet pressure	Brake
1	Spacer 6×6	0.59 bar	Dam-zone
2	Spacer 6×6	0.60 bar	Closed outlet
3	No spacer	0.60 bar	None

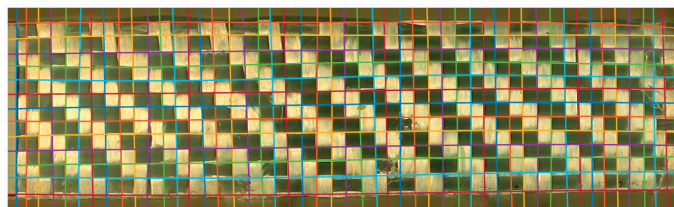


Fig. 5.6: Subdivision of preform top-view in unit cells for flow front detection and image analysis.

5.3.4 Impregnation with epoxy resin

The "closed-outlet" strategy investigated with a model fluid was subsequently applied to the production of two composite plates via TS-RTM, with the spacers of mesh 6×6 in PLA and PCL shown in Fig. 5.5. A third plate was produced with glass-fabric only (10 layers of G-WEAVE) for comparison.

Production of plates via TS-RTM

An epoxy resin Araldite® LY 8615 with hardener Aradur® 8615 (Huntsman), at a mixing ratio of 2:1, was used as matrix. The mixture was prepared at room temperature and degassed under vacuum for 10 min. According to the manufacturer, the gel time of this resin is between 34-38 min at 80°C and 16-20 min at 100°C, and initial viscosity in the range 80-160 mPa s at 40°C.

The plates were produced in the same setup used for flow experiments, which was also equipped with six heating cartridges embedded in the bottom steel part of the mold. The three preforms shown in Fig. 5.7 were prepared in size 5 cm \times 20 cm and carefully placed in the mold cavity of thickness 5 mm. For the two sandwiches, the same stacking sequence shown in Fig. 5.3 was used. The resin was kept at room temperature (20 °C) and injected in the mold at 1 bar of pressure. Vacuum was also applied at the outlet during the impregnation. The mold was pre-heated at 40 °C, and, after fabric impregnation was visibly achieved, it was raised to the curing temperature of 80 °C for 1 h. For the three cases, vacuum was pulled from the outlet for 1 min prior to the injection, and the resin was cured with closed outlet and under pressure from the inlet. Finally, the demolded plates were post-cured in a ventilated oven at 150 °C for 1 h.

Plates analysis

From the three plates, samples were cut off with a diamond blade for cross-section visualization with an optical magnifier and mechanical testing. Four rectangular beams of width 13 mm and length around 90 mm were cut from each plate along the flow direction for flexural tests (3-point bending configuration with a 125 kN load-cell), similarly to what is shown in Fig. 5.8. For G-WEAVE/PLA- 6×6 , each sample was cut such that it contained two spacer's beams in the flow direction. Given a thickness of around 5 mm, a

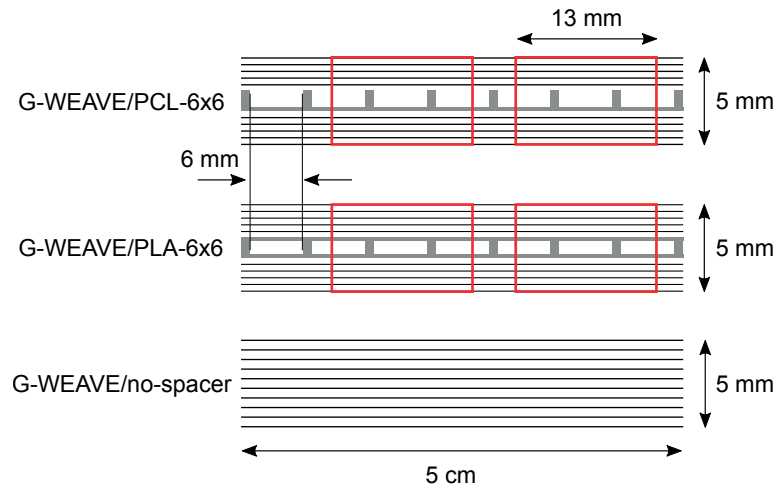


Fig. 5.7: Scheme of cross-sectional view perpendicular to flow of preform structures for three plates produced with epoxy resin via TS-RTM; the red boxes show the cross-sections of beams cut for flexural tests, each containing two beams of the spacers.

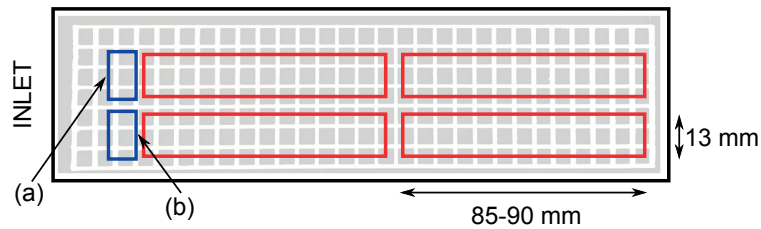


Fig. 5.8: Schematic view of a plate with spacer, showing the four samples cut for flexural tests (in red) and for cross-section visualization (in blue); (a) cross-section in the middle of a 3D unit cell; (b) cross-section close to a transverse beam.

span-length of 80 mm was selected, which gave a span-length-to-thickness ratio of 16:1. The flexural elastic modulus was taken as the slope of the stress-strain curve in the strain range between 0.006 and 0.008. Flexural strength was taken as the maximum stress before failure. Average modulus and strength were calculated from the four samples cut off from each plate.

5.4 Results and discussion

5.4.1 Compression and compaction

Fig. 5.9 shows the stress-strain compression curves and average compressive strength of the five PLA spacers and for the PCL-6x6 spacer. Unsurprisingly, the smaller the mesh size, the larger the number of beams carrying the load, the larger the compressive strength. PCL is much softer than PLA, and it might deform under the compaction of

the fabric. This shows a possible shortcoming of the use of low melting point material as spacers, requiring further material developments.

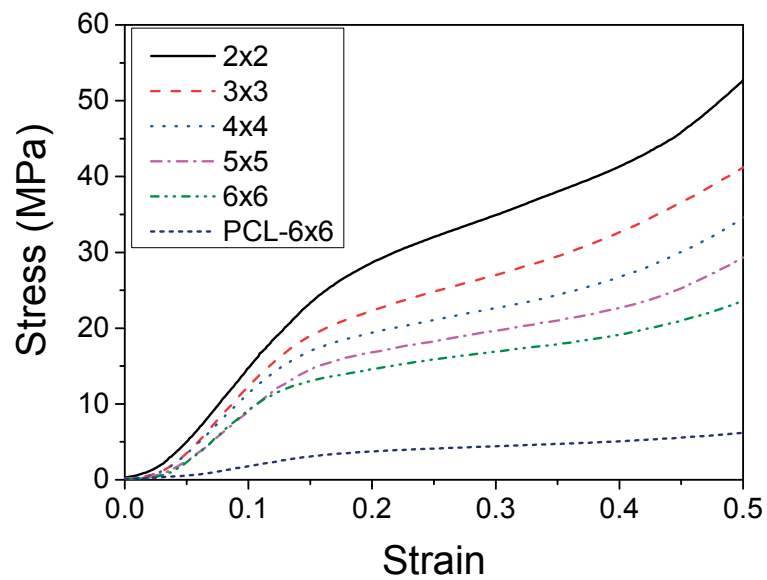
Pressure evolution during compaction and relaxation at constant thickness (5 mm) of sandwich preforms and plain glass-fabric is displayed in Fig. 5.10a. Spacers' thickness was measured with a caliper before and after the loading, and it was verified that they had not experienced any significant residual deformation, in accordance with the fact that the maximum pressure attained was much lower than the compressive strength of the spacers (Fig. 5.9b). The pressure required for compaction was higher for smaller mesh-size, in accordance with the compression results on the bare spacers. Normalization of relaxation by the maximum pressure shows that the curves of the PLA spacers during relaxation overlap (Fig. 5.10b). Hence no significant differences in the fabric rearrangement mechanisms with different mesh sizes are expected to take place. Conversely, the sandwich with PCL-6 × 6 spacer relaxed much less. This can be explained considering that this spacer had only one array of transverse beams (see Fig. 5.7) which is likely to allow nesting of the fabric already during loading (left-hand side of the graphs in Fig. 5.10a and b).

5.4.2 Flow experiments

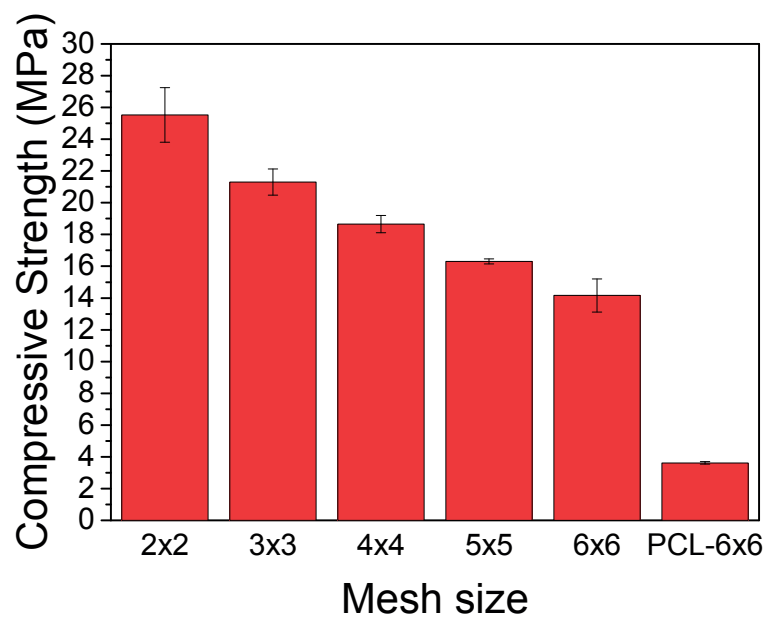
Flow experiments showed that the core spacer visibly enhanced flow in the principal in-plane direction. The fluid always flowed from inlet to outlet in a few seconds, leaving the fabric behind largely unsaturated. The spacer was responsible for an exaggerated duality in flow scales in the spacer's channels and through the fabric, where a combination of in-plane and out-of-plane flow was actually observed.

In the first series of experiments, where no brake mechanism was adopted, the fluid continued to flow preferentially through the spacer rather than to impregnate the fabric layers. A large amount of fluid flowed out of the mold before the fabric could be fully impregnated. As a result, there was no improvement in impregnation time, which was actually longer than for the plain fabric. Saturated permeability for the five sandwich structures, measured from fluid flow rate at the outlet is reported in Fig. 5.11. Permeability for plain G-WEAVE and G-PLY are also shown^{||}. The presence of spacers was

^{||}Values taken from Fig. 4.5 in Chapter 4.

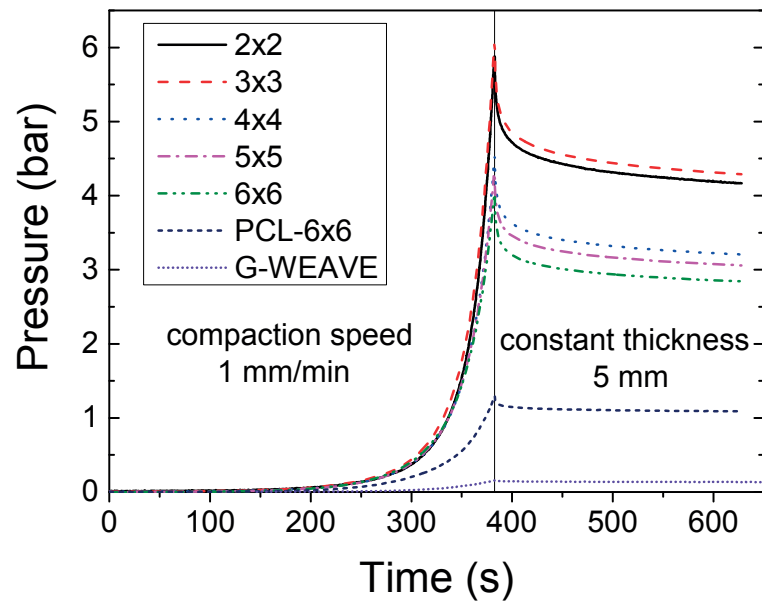


(a)

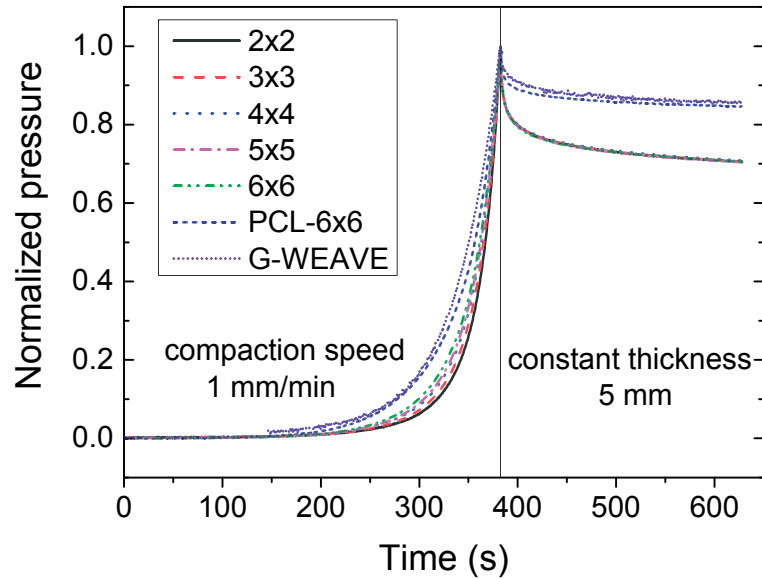


(b)

Fig. 5.9: (a) Compressive stress-strain curves and (b) compressive strength for the five PLA spacers of varying mesh-size and the PCL-6 × 6 spacer..



(a)



(b)

Fig. 5.10: (a) Absolute and (b) normalized pressure evolution during compaction-relaxation tests.

responsible for an increase of more than one order of magnitude in saturated permeability. The theoretical permeability values calculated from Eq. 5.2 are also reported in Fig. 5.11, and they are in the same order of magnitude as the experimental values. However, theoretical permeability increases monotonically with channel width, whereas a maximum for the spacer 4×4 is observed for the experimental values. This could be caused by partial nesting of the tows in the spacers' pores, even though this was not observed in compaction experiments. Interestingly, there is a correspondence between the mesh size of maximum permeability and the tow width of the G-WEAVE (4 mm). However, these differences of permeability are rather small compared to the large increase with respect to the plain fabric. Moreover, a single experiment was carried out for each spacer, and considering the large uncertainty in permeability experiments, further experiments should be carried out to confirm this trend. Under these considerations, the spacer of mesh size 6×6 was selected for the second series of tests, due to shorter printing time and lower pressure required for compaction.

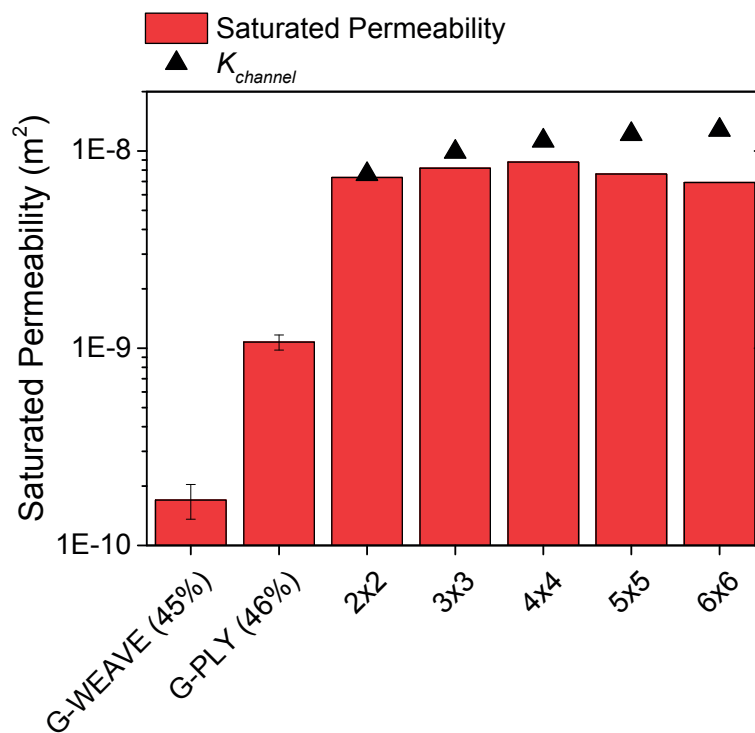


Fig. 5.11: Measured and calculated saturated permeability for preforms with spacers with different mesh size and without spacer; G-PLY fabric is also reported for comparison.

The results of the second series of flow experiments are summarized in Fig. 5.12. When no spacer was present, a standard slug-flow infiltration was observed (Fig. 5.12a),

and full impregnation was achieved after around 60 s. When a spacer was added in the preform, after 3 s, the fluid had already reached the outlet and thanks to the brake mechanism (dam-zone in Fig. 5.12b and closed outlet in Fig. 5.12c) fabric impregnation could rapidly start to take place through combination of in-plane and out-of-plane flow. When a dam-zone was used as brake mechanism (Fig. 5.12b), after 15 s a dry spot was present, and it was still there after 60 s. Although the low permeability zone slows down the fluid, it was not capable to completely block flow of fluid. Therefore the fluid was not forced to impregnate the highly-compressed fabric. When in-plane flow was stopped by closing the outlet (Fig. 5.12c), full impregnation was achieved after just 15 s, and no major improvement was obtained after 60 s.

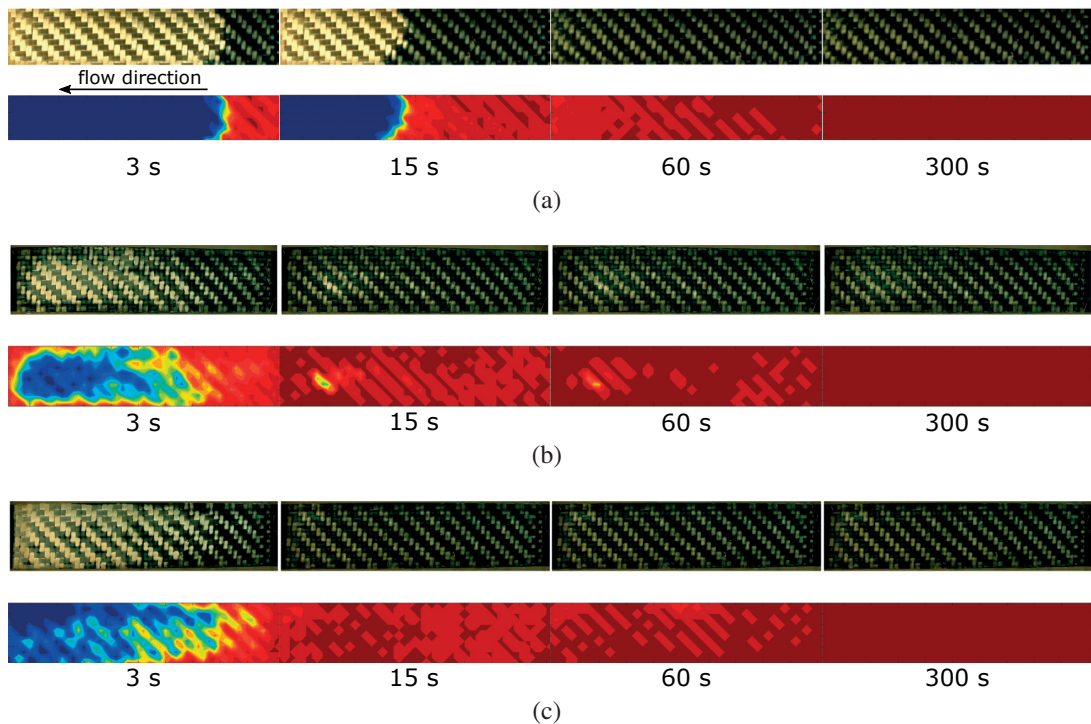


Fig. 5.12: Flow at different stages for experiments without any spacer (a) and with spacer and brake mechanism based on (b) dam-zone and (c) closed outlet (dark red = fully saturated, dark blue = dry).

5.4.3 Plates analysis

The flow pattern observed during impregnation of the sandwich preform with epoxy resin and using the "closed-outlet" strategy was similar to what was observed in the flow experiment with a model fluid. The resin reached the outlet quite quickly, then the outlet

was closed and the resin was continuously injected at the inlet for few more minutes so that the fabric was impregnated transversely.

Optical magnifications of the cross-section of the three plates are shown in Fig. 5.13. In the sample G-WEAVE/PLA-6 × 6 the channels created by the spacer are clearly seen (Fig. 5.13a and b). Partial nesting of both transverse and longitudinal fiber bundles is observed in the middle of a 3D unit cell (Fig. 5.13a) and next to a transverse beam (Fig. 5.13b). The pictures selected here are worst-case scenarios, as in some cases no nesting was observed at all. A cross-section of G-WEAVE/PCL-6 × 6 sample is shown in Fig. 5.13c. In this case the spacer is not clearly recognizable. Brighter areas can be observed corresponding to the PCL-spacer's beams. However, the original squared shape of the beam's cross-section is no longer visible. The spacer, softened by the temperature, is flattened under the effect of the fabric compaction. After enhancing the impregnation, PCL spacers dissolved (at least partly in the present case), allowing the fabric to relax and achieve a more homogeneous distribution of the fibers, similarly to a sample without any spacer (Fig. 5.13d).

Fig. 5.14 shows typical stress-strain curves for the three samples. The failure mechanism of samples with and without spacer is remarkably different. Samples without spacer, i.e. standard laminates of woven glass-fabric and epoxy resin, experienced a rather progressive failure. Conversely, samples with spacer definitely underwent abrupt failure, which was visibly due to delamination in correspondence with the core region.

The modulus and strength averaged on four tests per sample type are reported in Table 5.2. In the case of the PLA spacer, an increase of 20% in flexural modulus was observed. This is to be attributed to the core-skin structure of the sandwich, in which the fabric layers are confined in the skins to a volume fraction of $\approx 65\%$. The plate produced with the PCL spacer had a modulus, close to that of the equivalent composite with no spacer, albeit a bit lower. This confirms our observation of partial melting of the PCL and fabric relaxation to a more homogeneous structure, and to the lower mechanical properties of the PCL as compared to the epoxy matrix. Regarding the strength, there was not any improvement, neither with PLA nor with PCL. Indeed, delamination was responsible for early failure compared to the sample with no spacer. In principle, the fact that the core is made of the same material as the matrix should reduce the risk of

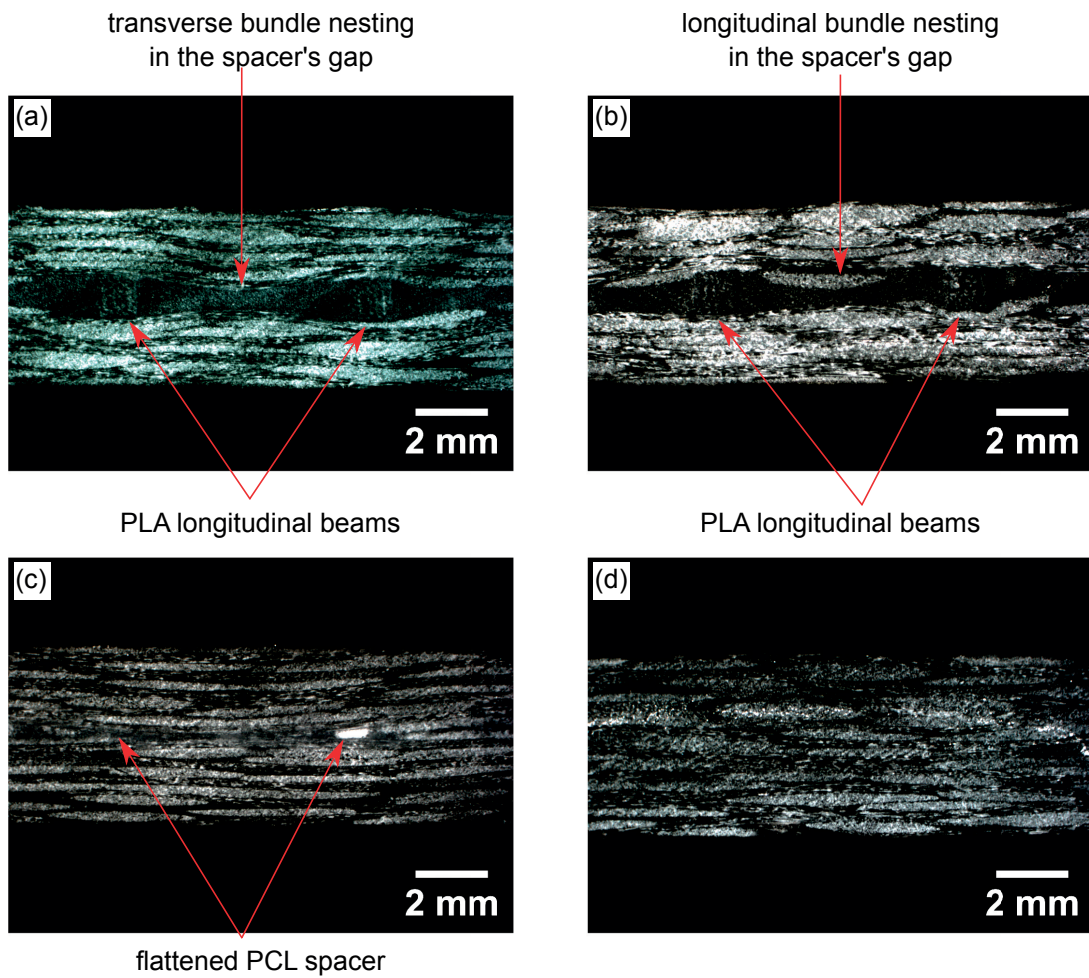


Fig. 5.13: Optical magnification of the cross-section of samples G-WEAVE/PLA-6 × 6 in the middle of a 3D unit cell (a) and close to a transverse beam (b), G-WEAVE/PCL-6 × 6 (c) and G-WEAVE/no-spacer; (a) and (b) are also referred to in Fig. 5.8.

delamination, as suggested for example by Wolfrath et al. [159], because there is no discontinuity between core and skins. However, in the present case the spacer itself constitutes a discontinuity.

Table 5.2: Elastic modulus and strength of samples produced via RTM measured by 3-point bending tests.

Sample	Flexural modulus (GPa)	Flexural strength (MPa)
G-WEAVE/PLA-6 × 6	11.41 ± 0.13	277 ± 19
G-WEAVE/PCL-6 × 6	9.18 ± 0.11	245 ± 5
G-WEAVE/no-spacer	9.50 ± 0.02	280 ± 2

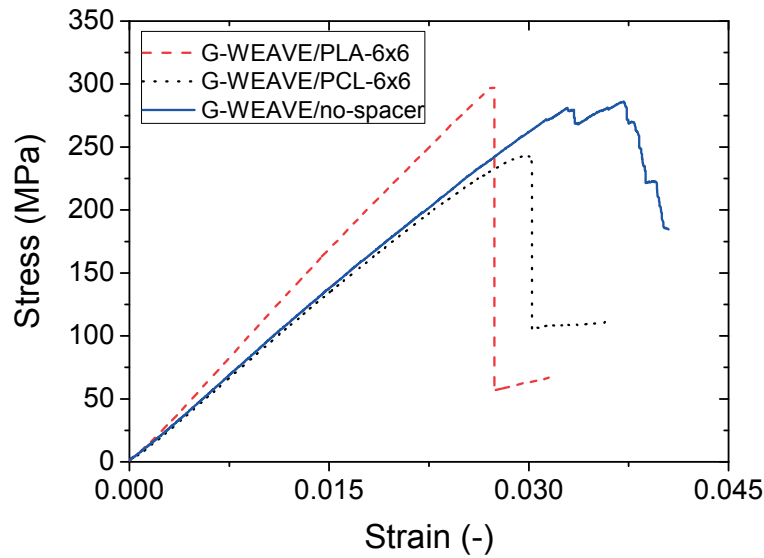


Fig. 5.14: Typical stress-strain curves for flexural tests on samples with and without spacers.

5.5 Conclusions and outlook

In this study, a preforming strategy involving the use of a second solid phase (spacer) as core of a sandwich stack was explored. Different architectures were compared in terms of compressive strength, compaction and permeability. Specifically, mesh size, and thus transverse gaps' size, was varied. This resulted in a varying number of longitudinal beams, which carry the load during compression, per unit area. The spacers were increasingly strong under compression when the mesh size was reduced from 6×6 to 2×2 mm. Lower mesh size means larger number of beams per unit area, which is reflected in a higher compressive strength. In addition, comparison between two 6×6 -spacers made of PLA and PCL showed that the latter had a much lower strength; in this case, this is to be attributed to the intrinsically lower mechanical properties of PCL compared to PLA. Compaction tests on the sandwich preforms (spacer and fabric) provided a measure of the required pressure to compact them in a mold, which is an important factor to take in consideration for mold design. The highest pressure (6 bar) was found for the PLA 2×2 -spacer, and it decreased for larger mesh-size. Normalized relaxation curves did not show any large differences between different mesh sizes, indicating a similarity in relaxation mechanism, although a difference was observed for the PCL-spacer, whose structure required a lower pressure to accommodate the fabric.

An increase of saturated permeability of more than one order of magnitude compared to the plain fabric was found for all the spacers. Apparently, the highest permeability was obtained in the case of 4×4 spacer, but differences are likely to fall within the experimental uncertainty, which reportedly can be as high as 20-30% [98]. The experimental permeability did not fully follow the values predicted from channels size, because for larger mesh-size, the fabric tends to nest in the spacer's gaps partially blocking the channels. However, the larger channel size spacers are less intrusive in terms of added TP material in the final part, so would be preferred. Such a large increase of permeability relates to the presence of wide channels, where flow is predominant (Chapter 4), and it is accompanied by extreme dual-scale flow and difficulty in achieving full fabric impregnation with standard RTM injection. Two different impregnation strategies were therefore explored on the spacer 6×6 and compared to standard injection without any spacer. Flow visualization indicated that the fastest impregnation is obtained when vacuum is pulled from the outlet prior and during the injection, thus reducing the risk of air entrapment; afterwards, the outlet is closed, so as to prevent outflow of fluid, and more fluid is injected from the inlet, thus forcing it to impregnate the fabric in out-of-plane direction. This concept can also be scaled-up to large parts rather easily, as the in-plane impregnation time will be dictated by the macro-permeability and remain rather short, while the saturation phase will be dictated by transverse flow and keep the same duration, whatever the part size.

In addition, as proof of concept, two plates were produced via TS-RTM by impregnating with an epoxy resin sandwich preforms with PCL and PLA spacers. It was demonstrated that these spacers can respectively either collapse during cure allowing a more homogeneous distribution of the fabric layers or remain intact in the final part. In the former case, deterioration of both flexural modulus and strength was observed, which was attributed to the poor mechanical properties of the PCL itself. This concept might as well be implemented in mTP-RTM. If possible, a material compatible with the matrix should be used, which nevertheless should be solid and rigid during the impregnation (i.e. have higher melting-point than the matrix and high glass-transition temperature); afterwards, by increasing the temperature, the spacer would melt and diffuse in the matrix without affecting its mechanical properties. In the case of the PLA spacer,

an increase of the apparent flexural modulus of 20%, compared to a sample with fabric only, was attained. The spacer had a dual role, acting both as flow-enhancer during injection and as stiffener in the final composite. This concept can similarly be implemented in mTP-RTM, as will be shown in the next chapter, where poly(ether ether ketone) (PEEK) reinforced with carbon fibers was successfully used as spacer during mTP-RTM.

Chapter 6

Process improvement

This chapter summarizes the efforts made in order to optimize fabric impregnation in mTP-RTM process in lab-scale conditions. In the first part, results of the characterization of basic physico-chemical properties of selected high-fluidity thermoplastic matrices are illustrated and discussed (Section 6.1). The second part concerns the design of the setup used for production of plates via mTP-RTM; preliminary tests with PP and HFPA6 are also shown (Section 6.2). In the third and final part, a series of mTP-RTM tests with HFPA6 and different preforms and impregnation strategies, adopted according to the findings of Chapter 4 and Chapter 5, is illustrated and discussed (Section 6.3).

6.1 Characterization of High-Fluidity Thermoplastics

In this section, results of characterization of HFTP used for process development are illustrated*.

6.1.1 Differential Scanning Calorimetry (DSC)

Melting points and glass transition temperatures of the HFPA66 and HFPA6, measured through DSC scans, are reported in Table 6.1. Crystallization temperature for HFPA66 was found to vary from 216 °C to 230 °C for cooling rates between 100 °C min⁻¹ and

*Materials and methods have been described in Section 3.1.3 and Section 3.2.2.

20 °C min⁻¹. The dependence of isothermal crystallization half-time $t_{1/2}$ on crystallization temperature is shown in Fig. 6.1. The inset shows an example of baseline subtraction. The Avrami fit is not shown, but values for the exponent n between 2.7 and 3 were found, in agreement with the results found in the thesis of Jalal Faraj [55], suggesting instantaneous nucleation and three-dimensional spherical shape of the spherulites.

Table 6.1: Melting point, glass transition and crystallization temperatures of the HFPAAs.

	T_g (°C)	T_m (°C)	T_c (°C)
HFPA66	67	265	216-230
HFPA6	59	223	170*

*from supplier

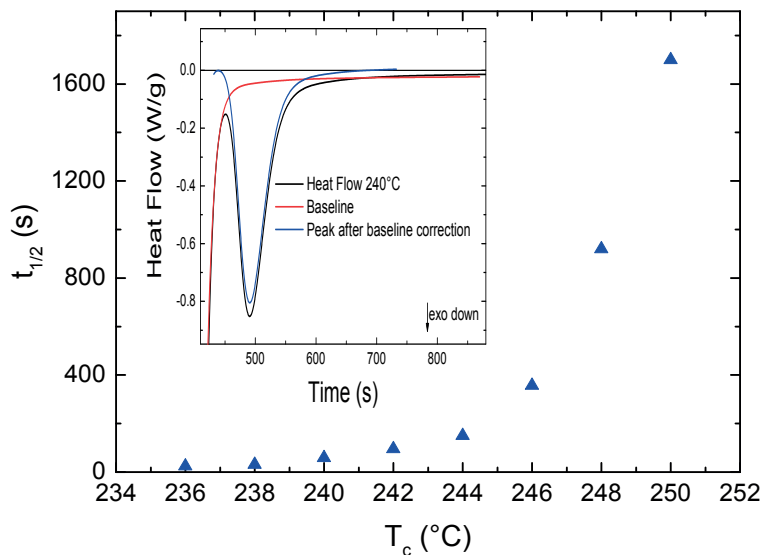


Fig. 6.1: Crystallization time $t_{1/2}$ against isothermal crystallization temperatures. Inset: isothermal crystallization peak at 240 °C with baseline subtraction.

6.1.2 Thermogravimetric Analysis (TGA)

The results of thermogravimetric analysis are shown in Fig. 6.2. Temperature scans in air at 20 °C min⁻¹ on the dried HFPA66 and HFPA6 are shown in Fig. 6.2a. The onsets of the thermal degradation are around 380 °C and 350 °C, respectively. The isothermal TGA result in Fig. 6.2b shows the effect of the drying treatment on the melt stability of HFPA66. The temperature was held at 280 °C for 30 minutes under air atmosphere, showing a non-negligible weight loss, which is more pronounced for the dried sample.

This might be related to the evaporation of water produced in the condensation reaction between amide and carboxylic groups, which takes place in the melt state of polyamides:



This equilibrium is well known for PAs in the melt state [160]. The effect of the drying is thus to shift the equilibrium towards the products (right-hand of Eq. 6.1), which results in more water produced and eventually removed. Subsequently, a loss of weight is recorded, which takes place more rapidly for a dried sample than for an undried one.

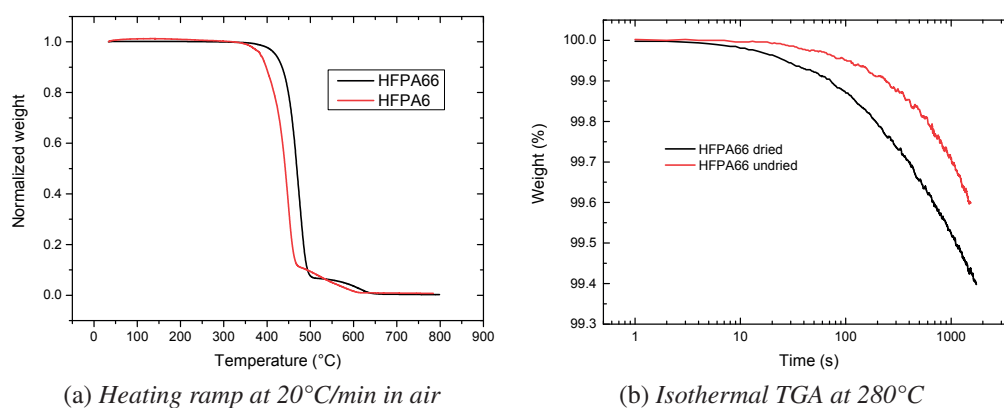


Fig. 6.2: TGA measurements on HFPA.

6.1.3 Rheology

Flow-mode measurements at a shear rate of 10 s^{-1} were conducted on dried HFPA66 at constant temperatures of 270, 280 and 290 °C, under N_2 or air. The shear rate was proven to be in the Newtonian range. Fig. 6.3a plots the viscosity versus time for these cases. The most remarkable feature is the very small difference of viscosity at different temperatures, with a gap of just 15 Pa s at time zero. Secondly, the trend is very different when changing temperature and atmosphere. At 270 °C under nitrogen viscosity steadily increases, while at 290 °C in air it falls dramatically after a certain time. The increase is due to the polycondensation, confirming what was discussed for the isothermal TGA (Eq. 6.1), while the decrease is due to degradation. The two effects are competitive in the intermediate temperature range. This suggests an optimal processing temperature range between 270 and 280 °C.

Table 6.2: Arrhenius activation energy and pre-exponential factor of HFPA6.

	E_a (kJ mol ⁻¹)	A (10 ⁻³ Pa s)
HFPA66	59.3	0.09
HFPA6	46.3	1.11

A second set of measurements has been conducted in oscillatory-mode on dried HFPA66, at 280 °C under nitrogen. Five successive frequency sweeps from 1 to 700 rad s⁻¹ were carried out on the same sample, each measurement lasting about 6 min. The first measure shows a Newtonian behavior in the range from 1 to 300 rad s⁻¹, where shear-thinning takes place. Typical shear forces in thermoplastic thermoforming are in the range 1-100 rad s⁻¹ [43], thus a Newtonian behavior is expected in a mTP-RTM. Successive measurements show a viscosity increase and a shift of the onset of the shear-thinning at lower frequencies, suggesting an increase of average molecular weight and a broadening of the molecular weight distribution [43, 161].

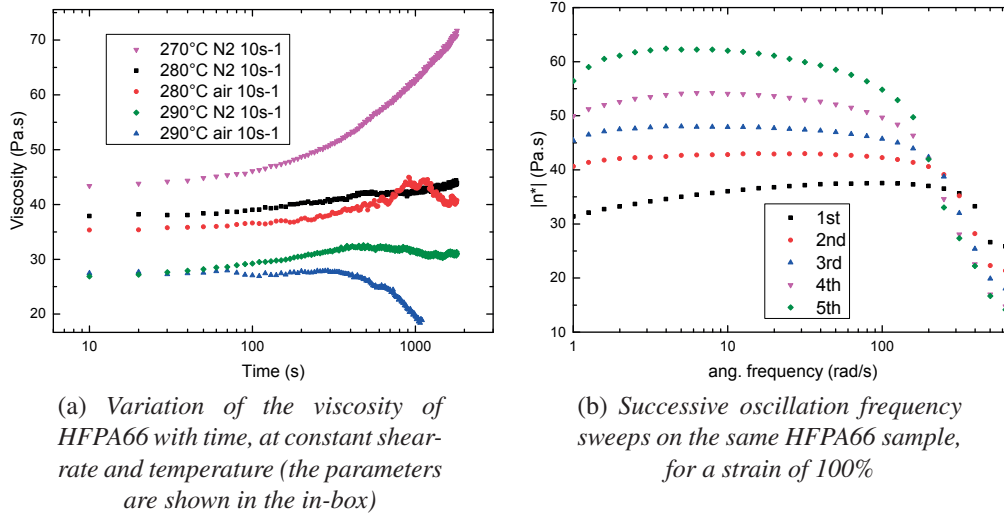


Fig. 6.3: Rheology measurements on HFPA66.

The rheology of HFPA6 and iPP Borflow was also characterized in flow-mode, in air at constant shear rate. Results in Fig. 6.4 show that HFPA6 is quite stable up to 280 °C, allowing a wider process window in terms of temperature than HFPA66. The viscosity of the iPP Borflow decreases slightly, probably due to thermal degradation, but it is more stable than that of polyamides, and it is not affected by moisture content.

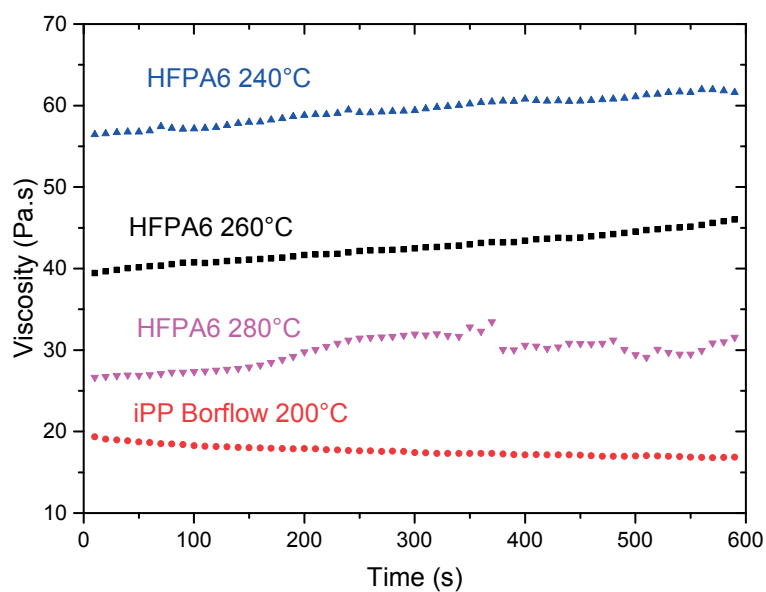


Fig. 6.4: Constant flow measurements on HFPA6 at 1 s^{-1} and iPP Borflow at 0.1 s^{-1} in air.

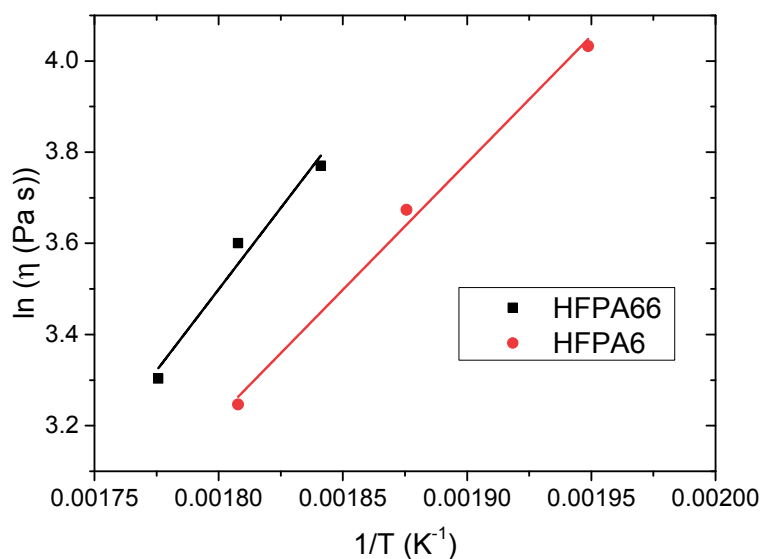


Fig. 6.5: Arrhenius plot for HFPA66 and HFPA6.

The initial viscosity values of HFPA66 and HFPA6 from constant shear-rate measurements were used to construct the Arrhenius plots (Fig. 6.5). The parameters of the Arrhenius fits[†] were found from the slope and the intercept, and are reported in Table 6.2; these can be used to calculate the viscosity of these polymers at any temperature.

[†]See Eq. 3.1 in Chapter 3.

6.1.4 Tensile tests

Typical tensile test curves performed on dog-bone samples of HFPA6, HFPA66 and a standard PA66 are reported in Fig. 6.6. Apparently, the novel HFPA66 formulated by Solvay is more rigid and less ductile with respect to a standard PA66 with similar molecular weight. Values for the ultimate tensile strength (maximum stress) and Young's modulus (calculated in the strain interval between 0 and 0.002) are reported in Table 6.3. Standard deviations of the mean values have been used to estimate the errors. The drying treatment on the pellets has the effect of increasing the tensile strength, but also reducing the ductility. This might be attributed to a higher final molecular weight in the sample processed with the dried pellets*.

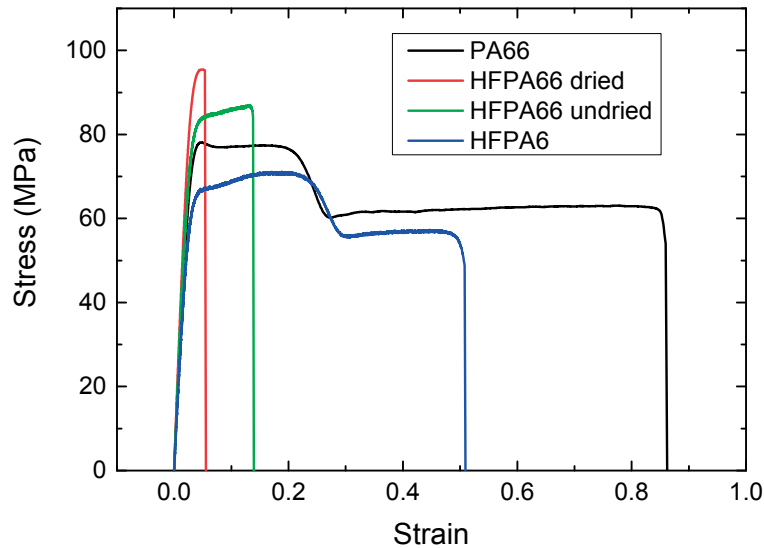


Fig. 6.6: Stress-strain curve of the tensile test on different polyamide samples.

Table 6.3: Ultimate tensile stress and elastic modulus of different polyamide samples.

	σ_t (MPa)	E (GPa)
HFPA66 dried	89 ± 4	3.49 ± 0.09
HFPA66 undried	81 ± 3	3.48 ± 0.04
HFPA6	68 ± 2	2.82 ± 0.02
PA66	78.0 ± 0.6	3.04 ± 0.02

*Two drying treatments, both at 110 °C in vacuum overnight, are considered. First, the pellets used to produce dog-bone samples, except for sample HFPA66 undried, were dried. In addition, all dog-bone samples were further dried prior the mechanical tests.

6.1.5 Dynamic Mechanical Analysis (DMA)

DMA measurements were performed on HFPA66 and HFPA6 using a single-cantilever setup. Flat rectangular samples of dimensions 70 mm × 20 mm were molded in a hot press (Fontijne) from dried pellets (110 °C under vacuum overnight) of HFPA6 and HFPA66, at temperatures of 250 °C and 290 °C, respectively. Subsequently, these were cut along the two sides so as to obtain four smaller samples of width ~ 8 mm and thickness ~ 3 mm. Span-length of the setup (between the fixed and the oscillating grips) was ~ 17.7 mm. All the dimensions were accurately measured with a caliper before each test.

A deformation of 0.01% was found to fall in the linear viscoelastic range for the two samples, both at low (0 °C) and high (200 °C) temperature. A frequency of 1 Hz was selected. Therefore, temperature ramps (heating rate 5 °C/min) between 0 and 200 °C (HFPA6) or 250 °C (HFPA66) were carried out while the samples were being submitted to oscillatory bending at a maximum of 0.01% and frequency of 1 Hz. Multiple tests were performed on different samples for each of the two polymers. All samples were further conditioned at 110 °C under vacuum overnight. Change of storage moduli with temperature for the two polyamides is displayed in Fig. 6.7. A dramatic drop is observed between 50 and 100 °C, as expected, since the T_g is about 50 °C for these materials (Table 6.1).

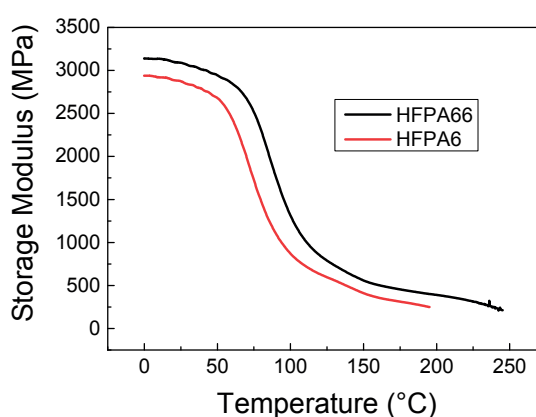


Fig. 6.7: Storage modulus evolution vs. temperature for HFPA66 and HFPA6.

6.1.6 Conclusion

Three TPs were characterized in terms of thermal, rheological and mechanical properties. These polymers have viscosity in the range 10-100 Pa s, which allows their use in mTP-RTM[‡]. HFPA66 has good mechanical properties, and it is promising for automotive structural applications, but it is still on a research phase, and its thermal stability has to be improved. HFPA6 is a commercial grade for semi-structural applications, with quite stable melt, and it is therefore chosen for the process improvement studies. PP has even lower viscosity than HFPAs, but it is not conceived for structural applications. Therefore, it was used for some preliminary impregnation tests (Section 6.2), also due to its lower melting point, which allowed to make tests with the available PET-stitched glass-fabric (G-PLY) and low-temperature consumables.

6.2 Preliminary tests

A series of preliminary tests were performed in order to identify possible issues with processing of HFTP, which helped to design and optimize a tool for mTP-RTM, define needed consumables, as well as establish laboratory procedures and samples analysis.

6.2.1 Design of mTP-RTM mold

Some preliminary tests were performed in compression molding in order to evaluate the processability of HFPAs*, helpful for the design of the setup used for mTP-RTM. Firstly, as a result of its low viscosity, polymer leakage through the space between two metal surfaces was often observed, which made difficult an exact control of fiber volume fraction. Even very narrow gaps or scratches between the mold walls were able to let fluid out of the mold. Moreover, the resin was very rigid and stuck strongly to the surface. As a consequence, demolding was sometimes tricky, with risk of sample cracking or mold damaging. These issues were taken in consideration for the mTP-RTM mold design.

[‡]See Fig. 1.3 in Chapter 1.

*A compression molding study is detailed in Appendix A.

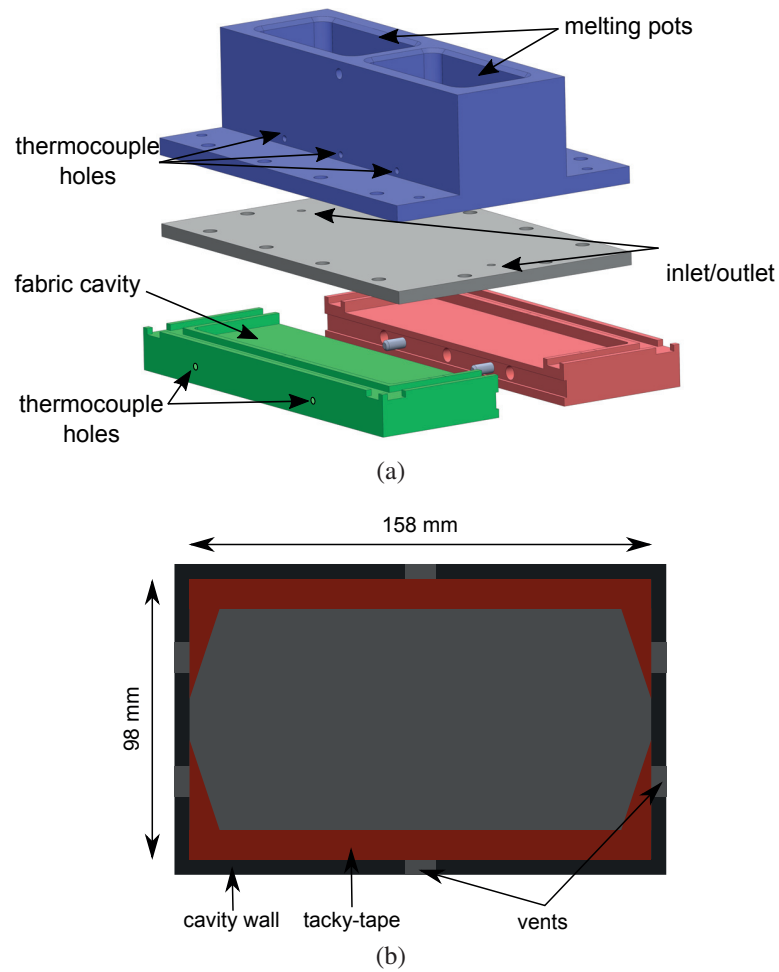


Fig. 6.8: (a) Mold assembly and (b) top-view of the fabric cavity.

The tool concept was shown in Section 3.2.3 along with the experimental procedure, while the real design, showing the assembly of the different parts, is shown in Fig. 6.8a. It can be observed that the original design was lacking of screws to control opening and closing of the gates, which were implemented only after the preliminary experiments of Section 6.2.2. This was done on the purpose of minimizing the cleaning step. A surface hardening treatment through nitrogen diffusion was performed on all the tool's parts, including the two pistons (not shown in Fig. 6.8a), so as to reduce the risk of scratching and damaging in general. In addition, high-temperature resistant (up to 500 °C) release agent XTEND™ W-4007 (Axel Plastics) was always carefully applied on the mold's surfaces once or twice before every injection, to facilitate demolding and cleaning and avoid risk of scratching.

Six vents were designed on the walls of the fabric cavity for air escaping, as shown

in Fig. 6.8b. However, this could be blocked with a sealant tape to let the air escape directly from the outlet. The sealant was often used to prevent both leakage from the cavity walls and race-tracking (i.e. preferential flow through the space between the fabric and the cavity side walls). As sealant, either TackyTape® SM5142 or SM5160, working up to 200 °C and 400 °C, respectively, were used, depending on the operating temperature.

Finally, several holes were drilled to measure the mold temperature, two on the mold cavity and three in correspondence with the melting pots.

6.2.2 Impregnation with iPP on G-PLY in two stacking configurations

Two single-side impregnation tests were performed on the two stacking configurations 5P and 5P-alt, i.e. five layers of G-PLY stacked respectively with the same lay-up sequence or with an alternate fashion[†], with polypropylene Borflow™ HL512B at 200 °C (viscosity ≈ 20 Pa s). The pellets were placed in one of the two melting pots, and the tool was heated in the oven and transferred to the press once the temperature on the pots had reached 200 °C. A force of 1.1 kN was applied on the piston to force the impregnation at a constant inlet pressure of 3.6 bar. After 450 s of injection, the cooling was started, and the plates demolded at room temperature.

The void content was measured by burn-off method on 8 different points along the flow direction, from the inlet to the outlet. The void content distribution along the flow direction is displayed in Fig. 6.9. Firstly, it was noticed during the experiment that, impregnation time and temperature being equal, the resin could reach the outlet in the 5P-alt, but not in the 5P, as a consequence of the former's higher permeability (Section 4.1). This is reflected in the void content distribution (Fig. 6.9), which is higher for the 5P, especially close to the outlet where a value around 42% is found, against 20% for the 5P-alt.

Secondly, the void content is always very high, even for sample 5P-alt, for which the resin could reach the outlet. This can be explained in the light of the considerations made in Chapter 4. The channels in the structure of the G-PLY fabric are conceived to be large to allow a fast flow of the resin throughout the mold. As a result, however, a

[†] See Fig. 4.1 and Table 4.1.

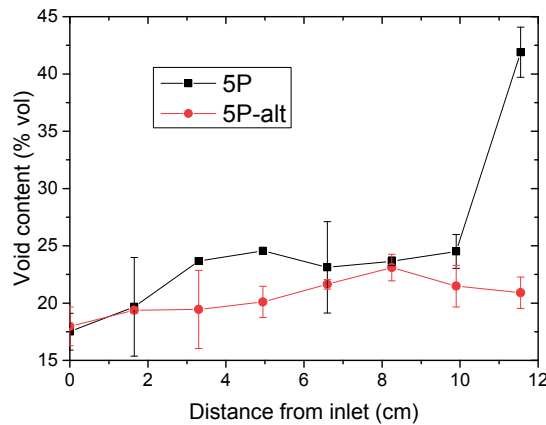


Fig. 6.9: Void distribution on two plates of G-PLY, with stacking architecture 5P and 5P-alt, impregnated with iPP (Borflow™ HL512B).

large unsaturated area was left behind, which resulted in a low degree of impregnation inside the denser tows. Once the resin had reached the outlet, it continued to flow in the longitudinal channels, where it faced a lower resistance, and only partly in the denser tows. Therefore, a strategy analogous to the "closed-outlet" one investigated in Chapter 5 could be applied to mTP-RTM to optimize the impregnation by forcing the resin to flow radially from the channels to the tows. The outlet should be closed while continuing injection at the inlet, in order to saturate any residual impregnation.

Optical microscopy images seem to confirm these observations (Fig. 6.10). The cross sections are taken transversely to the resin flow at three different locations, namely close to inlet, in the middle, and close to outlet. The tows in the flow direction are quite dry in the middle, which proves that the resin, which flows radially from the channels, has penetrated only partially. It should also be noticed that the void content is so high that the epoxy resin used for embedding has partially impregnated the dry fibers, which makes quite difficult any quantitative analysis.

Another observation should be made on these micrographs. Very large voids are clearly visible in the inter-tow channels, and these also contribute to the high void content measured. These voids are likely to be air bubbles entrapped in the polymer melt. Bubbles might have formed as a consequence of air entrapped between the polymer pellets during the melting stage that are then carried inside the fabric during the injection, forming macro-porosity in the matrix. Large voids may form during solidification, as a result of crystallization shrinkage of the PP that is not fed, as no pressure was applied on in during cooling. To avoid air entrapment during pellets melting, a pre-compaction

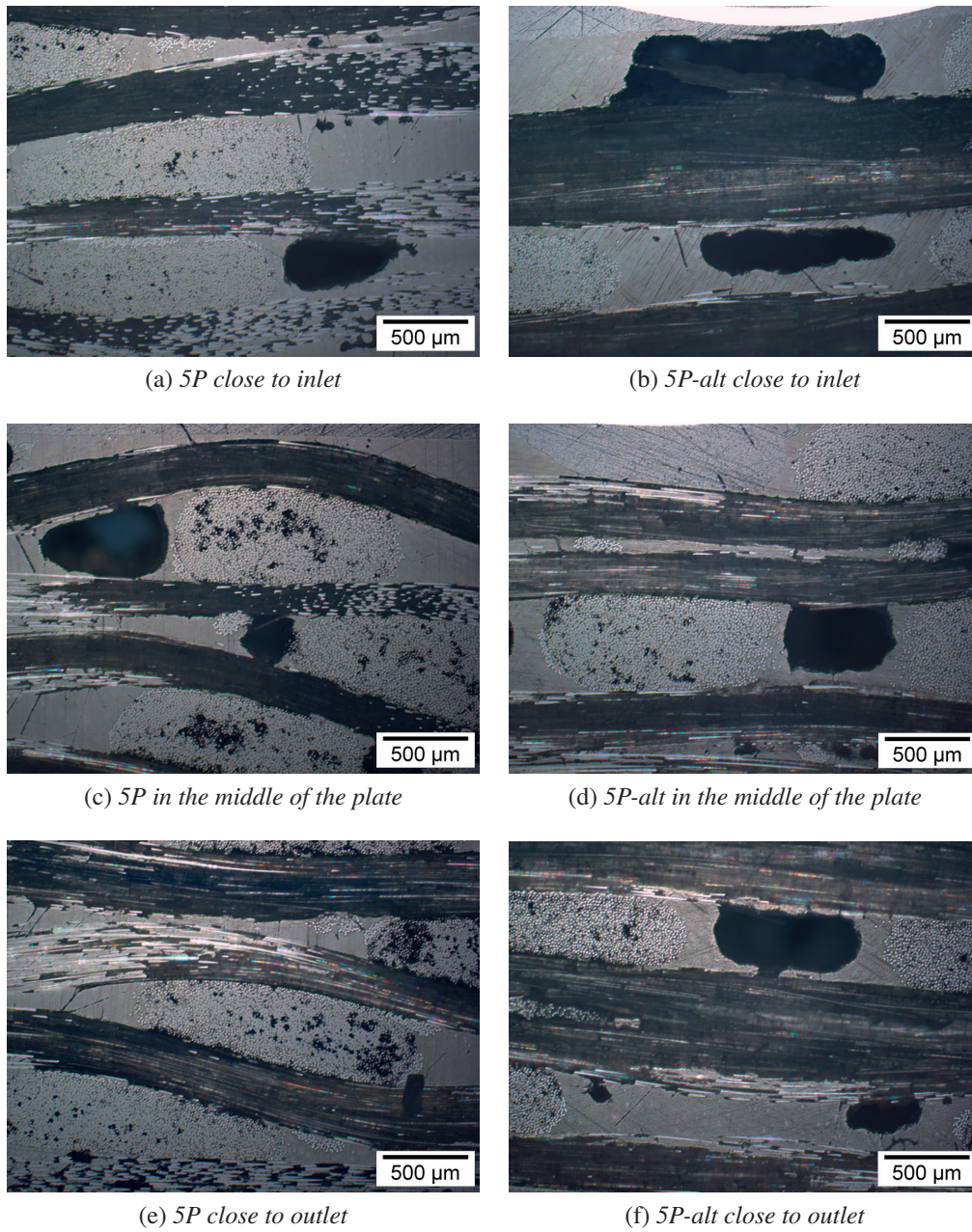


Fig. 6.10: Optical microscopy images of transverse cross section for the two plates 5P and 5P-alt at three different position (close to inlet, middle of the plate, close to outlet).

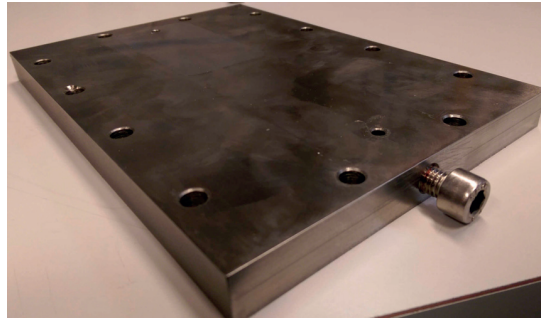


Fig. 6.11: Middle plate of the mTP-RTM modified with a screw, which allows to control opening/closing of the inlet/outlet.

step is necessary. For this purpose, a modification was made to the middle-plate of the mold (Fig. 6.8), by adding a screw to the two gates[‡]. In this way, the gate can be closed, allowing the pellets to be compacted by the piston. Regarding the air bubbles that are entrapped during the impregnation, a vacuum should be pulled from the outlet before the injection. With this modification, a vacuum-plug can be simply screwed at the outlet. The modified setup was used for the experiments in the next section.

6.2.3 Impregnation strategies of G-PLY with iPP

A series of tests was then carried out on the mTP-RTM mold using iPP Borflow™ at 200 °C and G-PLY glass fabric in the 5P-alt configuration, i.e. five layers of G-PLY with alternate stacking sequence in 3 mm thick cavity for an expected fiber volume fraction of 46%*. The five different impregnation strategies listed in Table 6.4 were compared. In four tests, vacuum was pulled from the outlet prior and during the injection, while in the fourth the polymer was injected from two sides (double inlet). The three tests under vacuum differed in the injection pressure, impregnation time before cooling, and presence of a saturation step. The concept is the same as the one described in Section 5.3.3 for injection with closed outlet and fluid continuously injected in the mold cavity.

A typical temperature-cycle from room temperature for this type of process is illustrated in Fig. 6.12. At the beginning (pre-compaction+vacuum step), the inlet gate is closed, while the outlet is connected to a pump. A constant force is applied on the piston to compact the melt before the injection and remove the air bubbles. At the same time,

[‡]The two screws to control opening and closing of the gates were already depicted in Fig. 3.6 in Chapter 3.

*See Fig. 4.1 and Table 4.1.

the pump at the outlet is switched on to pull out the air from the cavity. After this step (1 to 2 min), the inlet is opened and the melt polymer is injected (impregnation step). Once the resin reaches the outlet, this is closed while injection goes on (saturation step). Finally, water cooling is activated. In test #4 (Table 6.4) both gates shown in Fig. 3.6 were used as inlets, meaning that flow distance is halved. Therefore, pressure difference being equal, impregnation time should be reduced by a factor 4, as it is linearly dependent on the square of flow distance[†]. Two flow fronts meet in the middle of the mold cavity, and air is escaped at atmospheric pressure from two vents in the middle (Fig. 6.8b).

Table 6.4: Impregnation strategies of G-PLY with iPP.

#	Conditions	Inlet pressure	Impregnation time	Saturation time
1	vacuum	3.6 bar	5.5 min	5 min
2	vacuum	7.1 bar	1.5 min	5 min
3	vacuum	3.6 bar	5 min	-
4	double inlet	3.6 bar	3 min	-
5	vacuum	14.2 bar	40 s	5 min

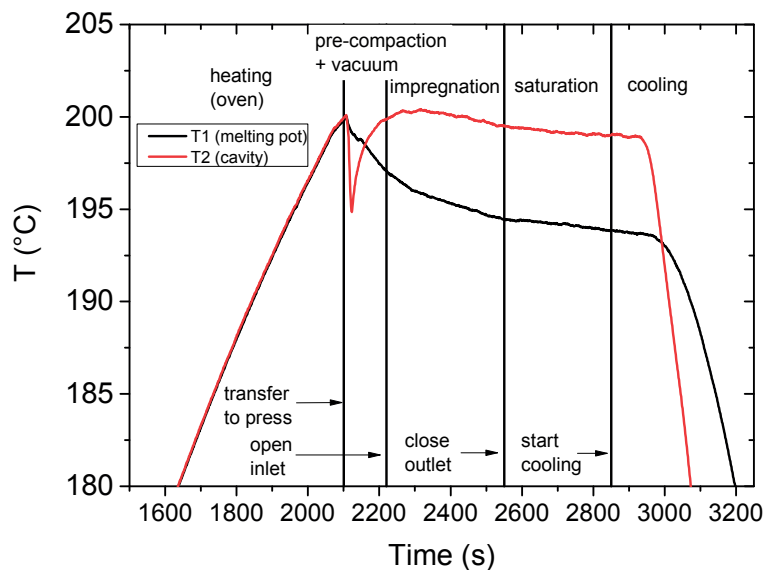


Fig. 6.12: Temperature cycle for an injection with application of vacuum and saturation step.

Four plates were produced out of tests from #1 to #4. Sample #5 was discarded because excessive pressure caused fabric displacement. This gives an upper limit for applicable pressure for this fabric configuration. Void content and distribution on sample plates from #1 to #4 was analyzed by burn-off method and optical microscopy on small

[†]Refer to Eq. 2.17 in Chapter 2.

samples cut off at different locations, as depicted in Fig. 6.13. Three samples equally distant from the inlet were averaged at four or three different locations for single and double inlet injections, respectively. Resulting void content vs. distance from inlet is reported in Fig. 6.14. Overall, a lower void content can be observed compared to the previous tests (Section 6.2.2), with single inlet and no vacuum. Remarkably, sample #2 had lower standard deviations and more constant void content, meaning that a higher pressure allows a more homogeneous impregnation throughout the plate. Sample #4 had higher void content in the middle of the plate, where the two flow fronts met, than closer to the two gates. Comparison of sample #1 and #3 suggests that the addition of a saturation step might help to slightly reduce void content. This is visible at locations closer to the inlet, suggesting that longer time for this step might be required. However, no major differences on the overall void distribution can be observed between the four strategies. It is likely that a certain degree of porosity is caused by shrinkage related to crystallization during cooling. In thermoplastic molding an external pressure is continuously applied on the polymer during cooling, so as to compensate for the shrinkage and prevent formation of porosity. In these tests, the inlet was closed right before cooling activation, and therefore no active pressure was being applied on the polymer during cooling. We can infer that crystallization porosity masked porosity related to flow propagation, and that inlet should be kept open so that polymer is kept under pressure during cooling.

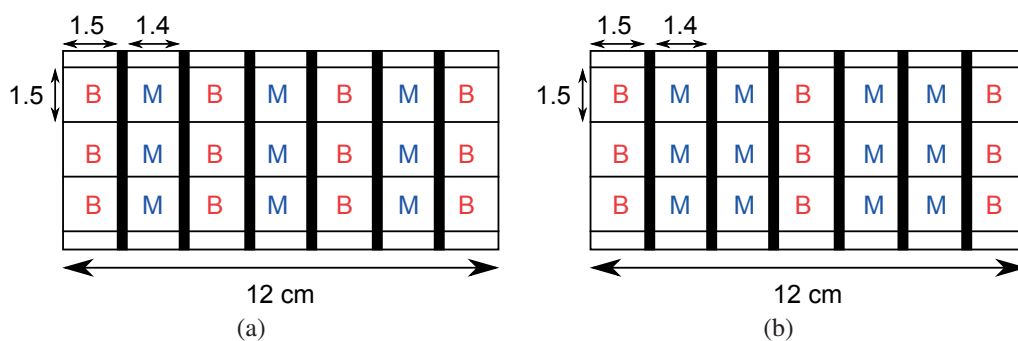


Fig. 6.13: Scheme of cut-off samples for burn-off analysis (B) and optical microscopy (M), for (a) single and (b) double inlet injections (dimensions in cm).

Samples labeled as M in Fig. 6.13 were embedded in epoxy resin dyed with Rhodamine B, so that the residual porous volume got filled with this fluorescent phase and allowed better contrast with the translucent PP matrix. Imaging of cross-sections was

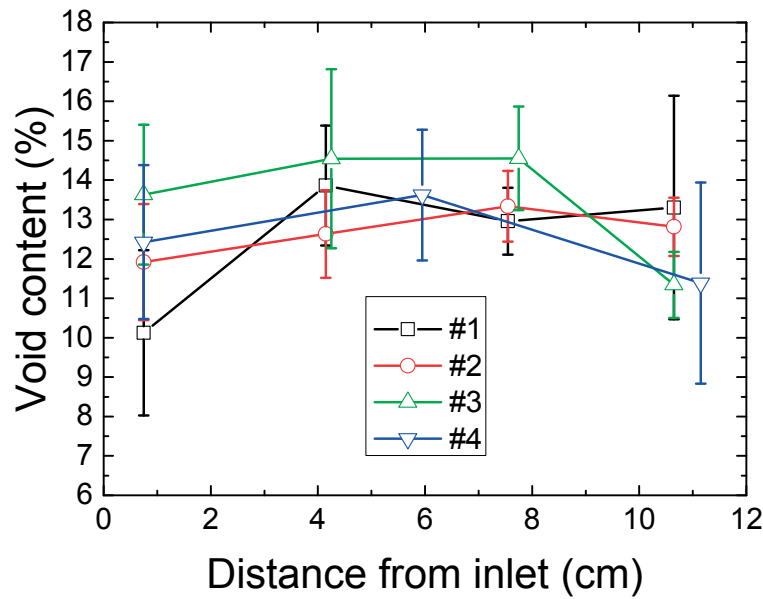


Fig. 6.14: Void distribution along the plate; each point is averaged on three locations equally distant from the inlet. (Refer to Table 6.4 for the # number)

done using a fluorescence microscope Leica DMI4000 using a blue filter; some examples for samples #1 and #3 are reported in Fig. 6.15. Macro-voids are visible in the inter-tow space, whereas the matrix appears to have infiltrated well within the fiber bundles. However, the brittleness of this polymer caused cracking to propagate through the fiber bundles, affecting their integrity. In other cases this caused detachment and cracking at the border of the bundles, which is evident from the fact that fluorescence is brighter at the border than inside the bundle. It should be noticed that this fabric has a sizing compatible with polyamide, which is highly hydrophilic, while polypropylene is rather hydrophobic. Hence, interface quality is not expected to be optimal.

6.2.4 Impregnation of G-PLY with HFPA6

Two more plates were produced with the 5P-alt fabric configuration[‡] and using HFPA6 as impregnating matrix. The two tests were performed with the "closed outlet" strategy described previously, i.e. with application of vacuum at the outlet and a saturation step at the end. The two tests differed in the temperature, which was set to 250 °C and 280 °C (Table 6.5). In spite of a decrease of viscosity with temperature, the time for the polymer to reach the outlet was observed to be longer at 280 °C. This longer impregnation

[‡]See Fig. 4.1 and Table 4.1.

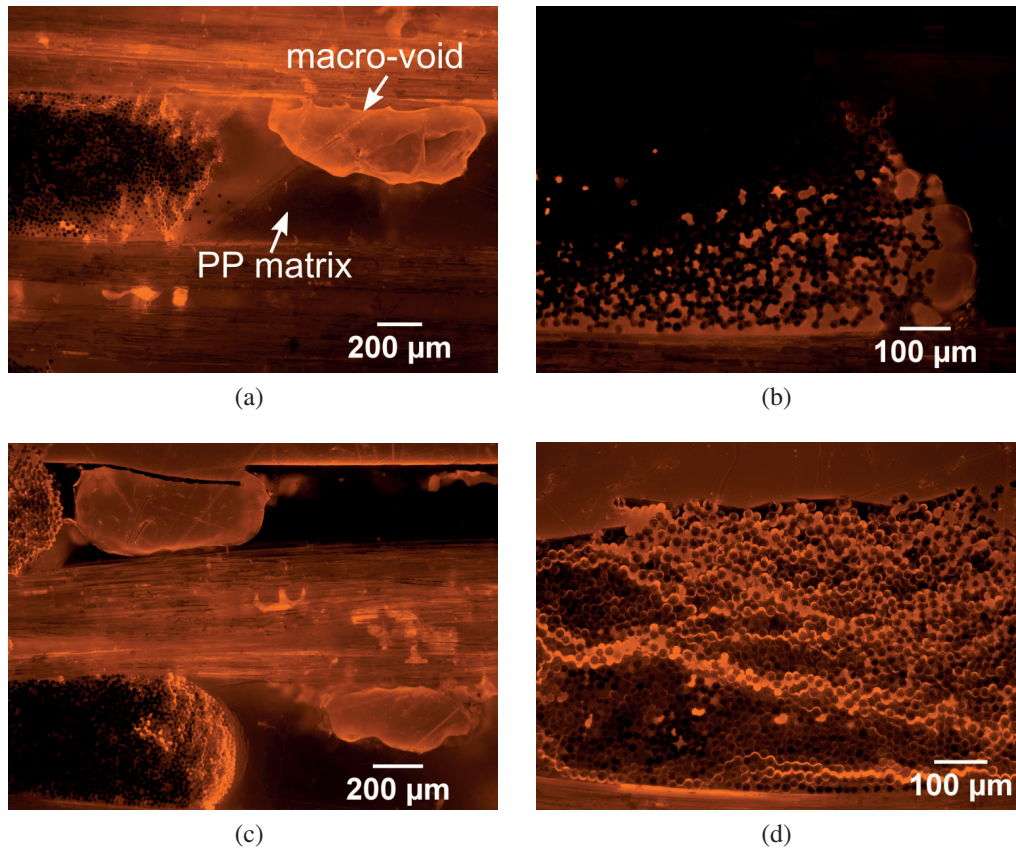


Fig. 6.15: Fluorescence micrographs for samples #1 (a-b) and #3 (c-d).

time is attributed to a reduction in the fabric permeability, as the channel-wise structure of the fabric was destroyed, because of polyester stitches degradation at this temperature. This is in agreement with void distribution measured from burn-off method shown in Fig. 6.16. Lower void content was observed for the plate produced at lower temperature, where the channel-wise structure of the preform was still intact. Void content lower than 10% on sample #6 shows that the combination of preform with channels, air evacuation and saturation step is promising for the production of small plates. The residual void content can be attributed to both crystallization shrinkage and high resin viscosity ($\sim 46 \text{ Pa s}$ at 250°C), which results in incomplete tow impregnation. The former issue can be overcome by application of pressure on the polymer at the inlet, as discussed in the previous section. The resin viscosity can be lowered by increasing processing temperature; this would require to have a fabric with stitches with higher thermal stability, such as polyphenylene sulfide (PPS) or even glass stitches.

Table 6.5: Impregnation with HFPA6 and 5P-alt.

#	Conditions	Inlet pressure	Impregnation time	Saturation time	Temperature	Viscosity
6	vacuum	3.6 bar	2 min	5 min	250 °C	46 Pa s
7	vacuum	3.6 bar	6.5 min	5 min	280 °C	26 Pa s

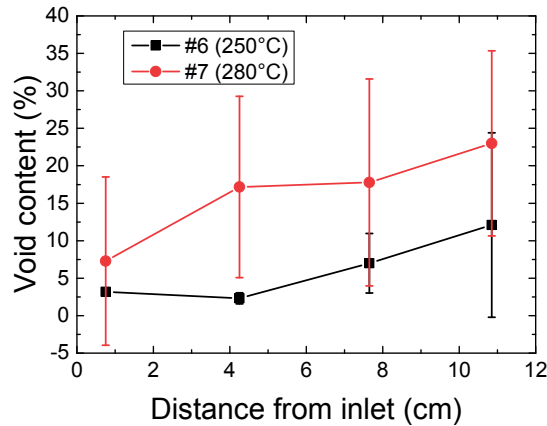


Fig. 6.16: Void distribution along the plate for samples referred in Table 6.5.

6.3 Strategies for faster impregnation with HFPA6

A second series of tests was performed using various preforms and test conditions in order to find an optimum between impregnation time and quality. The same temperature was used in all the tests (around 280 °C) and pressure was maintained on the polymer during cooling, in order to feed crystallization-shrinkage as much as possible. Unlike for preliminary tests (where the cavity was set to 3 mm thick), fabric cavity thickness was set to 5 mm, so as to explore the possibility of using spacers as flow-enhancers similarly to what has been shown in Chapter 5.

6.3.1 Mold modification

For these tests, the mold was improved by introducing heating cartridges in the middle plate, which allowed to reduce the heating time from room temperature to 280 °C to less than 20 min. Three electrical heating cartridges of 10 W power each were installed in the middle plate of the mold (Fig. 6.17a and b). Thereby, the mold could be placed directly in the hot press; heating from room temperature was performed simultaneously from the press plates and the electrical cartridges in the middle plate. Heat distribution recorded with an infra-red camera (Fig. 6.17c) was observed to be quite homogeneous. During all

tests, the temperature was monitored on three different locations by means of three thermocouples, namely one at the melting-pot and two right below the cavity (Fig. 6.17b). However, only temperature data from one of the two thermocouples below the cavity was recorded. When temperature reached the desired value (between 280 and 285 °C) both at cavity and pot locations, the inlet screw was opened and the injection started. When cooling was started, the heating cartridges were switched off. The inlet was always kept open during the cooling, so as to keep the solidifying melt under pressure, in order to feed crystallization shrinkage. Indeed, it was verified with IR camera that cooling takes place directionally and starting from the bottom (Fig. 6.17d); therefore, the plate solidifies from the bottom to the top, and the melt polymer is actually under pressure during cooling. Temperature evolution for a typical test is shown in Fig. 6.18.

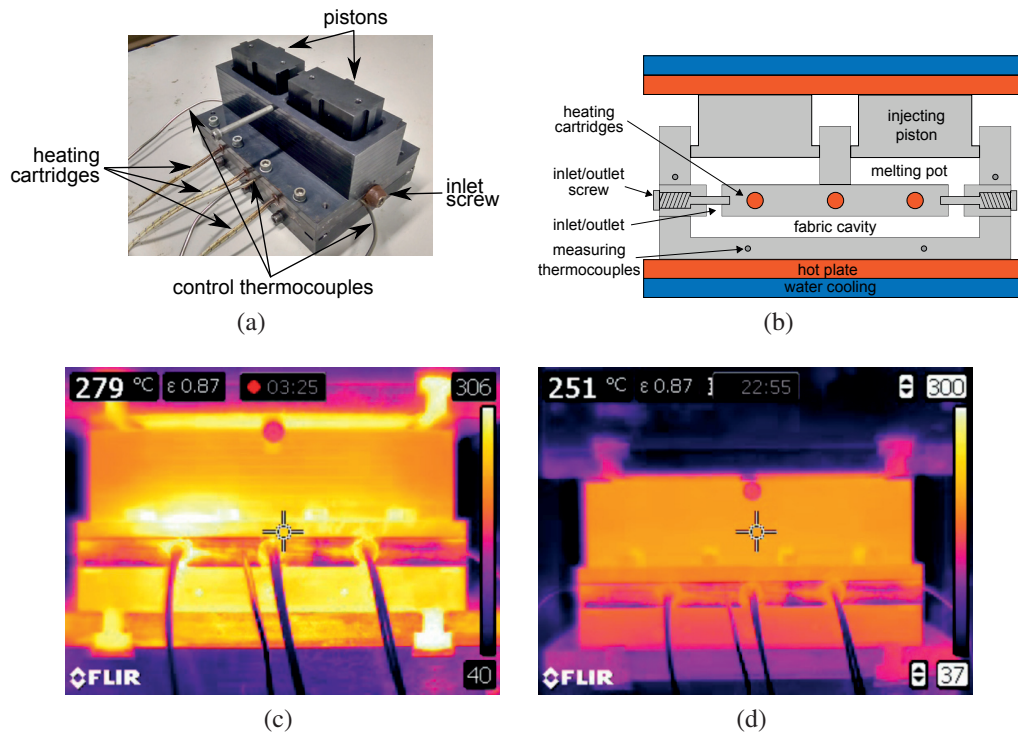


Fig. 6.17: (a) Picture of the mold after modification with heating cartridges and inlet screw, and side-view of the mold in a hot press in a schematic representation (b) and with IR camera during heating (c) and cooling (d) (the temperature scale on the right is in °C, while the temperature on the top-left refers to the center of the image).

6.3.2 Preforms

The three different types of preforms used for this study are schematically depicted in Fig. 6.19. The fabrics were manually cut with a roll-cutter to rectangles of sides

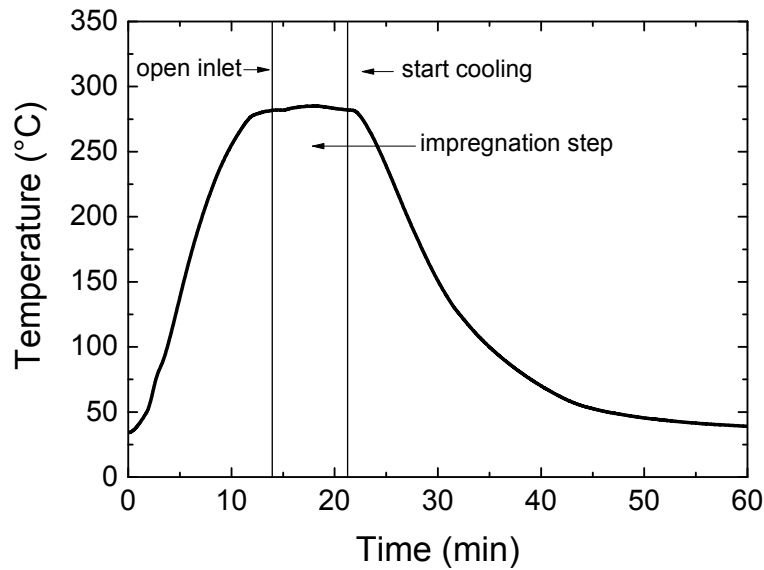


Fig. 6.18: Typical temperature evolution measured at the mold cavity.

7.5 × 11cm. G-WEAVE and G-PLY glass fabrics have been introduced in Section 3.1.2 and extensively discussed in Chapter 4. However, the G-PLY used here differs in that it contains glass stitches rather than polymer ones. In addition, the areal weight is higher (960 g/m², with 480 g/m² in both warp and weft directions) and, consequently, gaps width is narrower (ca. 2 mm). In all cases, the cavity thickness was set to 5 mm, which led to a glass fiber volume fraction of around 45%. "G-WEAVE" (Fig. 6.19a) and "G-PLY (GS)" (Fig. 6.19b) preforms consisted in respectively ten and six plies all laid up with the same orientation. In "G-WEAVE + spacers" preforms (Fig. 6.19c), rigid spacers were inserted between the fifth and sixth layers of G-WEAVE in order to create gaps of 8 mm width. Specifically, the spacers were cylindrical rods of 1.4 mm in diameter made of polyether-ether-ketone (PEEK) reinforced with 52%vol of continuous carbon fibers. A picture of the rods placed on top of the fifth layer during preform preparation is reported in Fig. 6.19d.

6.3.3 Experiment: plates production and analysis

Table 6.6 lists nine impregnation tests performed with the three preforms described in Section 6.3.2. In "standard" tests, the melt is injected under constant pressure at the inlet and flow propagates unidirectionally with a "slug-flow" morphology (Fig. 6.20a).

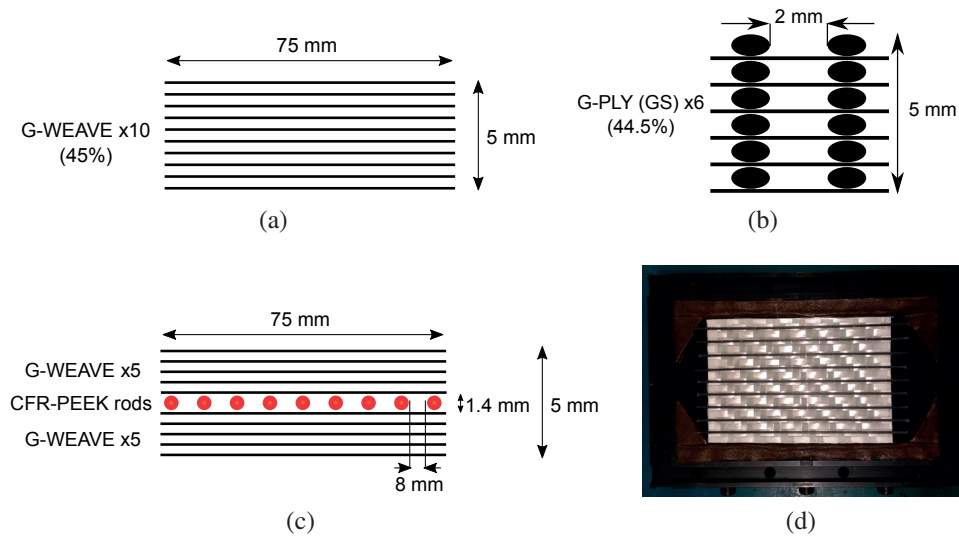


Fig. 6.19: Schematic structure of the preforms (a) G-WEAVE only, (b) G-PLY and (c) G-WEAVE+spacers, and (d) top-view of CFR-PEEK rod spacers placed on top of the fifth layer of G-WEAVE.

Following Darcy's law for 1D-flow, expected impregnation time is

$$t = \frac{\eta(1 - V_f)}{2K\Delta P} L^2, \quad (6.2)$$

where η is polymer melt viscosity, V_f the glass fiber volume fraction, K the preform permeability, ΔP the applied pressure difference between inlet and outlet, and L the length of the preform. In "double inlet" tests, the polymer is injected from both gates, resulting in two flow fronts meeting in the middle of the cavity. From Eq. 6.2, a reduction of a factor 4 to the impregnation time is expected, since flow distance is halved. In preforms which exhibit a pronounced dual-scale of porosity, like "G-WEAVE + spacers" and "G-PLY" preforms, the resin reaches the outlet leaving behind a large degree of unsaturation. Therefore, a "saturation step" is added in order to force the resin to saturate the cavity (Fig. 6.20b). This is achieved by closing the outlet once it is reached by the resin and by continuing to inject resin at the inlet. In "vacuum + free flow" tests, a vacuum pump is connected to the outlet so as to pull out the air from the cavity before and during the injection, but no saturation step was performed*. Conversely, in "vacuum + saturation" tests, the saturation step was performed. During each test, impregnation

*The "vacuum + saturation" strategy is analogous to the "closed outlet" strategy of Chapter 5.

was carried out at constant pressure applied at the inlet, except in one case (test 2-6), for which the pressure was increased during the saturation step.

Table 6.6: List of mTP-RTM tests performed with HFGPA6 on three different preforms and with different impregnation strategies.

#	Preform	Test condition	Flow time (min)	Saturation time (min)	Inlet pressure (bar)
2-1	G-WEAVE	standard	15	-	3.6
2-2	G-WEAVE	standard	15	-	1.6
2-3	G-WEAVE	standard	45	-	1.6
2-4	G-WEAVE + spacers	vacuum + free flow	15	-	3.6
2-5	G-WEAVE + spacers	vacuum + saturation	1	6	3.6
2-6	G-WEAVE + spacers	vacuum + saturation	1	6	7.1, up to 28.6
2-7	G-PLY (GS)	vacuum + saturation	4	3	3.6
2-8	G-PLY (GS)	double inlet	2.5	-	3.6
2-9	G-PLY (GS)	vacuum + saturation	1	1.5	7.1

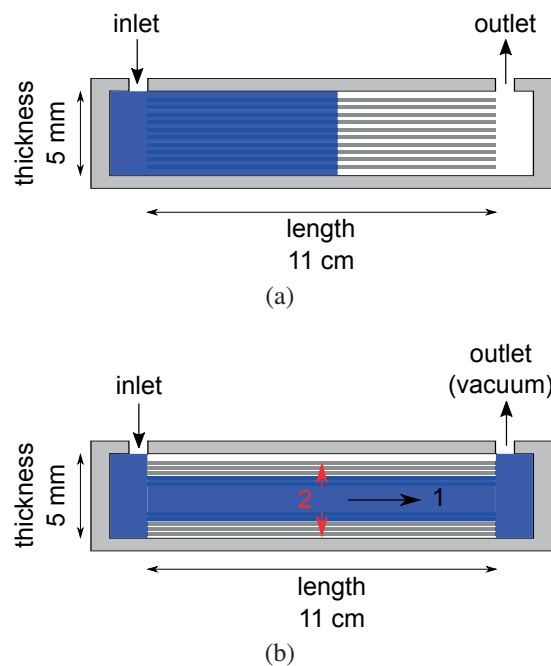


Fig. 6.20: Schematic side-views of impregnation morphology for (a) "standard" in-plane flow and (b) "vacuum + saturation" dual-scale flow; in the latter, 1 and 2 correspond to the "flow step" and "saturation step", respectively.

Samples were cut with a diamond blade as depicted in Fig. 6.21 from plates which had a good enough degree of impregnation at the macro-scale (namely for samples 2-3, 2-5, 2-6, 2-7, 2-8, and 2-9) for analysis by optical microscopy for microstructural observation, matrix burn-off test for void content and 3-point bending test for flexural modulus, following the experimental methodology introduced in Section 3.2.3. For flexural

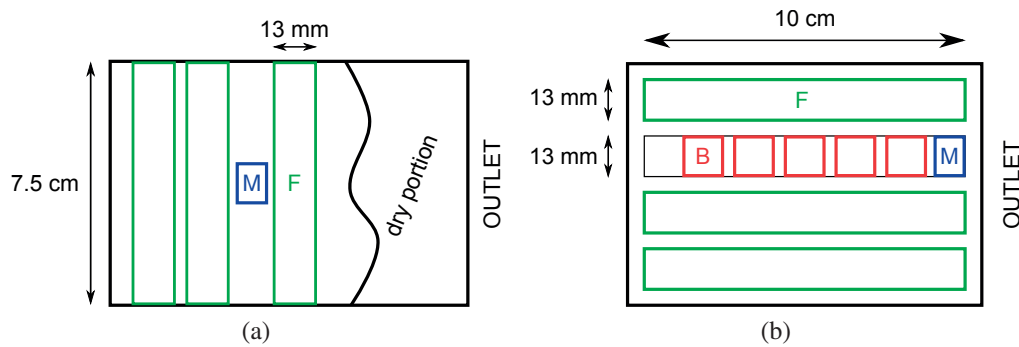


Fig. 6.21: Schematics of samples cut from plates for flexural test (F, green), burn-off (B, red) and optical microscopy (M, blue) analysis, and (a) for sample 2-3 and (b) for samples 2-5, 2-6, 2-7, 2-8, 2-9 (burn-off was performed only on G-PLY samples).

tests, three beams of length between 7.5 and 10 cm and width of 13 mm were cut from each plate along the flow direction, except for sample 2-3[†], for which the resin never reached the outlet, as will be shown in the results. Flexural tests were carried out in 3-point-bending configuration using a span-length of 6 cm for all the tests, which results in a span-length-to-thickness ratio of 12:1. Displacement speed was set to 1 mm/min and a load-cell of 10 kN was used for force measurement. Only the elastic regime was investigated. The force-displacement curve was transformed into a stress-strain curve using Eqs. 3.9 and 3.10 and flexural modulus was defined as the slope of this curve between strain 0.006 and 0.008. Burn-off tests were made only for G-PLY plates (2-7, 2-8 and 2-9) on square samples of side 13 mm cut from different locations of the plates. The samples' dimensions, sides and thickness, were accurately measured respectively with a caliper (0.01 mm accuracy) and a micrometer (0.001 mm accuracy). At least four measurements were made for each dimension, and the error was calculated as the standard deviation. The error on the void volume fraction was then propagated according to Eqs. 3.11 and 3.12, discarding errors on mass and density. Finally, optical microscopy was used to observe the impregnation at the micro-scale for the cross-section transverse to the flow direction and near the outlet, with magnification from 5x to 500x.

[†]For this sample, cutting scheme is shown in Fig. 6.21a.

6.3.4 Results and discussion

Macro-scale impregnation

Photographs of the produced plates are shown in Fig. 6.22. Bare eye-observation is an immediate and useful way to verify the influence of process parameters (pressure, temperature and time) and preform architecture (woven, woven with spacers, and channel-wise non-crimp fabric).

Firstly, the effect of pressure can be observed. G-WEAVE samples are not capable of sustaining too high pressure, as a melt pressure of 3.6 bar was already too high and caused visible fabric displacement (sample 2-1). Reducing the pressure to 1.6 bar prevented fabric deformation, but resulted in very long impregnation time, and even after 45 min the resin could not reach the outlet; in fact, from Eq. 6.2 an impregnation time longer than 2 h is expected for G-WEAVE (specifically 139 min using $V_f = 0.45$, $L = 11$ cm, $K = 1.7 \cdot 10^{-10} \text{m}^2$ *, $\Delta P = 0.6 \text{ bar}$ †, $\eta = 26 \text{ Pa s}$). Hence, even considering a significant deviation from this theoretical value (which is likely to arise from errors in local temperature measurement, and consequently in viscosity, and pressure calculated from the press force and piston area, as well as from actual fabric permeability), it is clear that the combination of high viscosity and low permeability limits the applicable pressure. It should be noticed that short cycle-time is not only required to achieve high-volume production, but also to prevent detrimental effects on the polymer properties (thermal degradation or condensation‡).

The introduction of spacers in the G-WEAVE preform modifies the architecture in such a way that it is capable of sustaining a much higher pressure (samples 2-4, 2-5 and 2-6), up to 28.6 bar. This can be explained both by the presence of longitudinal channels and by the higher compaction applied on the fabric against the mold's upper and lower walls. The presence of flow-enhancing channels is responsible for strong dual-scale flow, similarly to what was observed in permeability experiments of previous chapter on G-PLY (Fig. 4.11) and G-WEAVE + spacer (Fig. 5.12). Here it is evident on sample 2-4, for which the resin, after having quickly reached the outlet (in about

*See Fig. 4.5 in Chapter 4.

†Obtained subtracting 1 bar from the inlet pressure shown in Table 6.6.

‡See Section 6.1.

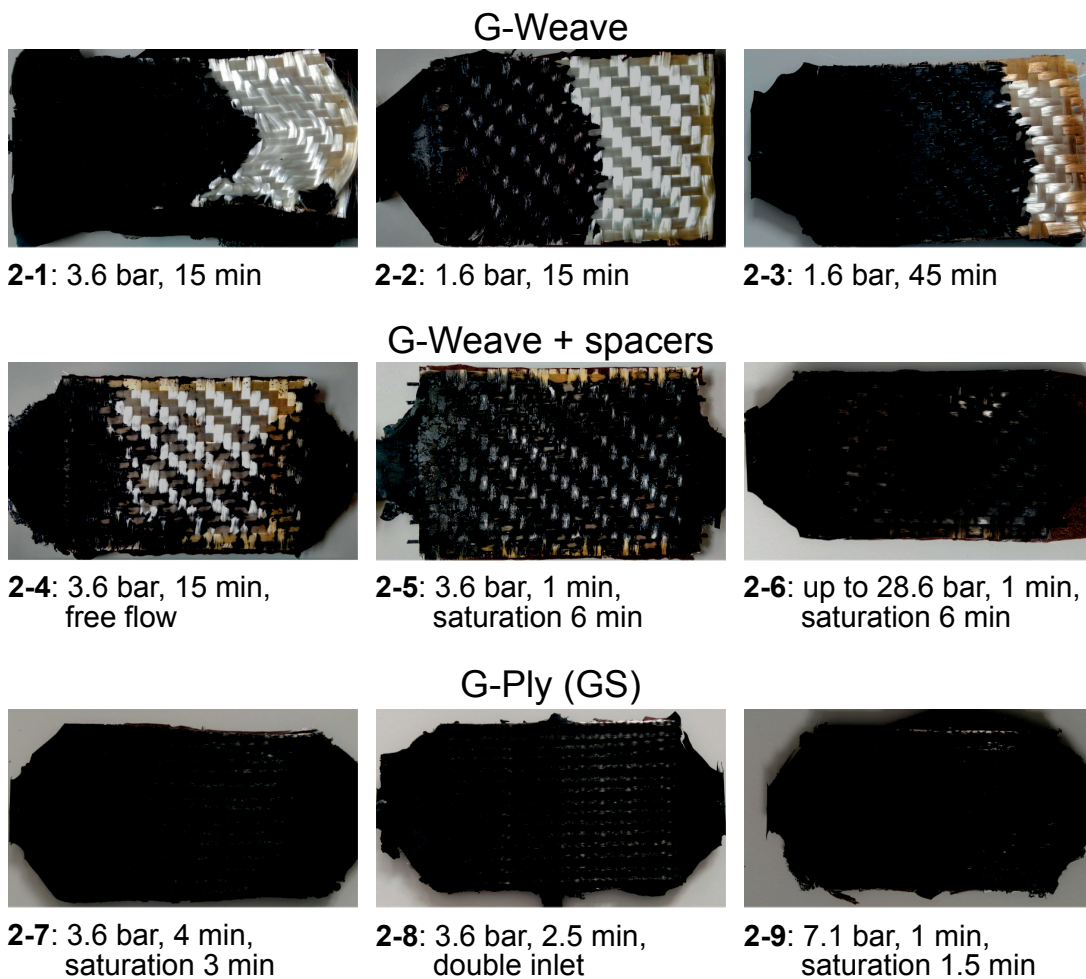


Fig. 6.22: Top-side view of the plates produced from the tests listed in Table 6.6; flow direction from left to right (both sides for sample 2-8); plates dimensions of 11×7.5 cm.

1 min), was let to flow out freely. As a consequence, the preform remained distinctly unsaturated even after 15 min of injection. Conversely, when the outlet was closed to force saturation (sample 2-5) a much better impregnation was achieved in half the time (7 min). A further improvement was obtained with the same type of cycle (1 min flow + 6 min saturation) by applying an incremental pressure during the saturation step (up to 28.6 bar), though few dry spots were still visible on the surface. Nevertheless, these three tests confirmed the efficacy of using spacers to achieve a better impregnation in shorter time also in mTP-RTM.

An improvement in cycle time was also observed for the G-PLY (GS), which is not astonishing in light of previous results that showed that this type of fabric has one

order of magnitude higher permeability compared to G-WEAVE thanks to its channel-wise structure*. Similarly to "G-WEAVE + spacers", G-PLY allowed to apply a higher pressure. However, a slight deformation of the fabric was observed on sample 2-9 (on the bottom side of the plate, not shown in Fig. 6.22). Thus, 7.1 bar can be considered as the upper limit for this fabric. Finally, the shortest impregnation time was observed for the double inlet injection (sample 2-8). In this case, two flow-fronts met in the middle of the cavity and escaped from the two side-vents, and no vacuum or saturation step could be applied. In this type of tests, if one of the flow-fronts runs faster (for instance because of non-homogeneous temperature) it might occur that it reaches the vents sooner and slow-down the opposite flow-front, resulting in a high degree of unsaturation. Hence, a particular care should be taken in multiple inlet injections to guarantee homogeneous thermal distribution, inlet-opening synchronization and inlets/vents location.

Micro-scale impregnation and residual porosity

The impregnation at the micro-scale for samples 2-3, 2-5 and 2-6 can be observed in the optical micrographs in Fig. 6.23, which shows the cross-sections transverse to the flow direction for different magnifications. Sample 2-3 had quite a large amount of inter-bundle macro-voids, both in the bulk (Fig. 6.23a) and on the surface (Fig. 6.23b) of the plate. However, only little intra-bundle porosity was observed (Fig. 6.23c-e). In samples 2-5 and 2-6, the presence of the spacers (CFR-PEEK rods visible in Fig. 6.23f and k) was responsible for large matrix-rich zones, which correspond to the meso-channels in the preform. A certain degree of porosity was observed in the spacers, but this has to be ascribed to the CFR-PEEK rods manufacturing process. In sample 2-5 both macro- and micro-voids were observed (Fig. 6.23g-j). In sample 2-6 few macro-voids were mainly observed on the surface (Fig. 6.23l), whereas the resin appeared to have well filtrated inside the bundles (Fig. 6.23m-o), probably as a result of the higher applied pressure.

The micrographs of the cross-section transverse to the flow direction for samples 2-7, 2-8 and 2-9 are given in Fig. 6.24. The channel-wise architecture is clearly visible from Fig. 6.24a, f and k. Sample 2-7, for which total impregnation time was the longest

*See Chapter 4 and [162]; however it should be remembered that the G-PLY (GS) used in the present chapter has a slightly different structure, notably a higher areal weight and glass stitches instead of PET ones.

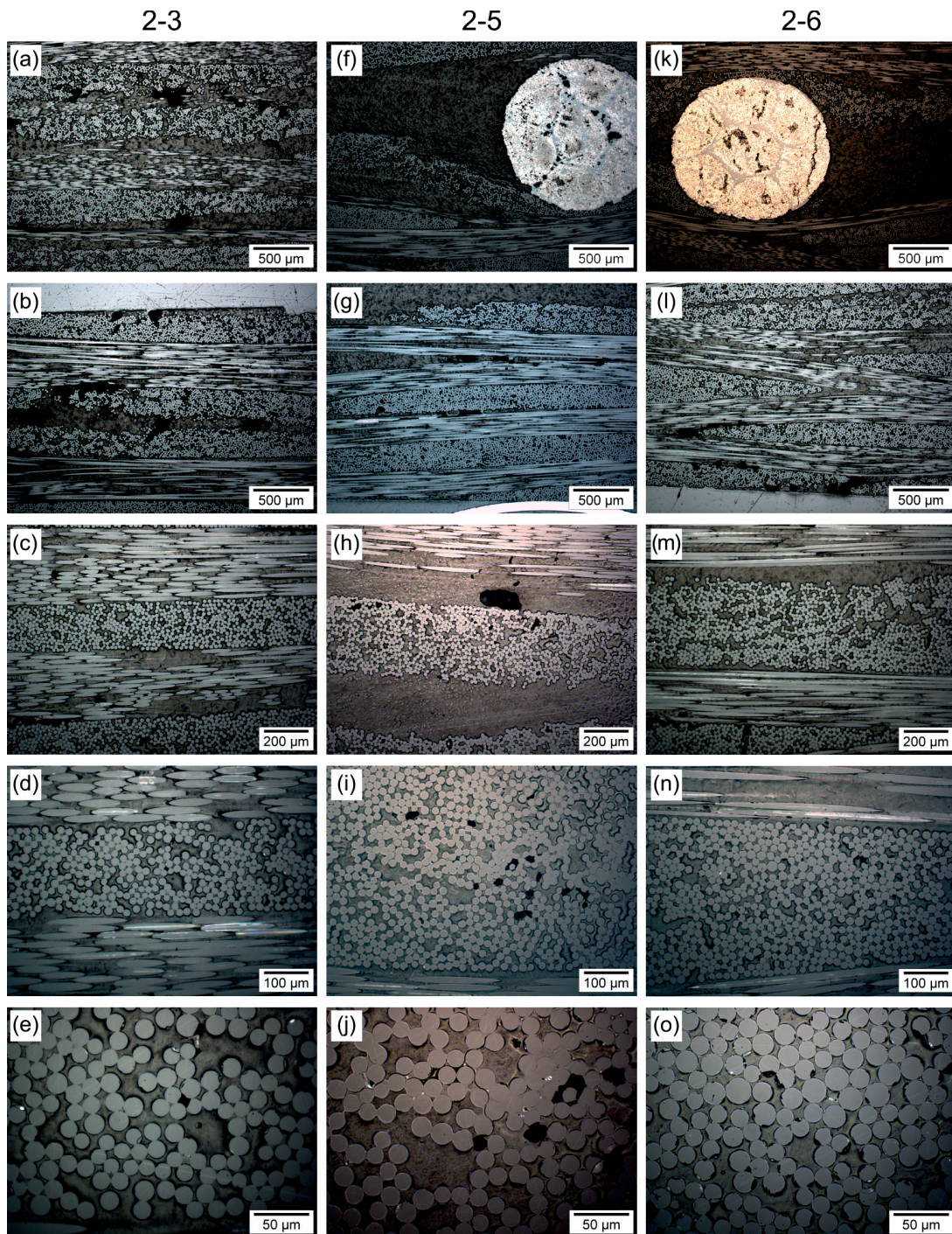


Fig. 6.23: Optical micrographs of the cross-sections transverse to flow direction and close to the outlet for plates 2-3, 2-5 and 2-6.

(7 min), appears to have the least void content, both in the intra- and inter-bundle regions (Fig. 6.24a-e). Both samples 2-8 and 2-9 had macro-voids in the inter-bundle regions (Fig. 6.24f, g, k and l), and more than all the other samples in this series of tests. It can be inferred that flow time was too short to allow migration of bubbles to the outlet, which therefore remained entrapped. In addition, partial unsaturation of the intra-bundle regions was also observed (Fig. 6.24g-j and l-o).

These visual observations were also reflected in the percentage of void volume measured by burn-off method, keeping in mind that optical microscopy was done on a sample located near the outlet (Fig. 6.21). The variation of void content along the flow direction is displayed in (Fig. 6.25). First, with reference to Figs. 6.14 and 6.16, a comparison with preliminary tests reveals that in this second series of tests a much lower overall void content (in the order of 4%) was obtained and in shorter cycle time, thanks to improved process strategies and fabric preform. Secondly, it can be noticed that in sample 2-9 (high pressure, short time) a higher void content was measured near the outlet, which could confirm that too short flow time prevented possible bubbles from escaping.

Flexural test

The elastic modulus measured in 3-point-bending is reported in Table 6.7, along with the total impregnation time. These values fall in between the upper and lower bounds of 12.3 GPa and 3.5 GPa theoretically calculated from the mixture rule, i.e.

$$E_{up} = V_f E_f + (1 - V_f) E_m$$

$$E_{low} = \left[\frac{V_f}{E_f} + \frac{(1 - V_f)}{E_m} \right]^{-1},$$

where V_f is the volume fraction of fibers oriented along the sample length (transverse to the cross-head), i.e. half of the overall fiber content for both G-PLY and G-WEAVE[†], E_f is the glass-fiber elastic modulus (~ 45 GPa) and E_m the elastic modulus of HFPA6 (~ 2.8 GPa, from Table 6.3).

[†]See Table 3.1 in Chapter 3.

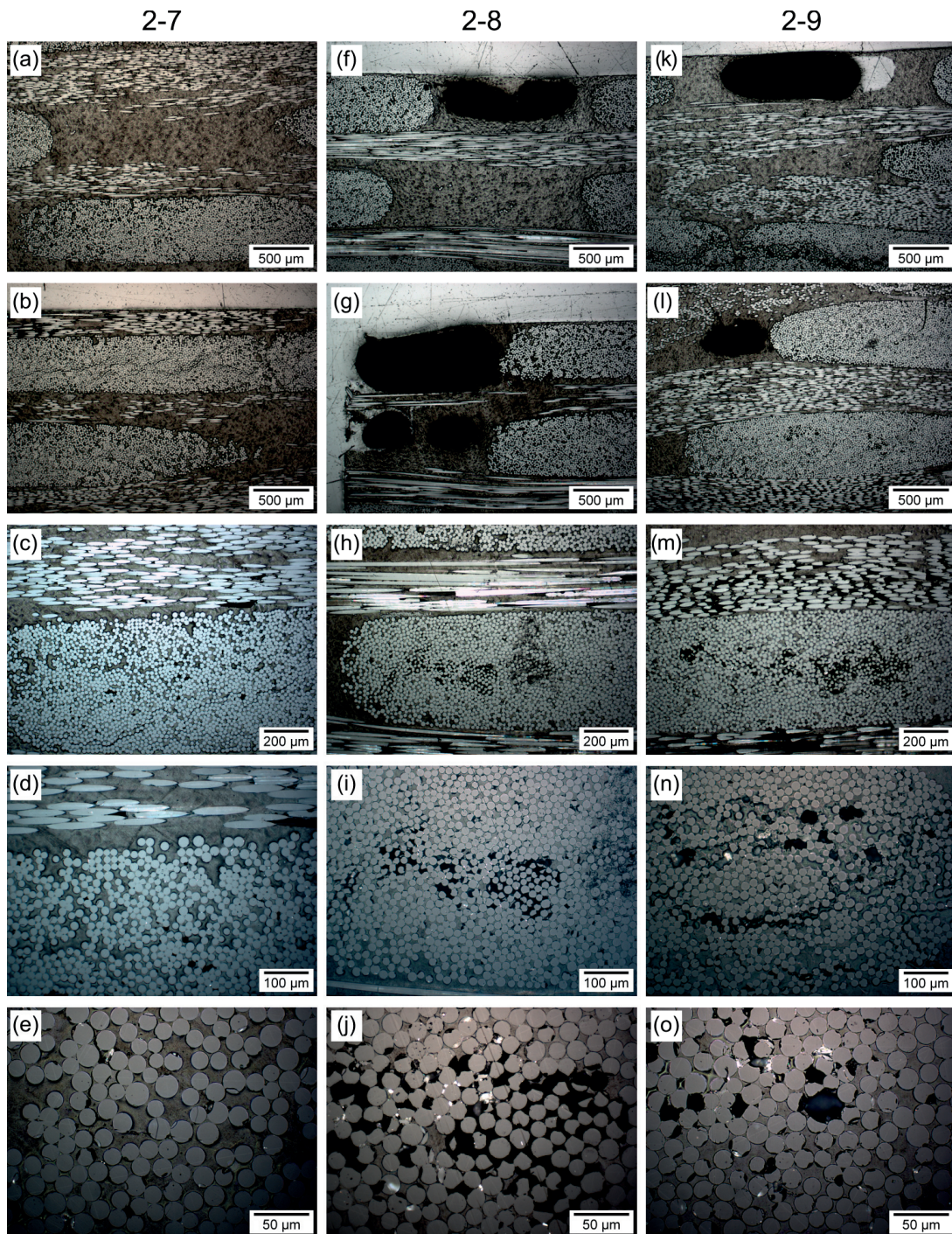


Fig. 6.24: Optical micrographs of the cross-sections transverse to flow direction and close to the outlet for plates 2-7, 2-8 and 2-9.

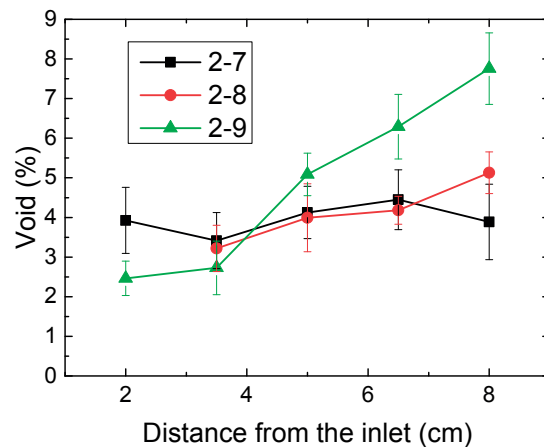


Fig. 6.25: Void content along the plate measured by burn-off method for samples 2-7, 2-8 and 2-9.

The samples with spacers (2-5 and 2-6) were found as expected to be those with the highest modulus, with an increase of up to 26% compared to G-WEAVE only, while greatly reducing impregnation time. The increase of apparent bending modulus is in accordance with the results of flexural tests performed on G-WEAVE/epoxy samples, for which an increase of 20% was observed when a PLA spacer was used[‡]. The lower absolute values obtained here might be explained considering the lower span-to-thickness ratio used in the 3-point bending test, which might dramatically affect the measured flexural modulus*, as shown for instance in [163, 164]. G-PLY samples (2-7, 2-8 and 2-9) allowed even lower impregnation time, but resulted in a deterioration of bending stiffness[†]. Ultimately, the comparison is between two flow-enhancing strategies. On the one hand, thick spacers provide the dual feature of flow-enhancement and stiffening, though polymer filtration from the core to the surface requires some time and higher pressure. On the other hand, fibers clustering, which causes formation of meso-channels homogeneously distributed throughout the thickness, allows for even faster impregnation time (although void content remains an issue) but results in deterioration of mechanical properties.

[‡]See Table 5.2 in Chapter 5.

*The epoxy resin Araldite/Aradur used in Chapter 5 has similar modulus to HFPA6, namely around 2.8 GPa for a curing cycle of 90 min at 80 °C + 1 h at 150 °C + 1 h at 180 °C (from manufacturer's data-sheet).

[†]The issue of mechanical properties deterioration in fabrics with fiber clustering for flow enhancement has been investigated by previous authors, such as in [131] and [132].

Table 6.7: Impregnation time and flexural modulus of six samples produced via mTP-RTM.

Sample#	Preform	Total impregnation time (min)	Flexural modulus (GPa)
2-3	G-WEAVE	45*	6.6 ± 0.5
2-5	G-WEAVE + spacers	7	7.5 ± 0.3
2-6	G-WEAVE + spacers	7	8.3 ± 0.4
2-7	G-PLY (GS)	7	6.0 ± 0.4
2-8	G-PLY (GS)	2.5	5.3 ± 0.2
2-9	G-PLY (GS)	2.5	6.1 ± 0.2

*Only partially impregnated

6.3.5 Conclusion

In this section, a series of mTP-RTM tests with HFGPA6 matrix and glass fabrics was presented. Three preforms were compared, namely a woven fabric ("G-WEAVE"); the same woven fabric with the addition of rigid CFR-PEEK rods spacers as flow-enhancers ("G-WEAVE + spacers"); and a channel-wise non-crimp fabric with glass stitches ("G-PLY (GS)"). Depending on the type of preform, different impregnation strategies were also investigated. For G-WEAVE, only slug-flow-like impregnation could be performed, which led to ridiculously long cycle-time. The other two types of preforms were responsible for strong dual-scale flow, which allows faster impregnation, but could result in large void content. In these cases, the "vacuum + saturation" concept was applied to improve the degree of impregnation. In addition, double-inlet injection was also explored for G-PLY (GS), along with different conditions in terms of injection pressure and time.

A total of nine plates were produced, six of which analyzed in terms of impregnation and bending stiffness. "G-WEAVE" preforms did not allow application of high pressure due to fabric deformation, and the low permeability resulted in impractical impregnation time. "G-WEAVE + spacers" preforms allowed a much higher pressure (up to 28.6 bar) and a dramatic reduction of impregnation time, although melt filtration from the core to the layers compacted against the mold walls remained an issue and unsaturated spots on the surface were visible; however, a good micro-scale impregnation was observed in the bulk of the plate. The impregnation could be possibly improved by placing the spacers on different layers, so as to create a more regular distribution of channels throughout the preform cross section, which would allow the resin to reach the surface more efficiently. In addition, the spacers acted not only as flow-enhancers, but

also as stiffeners, leading to an increase of flexural modulus up to 26%. Finally, G-PLY (GS) preforms were also limited in terms of pressure (a little deformation was visible at 7.1 bar), but the more regular distribution of meso-channels throughout the thickness of the preforms allowed to achieve a reasonably good macro-scale impregnation in even shorter times; however, void entrapment remained an issue, and so was the detrimental effect of fibers clustering on the mechanical properties. Double-inlet injection was proven to be a viable option to reduce impregnation time, but it requires optimal control of local temperature at the two inlets and synchronization of inlets opening, and it could not allow application of vacuum, at least not in our current experimental set-up.

6.4 Conclusions and outlook

Development of a novel process frequently requires the combination of solutions from existing technologies. The process investigated in this chapter is a combination of high temperature thermoplastic manufacturing and liquid composite molding. Special formulations of polyamide with exceptionally low melt-viscosity, yet two or three orders of magnitude higher than thermoset resins, have been characterized and used for process optimization. In particular, PP and HFPA6 as matrix have been employed as model materials for production of composite plates. The former is a very brittle polymer, which has a lower melting point and allowed impregnation trials at just 200 °C. The latter has a higher melting point, and requires to be heated up to 280 °C in order to reach a low enough viscosity. However, the HFPA6 has better integrity and stability, and it is best suited for process development. At this temperature, adequate consumables (release agent, sealing, etc.) are needed. Moreover, polyester stitches of glass fabrics (G-PLY) degrade, and the fabric's architecture collapses, preventing proper flow and impregnation.

A custom setup was designed and fabricated from scratch with a simple concept. Main components are two melting pots equipped with pistons and a mold cavity, connected to each other through holes for melt transfer. The tool was conceived to be heated in an oven and subsequently transferred in a hot press, in order to apply a constant force on the piston(s), and therefore perform impregnation at constant pressure gradient on the fabric. However, this strategy turned out to be exaggeratedly time-consuming, due

to low efficiency of convection heating. Therefore, a new improvement was conceived, which allowed more efficient heating by means of electrical cartridges.

Preliminary tests have been performed both in compression and mTP-RTM conditions, using either HFPA66, HFPA6 or iPP as matrix. These experiments were useful to explore the processability of these polymers, to identify issues (e.g. melt leakage, crystallization shrinkage, stitches degradation, air entrapment), try high-temperature consumables (sealant, release agent), and optimize equipment and lab procedures.

The main part of this chapter concerned the investigation of strategies to reduce the impregnation time in mTP-RTM. The study was carried out using HFPA6 as a matrix and different preform architectures, and under different test conditions. It was demonstrated that a great reduction of the impregnation step with mid-viscosity matrix can be achieved by introducing meso-channels within the preform, be they intrinsically linked to the fabric architecture (non-crimp fabric) or due to introduction of spacers as a second solid phase. The former has the advantage of having a homogeneous distribution of the channels in the preform, which allows a more uniform distribution of the melt, but the mechanical properties could be negatively affected. The latter brings a second feature, functioning as a flow-enhancer during the process and as stiffener in the final part. It should be noticed that this kind of feature is an intrinsic benefit given by RTM processes and which could hardly be implemented in compression molding.

The process presented in this chapter has been conceived at a lab-scale, and as such it was not optimized for high volumes of production. However, speculations can be made about how the process could be possibly scaled up. Firstly, the most time-consuming parts of the process were heating and cooling. More efficient systems would be used at an industrial scale, which could allow a reduction to few minutes for heating and cooling, depending on the mold size. In addition, it would not be necessary to wait for the the mold to be at room temperature for demolding. Instead, it could be done right below the crystallization temperature, just cold enough to avoid deformation caused by crystallization shrinkage. Secondly, a screw-extruder machine could be used to melt and inject the melt polymer in the mold, allowing, on the one hand, to decouple the heating/-cooling systems of mold and melt with consequent savings in terms of time and energy, and, on the other hand, to guarantee a better mixing of the melt thus reducing the risk of

injecting air bubbles in the mold. Thirdly, the whole process could be further enhanced by splitting the heating and cooling into different stations, so as to allow simultaneous use of more than one mold.

A final consideration can be made on the part's size that can be produced with mTP-RTM. Even though major cycle-time reduction has been achieved, part size remains quite small if compared for instance to large automotive components (e.g. door panels). It is possible that large components that are rather simple in shape will continue to be produced by compression molding or by compression-RTM with through-thickness impregnation, but it is also likely that a combination of through-thickness and in-plane impregnation would occur in more complex parts. In fact, mTP-RTM is not meant to be in competition with these processes, but rather complementary, at least for production of large parts. However, when it comes to shape complexity, with tubular and small parts, mTP-RTM provides more freedom in terms of design and allows production of complex parts in one shot, thus avoiding successive steps of joining and welding.

Chapter 7

Scale-up scenarios

In the previous chapter, we have shown that the thermoplastic RTM process, at laboratory scale, can successfully produce structural parts, using molten polymers in the 30 Pa s viscosity range, a reinforcement architecture adapted to provide flow channels and injection strategies combining initial vacuum, a saturation phase and a well controlled cooling phase. The next step is to evaluate the possibility to scale-up the process, from a technical but also economic and environmental point of view. To this end, a cost model for the mTP-RTM process based on the lab-scale conditions illustrated in Chapter 6 was first developed, then a number of assumptions were also adopted, so as to evaluate a realistic scale-up to industrial conditions. A comparison was made with a standard TS-RTM with epoxy and with a process under development at Solvay*, in which an injection molding machine is adapted for composite manufacturing by Compression RTM, implying direct through-thickness impregnation. This process will be introduced in Section 7.1. The cost model is presented in Section 7.2 with the main results.[†]

**Centre de Recherche de Lyon*, 85 Avenue des Frères Perret, 69190 Saint-Fons (Lyon), France.

[†]The cost analysis presented in this chapter is partly based on the Master thesis of Lucien Berret, which also includes a life-cycle assessment study [165].

7.1 Compression RTM

A semi-industrial C-RTM equipment has been set up at Solvay's for research purposes, in order to perform through-thickness impregnation of fabrics with high-fluidity thermoplastics driven by axial compression, as schematically shown in Fig. 7.1. Albeit still in research phase, the equipment, which comprises an adapted injection molding machine, an adapted flat mold and dedicated and optimized heating and cooling systems, can be considered as close to an industrial scale. The major components are a standard injection-molding extruder, for polymer melting and mixing, a flat steel mold with a cavity area of about $200 \times 270\text{mm}^2$ and a 125-tons electric press activated by a toggle mechanism, which operates horizontally and allows fine control of the cavity thickness. The melt is injected from the extruder through a hole in the male fixed part (F), while the fabric is placed in the female movable part (M) of the mold.

The mold is heated by means of heating cartridges embedded in both parts of the mold, which ensure a heating rate around $20\text{ }^\circ\text{C}/\text{min}$. Air and water are alternately pumped through channels running through the mold, which allows optimal cooling at a rate of up to $40\text{ }^\circ\text{C}/\text{min}$. Resin flow is monitored by pressure sensors emerging on both the fixed and movable surfaces of the mold's cavity. The axial compression achieves high pressure and high volume fractions, with less risk of destroying the preform structure. However, the mold being movable requires a high degree of precision in the design and manufacturing, which, summing up with the cost of the injection molding unit and heating/cooling system, results in a high necessary capital investment for the equipment. In addition, this sets a limit in the degree of geometrical complexity of the part.

7.2 Cost model

The cost analysis is adapted from the activity-based model by Verrey et al. [63], where only manufacturing cost is considered, which includes fixed (equipment, maintenance, invested capital, etc.) and variable (labor, materials, scrap, etc.) costs of production. The following scenarios are compared: (i) RTM with epoxy resin and G-WEAVE fabric; (ii) mTP-RTM with HFPA6 and G-PLY fabric; (iii) mTP-RTM with HFPA6 and G-WEAVE fabric + spacer; and (iv) C-RTM with HFPA6 and G-WEAVE fabric.

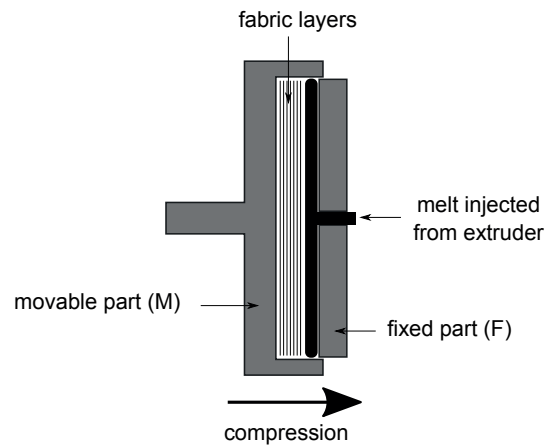


Fig. 7.1: Schematics of the impregnation in C-RTM process at Solvay's.

7.2.1 Materials

The amount of material was kept constant, so as to produce a flat plate of thickness 5 mm and size 270 cm × 200 cm, and a glass fiber volume fraction of 0.46. Cost for fabric and resins were set to 5 €/kg and 3 €/kg, respectively. For scenario (iii), additional spacer material had to be considered. A spacer with a design analogous to the 6 × 6-spacer of Chapter 5, would have a volume of $\approx 15 \text{ cm}^3$. Assuming as spacer material a nylon reinforced with carbon fibers, which has a density of $\approx 1.1 \text{ g/cm}^3$, around 16 g per part would be required. Considering a cost of $\approx 90 \text{ €/kg}$ for this material in filament form suitable for 3D printing, a cost of 1.5 €/part was simply added for this scenario.

7.2.2 Production line

The production lines for the four scenarios are shown in Fig. 7.2 for scenario (i); Fig. 7.3 for scenario (ii); Fig. 7.4 for scenario (iii); and Fig. 7.5 for scenario (iv). Each line can be split into four sub-units, or cells: fabric cutting; preforming; RTM; and trimming. A cycle time is attributed to each cell. Here the same duration was considered for the four scenarios except for the RTM cell, where the impregnation is highly dependent on the scenario under consideration. The duration attributed to each scenario for the RTM cell is displayed in Table 7.1. In epoxy-RTM (i), the duration includes time for impregnation and cure (estimating resin viscosity to 0.5 Pa.s, and impregnation/cure about 5 minutes); a post-cure step in an oven is typically performed to fully cure the resin. This operation is generally performed with several parts together, so its duration is spread among several

parts, about 200s. In the two mTP-RTM scenarios, injection time was calculated from Eq. 6.2 (Chapter 6), using $\Delta P = 3.6$ bar and $K = 10^{-9}$ m² for (ii), and $\Delta P = 7.1$ bar and $K = 10^{-8}$ m² for (iii), and in both cases $L = 270$ mm and $\eta = 26$ Pa s. Average heating and cooling rates of 20 °C and 40 °C, respectively, were considered; heating and cooling time were calculated for a cycle between 160 °C (starting and demolding) and 280 °C (injection). The same heating and cooling times were used for scenarios (ii), (iii) and (iv). It should be noticed that in (ii) and (iii) heating and cooling are decoupled, whereas in (iv) they take place in sequence on the same station. Indeed, mTP-RTM uses a simpler mold, which can be made movable from a heating station to an injection station, where an extruder is maintained hot and ready for the injection; this means that two molds can operate at the same time, one being heated during the injection of the other. For this reason, heating time was not taken in consideration for (ii) and (iii). In C-RTM, the mold is embodied in an injection molding machine, and as such it cannot be moved; to have two molds operating simultaneously, a second extruder and electrical press should be purchased, which is much more costly than a second mTP-RTM mold.

Table 7.1: Duration of the RTM cell for each scenario.

Scenario	Step	Duration (s)	Total (s)
(i) RTM Epoxy	Injection + Cure	500	500
(ii) mTP-RTM HFPA6/G-PLY	Injection	2020	2500
	Saturation	300	
	Cooling	180	
(iii) mTP-RTM HFPA6/G-WEAVE+spacer	Injection	75	855
	Saturation	600	
	Cooling	180	
(iv) C-RTM HFPA6/G-WEAVE	Heating	360	760
	Injection	20	
	Compression	200	
	Cooling	180	

7.2.3 Data input

The main input data common to all scenarios are listed in 7.2. These include inputs for cutting, preforming and trimming cells. Inputs of time, labor, rejection and scrap rate for each cell are indicated in the process line diagrams (Fig. 7.2, 7.3, 7.4 and 7.5). Additional data inputs, differing between scenarios, are listed in Table 7.3.

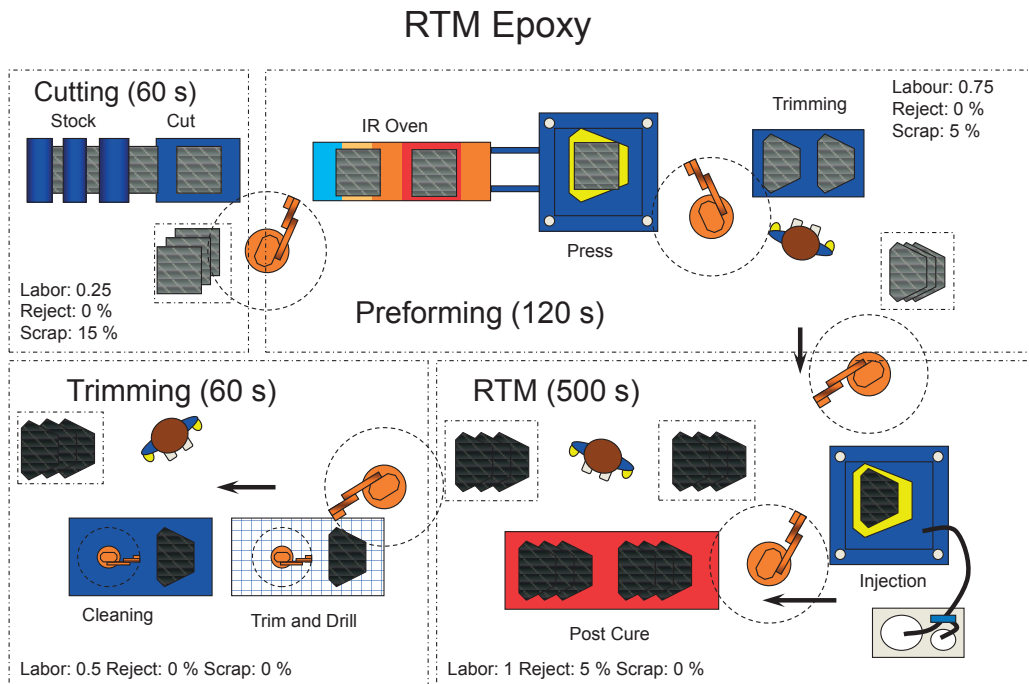


Fig. 7.2: Production line for RTM process with epoxy and G-WEAVE.

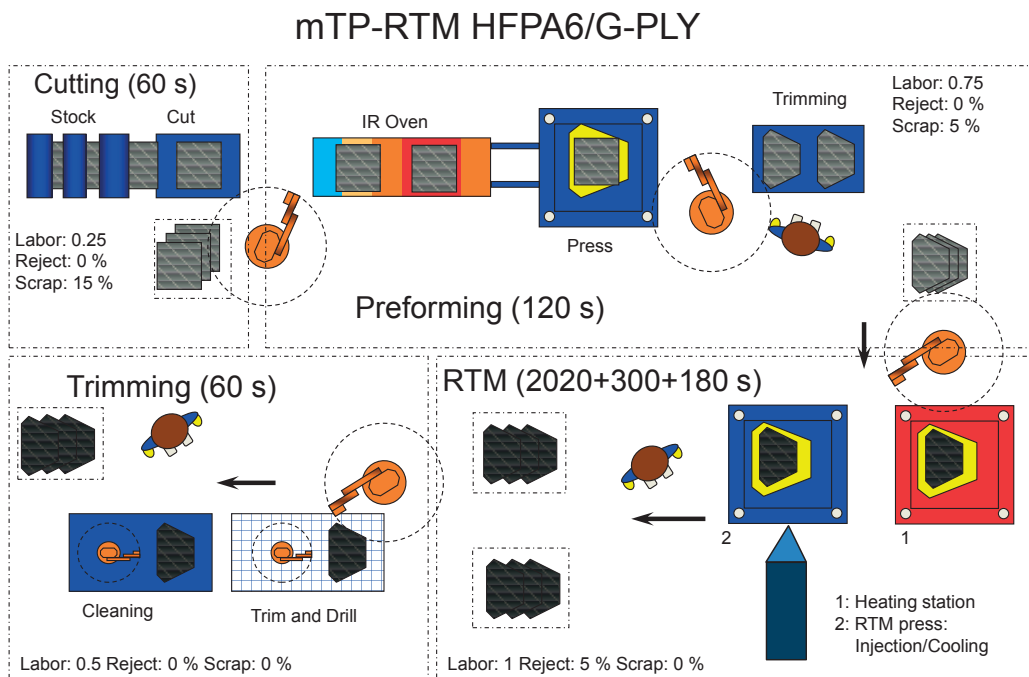


Fig. 7.3: Production line for mTP-RTM process with HFPA6 and G-PLY.

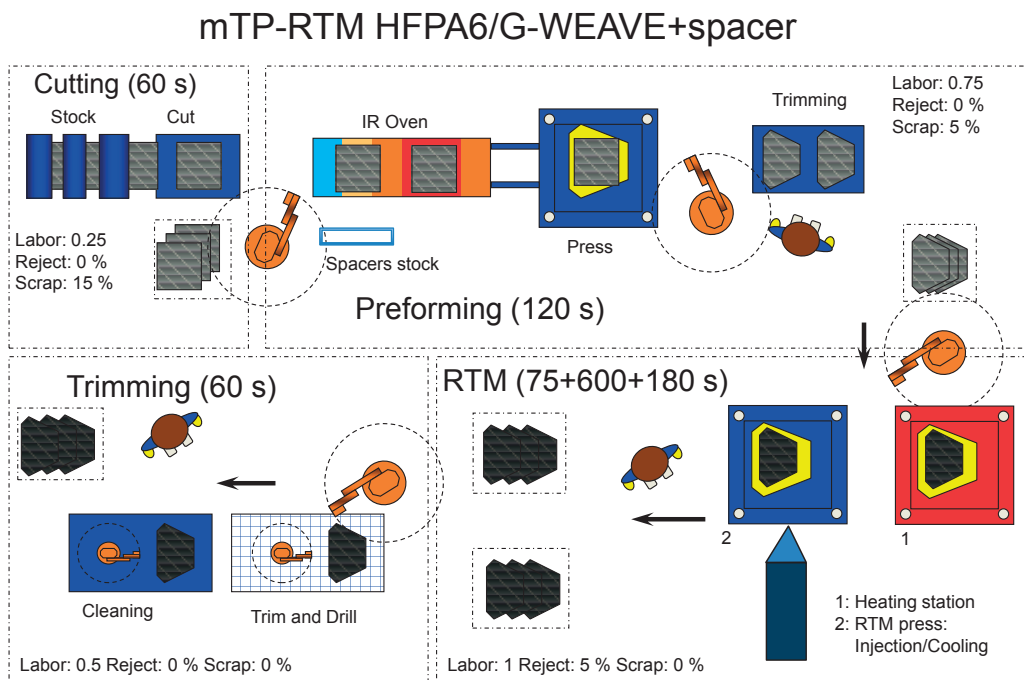


Fig. 7.4: Production line for mTP-RTM process with HFFPA6 and G-WEAVE + spacer.

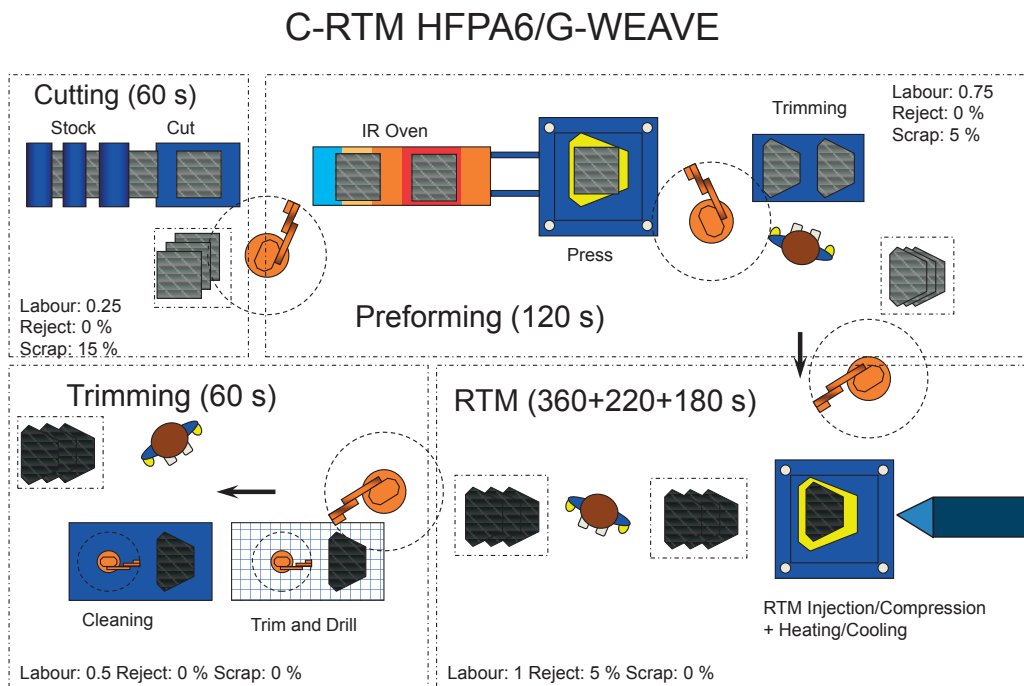


Fig. 7.5: Production line for C-RTM process with HFFPA6 and G-WEAVE.

Table 7.2: Common input data for all the scenarios.

	Input	Value
General	Production duration	5 years
	Shift duration	7.5 h/d per shift
	Days per year	233 d
	Max number of shifts	3/d
	Time efficiency	100%
	Cycle time	See Fig.7.2-7.5
	Equipment dedication	1
Materials	Matrix cost	3 €/kg
	Fabric cost	5 €/kg
	Matrix quantity	0.172 kg/part
	Fabric quantity	0.323 kg/part
	Scrap rate	See Fig.7.2-7.5
Equipment cost (Robots included)	Cutting	214 000 €
	Preforming	180 000 €
	Trimming	100 000 €
Plant	Operating cost	140 €/m ² /year
	Cutting area	40 m ²
	Preforming area	40 m ²
	Trimming area	45 m ²
Energy	Unitary cost	0.1 €/kWh
	Cutting power	25 kW
	Preforming power	40 kW
	Trimming power	26 kW
Labor	Direct labor cost per person	25 €
	Number of direct persons	See Fig.7.2-7.5
	Indirect labor cost per person	38 €

7.2.4 Results

The variation of manufacturing cost with the volume of production for the four scenarios is shown in Fig. 7.6. The visible variations, or spikes, are due to new capital investments, which are needed when the maximum output per year in a cell is reached. In practice, new RTM cells had to be added in order to increase the production, which means new investment in equipment, plant space, energy, molds and labor. For instance, many parallel RTM cells had to be considered for scenario (ii), since the cycle time is so long that a rather small number of parts per year could be produced with a single cell. To reach an annual volume of 70k, 2 cells had to be used for scenario (i), 10 for scenario (ii), 4

Table 7.3: Input data for the RTM cell of the four scenarios.

Scenario	Input	Value
(i) RTM Epoxy	Injection unit	60 000 €
	Oven	10 000 €
	Robots (x2)	60 000 €
	Mold	20 000 €
	Machine power	40 kW
	Plant area	30 m ²
(ii) mTP-RTM HFPA6/G-PLY	Injection	50 000 €
	RTM press	100 000 €
	Cooling system	70 000 €
	Robot	30 000 €
	Molds (x2)	40 000 €
	Machine power	30 kW
	Plant area	30 m ²
(iii) mTP-RTM HFPA6/G-WEAVE+spacer	Injection	50 000 €
	RTM press	100 000 €
	Cooling system	70 000 €
	Robot	30 000 €
	Molds (x2)	40 000 €
	Machine power	30 kW
	Plant area	30 m ²
	Spacer	1.5 €/part
(iv) C-RTM HFPA6/G-WEAVE	Injection-Press	170 000 €
	Cooling system	70 000 €
	Robot	30 000 €
	Mold	95 000 €
	Machine power	30 kW
	Plant area	30 m ²

for scenario (iii) and 3 for scenario (iv).

Apparently, the stabilized cost is highly correlated with the duration of the RTM cell step. RTM with epoxy and mTP-RTM with G-PLY are respectively the cheapest and the most costly routes. The other two processes, mTP-RTM with a spacer and C-RTM are much closer to RTM-epoxy, yet around 43% and 55% more expensive for 70k parts, respectively. Interestingly, these two scenarios are very close, with only a difference of ca 2.3 €/part at a volume of 70k. Even though cycle time of scenario (iii) is longer and equipment capital investment is quite similar, the mold complexity makes the difference. On the one hand, the fabrication and design of such a mold with moving

parts at high temperatures requires an accurate design to fine tune tolerances taking into account the thermal expansion of the material, which causes its cost to rise. On the other hand, the mold/press/injection unit constitutes a whole block, and heating and cooling happen at the same station; thus, it is not possible to run two molds simultaneously. Conversely, in mTP-RTM the mold is supposedly simpler, requiring a standard RTM press for automatic closing, and two molds can be operated at the same time, with one being heated while the other is being injected and cooled. Nevertheless, it should be taken into account that C-RTM is still in development phase, and current expectations are for a significant decrease of cycle time to 3-5 min.

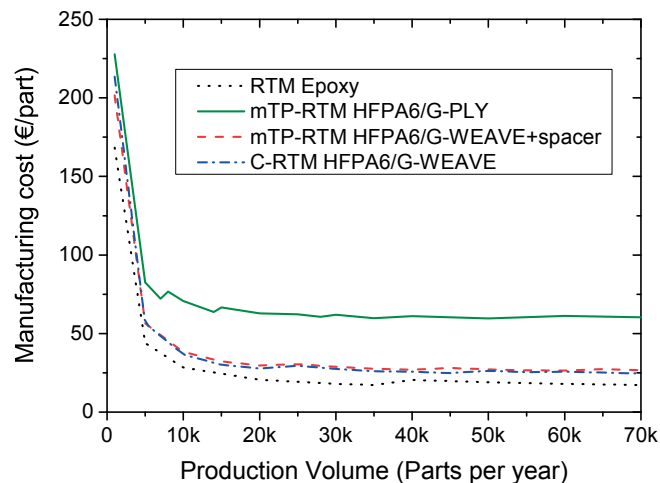


Fig. 7.6: Manufacturing cost per part as a function of the volume of production per year for the four scenarios.

Fig. 7.7 shows the segmentation into the various cost categories for the four scenarios. In all cases the highest cost-drivers are labor and equipment. The high cost of labor for scenario (ii) (Fig. 7.7b) is due to the larger number of parallel RTM cells operating, each requiring 1 unit of labor. In scenario (iii) (Fig. 7.7c), the higher cost of raw material is observed due to the relatively high cost attributed to the spacer. Regarding scenario (iv) (Fig. 7.7d) the importance of mold cost is observed, but also a slightly smaller labor cost compared to (iii), for which an additional RTM cell had to be included to reach the target production volume.

A last consideration can be made with regard to the contribution of materials (fabric, resin and spacer) on the total cost. At 70k parts per year, this amounts to 15% and

10.4% for scenarios (iii) and (iv), respectively. Therefore, the cost increase after upgrading to high-performance materials (e.g. replacing glass with carbon fibers and PA6 with PPS matrix) is not expected to be highly significant. As a first and simple approach, the cost variation can be calculated considering the same volume fraction of fibers and matrix and same part size, i.e. regardless of the mechanical properties. Using values for cost and density of 15 €/kg and 1.8 g/cm³ for carbon fibers, and 12 €/kg and 1.35 g/cm³ for PPS, the cost at 70k parts per year can be found to increase from 26.8 to 30.8 €/part for scenario (iii), and from 24.5 to 26.6 €/part for scenario (iv).

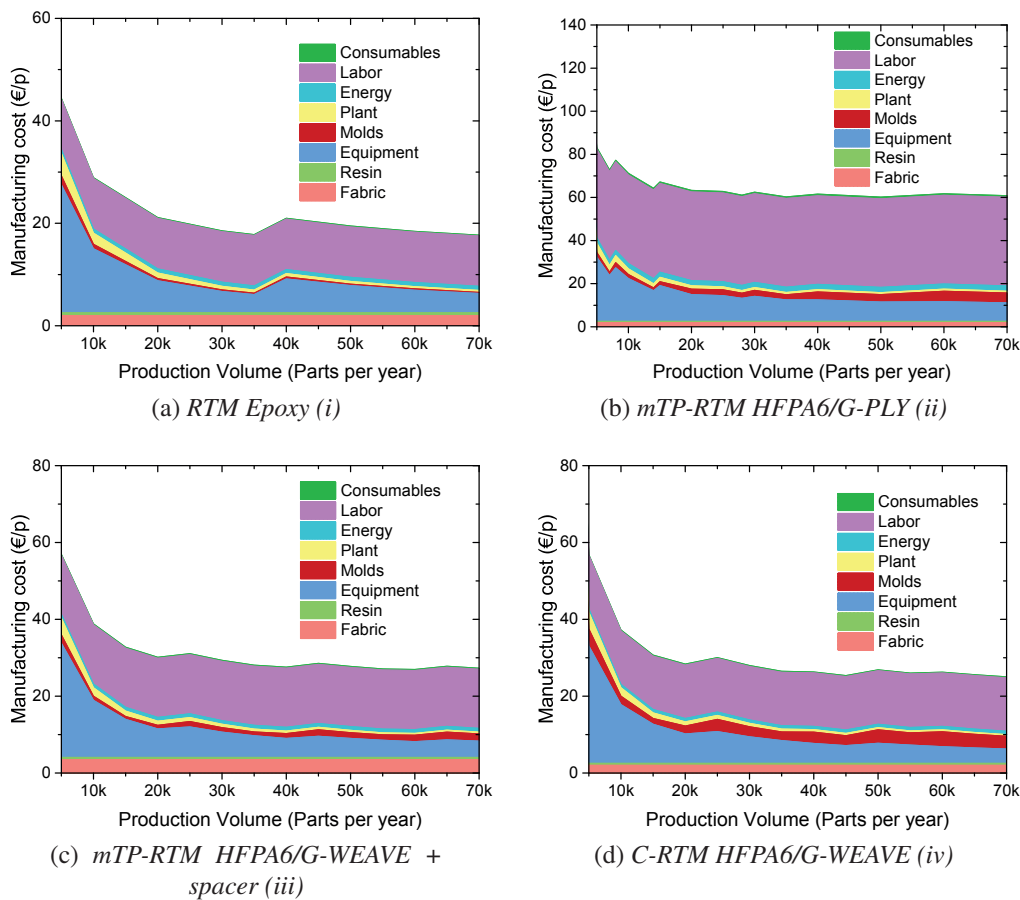


Fig. 7.7: Manufacturing cost vs. production volume for the four scenarios, broken down into cost categories, starting from 5k parts per year of production volume.

7.3 Conclusion

This preliminary cost estimate should definitely be further refined as the processes evolve, and should be applied to a more realistic part than a simple plate. However, several conclusions can be drawn from this study. First, the cost of mTP-RTM parts is higher than the well-developed epoxy based equivalent, not because of the material cost, which is similar, but because of the equipment cost and the long cycle time in large parts imposed by the heating and cooling steps. Novel mold concepts, with fast heating and cooling, as well as a further study on the highest temperature at which part demolding can be made without compromising part quality, would be required to limit this step. It is also important to note that if carbon fibers had been selected, since their material cost is higher and thus more dominant on the overall part cost, this difference would be less marked. Secondly, the comparison between scenarios (ii) and (iii) confirms that in-plane RTM, even with high permeability fabrics such as G-PLY, is not cost-effective with TP, unless possibly for small and very complex parts that cannot be made differently. Finally, comparison between scenarios (iii) and (iv) also confirms that the mTP-RTM that makes use of spacers leads to a rather similar part cost as C-RTM, although segmentation shows the importance of mold cost for (iv) and of labor cost for (iii). Both routes are thus of practical interest and complementary, C-RTM being more adapted to simple shapes, while the spacer approach can be efficient for rather large parts (because overall necessary mold closure and fluid pressure are lower) and most importantly for complex shaped parts that are difficult to produce with C-RTM, unless the latter is coupled with overmolding techniques to produce TP features on the composite part (e.g. stiffening ribs).

Chapter 8

Conclusions and perspectives

The ultimate goal of this thesis was to find an optimum between thermoplastic flow enhancement and fabric impregnation in a novel RTM process employing high-fluidity thermoplastics as impregnating resins. Flow enhancement is desired to reduce production time, so as to make the process affordable for high-volume industries; it can be achieved by increasing fabric permeability, according to the physics of flow represented by Darcy's law. Permeability enhancement is achieved by exploiting the dual size distribution of porosity in reinforcing textiles. However, the resulting heterogeneous distribution of fibers might be responsible for entrapment of voids during impregnation and for the formation of large resin-rich areas in the final part. Both aspects can detrimentally affect the properties of the final composite.

The relation between fabric architecture and permeability was firstly investigated on two high-flow glass-fabrics, so-called G-FLOW and G-PLY. The latter had higher in-plane permeability, up to $\approx 10^{-9} \text{ m}^2$ for $\approx 46\%$ fiber volume content, which, in principle, would allow impregnation with more viscous resins than benchmark fabrics. This represents an increase of one order of magnitude in comparison with a woven fabric (G-WEAVE) used as reference, which was attributed to the meso-structure of the G-PLY preforms, investigated by Computed X-Ray Tomography. This provided an insight into the fabric architecture under compaction. Permeability of G-PLY was then calculated based on channels' geometry, ignoring micro-flow inside the bundles, and it was found to match closely to the measured saturated permeability. The channels lead the macro-flow, and permeability along the channels' direction can be easily predicted by knowledge of

their geometry. A drawback of these fabrics is that the fluid flows very fast from inlet to outlet within the large channels, while the tows behind remain largely unsaturated. Capillary effects were evaluated using the ratio of unsaturated-to-saturated permeability, confirming that for G-PLY micro-flow is usually negligible, and that slug-flow conditions were achieved for low capillary numbers (10^{-3}). On the contrary, for G-WEAVE a transition from predominant micro-flow to predominant macro-flow, similarly to what is observed in literature, was found using this ratio, with an optimal capillary number around $5 \cdot 10^{-4}$. The capillary pressure was calculated from the permeability ratio, and its dependence on capillary number, found by previous authors with other methods, was confirmed. This method would need to be further confirmed with other fabric geometries and comparing with other methods; for instance, extrapolating the capillary pressure from pressure build-up in constant flow-rate injections [62]. An interesting result, which would also need to be further confirmed with other fabrics to test its limits, is that as long as the capillary number is high enough so that hydrodynamic effects in the channels dominate the flow, unsaturated permeability measurements from the flow front position provide results that are very close to saturated permeability, measured from flow rate through the fabric. The trend of permeability ratio vs. capillary number, can thus be used to evaluate the optimal flow conditions leading to the lowest porosity in the part, as it corresponds to the Ca value for which this ratio just reaches 1.

A further increase of permeability, up to $\approx 10^{-8} \text{ m}^2$, was obtained when a spacer was introduced in the core of a woven fabric stack (G-WEAVE), so as to create longitudinal channels which run straight from inlet to outlet. Spacers were produced by 3D-printing, which allows to make them in complex shapes, but in principle they could be produced with alternative techniques, such as injection molding; thus, this concept can be easily implemented in RTM process, where complex parts are produced. Measured saturated permeability was found to be in the same order of magnitude as values calculated from channels geometry, which in this case was known a priori from the 3D-printed model. Differences from theoretical values, especially when channel width was as large or larger than the fiber bundles, were attributed to fiber nesting, which partly blocked the channels, thus slowing down the flow. In any case, in presence of spacers the duality of flow scale was even more distinct than in G-PLY. A fluid of viscosity

≈ 0.1 Pa s ran a distance of 20 cm, from inlet to outlet, in a few seconds under a pressure difference of ≈ 1.6 bar. To achieve full fabric saturation, the outlet needs to be closed, otherwise the fluid would freely flow out of the mold, and it is necessary to keep the fluid under pressure at the inlet, in a saturation step, so as to force fabric impregnation. Air entrapment can be avoided by pulling vacuum out of the mold. With this strategy, in principle very long parts could be produced, as the duration of in-plane flow would not be much affected, and the bottle-neck of the process would be the flow through the thickness of the fabric, which in any case would take the same time, provided that the part thickness is uniform.

The final destiny of these spacers after impregnation remains to be further investigated. Two main routes were assessed: stiffening spacer and sacrificial spacer. The former should be made of a material, which is stiff enough to sustain fabric compaction, and thus remains intact and embedded in the core of the final composite, so as to create a sandwich structure with improved stiffness. The latter should be made of a material capable of sustaining fabric compaction during impregnation to ensure the opening of channels, but that collapses in a second phase, when for instance temperature is increased and the spacer would soften or even melt and mix with the infiltrating fluid. In the present thesis, PLA and PCL were used respectively to produce a stiffening and a sacrificial spacer during production of composite plates via TS-RTM, using an epoxy resin as proof-of-concept matrix. An increase of $\approx 20\%$ of apparent flexural modulus was observed with PLA. PCL, which has a melting point of around 60°C , melted and flattened during curing at approximately 80°C , and a more homogeneous distribution of the fibers was finally achieved; in this case, the flexural modulus was not much affected, but flexural strength was reduced by $\approx 12.5\%$. Indeed, in both cases, the flexural tests ended by abrupt failure due to delamination at the core region. This could be reduced by using a material that is more compatible at a physico-chemical level with the matrix. Further research should focus on the effect of the spacers on other properties, such as torsional stiffness, impact resistance and fatigue resistance. In addition, the pressure evolution in the two-step filling process needs to be investigated in flow experiments where pressure sensors embedded in the mold monitor the fluid pressure during injection. Expectedly, during the flow along the channels, when the preform is unsaturated, the pressure would

follow a parabolic curve; then, as saturation is achieved, it would evolve towards a linear curve from inlet to outlet [100]. However, since the outlet is closed, and the inlet remains at constant pressure, a decrease of the slope is also expected, until a state of constant pressure throughout the mold is achieved.

All these findings were successfully applied to mTP-RTM using HFPA6 as matrix, which has a viscosity of $\approx 26 \text{ Pa s}$ at 280°C , and various preforms for a flow distance of 11 cm. For a standard fabric, like G-WEAVE, injection pressure was limited to few bars, as fabric displacement occurred already at 3.6 bar; hence, impregnation time for even such a short length was impractical (more than 45 min). Preforms with channels, like G-PLY or G-WEAVE with spacers, allowed higher pressure injections without deforming significantly. For instance, for G-PLY minor displacement occurred at 7.1 bar. The use of CFR-PEEK rods as spacers in G-WEAVE, combined with the two-step strategy developed and tested with model fluids (in-plane channel flow + transverse saturation), allowed to apply up to 28.6 bar during the saturation step, and to greatly reduce impregnation time to just 7 min. Two strategies provided the best impregnation, as observed at the macro- and micro-scale, and through burn-off analysis. In the case of the G-WEAVE+spacer, it took 1 min at 7.1 bar for the resin to reach the outlet. In the case of the high-temperature G-PLY fabric with large channels, it took 4 min at 3.6 bar to reach the outlet. However, in the former case the channels were only in the core of the preform, and it was necessary to increase the pressure up to 28.6 bar for 6 min of saturation step to achieve a good impregnation. Conversely, in the latter case, where channels were more homogeneously distributed throughout the thickness of the preform, 3 min at 3.6 bar were enough. Some residual porosity was still visible, especially on the surface of G-WEAVE+spacer samples, where the fabric is highly compacted against the mold surface, making it difficult for the resin to infiltrate the bundles in direct contact with the mold. A more efficient vacuum in the mold could possibly lead to an even better impregnation. Regarding the mechanical properties, similarly to the PLA-spacer, the use of CFR-PEEK rods in the core of a G-WEAVE stack resulted in increased apparent flexural modulus of around 26 %, while G-PLY gave a rather comparable value to G-WEAVE alone. As a future development, three-dimensional sacrificial spacers could be produced via 3D-printing with TPs with melting-point slightly higher than the injection

temperature, similarly to the case of PCL-spacers in TS-RTM. These could then soften soon after injection and allow the fabric to relax, at least partly.

Finally, we showed that scaling-up this process to large volume production is promising, in terms of cost, only if spacers are used. Indeed, even with G-PLY fabric, the total process time is still too long for large parts, whereas with the spacer and G-WEAVE fabrics, the process route becomes comparable to C-RTM. Moreover, the comparison was performed for a simple geometry, which is easily processed by C-RTM. In case of a complex shape, such as a hollow or ribbed part, C-RTM would become more costly to implement, due to post-processing welding operations or complex molds.

In conclusion, mTP-RTM is a promising process for production of medium-size parts with complex shapes, provided that channels are created in the preform by using channel-wise fabrics or by introducing a flow-enhancer spacer in the middle of the preform. Depending on the application, the spacer could have a second role. In this work, it was proven that spacers can increase bending stiffness, but it is not excluded that other properties can be affected, negatively (for example, fatigue resistance may suffer from the presence of large resin pockets), or positively. For instance, Szebenyi et al. [148] observed an increase of ductility for carbon/epoxy plates when a PCL interphase was introduced between the fabric layers. The use of spacers could thus be tailored to provide the needed permeability increase during processing, even in complex shapes, then other effects in the final part, fulfilling its mechanical requirements.

Appendix A

Compression molding with HFPA66

A preliminary benchmark study was carried out in the frame of a student project to evaluate the processability of HFPA for direct impregnation of glass fabric.

A series of compression molding tests was performed to produce small laminate samples of HFPA66 and a 8-harness satin woven GF, supplied by Solvay, with areal mass of 300 g m^{-2} . Five plies of this fabric were cut and placed in the mold all with the same face up. The polymer pellets were placed on top of the fabric inside a simple mold with a rectangular cavity of size $7 \text{ cm} \times 2 \text{ cm}$ and a piston in direct contact with the pellets. Compression was then performed in a hot hydraulic press (Fontijne Presses). The mold was heated up above the melting point ($\approx 270 \text{ }^\circ\text{C}$); a pressure was applied to force the impregnation to take place through the thickness, from the top to the bottom. Finally, the pressure was removed below the crystallization point ($\approx 180 \text{ }^\circ\text{C}$).

The aim was to evaluate the effect of impregnation time and applied pressure. Concerning the pressure, two cases were evaluated. In the first, a constant pressure was applied during the whole impregnation until the demoulding. In the second, a minimum pressure was applied during the impregnation, and a high pressure was then applied between the beginning of the cooling and the demolding. A scheme of the process for the two cases is shown in Fig. A.1.

Table A.1 shows the list of samples prepared at different conditions. Samples 1 to 8 constitute a simple 2×2 multi-factorial design of experiment (DOE) with two replicates, with impregnation time and applied pressure as the two "input-factors" and flexural modulus and strength as the responses. Here the pressure is either applied at a

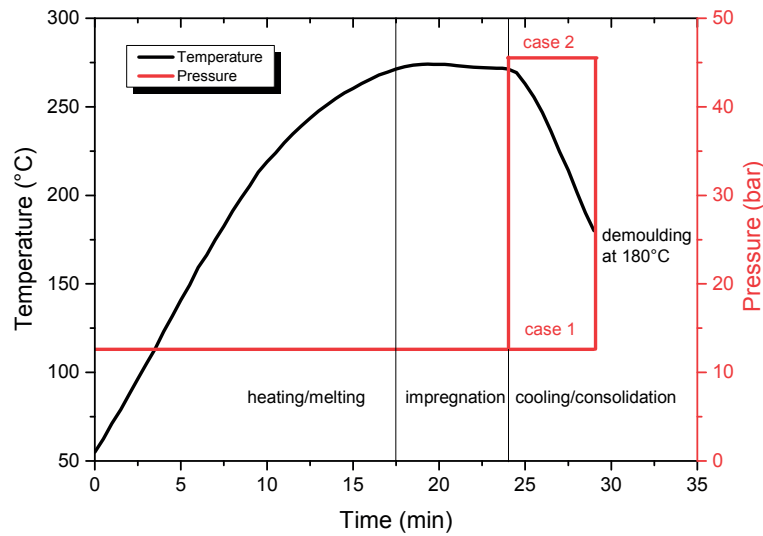


Fig. A.1: Scheme of a typical sample processing route. Case 1: constant pressure applied during the whole cycle. Case 2: a minimum pressure applied until the beginning of the cooling, then high pressure applied during the cooling phase.

Table A.1: List of samples prepared by compression molding.

Sample ID	Impregnation time (min)	Pressure (bar)	Fibre Volume Fraction (%)	Flexural Modulus (GPa)	Flexural Strength (MPa)
1	7.5	12.6	34.9	18.1	432
2	7.5	12.6	33.8	15.1	426
3	7.5	12.6, then 45.7	35	17.3	491
4	7.5	12.6, then 45.7	35.3	18.2	518
5	15	12.6	34.6	17.8	457
6	15	12.6	35.3	17.7	448
7	15	12.6, then 45.7	35.2	18.1	467
8	15	12.6, then 45.7	33.9	16.0	441
9	5	37.7	33.0	13.0	388
10	5	37.7	37.8	19.5	497
11	2.5	37.7	35.9	16.1	466

constant lower value (case 1 in Fig. A.1) or a high pressure is applied at the end of the cycle (case 2 in Fig. A.1).

Flexural tests were conducted in 3-points-bending. The samples, of thickness around 1.5 mm, were cut to 60 mm × 13 mm. The support span-length was set to 50 mm, which gave an aspect ratio (span-length to thickness) of about 32:1. The samples were conditioned prior to testing (vacuum-drying at 110 °C for 14 hours). Force-displacement data were transformed into stress-strain curves according to Eq. 3.9 and 3.10. Values of flexural strength and modulus, calculated as the slope in the strain range between 0.001 and 0.003, are reported in Table A.1.

Noticeably, these values differ from the flexural modulus of mTP-RTM samples shown in Chapter 6 (Table 6.7), which can be easily explained by differences in terms

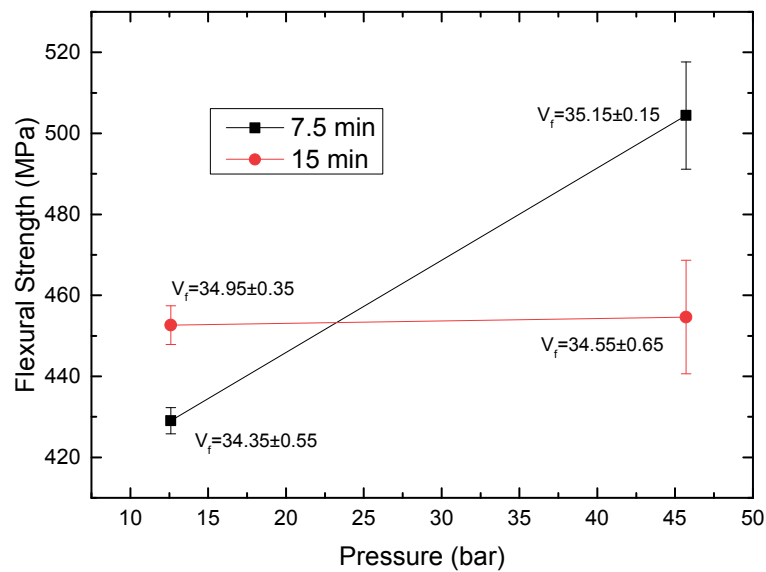


Fig. A.2: Interaction-plot for the flexural strength, within a set of four conditions of impregnation time and applied pressure.

of materials (matrix and fabric), sample and test geometry (thickness and span-length) and test conditions (deformation speed, operator). In particular, differences in samples geometry can dramatically affect the measured flexural modulus [163, 164]. CM samples had thickness of 1.5 mm, span-length 50 mm, length-to-thickness ratio 32:1, while RTM samples had thickness 5 mm, span-length 60 mm and length-to-thickness ratio 12:1.

Analysis of variance (ANOVA), conducted with the software Minitab Express on the samples 1-8, shows that there is no effect of the factors on the flexural modulus. On the contrary, for flexural strength p-values lower than 5% for pressure and time-pressure interaction factors were found. This means that these two factors have an effect on the flexural strength, which can be intuitively observed in the interaction-plot shown in Fig. A.2. In conclusion, with short impregnation times better properties are obtained by applying a higher pressure at the end of the cycle. It is thus conceivable to further reduce cycle time and retain good properties. Three more samples (9 to 11) were processed at shorter time and high constant pressure (during the whole cycle), for which comparable properties were found. A good degree of impregnation was observed also for the sample processed with the shortest time (sample 11, Fig. A.3).

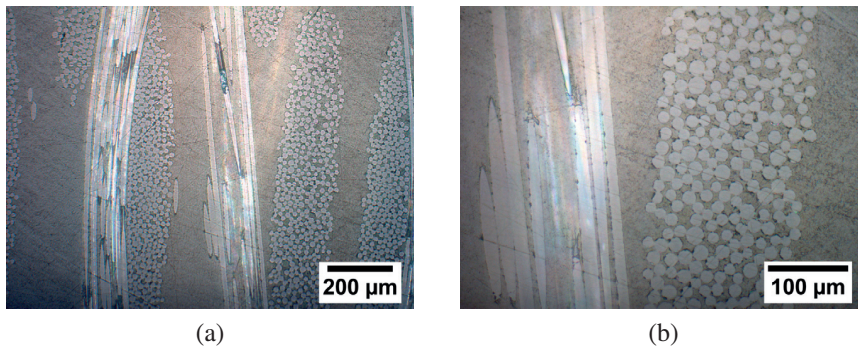


Fig. A.3: Cross-section of sample 11 at two different magnifications.

Appendix B

Viscosity reduction with nanoparticles

The HFTPs used in this thesis are special formulation with rather low molecular weight, but chemically modified such that they retain mechanical properties comparable to standard TPs. A side-project was carried out with the objective to investigate an alternative method to reduce viscosity of melt TPs, which would be possibly used in mTP-RTM.

B.1 Introduction

It is well established that the presence of particles in a fluid causes an increase in viscosity which depends on the amount of particles. For dilute suspensions, Einstein equation predicts a linear increase of viscosity with particles volume fraction ϕ :

$$\eta = \eta_0(1 + k_e\phi) \quad (\text{B.1})$$

where η_0 is the initial viscosity of the fluid and k_e a constant, which is equal to 2.5 for spherical particles. This equation is generally valid for $\phi < 2\%$. For higher particles concentration, a quadratic term is added:

$$\eta = \eta_0(1 + k_e\phi + k_H\phi^2). \quad (\text{B.2})$$

However, in the past few years, a number of articles were published on a newly discovered phenomenon of strong viscosity reduction of linear-chain polymers when very

small nanoparticles (NP) were dispersed [166–171]. It was observed that this effect depends on the size and concentration of the nanoparticles. In particular, the particle size should be approximately the same as the radius of gyration of the free molecular chain. In this case, the macromolecule can partly adsorb on the surface of the nanoparticle. As a consequence, it does not contribute any longer to melt entanglement; hence the melt viscosity is reduced. The effect is also dependent on the concentration of particles. At first, the viscosity is reduced due to the aforementioned effect. When particle concentration exceeds a certain threshold, viscosity starts to increase again, due to the increased interaction between particles. The effect was found in melt-particle systems, in particular for a melt PP-silica nanocomposite a decrease of 80% in viscosity was observed [172].

The goal of this study is to exploit the non-Einstein-like behavior of nanoparticles-thermoplastic dispersions in order to reduce TP viscosity and enhance their processability in composite manufacturing. In order to prove the concept, silica NPs were added to concentrated aqueous solutions of PEG at different molecular weights. PEG was chosen because it is highly soluble in water, and it can be used to perform fabric impregnation in RTM conditions at room temperature. First, the effect of polymer size and nanoparticles concentration on the viscosity of various PEG-silica samples is investigated. Finally, the feasibility for melt TP-RTM process is demonstrated by direct impregnation of dry fabrics in an RTM mould.

B.2 Materials and methods

B.2.1 Materials

Colloidal silica NPs (LUDOX® SM, 30%wt in water, Sigma Aldrich) were used as nanofillers; one size of nanoparticles was selected. The polymer size was changed by varying its molecular weight. The following empirical relation was used to determine the radius of gyration of PEG [173]

$$R_g = 0.0215M_w^{0.583} \quad (\text{B.3})$$

where M_w is the molecular weight of a chain of PEG. PEG at different molecular weights (20 and 35 kg mol⁻¹, Sigma Aldrich) was used in water solutions as test fluids to prove the concept of viscosity reduction.

B.2.2 Samples preparation

Two types of samples were prepared and studied: PEG-silica water suspension and a PEG-silica nanocomposite powder. A list of all the samples is displayed in Table B.1*.

The PEG-silica suspensions were prepared by direct mixing in water. The concentration of PEG was kept constant at 50%wt in water, while SiO₂ was varied from 0 to 2%wt, with respect to the amount of PEG. To prepare the suspensions, a proper amount of colloidal silica LUDOX® SM was first diluted in water. Then PEG was added to the suspension and dissolved by means of sonication.

The nanocomposites were prepared by solvent casting of suspensions in Teflon molds. Water evaporation was carried out in a vacuum chamber at ambient temperature. The dry polymer was then ground in a ceramic mortar and mechanically mixed.

B.2.3 Dynamic Light Scattering (DLS)

To determine the size of silica nanoparticles, DLS measurements were performed on a Zetasizer Nano ZS™(Malvern).

The LUDOX® SM suspension was diluted in DI water up to a final concentration of silica of 1 mg ml⁻¹. Around 1 ml in a disposable plastic cuvette was used for each measurement.

B.2.4 Rheology

Viscosity was measured on a rheometer AR2000ex (TA Instruments) in plate-plate configuration, and shear-rate ramps in flow-mode were conducted between 0.1 and 100 s⁻¹. A peltier-plate temperature control system was used for the suspension to perform measurements at 15 °C, while an oven-heating system was used for the measurements on the melt PEG-silica nanocomposite at 90 °C.

*Notice that the sample labeled PEG35K-50% coincides with the PEG-50% of Table 3.2, Chapter 3.

Table B.1: List of samples PEG-silica for rheological study.

Designation	PEG (kg mol ⁻¹)	SiO ₂ (%wt)	Sample type
PEG35K-50%	35	0	water suspension
PEG35K-50%-01	35	0.1	water suspension
PEG35K-50%-02	35	0.2	water suspension
PEG35K-50%-03	35	0.3	water suspension
PEG35K-50%-05	35	0.5	water suspension
PEG35K-50%-1	35	1	water suspension
PEG35K-50%-2	35	2	water suspension
PEG20K-50%	20	0	water suspension
PEG20K-50%-01	20	0.1	water suspension
PEG20K-50%-02	20	0.2	water suspension
PEG20K-50%-03	20	0.3	water suspension
PEG20K-50%-05	20	0.5	water suspension
PEG20K-50%-1	20	1	water suspension
PEG20K-50%-2	20	2	water suspension
PEG35K	35	0	solvent casted
PEG35K-01	35	0.1	solvent casted
PEG35K-02	35	0.2	solvent casted
PEG35K-03	35	0.3	solvent casted

Relative viscosity, defined as the ratio between the viscosity of the particle-filled fluid η and the viscosity of the pure fluid η_0 , that is

$$\eta_{rel} = \frac{\eta}{\eta_0}, \quad (\text{B.4})$$

is plotted against silica volume fraction ϕ , which is directly calculated from the mass fraction w as

$$\phi = \frac{\rho_{PEG}}{\rho_{PEG} + \rho_{SiO_2}(1/w - 1)} \quad (\text{B.5})$$

where ρ_{PEG} and ρ_{SiO_2} are the densities of PEG and silica. For PEG the density is 1.2 g/cm³ (from producer) and for the density for amorphous silica is taken as 2.2 g/cm³. At least three measurements were performed for each silica concentration, so as to determine a standard deviation.

B.2.5 Impregnation

In order to prove a practical application in TP-RTM of this viscosity-reduction effect, constant-pressure in-plane impregnation of glass-fabric were performed on the same setup used for permeability measurements described in Section 3.2.1. Two impregnations were performed on a stack of five layers of G-PLY with PEG35K-50% and PEG35K-50%-03 as fluids, which is the suspension with the lowest viscosity, as will be shown later in the results.

B.3 Results

Particle-size distributions (PSD) from dynamic light scattering (DLS) on the colloidal silica Ludox® SM are displayed in Fig. B.1. The mean is around 32 nm for intensity PSD, 16 nm for volume PSD and 12 nm for number PSD. Therefore, an average particle size of 20 nm can be estimated. From Eq. B.3, radii of gyration of PEG 20 and 35 kg mol⁻¹, are found to be 6.9 and 9.6 nm, respectively.

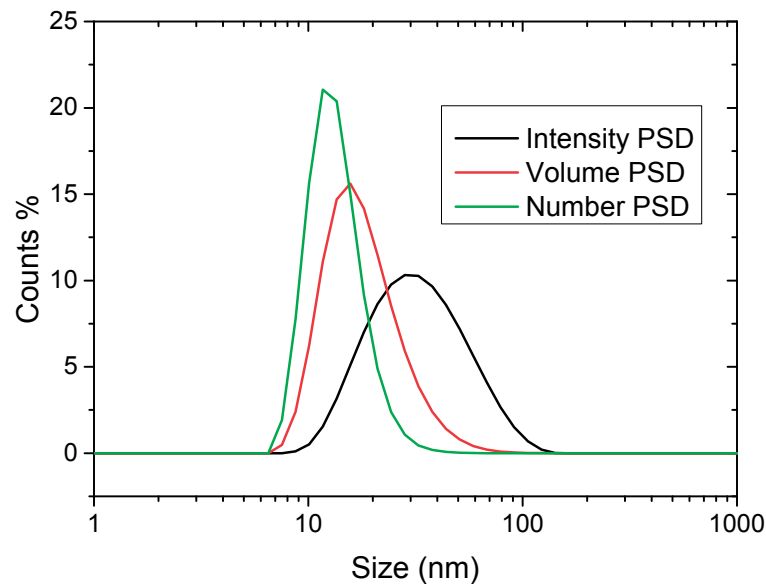


Fig. B.1: Particle-size distributions of colloidal silica Ludox® SM.

The variation of relative viscosity with silica volume fraction is plotted in Fig. B.2 for the three types of samples, namely the two PEG-silica suspensions and PEG-silica nanocomposite melt. Einstein relation (also displayed in the graph) is not always respected. In particular, in the case of PEG35K suspensions, a decrease of viscosity down

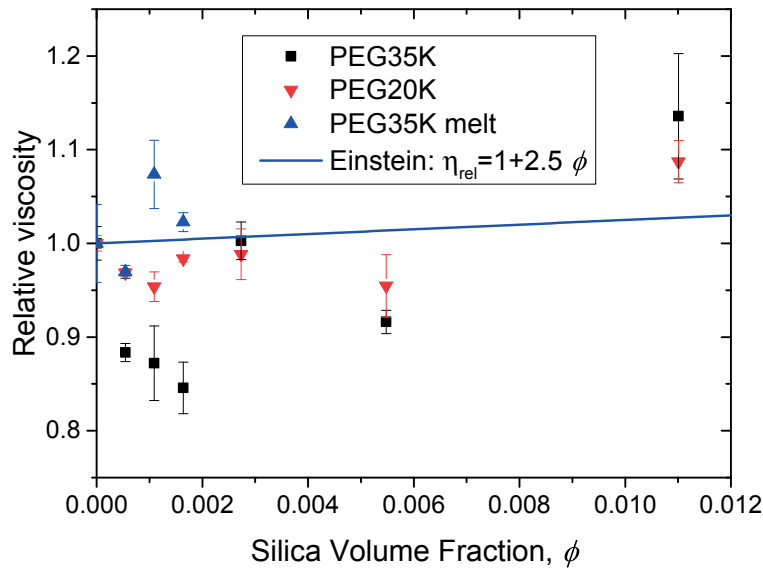


Fig. B.2: Relative viscosity as a function of silica nanoparticles volume fraction for the three different fluids.

to 15% was measured for the sample PEG35K-50%-03, which corresponds to a volume fraction around 0.0015. When further increasing silica content, the viscosity increases again. It might be remarked that the decrease is not as strong as that reported in literature, for instance in the case of melt silica-PP nanocomposite [172], where 80% viscosity reduction was achieved. This might be due to the different type of system here examined. In the present case, polymer and particles are dissolved/dispersed in 50%wt of water, which does not contribute to the viscosity-reduction effect. Also, the particles have a certain probability to be freely dispersed in the solvent, rather than in contact with the macromolecules. For the PEG20K this behavior is less marked, perhaps due to the fact that the size of the PEG35K is closer to the size of the particles. In the case of the melt nanocomposite, it seems to follow well the Einstein relation. Perhaps, particles aggregation has occurred during water evaporation, or the particles might not be well distributed in the PEG matrix.

The results from flow experiments performed with the fluids PEG35K-50% and PEG35K-50%-03 are reported in Fig. B.3. The squared flow-front position normalized with the applied pressure is plotted versus time, demonstrating that flow was enhanced in for the solution filled with NPs. From Darcy's law, the time evolution of squared flow-front is given by

$$\frac{L^2}{-\Delta P_{app}} = \frac{2K}{(1 - V_f)\eta} t = mt \quad (\text{B.6})$$

thus, a change in viscosity should be reflected in a change in the slope m :

$$\frac{m_1 - m_2}{m_1} = \frac{\eta_1 - \eta_2}{\eta_1}. \quad (\text{B.7})$$

A variation of 35% in slope is found, which is even higher compared to the decrease in viscosity between the two fluids (15%). It can be due to the fact that the rheology measurements were performed at lower temperature (15 °C), whereas the impregnation was performed at room temperature (≈ 20 °C). In addition, a slight difference in fabric permeability and volume fraction, or temperature difference between the two experiments might have contributed to overestimate the slope change. Moreover, permeability measurements are affected by high uncertainty, thus a larger number of experiments should be performed to confirm this trend.

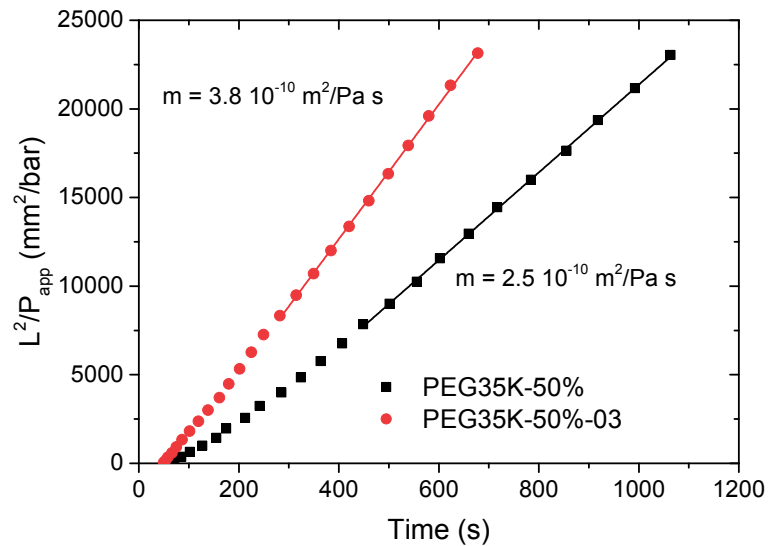


Fig. B.3: Time-evolution of pressure-normalized squared flow-front position for PEG solutions with and without silica nanoparticles.

B.4 Conclusions and outlook

In this study, we investigated the opportunity to exploit a newly-discovered nano-size effect of viscosity reduction of TPs with NPs.

At this stage, preliminary studies have been conducted on model systems. Two types of PEG-silica systems were investigated, namely aqueous suspensions and nanocomposites. As the mutual size of particle and polymer supposedly plays a significant role,

it is necessary to target the appropriate size. Dynamic light scattering was used to determine the size range of commercial colloidal silica nanoparticles. No effect was found on the melt nanocomposite, probably due to aggregation or inhomogeneous particles distribution, but viscosity reduction was observed for the aqueous suspensions. The reduction was stronger for the PEG with higher molecular weight (35kDa), which has a size closer to the one of the nanoparticles. As a proof of concept, a fabric impregnation at constant applied pressure was performed in a transparent RTM mold, in order to record the evolution. Flow-enhancement was successfully demonstrated.

Further studies should be carried out on industrially relevant polymers, such as polyamides. The issue with PAs is that they dissolve in very strong solvents, such as hexafluoroisopropanol (HFIP), which is highly acidic. LUDOX SM suspension is stabilized at basic pH, and mixing in HFIP causes instantaneous agglomeration. A procedure was fine tuned in order to efficiently disperse silica nanoparticles in HFIP and dissolve HFPA66 in it. LUDOX suspension was dispersed in a solution of HFIP, ethanol (EtOH) and octanol (OcOH), at a volume ratio of HFIP:EtOH:OcOH=40:10:1. Different volumes of LUDOX were dispersed in the same volume of solution (25.5 ml). After sonication, 2 g of HFPA66 were added to the solution and stirred with a magnet overnight. The solutions appeared clear and the polymer well dissolved. Subsequently, they were poured in Petri dish to facilitate solvent evaporation. However, excessive degradation of the polymer resulted, and it was not possible to use these suspensions for rheological measurement. Another possibility is to use solid NPs, and directly mix with the polymer in a twin-extruder. Then, the shear forces might help to avoid particle aggregation, and this way no solvents are needed.

Bibliography

- [1] Communication from the Commission to the European Parliament, the Council, the European Economic and Social Committee and the Committee of the Regions: A Roadmap for moving to a competitive low carbon economy in 2050, European Commission, Brussels 8 March 2011, COM(2011) 112 final.
- [2] Communication from the Commission to the European Parliament, the Council, the European Economic and Social Committee and the Committee of the Regions: A European Strategy for Low-Emission Mobility, European Commission, Brussels 27 July 2016, COM(2016) 501 final.
- [3] Proposal for a Regulation of the European Parliament and of the Council: Setting emission performance standards for new passenger cars as part of the Community's integrated approach to reduce CO₂ emissions from light-duty vehicles, European Commission, Brussels 26 January 2018, COM(2017) 676 final/2.
- [4] Andrew McWilliams. Lightweight materials in transportation. Report overview, BCC Research, January 2013.
- [5] Technology roadmap for energy reduction in automotive manufacturing. Technical report, U.S. Department of Energy, Office of Energy Efficiency & Renewable Energy Industrial Technologies Program & U.S. Council for Automotive Research, September 2008.
- [6] Light duty automotive technology and fuel economy trends: 1975 through 2008. Technical Report EPA420-R-08-015, U.S. Environmental Protection Agency (U.S. EPA), September 2008.
- [7] An assessment of mass reduction opportunities for a 2017 – 2020 model year vehicle program. Technical Report REV 006A, Lotus Engineering Inc., 2010.
- [8] Nicholas Lutsey. Review of technical literature and trends related to automobile mass-reduction technology. Technical Report UCD-ITS-RR-10-10, Institute of Transportation Studies, Davis, California 95616, May 2010.
- [9] ITF (International Transport Forum). Lightening Up: How Less Heavy Vehicles Can Help Cut CO₂ Emissions. Technical report, Paris, 2017.
- [10] Elaheh Ghassamieh. Materials in automotive application, state of the art and prospects, new trends and developments in automotive industry. In Prof. Marcello Chiaberge, editor, *New Trends and Developments in Automotive Industry*, InTech, pages 365–394. January 2011. ISBN 978-953-307-999-8.
- [11] Ahmed Elmarakbi, editor. *Advanced Composite Materials for Automotive Applications: Structural Integrity and Crashworthiness*. Automotive Series. Wiley, 2014. ISBN 978-1-118-42386-8.
- [12] C-K. Park, C-D. Kan, W. Hollowell, and S.I. Hill. Investigation of opportunities for lightweight vehicles using advanced plastics and composites. Technical

- Report DOT HS 811 692, U.S. Department of Transportation, National Highway Traffic Safety Administration, Washington, DC, December 2012.
- [13] Jürgen Hirsch. Aluminium in innovative light-weight car design. *Materials Transactions*, 52(5):818–824, 2011.
- [14] W.F. Powers. Automotive materials in the 21st century. *Advanced Materials and Processes*, 157(5):38–42, 2000.
- [15] R. A. Witik, J. Payet, V. Michaud, C. Ludwig, and J.-A. E. Månson. Assessing the life cycle costs and environmental performance of lightweight materials in automobile applications. *Composites Part A: Applied Science and Manufacturing*, 42(11):1694–1709, 2011. doi: 10.1016/j.compositesa.2011.07.024.
- [16] Uday Vaidya. *Composites for automotive, truck and mass transit: materials, design, manufacturing*. DEStech Publications, Lancaster, Pa., 2011. ISBN 1932078797 9781932078794.
- [17] M. Holmes. Lowering the cost of carbon fiber. *Reinforced Plastics*, 61(5):279 – 283, 2017. doi: <https://doi.org/10.1016/j.repl.2017.02.001>.
- [18] K. van Rijswijk and H. E. N. Bersee. Reactive processing of textile fiber-reinforced thermoplastic composites – An overview. *Composites Part A: Applied Science and Manufacturing*, 38(3):666–681, 2007. doi: 10.1016/j.compositesa.2006.05.007.
- [19] E. De Luycker, F. Morestin, P. Boisse, and D. Marsal. Simulation of 3D interlock composite preforming. *Composite Structures*, 88(4):615–623, 2009. doi: 10.1016/J.COMPSTRUCT.2008.06.005.
- [20] F. Boussu, I. Cristian, and S. Nauman. General definition of 3D warp interlock fabric architecture. *Composites Part B: Engineering*, 81:171–188, 2015. doi: 10.1016/J.COMPOSITESB.2015.07.013.
- [21] N. Vernet and F. Trochu. Analysis and modeling of 3D Interlock fabric compaction behavior. *Composites Part A: Applied Science and Manufacturing*, 80: 182–193, 2016. doi: 10.1016/J.COMPOSITESA.2015.10.024.
- [22] D. Montarnal, M. Capelot, F. Tournilhac, and L. Leibler. Silica-like malleable materials from permanent organic networks. *Science*, 334(6058):965–968, 2011. doi: 10.1126/science.1212648.
- [23] M. Röttger, T. Domenech, R. van der Weegen, A. Breuillac, R. Nicolaj, and L. Leibler. High-performance vitrimers from commodity thermoplastics through dioxaborolane metathesis. *Science*, 356(6333):62–65, 2017. doi: 10.1126/science.aah5281.
- [24] S. Dalle Vacche, V. Michaud, M. Demierre, P.-E. Bourban, and J.-A.E. Månson. Curing kinetics and thermomechanical properties of latent epoxy/carbon fiber composites. *IOP Conference Series: Materials Science and Engineering*, 139(1):012049, 2016.
- [25] O. Geiger, F. Henning, P. Eyerer, R. Brüssel, and H. Ernst. LFT-D: materials tailored for new applications. *Reinforced Plastics*, 50(1):30 – 35, 2006. doi: 10.1016/S0034-3617(06)70870-0.
- [26] J. M. García, F. C. García, F. Serna, and J. L. de la Peña. High-performance aromatic polyamides. *Progress in Polymer Science*, 35(5):623–686, 2010. doi: 10.1016/j.progpolymsci.2009.09.002.
- [27] J. A. Brydson. Polyamides and polyimides. In J. A. Brydson, editor, *Plastics Materials (Seventh Edition)*, pages 478–530. Butterworth-Heinemann, Oxford,

1999. ISBN 978-0-7506-4132-6.
- [28] J. Cretenoud, S. Galland, C.J.G. Plummer, V. Michaud, A. Bayer, N. Lamberts, B. Hoffmann, and H. Frauenrath. High-temperature copolyamides obtained by the efficient transamidation of crystalline-crystalline polyamide blends. *Journal of Applied Polymer Science*, 134:44349, 2017. doi: 10.1002/app.44349.
- [29] G. Orange, E. Bessard, J. Bréard, L. Bizet, J. L. Bailleul, S. Comas-Cardona, Ch Binetruy, Ph Boisse, and M. Gomina. Development of composite parts with RTM process based on new high-fluidity thermoplastic polymers. In *12th International Conference on Flow Processes in Composite Materials*, Enschede, The Netherlands, July 2014. URL http://www.tech.plym.ac.uk/sme/fpcm/FPCM12%5CExtendedAbstracts%5Cfpcm12_submission_28.pdf.
- [30] George C. Jacob, John F. Fellers, Srdan Simunovic, and J. Micheal Starbuck. Energy absorption in polymer composites for automotive crashworthiness. *Journal of Composite Materials*, 36(07):813–850, 2002.
- [31] H. Hamada, S. Ramakrishna, and H. Sato. Effect of fiber orientation on the energy absorption capability of carbon fiber/PEEK composite tubes. *Journal of Composite Materials*, 30(8):947–963, 1996. doi: 10.1177/002199839603000806.
- [32] K. H. Tsai C. H. Chiu. Effects of braiding parameters on energy absorption capability of triaxially braided composite tubes. 32(21):1964–1983, 1998. doi: 10.1177/002199839803202105.
- [33] Chiara Bisagni, Giuseppe Di Pietro, Lara Frascini, and Davide Terletti. Progressive crushing of fiber-reinforced composite structural components of a formula one racing car. *Composite Structures*, 68(4):491–503, 2005. doi: 10.1016/j.compstruct.2004.04.015.
- [34] Jung-Seok Kim, Hyuk-Jin Yoon, and Kwang-Bok Shin. A study on crushing behaviors of composite circular tubes with different reinforcing fibers. *International Journal of Impact Engineering*, 38(4):198–207, 2011. doi: 10.1016/j.ijimpeng.2010.11.007.
- [35] S. Cauchi Savona and P. J. Hogg. Effect of fracture toughness properties on the crushing of flat composite plates. *Composites Science and Technology*, 66(13):2317–2328, 2006. doi: 10.1016/j.compscitech.2005.11.038.
- [36] George C. Jacob, J. Michael Starbuck, John F. Fellers, and Srdan Simunovic. Effect of fiber volume fraction, fiber length and fiber tow size on the energy absorption of chopped carbon fiber–polymer composites. *Polymer Composites*, 26(3):293–305, 2005. doi: 10.1002/pc.20100.
- [37] H.G. Herrmann, C. Mohrdieck, and R. Bjekovic. Materials for the automotive lightweight design. Technical report, Institut fur Kraftfahrzeuge, Aachen, Germany, 2002.
- [38] G. Caprino and A. D’Amore. Flexural fatigue behaviour of random continuous-fibre-reinforced thermoplastic composites. *Composites Science and Technology*, 58(6):957 – 965, 1998. doi: 10.1016/S0266-3538(97)00221-2.
- [39] M. A. Badie and E. Mahdi. An investigation into hybrid carbon/glass fiber reinforced epoxy composite automotive drive shaft. *Materials & Design*, 32(3):1485–1500, 2011. doi: 10.1016/j.matdes.2010.08.042.
- [40] W. W. Graessley and E. S. Shinbach. Flow properties of branched polydisperse polymers. *Journal of Polymer Science: Polymer Physics Edition*, 12(10):2047–2063, 1974. doi: 10.1002/pol.1974.180121007.

- [41] Ralph H. Colby, Lewis J. Fetters, and William W. Graessley. The melt viscosity-molecular weight relationship for linear polymers. *Macromolecules*, 20(9):2226–2237, 1987. doi: <http://dx.doi.org/10.1021/ma00175a030>.
- [42] Thomas G Fox and Paul J. Flory. Further studies on the melt viscosity of polyisobutylene. *The Journal of Physical Chemistry*, 55(2):221–234, 1951. doi: 10.1021/j150485a010.
- [43] Understanding rheology of thermoplastic polymers. Technical Report AAN013, TA Instruments. URL http://www.tainstruments.com/pdf/literature/AAN013_V_1_U_Thermoplast.pdf.
- [44] Anders Hult, Mats Johansson, and Eva Malmström. Hyperbranched polymers. In J. Roovers, editor, *Branched Polymers II*, number 143 in *Advances in Polymer Science*, pages 1–34. Springer Berlin Heidelberg, January 1999. ISBN 978-3-540-65005-8, 978-3-540-49780-6.
- [45] Markus Scholl, Zuzana Kadlecova, and Harm-Anton Klok. Dendritic and hyperbranched polyamides. *Progress in Polymer Science*, 34(1):24–61, 2009. doi: 10.1016/j.progpolymsci.2008.09.001.
- [46] C Gao and D Yan. Hyperbranched polymers: from synthesis to applications. *Progress in Polymer Science*, 29(3):183–275, 2004. doi: 10.1016/j.progpolymsci.2003.12.002.
- [47] B. Pettersson and K. Sörensen. In *Proceedings of the 21st Waterborne, Higher Solids & Powder Coatings Symposium*, page 753, New Orleans, Louisiana, 1994.
- [48] Melvin Avrami. Kinetics of phase change. i general theory. *The Journal of Chemical Physics*, 7(12):1103–1112, 1939. doi: 10.1063/1.1750380.
- [49] W.A. Johnson and R. Mehl. *Trans. AIME*, 135:416, 1939.
- [50] A.N. Kolmogorov. *Izv. Akad. Nauk USSR, Ser. Mater.*, 3:355, 1937.
- [51] Christopher C. Ibeh. *Thermoplastic Materials: Properties, Manufacturing Methods, and Applications*. CRC Press, 2011. ISBN 978-1-4200-9383-4.
- [52] R.J. Young and P.A. Lovell. *Introduction to Polymers*. Chapman and Hall, 1991. ISBN 0-412-30640-9.
- [53] C. J. G. Plummer, J.-E. Zanetto, P.-E. Bourban, and J.-a. E. Månson. The crystallization kinetics of polyamide-12. *Colloid and Polymer Science*, 279(4):312–322, 2001. doi: 10.1007/s003960000425.
- [54] J. Faraj, B. Pignon, N. Boyard, J.-L. Bailleul, D. Delaunay, and G Orange. Isothermal crystallization kinetics of low viscosity polyamide 66. In *16th European Conference on Composite Materials*, Seville, Spain, June 2014.
- [55] J. Faraj, N. Boyard, B. Pignon, J.-L. Bailleul, D. Delaunay, and G. Orange. Thermochimica Acta Crystallization kinetics of new low viscosity polyamides 66 for thermoplastic composites processing. *Thermochimica Acta*, 624:27–34, 2016. doi: 10.1016/j.tca.2015.11.025.
- [56] Krishan Kumar Chawla. *Composite materials science and engineering*. Springer, New York, 2012. ISBN 9780387743653 0387743650.
- [57] Suresh G. Advani and Kuang-Ting Hsaio. *Manufacturing techniques for polymer matrix composites (PMCs)*. Woodhead Publishing Limited, 2012. ISBN 978-0-85709-067-6.
- [58] P.-E. Bourban, N. Bernet, J.-E. Zanetto, and J.-A. E. Månson. Material phenomena controlling rapid processing of thermoplastic composites. *Composites Part A: Applied Science and Manufacturing*, 32(8):1045–1057, 2001.

- [59] M. D. Wakeman, L. Zingraff, P. E. Bourban, J. A. E. Månson, and P. Blanchard. Stamp forming of carbon fibre/PA12 composites – A comparison of a reactive impregnation process and a commingled yarn system. *Composites Science and Technology*, 66(1):19–35, 2006. doi: 10.1016/j.compscitech.2005.06.001.
- [60] L. Zingraff, V. Michaud, P.-E. Bourban, and J.-A.E. Månson. Resin transfer moulding of anionically polymerised polyamide 12. *Composites Part A: Applied Science and Manufacturing*, 36(12):1675–1686, 2005. doi: 10.1016/j.compositesa.2005.03.023.
- [61] Loïc Zingraff. *Void formation and transport during liquid moulding and forming of reactive thermoplastic composites*. PhD thesis, École Polytechnique Fédérale de Lausanne, Lausanne, 2004. URL http://infoscience.epfl.ch/record/33381/files/EPFL_TH2906.pdf.
- [62] J. Verrey, V. Michaud, and J.-A.E. Månson. Dynamic capillary effects in liquid composite moulding with non-crimp fabrics. *Composites Part A: Applied Science and Manufacturing*, 37(1):92–102, 2006. doi: 10.1016/j.compositesa.2005.04.011.
- [63] J. Verrey, M. D. Wakeman, V. Michaud, and J.-A. E. Månson. Manufacturing cost comparison of thermoplastic and thermoset RTM for an automotive floor pan. *Composites Part A: Applied Science and Manufacturing*, 37(1):9–22, 2006. doi: 10.1016/j.compositesa.2005.05.048.
- [64] A. Luisier, P.-E. Bourban, and J.-A. E. Månson. Time–temperature–transformation diagram for reactive processing of polyamide 12. *Journal of Applied Polymer Science*, 81(4):963–972, 2001. doi: 10.1002/app.1518.
- [65] K. van Rijswijk, H. E. N. Bersee, A. Beukers, S. J. Picken, and A. A. van Geenen. Optimisation of anionic polyamide-6 for vacuum infusion of thermoplastic composites: Influence of polymerisation temperature on matrix properties. *Polymer Testing*, 25(3):392–404, 2006. doi: 10.1016/j.polymertesting.2005.11.008.
- [66] K. van Rijswijk, H. E. N. Bersee, W. F. Jager, and S. J. Picken. Optimisation of anionic polyamide-6 for vacuum infusion of thermoplastic composites: Choice of activator and initiator. *Composites Part A: Applied Science and Manufacturing*, 37(6):949–956, 2006. doi: 10.1016/j.compositesa.2005.01.023.
- [67] K. van Rijswijk, S. Lindstedt, D. P. N. Vlasveld, H. E. N. Bersee, and A. Beukers. Reactive processing of anionic polyamide-6 for application in fiber composites: A comparative study with melt processed polyamides and nanocomposites. *Polymer Testing*, 25(7):873–887, 2006. doi: 10.1016/j.polymertesting.2006.05.006.
- [68] K. van Rijswijk, A. A. van Geenen, and H. E. N. Bersee. Textile fiber-reinforced anionic polyamide-6 composites. Part II: Investigation on interfacial bond formation by short beam shear test. *Composites Part A: Applied Science and Manufacturing*, 40(8):1033–1043, 2009. doi: 10.1016/j.compositesa.2009.02.018.
- [69] K. van Rijswijk, J. J. E. Teuwen, H. E. N. Bersee, and A. Beukers. Textile fiber-reinforced anionic polyamide-6 composites. Part I: The vacuum infusion process. *Composites Part A: Applied Science and Manufacturing*, 40(1):1–10, 2009. doi: 10.1016/j.compositesa.2008.03.018.
- [70] Julie J. E. Teuwen, Ab A. van Geenen, and Harald E. N. Bersee. Temperature evolution during processing of thick-walled anionic polyamide 6 composites: Experiment and simulation. *Macromolecular Materials and Engineering*, 298(7):

- 722–729, 2013. doi: 10.1002/mame.201200083.
- [71] Chun Yan, Hongzhou Li, Xiaoqing Zhang, Yingdan Zhu, Xinyu Fan, and Liping Yu. Preparation and properties of continuous glass fiber reinforced anionic polyamide-6 thermoplastic composites. *Materials & Design*, 46:688–695, 2013. doi: 10.1016/j.matdes.2012.11.034.
- [72] P. O. Mairtin, P. McDonnell, M.T. Connor, R. Eder, and C.M.O. Bradaigh. Process investigation of a liquid PA-12/carbon fibre moulding system. *Composites Part A: Applied Science and Manufacturing*, 32(7):915 – 923, 2001. doi: [http://dx.doi.org/10.1016/S1359-835X\(01\)00005-7](http://dx.doi.org/10.1016/S1359-835X(01)00005-7).
- [73] A. Maazouz, K. Lamnawar, and M. Dkier. Chemorheological study and in-situ monitoring of PA6 anionic-ring polymerization for RTM processing control. *Composites Part A: Applied Science and Manufacturing*, 107:235–247, 2018. doi: 10.1016/J.COMPOSITESA.2018.01.007.
- [74] Hilde Parton, Joris Baets, Pascale Lipnik, Bart Goderis, Jacques Devaux, and Ignaas Verpoest. Properties of poly(butylene terephthalate) polymerized from cyclic oligomers and its composites. *Polymer*, 46(23):9871 – 9880, 2005. doi: <http://dx.doi.org/10.1016/j.polymer.2005.07.082>.
- [75] John P. Ciovacco and Steven J. Winckler. Processing with cyclic PBT to produce thermoplastic composites. *International SAMPE Symposium and Exhibition (Proceedings)*, 45, 2000.
- [76] Z.A. Mohd Ishak, Y.W. Leong, M. Steeg, and J. Karger-Kocsis. Mechanical properties of woven glass fabric reinforced in situ polymerized poly(butylene terephthalate) composites. *Composites Science and Technology*, 67(3–4):390 – 398, 2007. doi: <http://dx.doi.org/10.1016/j.compscitech.2006.09.012>.
- [77] W. Michaeli, J. Strohhäcker, R. Schöldgen, L. Winkelmann, and J. Wessels. Production of thermoplastic composites with LCM-techniques. *International SAMPE Symposium and Exhibition (Proceedings)*, 54, 2009.
- [78] Kathy C. Chuang, Jim M. Criss, Jr., Eric A. Mintz, Daniel A. Scheiman, Baochau N. Nguyen, and Linda S. McCorkle. Low-melt viscosity polyimide resins for resin transfer molding (RTM) II. Baltimore, MD, June 2007.
- [79] Elium® resins for composites, accessed on 01-05-2018. URL <https://www.arkema.com/en/products/product-finder/range-viewer/Elium-resins-for-composites/>.
- [80] D. Becker, G. Francois, V. Bozsak, and P. Mitschang. Combining the best of two polymer worlds. Thermoformable acrylic resin systems for large-scale production. *Kunststoffe International*, 12, 2016.
- [81] M. Haggui, A. El Mahi, Z. Jendli, A. Akrouf, and M. Haddar. Damage Analysis of Flax Fibre / Elium Composite Under Static and Fatigue Testing. In M. Haddar, F. Chaari, A. Benamara, M. Chouchane, C. Karra, and N. Aifaoui, editors, *Design and Modeling of Mechanical Systems—III. CMSM 2017. Lecture Notes in Mechanical Engineering*, pages 681–691. Springer, Cham, Lecture Notes in Mechanical Engineering edition, 2018. ISBN 9783319666976. doi: 10.1007/978-3-319-66697-6_66.
- [82] C. Vicard, O. De Almeida, A. Cantarel, and G. Bernhart. Experimental study of polymerization and crystallization kinetics of polyamide 6 obtained by anionic ring opening polymerization of ϵ -caprolactam. *Polymer*, 132:88–97, 2017. doi: 10.1016/J.POLYMER.2017.10.039.

- [83] Gilles Orange, Roland Durand, and Franck Touraud. Composite polyamide article, US 2012/0322326 A1, December 2012. URL <http://www.google.com/patents/US20120322326>.
- [84] Franco Speroni and Damien Zaher. High-flow polyamides, US 2012/0245282 A1, September 2012. URL <http://www.google.com/patents/US20120245282>.
- [85] Guillaume Cazaux. *Faisabilité des procédés LCM pour l'élaboration de composites fibres longues à matrice polyamide*. PhD thesis, Normandie Université, 2016.
- [86] Jalal Faraj. *Analyse thermocinétique de la cristallisation en milieu confiné d'un composite à base d'une résine thermoplastique (Polyamide 66)*. PhD thesis, Université de Nantes, 2016.
- [87] G. Cazaux, L. Bizet, J. Bréard, M. Gomina, S. Comas-Cardona, C. Binetruy, and G. Orange. Design of a quasi-unidirectional fabric for RTM process with high-fluidity thermoplastic: Longitudinal permeability and microstructure. In *12th International Conference on Flow Processes in Composite Materials*, Enschede, The Netherlands, July 2014. URL http://www.tech.plym.ac.uk/sme/fpcm/FPCM12{%}5CExtendedAbstracts{%}5Cfpcm12{%}_submission{%}_39.pdf.
- [88] G. Cazaux, L. Bizet, J. Bréard, M. Gomina, E. Syerko, S. Comas-Cardona, C. Binetruy, and G. Orange. Permeability enhancement with different glass fiber quasi-UD sutructure arrangements for RTM-TP process. In *20th International Conference on Composite Materials*, Copenhagen, Denmark, July 2015.
- [89] G. Cazaux, L. Bizet, B. Duchemin, J. Bréard, M. Gomina, and G. Orange. Caractérisation des tensions de surface de différents polyamides 6,6 utilisés dans le procédé RTM. In *19ème Journée Nationale sur les Composites*, Lyon, France, June 2015.
- [90] E. Syerko, C. Binetruy, S. Comas-Cardona, and A. Leygue. A numerical approach to design dual-scale porosity composite reinforcements with enhanced permeability. *Materials and Design*, 131:307–322, 2017. doi: 10.1016/j.matdes.2017.06.035.
- [91] J. Faraj, J.-L. Bailleul, N. Boyard, D. Delaunay, N. Lefevre, and G. Orange. Thermal Analysis During The Consolidation Of PA 66 composite By RTM Process. In *19th International ESAFORM Conference on Material Forming*, Nantes, France, 2016. AIP Publishing. ISBN 9780735414273. doi: 10.1063/1.4963575.
- [92] V. Michaud and A. Mortensen. Infiltration processing of fiber reinforced composites: governing phenomena. *Composites Part A*, 32:981–996, 2001.
- [93] Véronique Michaud. Permeability properties of reinforcements in composites. In *Composite Reinforcements for Optimum Performance*, page 431. 2011.
- [94] Henry Darcy. *Les fontaines publiques de la ville de Dijon*. Victor Dalmont (Paris), 1856. URL <http://gallica.bnf.fr/ark:/12148/bpt6k624312>.
- [95] P. C. Carman. Fluid flow through granular beds. *Chemical Engineering Research and Design*, 15:S150–S166, 1937.
- [96] Adrian E. Scheidegger. *The physics of flow through porous media*. University of Toronto Press, Toronto, 3rd edition, 1974. ISBN 0802018491.
- [97] B. R. Gebart. Permeability of unidirectional reinforcements for RTM. *Journal of Composite Materials*, 26(8):1100–1133, 1992. doi: 10.1177/002199839202600802.

- [98] R. Arbter, J. M. Beraud, C. Binetruy, L. Bizet, J. Bréard, S. Comas-Cardona, C. Demaria, A. Endruweit, P. Ermanni, F. Gommer, S. Hasanovic, P. Henrat, F. Klunker, B. Laine, S. Lavanchy, S. V. Lomov, A. Long, V. Michaud, G. Morren, E. Ruiz, H. Sol, F. Trochu, B. Verleye, M. Wietgreffe, W. Wu, and G. Ziegmann. Experimental determination of the permeability of textiles: A benchmark exercise. *Composites Part A: Applied Science and Manufacturing*, 42(9):1157–1168, 2011. doi: 10.1016/j.compositesa.2011.04.021.
- [99] N. Vernet, E. Ruiz, S. Advani, J. B. Alms, M. Aubert, M. Barburski, B. Barari, J. M. Beraud, D. C. Berg, N. Correia, M. Danzi, T. Delavière, M. Dickert, C. Di Fratta, A. Endruweit, P. Ermanni, G. Francucci, J. A. Garcia, A. George, C. Hahn, F. Klunker, S. V. Lomov, A. Long, B. Louis, J. Maldonado, R. Meier, V. Michaud, H. Perrin, K. Pillai, E. Rodriguez, F. Trochu, S. Verheyden, M. Wietgreffe, W. Xiong, S. Zaremba, and G. Ziegmann. Experimental determination of the permeability of engineering textiles: Benchmark II. *Composites Part A: Applied Science and Manufacturing*, 61:172–184, 2014. doi: 10.1016/j.compositesa.2014.02.010.
- [100] J. Bréard, Y. Henzel, F. Trochu, and R. Gauvin. Analysis of dynamic flows through porous media. Part I: Comparison between saturated and unsaturated flows in fibrous reinforcements. *Polymer Composites*, 24(3):391–408, 2003.
- [101] R. L. Hoffman. A study of the advancing interface. I. Interface shape in liquid—gas systems. *Journal of Colloid and Interface Science*, 50(2):228–241, 1975.
- [102] L.H. Tanner. The spreading of silicone oil drops on horizontal surfaces. *Journal of Physics D: Applied Physics*, 12(9):1473–1484, 1979.
- [103] A. Mortensen and J. A. Cornie. On the infiltration of metal matrix composites. *Metallurgical Transactions A*, 18(13):1160–1163, 1987.
- [104] A. Mortensen and T. Wong. Infiltration of fibrous preforms by a pure metal: Part III. Capillary phenomena. *Metallurgical Transactions A*, 21(8):2257–2263, 1990.
- [105] S. Amico and C. Lekakou. An experimental study of the permeability and capillary pressure in resin-transfer moulding. *Composites Science and Technology*, 61(13):1945–1959, 2001.
- [106] M. F. Pucci, P.-J. Liotier, and S. Drapier. Capillary wicking in a fibrous reinforcement – Orthotropic issues to determine the capillary pressure components. *Composites Part A: Applied Science and Manufacturing*, 77:133–141, 2015. doi: 10.1016/j.compositesa.2015.05.031.
- [107] V. Michaud, L. M. Compton, and A. Mortensen. Capillarity in isothermal infiltration of alumina fiber preforms with aluminum. *Metallurgical and Materials Transactions A*, 25(10):2145–2152, 1994.
- [108] A. Léger, L. Weber, and A. Mortensen. Influence of the wetting angle on capillary forces in pressure infiltration. *Acta Materialia*, 91:57–69, 2015.
- [109] V. Michaud and A. Mortensen. On measuring wettability in infiltration processing. *Scripta Materialia*, 56(10):859–862, 2007.
- [110] C. Binetruy, J. Pabiot, and B. Hilaire. The influence of fiber wetting in resin transfer molding: Scale effects. *Polymer Composites*, 21(4):548–557, 2000.
- [111] K. J. Ahn, J. C. Seferis, and J. C. Berg. Simultaneous measurements of permeability and capillary pressure of thermosetting matrices in woven fabric reinforcements. *Polymer Composites*, 12(3):146–152, 1991.

- [112] N. Patel and L.J. Lee. Effects of fiber mat architecture on void formation and removal in liquid composite molding. *Polymer Composites*, 16(5):386–399, 1995. doi: 10.1002/pc.750160507.
- [113] N. Patel and L. J. Lee. Modeling of void formation and removal in liquid composite molding. Part I: Wettability analysis. *Polymer Composites*, 17(1):96–103, 1996. doi: 10.1002/pc.10594.
- [114] E. Ruiz, V. Achim, Sofiane Soukane, F. Trochu, and J. Bréard. Optimization of injection flow rate to minimize micro/macro-voids formation in resin transfer molded composites. *Composites Science and Technology*, 66(3-4):475–486, 2006. doi: 10.1016/j.compscitech.2005.06.013.
- [115] J.S. Leclerc and E. Ruiz. Porosity reduction using optimized flow velocity in Resin Transfer Molding. *Composites Part A: Applied Science and Manufacturing*, 39(12):1859–1868, 2008. doi: 10.1016/j.compositesa.2008.09.008.
- [116] C.H. Park, A. Lebel, A. Saouab, J. Bréard, and W.I. Lee. Modeling and simulation of voids and saturation in liquid composite molding processes. *Composites Part A: Applied Science and Manufacturing*, 42(6):658–668, 2011. doi: 10.1016/j.compositesa.2011.02.005.
- [117] F. LeBel, A. E. Fanaei, É. Ruiz, and F. Trochu. Prediction of optimal flow front velocity to minimize void formation in dual scale fibrous reinforcements. *International Journal of Material Forming*, 7(1):93–116, 2014. doi: 10.1007/s12289-012-1111-x.
- [118] Véronique Michaud. A Review of Non-saturated Resin Flow in Liquid Composite Moulding processes. *Transport in Porous Media*, 115(3):581–601, 2016. doi: 10.1007/s11242-016-0629-7.
- [119] Sébastien Guérout. *Analyse expérimentale de la saturation des milieux fibreux à double échelle de pores : application à la mise en oeuvre des matériaux composites par procédé RTM*. PhD thesis, Université du Havre, 2012.
- [120] D.A. Steenkamer, S.H. McKnight, D.J. Wilkins, and V.M. Karbhari. Experimental characterization of permeability and fibre wetting for liquid moulding. *Journal of Materials Science*, 30(12):3207–3215, 1995. doi: 10.1007/BF01209239.
- [121] T.S. Lundstrom, R. Stenberg, R. Bergstrom, H. Partanen, and P.A. Birkeland. In-plane permeability measurements: a nordic round-robin study. *Composites Part A: Applied Science and Manufacturing*, 31:29–43, 2000.
- [122] Y. Luo, I. Verpoest, K. Hoes, M. Vanheule, H. Sol, and A. Cardon. Permeability measurement of textile reinforcements with several test fluids. *Composites Part A: Applied Science and Manufacturing*, 32(10):1497–1504, 2001. doi: 10.1016/S1359-835X(01)00049-5.
- [123] F. D. Dungan and A. M. Sastry. Saturated and Unsaturated Polymer Flows: Microphenomena and Modeling. *Journal of Composite Materials*, 36(13):1581–1603, 2002. doi: 10.1177/0021998302036013179.
- [124] Krishna M. Pillai. Modeling the Unsaturated Flow in Liquid Composite Molding Processes: A Review and Some Thoughts. *Journal of Composite Materials*, 38(23):2097–2118, 2004. doi: 10.1177/0021998304045585.
- [125] Sung H. Kim, Jae W. Jung, Mei X. Li, Sung W. Choi, Woo I. Lee, and Chung H. Park. Unsaturated flow behavior in double-scale porous reinforcement for liquid composite molding processes. *Journal of Reinforced Plastics and Composites*, 36(2):85–97, 2017. doi: 10.1177/0731684416671422.

- [126] V. H. Hammond and A. C. Loos. The Effects of Fluid Type and Viscosity on the Steady-State and Advancing Front Permeability Behavior of Textile Preforms. *Journal of Reinforced Plastics and Composites*, 16(1):50–72, 1997. doi: 10.1177/073168449701600105.
- [127] J. Summerscales. A model for the effect of fibre clustering on the flow rate in resin transfer moulding. *Composites Manufacturing*, 4(1):27–31, 1993. doi: 10.1016/0956-7143(93)90013-X.
- [128] P. R. Griffin, S. M. Grove, F. J. Guild, P. Russel, and J. Summerscales. The effect of microstructure on flow promotion in resin transfer moulding reinforcement fabrics. *Journal of Microscopy*, 177(3):207–217, 1995.
- [129] P. R. Griffin, S. M. Grove, P. Russell, D. Short, J. Summerscales, F. J. Guild, and E. Taylor. The effect of reinforcement architecture on the long-range flow in fibrous reinforcements. *Composites Manufacturing*, 6(3-4):221–235, 1995. doi: 10.1016/0956-7143(95)95015-Q.
- [130] J. Summerscales, P. R. Griffin, S. M. Grove, and F. J. Guild. Quantitative microstructural examination of RTM fabrics designed for enhanced flow. *Composite Structures*, 32(1-4):519–529, 1995. doi: 10.1016/0263-8223(95)00025-9.
- [131] D. M. Basford, P. R. Griffin, S. M. Grove, and J. Summerscales. Relationship between mechanical performance and microstructure in composites fabricated with flow-enhancing fabrics. *Composites*, 26(9):675–679, 1995.
- [132] N.R.L. Pearce, F.J. Guild, and J. Summerscales. An investigation into the effects of fabric architecture on the processing and properties of fibre reinforced composites produced by resin transfer moulding. *Composites Part A: Applied Science and Manufacturing*, 29(1-2):19–27, 1998. doi: 10.1016/S1359-835X(97)00028-6.
- [133] C.-H. Shih and L.J. Lee. Effect of fiber architecture on permeability in liquid composite molding. *Polymer Composites*, 19(5):626–639, oct 1998. doi: 10.1002/pc.10136.
- [134] T.S. Lundström. The permeability of non-crimp stitched fabrics. *Composites Part A: Applied Science and Manufacturing*, 31(12):1345–1353, 2000. doi: 10.1016/S1359-835X(00)00037-3.
- [135] M. Nordlund, T. S. Lundström, V. Frishfelds, and A. Jakovics. Permeability network model for non-crimp fabrics. *Composites Part A: Applied Science and Manufacturing*, 37(6):826–835, 2006. doi: 10.1016/j.compositesa.2005.02.009.
- [136] C. Lekakou, S. Edwards, G. Bell, and S. C. Amico. Computer modelling for the prediction of the in-plane permeability of non-crimp stitch bonded fabrics. *Composites Part A: Applied Science and Manufacturing*, 37(6):820–825, 2006. doi: 10.1016/j.compositesa.2005.04.002.
- [137] S. Dong, H. He, Y. Jia, C. Wang, and X. Jiao. A new structure-related model to predict the permeability of non-crimp fabric preform. *Journal of Composite Materials*, 47(24):3053–3063, 2012. doi: 10.1177/0021998312462156.
- [138] H. Grössing, E. Fauster, M. Weninger, and R. Schledjewski. Influence of Textile Parameters on the In-Plane Permeability Characteristics of Non-Crimped Fabric Preforms. *Polymer Composites*, 37(6):1854–1863, 2015. doi: 10.1002/pc.23360.
- [139] B. Martin, S. Comas-Cardona, C. Binetruy, N. Billon, J.-L. Bouvard, and P. Lucas. Influence of fabrics' design parameters on the morphology and 3D permeability tensor of quasi-unidirectional non-crimp fabrics. *Composites Part A: Applied Science and Manufacturing*, 90:470–479, 2016. doi: 10.1016/j.compositesa.

- 2016.08.013.
- [140] G. Rieber, J. Jiang, C. Deter, N. Chen, and P. Mitschang. Influence of textile parameters on the in-plane Permeability. *Composites Part A: Applied Science and Manufacturing*, 52:89–98, 2013. doi: 10.1016/j.compositesa.2013.05.009.
- [141] X. Sun, S. Li, and L.J. Lee. Mold filling analysis in vacuum-assisted resin transfer molding Part I: SCRIMP based on High-Permeable Medium. *Polymer Composites*, 19(6):807–817, 1998. doi: 10.1002/pc.10156.
- [142] J. Ni, S. Li, X. Sun, and L.J. Lee. Mold filling analysis in vacuum-assisted resin transfer molding Part II: SCRIMP based on Grooves. *Polymer Composites*, 19(6):818–829, 1998. doi: 10.1002/pc.10156.
- [143] A. Hammami. Effect of reinforcement structure on compaction behavior in the vacuum infusion process. *Polymer Composites*, 22(3):337–348, 2001. doi: 10.1002/pc.10542.
- [144] D. Heider, P. Simacek, A. Dominauskas, H. Deffor, S. Advani, and J.W. Gillespie. Infusion design methodology for thick-section, low-permeability preforms using inter-laminar flow media. *Composites Part A: Applied Science and Manufacturing*, 38(2):525–534, 2007. doi: 10.1016/j.compositesa.2006.02.016.
- [145] J. Vilà, C. González, and J. LLorca. Fabric compaction and infiltration during vacuum-assisted resin infusion with and without distribution medium. *Journal of Composite Materials*, 51(5):687–703, 2017. doi: 10.1177/0021998316649783.
- [146] C. Kracke, A. Nonn, C. Koch, M. Nebe, E. Schmidt, S. Bickerton, T. Gries, and P. Mitschang. Interaction of textile variability and flow channel distribution systems on flow front progression in the RTM process. *Composites Part A*, 106:70–81, 2018. doi: 10.1016/j.compositesa.2017.12.010.
- [147] B. Caglar, L. Orgéas, S. Rolland du Roscoat, E. M. Sozer, and V. Michaud. Permeability of textile fabrics with spherical inclusions. *Composites Part A: Applied Science and Manufacturing*, 99:1–14, 2017. doi: 10.1016/j.compositesa.2017.03.031.
- [148] G. Szebényi, T. Czigány, and B. Magyar. 3D printing-assisted interphase engineering of polymer composites: Concept and feasibility. *eXPRESS Polymer Letters*, 11(7):525–530, 2017.
- [149] M. Tonejc, M. Pletz, E. Fauster, and R. Schledjewski. Permeability Customisation Through Preform Manipulation Utilising 3D-Printing Technology. *Polymers and Polymer Composites*, 25(9):651–660, 2017.
- [150] S. Kirinčič and C. Klofutar. A volumetric study of aqueous solutions of poly(ethylene glycol)s at 298.15 K. *Fluid Phase Equilibria*, 149(1-2):233–247, 1998. doi: 10.1016/s0378-3812(98)00369-0.
- [151] B. Chen, E.J. Lang, and T.-W. Chou. Experimental and theoretical studies of fabric compaction behavior in resin transfer molding. *Materials Science and Engineering: A*, 317(1–2):188 – 196, 2001. doi: [http://dx.doi.org/10.1016/S0921-5093\(01\)01175-3](http://dx.doi.org/10.1016/S0921-5093(01)01175-3).
- [152] ASTM D638-10: Standard Test Method for Tensile Properties of Plastics. Technical report, ASTM International, West Conshohocken, PA, 2010. URL <https://doi.org/10.1520/D0638-10>.
- [153] ASTM D7264-07: Standard Test Method for Flexural Properties of Polymer Matrix Composite Materials. Technical report, ASTM International, West Conshohocken, PA, 2007. URL https://doi.org/10.1520/D7264_D7264M-07.

- [154] ASTM D2734-09: Standard Test Methods for Void Content of Reinforced Plastics. Technical report, ASTM International, West Conshohocken, PA, 2003. URL <https://doi.org/10.1520/D2734-09.2>.
- [155] ASTM D2584-11: Standard Test Method for Ignition Loss of Cured Reinforced Resins. Technical report, ASTM International, West Conshohocken, PA, 2011. URL <https://doi.org/10.1520/D2584-11.2>.
- [156] J. Schindelin, I. Arganda-Carreras, E. Frise, V. Kaynig, M. Longair, T. Pietzsch, S. Preibisch, C. Rueden, S. Saalfeld, B. Schmid, J.-Y. Tinevez, D. J. White, V. Hartenstein, K. Eliceiri, P. Tomancak, and A. Cardona. Fiji: an open-source platform for biological-image analysis. *Nature Methods*, 9(7):676–682, 2012. doi: 10.1038/nmeth.2019.
- [157] Henrik Bruus. *Theoretical Microfluids*. Oxford University Press, 2008. ISBN 9780199235087.
- [158] ASTM D1621-16: Standard Test Method for Compressive Properties of Rigid Cellular Plastics. Technical report, ASTM International, West Conshohocken, PA, 2016. URL <https://doi.org/10.1520/D1621-16>.
- [159] J. Wolfrath, V. Michaud, and J.-A. E. Månson. Graded Glass Mat – Reinforced Polypropylene. *Polymer Composites*, 26(3):361–369, 2005. doi: 10.1002/pc.20110.
- [160] Y. P. Khanna, P. K. Han, and E. D. Day. New developments in the melt rheology of nylons. Part I: Effect of moisture and molecular weight. *Polymer Engineering & Science*, 36(13):1745–1754, 1996. doi: 10.1002/pen.10570.
- [161] R. P. Chhabra and J. F. Richardson. Chapter 1 - Non-Newtonian Fluid Behaviour. In R. P. Chhabra and J. F. Richardson, editors, *Non-Newtonian Flow and Applied Rheology (Second Edition)*, pages 1–55. Butterworth-Heinemann, Oxford, 2008. ISBN 978-0-7506-8532-0.
- [162] D. Salvatori, B. Caglar, H. Teixidó, and V. Michaud. Permeability and capillary effects in a channel-wise non-crimp fabric. *Composites Part A: Applied Science and Manufacturing*, 108:41–52, 2018. doi: 10.1016/j.compositesa.2018.02.015.
- [163] L.C. Bank. Flexural and Shear Moduli of Full-Section Fiber Reinforced Plastic (FRP) Pultruded Beams. *Journal of Testing and Evaluation*, 17(1):40, 1989. doi: 10.1520/JTE11531J.
- [164] A. Mehndiratta, S. Bandyopadhyaya, V. Kumar, and D. Kumar. Experimental investigation of span length for flexural test of fiber reinforced polymer composite laminates. *Journal of Materials Research and Technology*, 7(1):89 – 95, 2018. doi: 10.1016/j.jmrt.2017.06.010.
- [165] Lucien Berret. *Life cycle assessment and cost analysis of novel manufacturing processes for thermoplastic composites*. Master thesis, Ecole Polytechnique Fédérale de Lausanne, 2018.
- [166] M.E. Mackay, T.T. Dao, A. Tuteja, D.L. Ho, B. Van Horn, H.-C. Kim, and C.J. Hawker. Nanoscale effects leading to non-Einstein-like decrease in viscosity. *Nature Materials*, 2(11):762–766, 2003.
- [167] A. Tuteja, M.E. Mackay, C.J. Hawker, and B. Van Horn. Effect of Ideal, Organic Nanoparticles on the Flow Properties of Linear Polymers: Non-Einstein-like Behavior. *Macromolecules*, 38(19):8000–8011, 2005.
- [168] A. Tuteja, P.M. Duxbury, and M.E. Mackay. Multifunctional Nanocomposites with Reduced Viscosity. *Macromolecules*, 40(26):9427–9434, 2007.

-
- [169] R.G. Schmidt, G.V. Gordon, C.A. Dreiss, T. Cosgrove, V.J. Krukonis, K. Williams, and P.M. Wetmore. A Critical Size Ratio for Viscosity Reduction in Poly(dimethylsiloxane)-Polysilicate Nanocomposites. *Macromolecules*, 43(23): 10143–10151, 2010.
- [170] K. Nusser, G.J. Schneider, W. Pyckhout-Hintzen, and D. Richter. Viscosity Decrease and Reinforcement in Polymer - Silsesquioxane Composites. *Macromolecules*, 44:7820–7830, 2011.
- [171] J.T. Kalathi, G.S. Grest, and S.K. Kumar. Universal viscosity behavior of polymer nanocomposites. *Physical Review Letters*, 109(19):198301, nov 2012.
- [172] S. Jain, J.G.P. Goossens, G.W.M. Peters, M. van Duin, and P.J. Lemstra. Strong decrease in viscosity of nanoparticle-filled polymer melts through selective adsorption. *Soft Matter*, 4(9):1848, 2008.
- [173] K. Devanand and J.C. Selser. Asymptotic Behavior and Long-Range Interactions in Aqueous Solutions of Poly(ethylene oxide). *Macromolecules*, 24:5943–5947, 1991.

Curriculum Vitae of Damiano SALVATORI

Avenue de Lavaux 10, 1009 Pully, Switzerland
salvatori.damiano@gmail.com
+41 (0)78 814 1800
<https://www.linkedin.com/in/damiano-salvatori>
Skype: damiano.salvatori.com

EDUCATION

- 2014-2018 **Ecole Polytechnique Fédérale de Lausanne (EPFL)**
PhD in Materials Science and Engineering
- 2011-2013 **University of Rome "Tor Vergata"**
Via della Ricerca Scientifica 1, 00133 Rome, Italy
Master's Degree in Materials Science and Technology (GPA: 28.6/30)
"Synthesis and characterization of random-lasers made of hybrid materials based on nanostructured biosilica"
- 2007-2011 **University of Rome "Tor Vergata"**
Bachelor's Degree in Materials Science (GPA: 27.3/30)
"Characterization of Indium Tin Oxide films deposited via Physical Vapor Deposition under varying process conditions"
- 2002-2007 **Liceo Scientifico Statale di Roma "Primo Levi"**
Secondary Diploma of Science

WORK EXPERIENCE

- 2014-2018 **Laboratory for Processing of Advanced Composites**
Ecole Polytechnique Fédérale de Lausanne (EPFL)
Station 12, 1015 Lausanne, Switzerland
Research Assistant
- Industrial research on composite manufacturing
 - Testing of thermoplastic polymers and composites
 - Investigation of strategies to increase volume of production
 - Responsible for maintenance and training of a rheometer
 - Supervision of students' projects and teaching assistant in rheology class
 - Organization of a summer school on 3D Printing
- 2011 **RINA CONSULTING** (prev. Centro Sviluppo Materiali S.p.A.)
Via di Castel Romano 100, 00128 Rome, Italy
Research Intern
- Characterization of ceramic coatings (Indium Tin Oxide)
 - Studying the influence of process conditions (RF sputter deposition) on material properties (optical absorbance, electrical conductivity, cristallinity)

CORE SKILLS

- Processing of thermoplastics: 3D printing by Fused Deposition Modeling (FDM), injection molding
- Processing of composites: Resin Transfer Molding (RTM), compression molding, thermoplastic melt impregnation, solvent casting
- Mechanical characterization: flexural and tensile tests (UTM), Dynamic Mechanical Analysis (DMA)
- Fluid flow through porous media: fabric permeability, unsaturated flow
- Rheology of polymers and chemorheology
- Solution synthesis of ceramic nano-/micro-particles (SiO₂, ZnO)
- Optical properties: absorbance, photoluminescence
- Data analysis and visualization (Excel, Origin, Tableau)
- Advanced text editing and graphics (Latex, SolidWorks, Photoshop, Illustrator)

LANGUAGES

English: Fluent
French: Fluent
German: Basics
Italian: Native

PERSONAL INTERESTS

Climbing and mountaineering
Geopolitics
Following an online course on Data science and visualization

PERSONAL INFORMATION

Birth: 1988
Citizenship: Italian
Civil status: Single
Swiss residence permit: B
Swiss driving license: B

PUBLICATIONS AND CONFERENCES

D. Salvatori, B. Caglar, V. Michaud. “Enhancing permeability of a woven glass-fabric preform with 3D spacers”, *18th European Conference in Composite Materials*, Athens (Greece), June **2018**.

B. Caglar, D. Salvatori, E.M. Sozer, V. Michaud. “In-plane permeability characterization using an inverse method based on flow front visualization”, *18th European Conference in Composite Materials*, Athens (Greece), June **2018**.

B. Caglar, D. Salvatori, E.M. Sozer, V. Michaud. “In-plane permeability distribution mapping using resin flow front detection”, *Composites Part A*, under revision (**2018**).

D. Salvatori, V. Michaud. “Strategies for in-plane thermoplastic melt impregnation of glass fabrics”, *14th International Conference on Flow Processes in Composite Materials*, Luleå (Sweden), June **2018**.

D. Salvatori, B. Caglar, H. Teixidó, V. Michaud. “Permeability and capillary effects in a channel-wise non-crimp fabric”, *Composites Part A* 108 (**2018**).

D. Salvatori, V. Michaud. “Capillary effects in LCM with high-viscosity matrices and highly anisotropic non-crimp fabrics”, *13th International Conference on Flow Processes in Composite Materials*, Kyoto (Japan), July **2016**.

B. Caglar, D. Salvatori, E.M. Sozer, V. Michaud. “A tool for minimization of race-tracking effects in permeability measurements”, *13th International Conference on Flow Processes in Composite Materials*, Kyoto (Japan), July **2016**.

F.R. Lamastra, M.L. Grilli, G. Leahu, A. Belardini, R. Li Voti, C. Sibilia, D. Salvatori, I. Cacciotti, F. Nanni. “Diatom frustules decorated with zinc oxide nanoparticles for enhanced optical properties”, *Nanotechnology* 28 (**2017**).

F.R. Lamastra, R. De Angelis, A. Antonucci, D. Salvatori, P. Proposito, M. Casalboni, R. Congestri, S. Melino and F. Nanni. “Polymer composite random lasers based on diatom frustules as scatterers”, *RSC Advances* 4 (**2014**).